THE UNIVERSITY *of* EDINBURGH

MAGNETIC RESONANCE IMAGING

IN

CARDIOVASCULAR DISEASE

BY

Jennifer Margaret Jane Richards

A thesis presented for the degree of Doctor of Philosophy at the

University of Edinburgh

2012

ABSTRACT

Background Superparamagnetic particles of iron oxide (SPIO) are part of a novel and exciting class of 'smart' magnetic resonance imaging (MRI) contrast agents that are taken up by inflammatory cells. Ultrasmall SPIO (USPIO; ~30 nm diameter) can be used to assess cellular tissue inflammation and SPIO (80-150 nm) have the potential to be used to label cells *ex vivo* for *in vivo* cell tracking studies.

Objectives The aims of the thesis were therefore (i) to develop and validate quantitative MRI methodology for assessing SPIO uptake within tissues, (ii) to demonstrate USPIO accumulation within the aortic wall and its implications in patients with abdominal aortic aneurysms (AAA), and (iii) to develop and apply a Good Manufacturing Practice (GMP) compliant method of SPIO cell labelling in healthy volunteers.

Methods Patients with asymptomatic AAA >4.0 cm in diameter were recruited. Imaging sequences were optimised in eight patients using a 3 tesla MRI scanner. Data were analysed using the decay constant for multi echo T2* weighted (T2*W) sequences (T2*) or its inverse (R2*) and the repeatability of these measurements was established. A further twenty-nine patients underwent MRI scanning before and 24-36 hours after administration of USPIO. T2 and multi echo T2*W sequences were performed and ultrasound-based growth rate data were collected. Operative aortic wall tissue samples were obtained from patients undergoing open surgical aneurysm repair.

A GMP compliant protocol was developed for labelling cells with SPIO for clinical cell tracking studies. The effects of SPIO-labelling on cell viability and function were assessed *in vitro*. A phased-dosing protocol was used to establish the safety of intravenous administration of SPIO-labelled cells in healthy volunteers. The feasibility of imaging cells at a target site *in vivo* following local or systemic administration was assessed. Tracking of SPIO-labelled cells to a target site was investigated by inducing an iatrogenic inflammatory focus in the skin of the anterior thigh of healthy volunteers, following which autologous SPIO-labelled cells were administered and their accumulation was assessed using MRI scanning and histology of skin biopsies.

Results Robust and semi-quantitative data acquisition and image analysis methodology was developed for the assessment of SPIO accumulation in tissues. In patients with AAA, histological analysis of aortic wall tissue samples confirmed USPIO accumulation in areas of cellular inflammation. USPIO-enhanced MRI detected aortic wall inflammation and mural USPIO uptake was associated with a 3-fold higher aneurysm expansion rate.

Human mononuclear cells were labelled with SPIO under GMP compliant conditions without affecting cell viability or function. Both local and intravenous administration of SPIO-labelled cells was safe and cells were detectable *in vitro* and *in vivo* using a clinical MRI scanner. SPIO-labelled cells tracked to a focal iatrogenic inflammatory

focus following intravenous administration in humans and were detectable on MRI scanning and histological examination of skin biopsies.

Conclusions SPIO contrast agents have an extensive range of potential clinical applications. USPIO uptake in the wall of AAA appears to identify cellular inflammation and predict accelerated aneurysm expansion. This is therefore a promising investigative tool for stratifying the risk of disease progression in patients with AAA, and may also be considered as a biomarker for response to novel pharmacological agents. The ability to label cells for non-invasive cell tracking studies would facilitate the further development of novel cell-based therapies and would enable assessment of dynamic inflammatory processes through inflammatory cell tracking.

CONTENTS

ABBREVIATIONS

AAA	Abdominal aortic aneurysm
ACE	Angiotensin-converting enzyme
ANOVA	Analysis of variance
ApoE	Apoliprotein E
β-blockers	Beta-adrenoceptor blockers
B_0	External magnetic field
CD	Cluster of differentiation
CFP	Cyan fluorescent protein
COPD	Chronic obstructive pulmonary disease
COX-2	Cyclooxygenase-2
CRP	C-reactive protein
CT	Computed tomography
CTIMP	Clinical Trial of an Investigational Medicinal Product
CV	Coefficient of variation
DNA	Deoxyribose nucleic acid
ECM	Extracellular matrix
EDTA	Ethylenediaminetetraacetic acid
eGFR	Estimated glomerular filtration rate
EVAR	Endovascular aneurysm repair
FDA	Food and Drug Administration
^{18}F-FDG	^{18}F-fluorodeoxyglucose
^{18}F-NaF	^{18}F-sodium fluoride
FITC	Fluorescein isothiocyanate
GFP	Green fluorescent protein
GMP	Good Manufacturing Practice
HBSS	Hank's balanced salt solution
HIV-Tat	Human immunodeficiency virus transactivator of transcription
HLA	Human leucocyte antigen
IFNγ	Interferon gamma
IL	Interleukin
ILT	Intraluminal thrombus

IMDM	Iscove's modified Dulbecco's medium
iNOS	Inducible nitric oxide synthetase
IRON	Inversion Recovery with ON - resonant water suppression
JNK	c-Jun N-terminal kinase
LDH	Lactate dehydrogenase
LDL	Low-density lipoprotein
MACS	Magnetic-activated cell sorting
MASS	Multicentre Aneurysm Screening Study
MCP-1	Monocyte chemoattractant protein-1
MHRA	Medicines and Healthcare products Regulatory Agency
MMP	Matrix metalloproteinase
MPIO	Micron-sized particles of iron oxide
MRI	Magnetic resonance imaging
MSC	Mesenchymal stem cells
NADPH	Nicotinamide adenine dinucleotide phosphate
NIRF	Near infrared fluorescent
NK cells	Natural killer cells
NMV	Net Magnetisation Vector
NSF	Nephrogenic systemic fibrosis
PBMC	Peripheral blood mononuclear cells
PBS	Phosphate buffered saline
PET	Positron emission tomography
PET-CT	Positron emission tomography-computed tomography
PI	Propidium iodide
PLL	Poly-L-lysine
PO_2	Partial pressure of oxygen
PPD	Purified protein derivative
r^2	Coefficient of determination
RANTES	Regulated on Activation, Normal T-cell Expressed and Secreted
ROI	Region of Interest
ROS	Reactive oxygen species

RPMI	Roswell Park Memorial Institute
SEM	Standard error of the mean
SI	Signal intensity
SPECT	Single photon emission computed tomography
SPIO	Superparamagnetic particles of iron oxide
SPSS	Statistical Package for the Social Sciences
SSE	Sum of squared deviations due to error
T	Tesla
T2W	T2 weighted
TE	Echo time
T_h	T helper
TIMP	Tissue inhibitor of metalloproteinases
TNFα	Tumour necrosis factor alpha
TNFβ	Tumour necrosis factor beta
TR	Repetition time
UKSAT	United Kingdom Small Aneurysm Trial
USADAM	United States Aneurysm Detection and Management study
USPIO	Ultrasmall superparamagnetic particles of iron oxide
USS	Ultrasound scanning
VSMC	Vascular smooth muscle cells

DECLARATION

This thesis represents research that I have undertaken in the British Heart Foundation University of Edinburgh Centre for Cardiovascular Science and the Vascular Surgery Service, Royal Infirmary of Edinburgh between August 2006 and August 2010.

I was personally involved in every aspect of the work presented in this thesis. In keeping with the collaborative nature of this work, assistance was received and is acknowledged. Dr Ninian Lang undertook the intramuscular administration of labelled cells presented in Chapter 5. Dr Catherine Shaw undertook the flow cytometry presented in Chapter 5.

This thesis has not been submitted elsewhere in application for a university degree and all sources of information have been acknowledged. All studies were undertaken vin accordance with the regulations of the Scotland A Research Ethics Committee, the Lothian Local Research Ethics Committee, the Medicines and Healthcare products Regulatory Agency and the Declaration of Helsinki of the World Medical Association. The written informed consent of each participant was obtained before entry into the studies.

The British Heart Foundation funded these studies through a Clinical Research Training Fellowship (FS/07/060) and Centre of Research Excellence Award. This work was also supported through grants from the Translational Medicine Researchers Collaboration (CVMD-EU-112/120) and the Royal College of Surgeons Edinburgh.

Jennifer Richards 28 February 2012

ACKNOWLEDGEMENTS

This thesis has been conducted under the primary supervision of Professor David Newby. As a vascular surgeon, it was great to be welcomed into the Newby team and I very much enjoyed working with the cardiology research fellows in the productive and convivial environment that he has cultivated. I am most grateful to Professor Newby for his endless enthusiastic support and encouragement that was crucial in giving me the momentum to surmount the many hurdles that I encountered along the way. The mere mention of the charming Professor Newby opened many doors and facilitated my navigation through the most beaurocratic aspects of conducting clinical trials. From the surgical side, I am also grateful to my other supervisors Professor O James Garden and Mr Roderick Chalmers both of whom have guided and supported me throughout and whose backing was critical in enabling the studies to be undertaken in the Department of Surgery. In addition, I was grateful for the help and know-how of Dr Scott Semple, Dr Katie Shaw, Dr Kev Dhaliwal, Professor John Simpson, Dr William Wallace, Dr Graham McKillop and all of the cardiology research fellows who have provided extra pairs of hands at critical moments.

This work was funded through grants from the British Heart Foundation, the Translational Medicine Research Collaboration and the Royal College of Surgeons of Edinburgh. The work presented here would not have been possible without their generous support.

By its nature, this work was highly collaborative and I have relied upon the co-operation of very many people and departments. In particular I would like to thank

the staff of the Wellcome Trust Clinical Research Facility, the Cell Separator Unit, the Tuberculosis Specialist Nurses, the Scottish Blood Transfusion Service, the Vascular Surgical Service and the Clinical Research Imaging Centre radiographers and Image Analysis team. Importantly, none of this work would have been possible without the patients and participants who gave up their time to be part of the studies.

It was at times almost disappointing to find that, having slaved away on a paper or a chapter for two or three weeks, it would be delivered back into my court after only a couple of hours respite in Professor Newby's inbox. However, I am indebted to him for this efficiency which has got me to the finishing line without too much time having elapsed. And without the perseverance of Jean Cunningham I would probably still be battling with page numbers and trying to conjure up a list of abbreviations!

My friends and fellowship group have sustained me during the last four years and have managed an impressive level of interest in what I have been up to. Most important of all, however, my parents, grandparents, brother James and wonderful husband Andrew have been amazing throughout, and during the writing of this thesis have (for the most part!) done a good job of treading the fine line between encouraging and nagging. I hope that this thesis is a credit to their love and support.

CHAPTER 1

INTRODUCTION

1.1 INTRODUCTION

An aneurysm may be defined as an abnormal, permanent, focal dilatation of a blood vessel to more than 1.5 times its normal diameter, differentiating it from vascular ectasia which is typically diffuse and widespread.

Abdominal aortic aneurysm (AAA) is the 13th leading cause of death in the United Kingdom and other western countries. Around 6,800 deaths each year in the United Kingdom and 15,000 deaths annually in the United States are attributed to AAA [Ashton *et al* 2002; General Register Office for Scotland Mortality Statistics 2008; Office for National Statistics England and Wales 2008]. The condition is most prevalent amongst elderly men. With 5-7.6% of men over the age of 65 years affected, AAA accounts for 2-3% of deaths in this age group [Gillum 1995; UK National Screening Committee 2010].

1.2 AETIOLOGY OF ABDOMINAL AORTIC ANEURYSM DISEASE

The aetiology of aneurysm disease is multifactorial with contributions from both environmental and genetic influences. Cigarette smoking, hypertension, increasing age, male sex and hypercholesterolaemia (elevated serum low-density lipoprotein (LDL)) have been correlated positively with the incidence of AAA, whilst for reasons that are not fully understood, diabetes mellitus is associated with a reduced risk of aneurysm development [Brady *et al* 2004; Shantikumar *et al* 2010]. The main determinant of rupture is aneurysm diameter but interestingly, whilst continued

cigarette smoking and hypertension are also associated with increased risk of aneurysm rupture, age is not influential and female rather than male sex increases rupture risk [Brown and Powell 1999; Brady *et al* 2004; Mofidi *et al* 2007; Grootenboer *et al* 2009]. Chronic obstructive pulmonary disease (COPD) and reduced forced expired volume also increase risk of rupture but are difficult to disentangle from smoking history as independent risk factors [Brown and Powell 1999].

Familial clustering of AAA is well described with an incidence of 19.2% amongst first-degree relatives of patients with AAA corresponding to a relative risk of 11.6 compared to the general population [Johansen and Koepsell 1986]. Data from the Swedish twin registry further support the heritability of AAA [Wahlgren *et al* 2010]. Whilst single gene connective tissue disorders including Marfan's syndrome (defect in fibrillin 1 gene) and Ehlers-Danlos syndrome (defect in collagen III synthesis), and vasculitides, such as Takyasu's arteritis and Behçets disease, account for a small proportion of these cases, the majority are likely to be polygenetic [Kontusaari *et al* 1990; Matsumura *et al* 1991; Devereux and Roman 1999; Erentug *et al* 2003]. This has led to a number of candidate gene studies. Polymorphisms of putative genes involved in processes known to contribute to the pathogenesis of AAA, such as inflammation and proteolysis, have been pursued, including matrix metalloproteinase (MMP)-2, MMP-9, human leucocyte antigen (HLA) and angiotensin-converting enzyme (ACE) [Sandford *et al* 2007]. More recently whole genome expression profiling using microarrays has been used to identify putative genes that are differentially expressed in patients with AAA compared to controls,

and at sites of AAA rupture compared to elsewhere in the aneurysm [Choke *et al* 2009; Giusti *et al* 2009]. No single causative gene has yet been identified however.

1.3 ANEURYSM DISEASE AND ATHEROSCLEROSIS

Aneurysm disease was traditionally thought to lie within the spectrum of atherosclerosis. However, whilst atherosclerosis is a ubiquitous finding in patients with AAA and the two processes share a number of common risk factors, there are also a number of differences suggesting that aneurysm disease and atherosclerosis represent separate pathological entities [Reed *et al* 1992; Lederle *et al* 2003].

Microscopically, atherosclerosis primarily affects the tunica intima and involves loss of endothelial function, inflammatory infiltration, deposition of LDL within activated macrophages (foam cells) and migration of vascular smooth muscle cells (VSMC) from the media into the resulting plaque [Naghavi *et al* 2003]. In contrast, aneurysm disease involves inflammation, loss of VSMC and proteolytic degradation of elastin fibres within the tunica media [Choke *et al* 2005]. Additionally, different stimuli are used to induce AAA *versus* atherosclerosis in animal models, and in human populations, whilst atherosclerosis is common, AAA is comparatively rare [Jaffer *et al* 2002]. Atherosclerosis is generally widespread throughout a number of vascular beds, including coronary, carotid, cerebral and infrainguinal vessels. Although many patients exhibit generalised vascular ectasia, aneurysm formation is typically confined to the infrarenal aorta. Within the aorta itself, aneurysm disease affects the entire infrarenal segment whilst the atherosclerotic burden is usually concentrated

distally around the bifurcation. Finally, whilst population-based primary and secondary prevention measures such as best medical therapy and smoking bans have reduced the mortality from atherosclerotic disease, AAA-related mortality continues to increase [Lederle *et al* 2003; Meyers *et al* 2009]. Together these data suggest that aneurysm disease is related to but distinct from atherosclerosis.

1.4 PATHOLOGY OF AORTIC ANEURYSMS

Until recently the formation, growth and rupture of aneurysms was attributed to the 'wear and tear' effect of pulsatile blood flow on the aortic wall over a number of decades, but is now recognised to be the result of a complex interaction between biomechanical factors and biological processes, which include neovascularisation, inflammation and proteolysis.

1.4.1 BIOMECHANICAL FACTORS

The Law of Laplace, which states that wall stress is proportional to the radius of the vessel, is no longer thought to be an adequate explanation of aneurysm disease. This Law is only valid for thin-walled, uniformly-cylindrical, biologically inert structures. It therefore does not take into account the complex geometry, heterogeneity of wall thickness, presence of intraluminal thrombus (ILT) or biologically active nature of AAA. Finite Element Analysis is evolving as a more accurate tool to predict the wall stress in AAA [Raghavan *et al* 2000]. Finite Element Analysis involves accurate delineation of the aneurysm geometry from computed tomography (CT) data with subsequent segmentation of the resulting 3-dimensional volume into a number of

finite elements. The biomechanical environment of each element can then be calculated using iterative mathematical modelling algorithms and combined to give a global picture for the whole aneurysm. However, whilst this improved method can estimate the radial wall stress more accurately, it fails to address the ability of the aneurysm wall to withstand the forces being applied to it, i.e. its tensile strength. There is currently no method available that can non-invasively highlight areas of the vessel wall that have become weakened and would therefore be more vulnerable to rupture.

1.4.2 BIOLOGICAL FACTORS

Aneurysm tissue is characterised by excessive medial neovascularisation, infiltration of inflammatory cells (principally macrophages and lymphocytes) and irreversible remodelling of the extracellular matrix (ECM).

Neovascularisation

In contrast to the thoracic aorta, the tunica media of the abdominal aorta is not normally supplied by vasa vasorum and the presence of microvasculature in the media of the abdominal aortic wall is a pathological finding [Wolinsky and Glagov 1969]. Since the aortic wall is nourished directly from the lumen, the presence of ILT, renders the inner layer of the media hypoxic [Vorp *et al* 2001; Choke *et al* 2006a]. This stimulus is thought to attract inflammatory cells and induce the secretion of angiogenic factors promoting neovascularisation [Vorp *et* al 2001; Choke *et al* 2006b]. These new vessels not only supply oxygen and nutrients to the arterial wall but also amplify the pathological process by promoting further

inflammatory infiltration [Thompson *et al* 1996; Reeps *et al* 2009b]. Endothelial cells within these immature vessels also contribute directly to the destruction of the aortic wall through secretion of proteolytic enzymes and cytokine release [Reeps *et al* 2009b]. The presence of neovessels in the aortic wall has been correlated with the degree of wasting of the ECM [Reeps *et al* 2009b].

1.4.3 INFLAMMATION

It is widely held that inflammation plays a critical role in the development and progression of AAA, and both cellular and humoral mechanisms are involved. Inflammatory cells are recruited into the aortic wall by secretion of a variety of cytokines and the products of ECM degradation. Inflammatory cells in the media and adventitia surround neovessels [Reeps *et al* 2009b]. The reported composition of the inflammatory infiltrate varies in the literature, likely reflecting significant heterogeneity amongst patients. Numerically T lymphocytes are the predominant cell type and are present along with macrophages and B lymphocytes in the media and adventitia [Houard *et al* 2009; Reeps *et al* 2009b]. Neutrophils are found in the tunica adventitia and in the luminal aspect of the ILT [Eliason *et al* 2005; Houard *et al* 2009]. Plasma cells and natural killer (NK) cells exist in smaller numbers, and more recently a role has been proposed for mast cells in AAA pathophysiology [Tsuruda *et al* 2008; Sun *et al* 2009].

Lymphocytes are predominantly T helper (T_h) cells with a smaller proportion of B cells and plasma cells. T helper cells are not themselves independently cytotoxic or phagocytic, but rather modify and orchestrate the actions of cells around them to

enhance and co-ordinate the inflammatory response. The humoral inflammatory response is induced by T_h2 **c**luster of differentiation (CD)3+ cells, the most numerous cell type in AAA, which secrete a range of pro- and anti-inflammatory cytokines (interleukin (IL)-4, IL-5, IL-6, IL-8, IL-10, IL-13) that are chemoattractant and angiogenic [Schonbeck *et al* 2002; Santana and Rosenstein 2003]. In addition they release the Fas ligand stimulating VSMC apoptosis. This is important because VSMC are the major source of ECM generation in the aortic wall. Furthermore, secretion of CD40 and interferon gamma (IFNγ) induce MMP production by monocytes and macrophages. T_h1 cells activate and enhance the function of macrophages through secretion of IL-2, tumour necrosis factor beta (TNFβ) and IFNγ [Santana and Rosenstein 2003].

Whilst fewer in number than lymphocytes, macrophages accumulate in the aortic wall early on during the process of aneurysm development, have a diverse range of functions and play a key role in the pathogenesis of AAA. Macrophages secrete pro-inflammatory cytokines which include IL-1β, IL-6, IL-8 and tumour necrosis factor alpha (TNFα) which exacerbate tissue injury, stimulate neovascularisation and induce the secretion of further cytokines by adjacent leucocytes. Macrophages also secrete a number of MMP including MMP-1, -2, -3, -8 and -9, and induce other cells, such as VSMC and immature endothelial cells, to secrete further MMP [Wilson *et al* 2005; Wilson *et al* 2006; Reeps *et al* 2009b]. Through induction of apoptotic pathways such as Perforin and Fas, macrophages also lead to loss of VSMC within the aortic wall [Geng *et al* 1997; Henderson *et al* 1999].

The cause of the inflammatory response in AAA remains unclear. Since the association was made between aneurysm formation and *Treponema pallidum*, the causative agent for syphilis, other microorganisms have been pursued as part of the investigation of the aetiology of inflammation in AAA. Cytomegalovirus infection has been associated with inflammatory AAA [Tanaka *et al* 1994]. Inflammatory aneurysms are a specific subtype of AAA characterised by the classical triad of thickening of the aortic wall, retroperitoneal fibrosis and adhesions to adjacent structures [Walker *et al* 1972]. Clinically such patients typically present with abdominal or back pain, weight loss and ureteric obstruction, along with evidence of systemic inflammation (such as elevated erythrocyte sedimentation rate). Rather than representing a distinct clinical entity, inflammatory aneurysms are likely to represent the extreme end of the spectrum since inflammation is evident to a varying degree in all aneurysms.

Chlamydia pneumoniae has also been implicated as a result of the finding of *Chlamydia pneumoniae* deoxyribose nucleic acid (DNA) in the aortic wall and the cross-reactivity of circulating antibodies to *Chlamydia pneumoniae* present in the serum of patients with AAA with components of the aortic wall [Juvonen *et al* 1997a; Lindholt *et al* 2003]. The nature of the immune response in AAA is consistent with that of an autoimmune disease with a polycolonal T cell response and the presence of memory B cells in the aortic wall [Freestone *et al* 1995]. The possibility of an autoimmune aetiology is further supported by the increased incidence of other autoimmune diseases in patients with AAA, and the association of AAA with specific HLA molecules [Haug *et al* 2003]. Human leucocyte

antigen-DR2**,** particularly the B1(*)02 and B1(*)04 alleles, are associated with inflammatory infiltration of the aortic wall and a doubling of the risk of AAA formation [Rasmussen *et al* 2001; Rasmussen *et al* 2002]. Molecular mimicry between *Chlamydia pneumoniae* antigens and components of the aortic wall has been proposed as a possible link between the infectious and autoimmune contributions to the pathophysiology of AAA [Lindholt and Shi 2006].

Circulating markers of inflammation provide further evidence of the role of inflammation in AAA and have attracted interest as potential diagnostic and prognostic biomarkers [Golledge *et al* 2008]. The cytokine profile in AAA is characteristically of the T_h2 type (IL-4, IL-5, IL-6, IL-8, IL-10, IL-13) rather than the T_h1 type (IL-2, TNFβ and IFNγ) that dominates in atherosclerotic disease [Libby 2002; Schonbeck *et al* 2002]. Interleukin-6, a pro-inflammatory cytokine, is produced by a variety of cell types including monocytes, macrophages, T_h2 lymphocytes, fibroblasts, endothelial cells and VSMC. It is elevated in both aortic tissue and serum in patients with AAA [Juvonen *et al* 1997b; Lindeman *et al* 2008]. Interestingly IL-6 levels are highest when blood is sampled just distal to the aneurysm suggesting that the aneurysm itself may be the source [Juvonen *et al* 1997b; Dawson *et al* 2006]. An increase in the ratio of IL-6 to the anti-inflammatory cytokine IL-10 was observed in patients with AAA [Wallinder *et al* 2009]. Interleukin-1β, IL-2, TNFα and IFNγ (female patients only) are also elevated in AAA compared to both healthy controls and patients with atherosclerotic disease [Juvonen *et al* 1997b]. Expressed by macrophages, T cells and B cells, and involved in leucocyte adhesion and migration, osteopontin is increased in the serum of

patients with AAA [Golledge *et al* 2007b]. Most studies have shown C-reactive protein (CRP) to be increased in AAA, particularly in symptomatic patients. However**,** two smaller studies showed no significant difference between patients and controls [Powell *et al* 1987; Hobbs *et al* 2003; Dawson *et al* 2007; Golledge *et al* 2007a; Sakthivel *et al* 2007; Tambyraja *et al* 2007].

Of these circulating factors, only osteopontin and IFNγ have shown a correlation with AAA expansion rate, and α1 antitrypsin has been associated with risk of rupture [Engstrom *et al* 2004; Golledge *et al* 2007b; Juvonen *et al* 1997b]. Whilst a range of cytokines has been related to the presence of AAA, none have sufficient power or specificity to predict clinical events accurately, and a biomarker for disease progression remains elusive.

In summary, through a number of mechanisms, inflammation plays a key role in the pathology of AAA, ultimately compromising the biomechanical properties of the aortic wall and rendering it vulnerable to aneurysm formation and rupture.

1.4.4 MACROPHAGES AND OXIDATIVE STRESS

Oxidative stress causes and amplifies tissue damage, and occurs when there is excessive generation of reactive oxygen species or an antioxidant deficit. Activated macrophages create a situation of oxidative stress in the aortic wall through nicotinamide adenine dinucleotide phosphate (NADPH) oxidase activity producing H_2O_2 and O_2 [McCormick *et al* 2007]. Both neutrophils and macrophages also generate HOCl from H_2O_2 through myeloperoxidase activity. Immature endothelial

cells in neovessels exhibit upregulation of inducible nitric oxide synthetase (iNOS). Whilst nitric oxide production is considered to be an important part of normal endothelial function in health, if produced in excess it can lead to tissue damage through a number of mechanisms including reaction with heavy metals and with oxygen free radicals leading to nitrosative stress. Activated smooth muscle cells and fibroblasts also contribute to oxidative stress. Mechanical forces acting on VSMC, oxidised-LDL and cytokines increase NADPH activity, exacerbating tissue oxidative stress [Hishikawa *et al* 1997; Grote *et al* 2003].

Free radicals induce tissue damage by reacting with proteins, lipids and DNA. In AAA, reactive oxygen species (ROS) lead to disease progression through a number of potential mechanisms which include increased secretion of cytokines (including IL-8, monocyte chemoattractant protein-1 (MCP-1)) [Lum and Roebuck 2001], expression of endothelial leucocyte adhesion molecules [Lum and Roebuck 2001], increased MMP and plasminogen activity [Rajagopalan *et al* 1996; Deng *et al* 2003; Ejiri *et al* 2003; Satoh *et al* 2009], increased osteopontin secretion leading to enhanced MMP-9 and NADPH activity [Bruemmer *et al* 2003; Lai *et al* 2006; Golledge *et al* 2007b], local VSMC apoptosis and systemic vascular hypertension [Laursen *et al* 1997].

In aneurysm tissue there is evidence of increased ROS production and reduced antioxidant availability. Both nitrotyrosine (a marker of amino acid oxidation) and nitrites (a marker of nitric oxide activity) are increased in aneurysm tissue [Paik and Tilson 1996; Zhang *et al* 2003]. Furthermore iNOS expression by macrophages and

lymphocytes is increased in the diseased aortic wall and superoxide levels in aneurysmal aorta are double those in the adjacent atherosclerotic aorta [Miller *et al* 2002; Zhang *et al* 2003]. Levels of antioxidants including zinc, copper, ascorbate, glutathione and manganese superoxide dismutase are reduced in the aortic wall in AAA [Dubick *et al* 1987; Dubick *et al* 1999]. Plasma vitamin E is reduced in patients with AAA compared to both healthy controls and patients with atherosclerotic disease [Sakalihasan *et al* 1996; Micheletta *et al* 2004]. In rodent models administration of vitamin E attenuates the size and frequency of AAA, although this effect has not yet been replicated in small-scale human studies of antioxidant administration [The Alpha-Tocopherol, Beta Carotene Cancer Prevention Study Group 1994; Tornwall *et al* 2001; Gavrila *et al* 2005].

Together these data support the importance of oxidative stress in AAA pathophysiology and emphasise the key role that macrophages play in this process [McCormick *et al* 2007].

1.4.5 PROTEOLYTIC ACTIVITY

The irreversible remodelling of the aortic wall that results in aneurysm formation, expansion and rupture, involves an imbalance between the synthesis and breakdown of elastin and collagen: the principal proteins of the ECM. In health, elastin fibres constitute the main load-bearing component of the aortic wall at physiological pressures. Depletion of elastin fibres in the aortic wall results in dilatation of the vessel, transfer of load-bearing to collagen fibres and increased wall stiffness [Raghavan *et al* 1996; Wilson *et al* 1999; Wilson *et al* 2001]. Initially, this is

accompanied by an increase in the collagen content but later on in the process, focal loss of collagen fibres and impairment of tensile strength precede rupture [Raghavan *et al* 1996]. The inflammatory infiltrate has been correlated with depletion of the elastin and collagen content of the aortic wall in AAA [Reeps *et al* 2009b].

Extracellular matrix is lost through a combination of reduced production and increased breakdown. Vascular smooth muscle cell apoptosis and senescence results in decreased ECM production. Increased ECM breakdown occurs through dysregulation of the ratio between MMP and their endogenous inhibitors, the tissue inhibitors of metalloproteinases (TIMP) [Choke *et al* 2005]. The resulting increase in proteolytic activity is central in the pathogenesis of AAA.

The role of fibroblasts in AAA is not well studied. They are a source of proteolytic enzymes and secrete chemotactic and pro-angiogenic factors, but as a source of collagen may also have a role in repair of the injured aortic wall [Choke *et al* 2005]. Indeed aneurysm disease is associated with increased numbers of fibroblasts in the aortic wall [Zou *et al* 2012].

Matrix metalloproteinases, a family of zinc-dependent endopeptidases, are proteolytic enzymes whose principal substrates are elastin (MMP-2, -7, -9 and -12) and collagen (MMP-1, -8 and -13). In particular, MMP-2 and MMP-9 have been widely implicated in the pathology of AAA [Freestone *et al* 1995; Longo *et al* 2002]. Matrix metalloproteinase-2 is elevated in the aneurysmal aorta, particularly in small diameter (4-5.5 cm) aneurysms [Freestone *et al* 1995]. Matrix metalloproteinase-9 is

localised to macrophages and is also over-expressed in aneurysm tissue, particularly in large AAA >5.5 cm [Thompson *et al* 1995; Tamarina *et al* 1997]. Furthermore, in ruptured AAA the concentration of MMP-9 is seven times higher at the site of rupture than elsewhere in the aneurysm sac [Wilson *et al* 2006]. It has been postulated, therefore, that MMP-2 may initiate aneurysm formation whilst MMP-9 is critical for further expansion and subsequent rupture.

1.4.6 THROMBUS

Intraluminal thrombus is found in the majority of aortic aneurysms with its deposition favoured by aortic tortuosity, turbulent flow, endothelial injury and low wall shear stress [Hans *et al* 2005]. Intraluminal thrombus is multi-layered with graded changes in composition between its luminal and abluminal surfaces [Adolph *et al* 1997; Matusik *et al* 2010; Folkesson *et al* 2011]. The luminal aspect is freshly deposited and is typically highly cellular with platelets, erythrocytes and polymorphonuclear leucocytes (neutrophils) trapped in a fibrin mesh. The abluminal component, in contrast, is virtually acellular consisting of dense, highly-organised fibrin through which canaliculi can permit passage of macromolecules [Gasser *et al* 2009].

The role of ILT is not well understood. Indeed it is not yet clear whether the presence of ILT favours, protects against or is simply a consequence of AAA expansion. Biomechanical models suggest that ILT dissipates the radial stress evenly across the aortic wall reducing peak wall stress [Wang *et al* 2001; Georgakarakos *et al* 2009; Speelman *et al* 2010]. Mechanical failure of the ILT, allowing blood to track through

a fissure into a plane between the thrombus and the aortic wall, may be critical in precipitating aneurysm rupture [Polzer *et al* 2011]. The so-called 'crescent sign' representing this phenomenon is recognised as a high-risk feature on CT and magnetic resonance imaging (MRI) scans [Mehard *et al* 1994; Roy *et al* 2008]. Thrombus volume has been shown to correlate with aneurysm expansion and rupture, although the ratio between ILT volume and total aneurysm volume does not appear to be influential so this is of uncertain significance [Stenbaek *et al* 2000; Speelman *et al* 2010].

The biological activity of ILT has also been studied in relation to aortic wall degradation. Intraluminal thrombus produces MMP, other proteases and plasmin, which it was thought might promote aortic wall destruction [Kazi *et al* 2005]. One study observed higher proteolytic activity at the abluminal surface of the thrombus, although this may derive from the wall itself rather than from the thrombus [Kazi *et al* 2003; Kazi *et al* 2005]. A recent study has shown that whilst proteases are expressed at both the luminal and abluminal surfaces of the ILT, actual protease activity is only found at the luminal surface because proteases at the abluminal surface are inactivated by an excess of inhibitors [Folkesson *et al* 2011].

An alternative mechanism through which the ILT may influence the aortic wall is by creation of a hypoxic environment inducing oxidative stress. The partial pressure of oxygen (PO_2) is lower in thrombus-covered wall in animal models and in patients with AAA [Vorp *et al* 1996; Bjornheden *et al* 1999; Vorp *et al* 2001; Choke *et al* 2006a]. Hypoxia alters the behaviour of VSMC and increases MMP-2 production

[Erdozain *et al* 2010]. Thrombus-covered wall has been found to be thinner, with evidence of medial neovascularisation, inflammatory infiltration, increased protease activity, destruction of elastin fibres and a reduction in tensile strength [Kazi *et al* 2003; Choke *et al* 2006b; Coutard *et al* 2009].

1.5 BIOLOGICAL 'HOTSPOTS'

These pathological processes do not affect the aorta uniformly but are focal in nature. Radial wall stress varies spatially within the aneurysm [Raghavan *et al* 2000], and tensile strength varies in different parts of the aneurysm sac [Vallabhaneni *et al* 2004]. Focal neovascularisation is present at the site of rupture [Choke *et al* 2006b] and its presence corresponds to the degree of inflammation [Thompson *et al* 1996]. Matrix metalloproteinases -8 and -9 are increased locally at the site of rupture [Wilson *et al* 2006] and areas of high proteolytic activity correspond to areas of low tensile strength [Vallabhaneni *et al* 2004].

These biological 'hotspots' appear to be weakened areas of the aortic wall and are thought to represent sites of potential expansion and rupture.

1.6 CLINICAL ASPECTS OF ANEURYSM DISEASE

1.6.1 RUPTURED AAA AND ANEURYSM SCREENING

Acute rupture, the most feared complication of AAA, is a catastrophic event associated with an overall mortality rate of 65-85%, with many patients succumbing

before even reaching hospital [Johansson and Swedenborg 1986; Bradbury *et al* 1997; Adam *et al* 1999; Kniemeyer *et al* 2000]. Patients with a ruptured aneurysm are considered for immediate open surgical or endovascular aneurysm repair (EVAR) for which the mortality rate is 35-40% [Bradbury *et al* 1997; Ashton *et al* 2002]. By comparison, elective open surgical or endovascular intervention to prevent rupture has an acceptable mortality rate of less than 6% [Brady *et al* 2000; Ashton *et al* 2002; Prinssen *et al* 2004; EVAR trial participants 2005; Schermerhorn *et al* 2008; Lederle *et al* 2009] and is therefore considered in medically fit patients when the perceived risk of rupture outweighs the risk of procedural complications.

Most patients with AAA are asymptomatic and, although AAA may be detected as a result of physical examination or an imaging investigation performed for another reason, the majority of AAA present for the first time with rupture. Aneurysm screening has been shown to reduce the risk of aneurysm-related death by 53-73% [Ashton *et al* 2002; Fleming *et al* 2005; Lindholt *et al* 2006]. A nationwide screening programme is being introduced currently in the United Kingdom [UK National Screening Programme 2010]. Men are invited to attend for a single focused ultrasound scan of the aorta at the age of 65 [UK National Screening Programme 2010]. Due to the low prevalence of AAA in women of a similar age (0.8%) screening was not found to be cost effective or of sufficient clinical benefit in this group [Lederle *et al* 2001; Ashton *et al* 2002; UK National Screening Programme 2010]. Patients are discharged if the aorta is found to be less than 3 cm in diameter. If the aorta is aneurysmal with a diameter of 3-5.4 cm the patient will remain under yearly (3-4.4 cm) or 3-monthly (4.5-5.4 cm) surveillance. Patients with an aneurysm

greater than 5.5 cm in diameter are referred to a vascular surgeon for consideration of surgical or endovascular repair. The results of the MASS trial [2002] show that in men aged 65, 4.9% are found to have an AAA of which 71% are small (3-4.4 cm), 17% are medium-sized (4.5-5.4 cm) and 12% are large measuring at least 5.5 cm in diameter [Ashton *et al* 2002]. The implementation of screening programmes will therefore increase considerably the number of patients under long-term surveillance.

1.6.2 CONTEMPORARY ELECTIVE MANAGEMENT OF AAA

Pharmacological measures

Patients with small- and medium-sized aneurysms are managed expectantly with ultrasound surveillance, lifestyle advice and best medical therapy. Whilst a pharmacological agent capable of attenuating or reversing aneurysm expansion is highly desirable, the main benefit derived from current agents is through prevention of other cardiovascular events, including myocardial infarction and stroke.

More than 90% of patients with AAA have smoked and up to half are current smokers [Lederle *et al* 2003]. Smoking is consistently associated with accelerated aneurysm expansion and, whilst there are no trials specifically addressing this question, it is likely that smoking cessation would limit AAA growth [The UK Small Aneurysm Trial Participants 1998; Lindholt *et al* 2001].

There is little association between serum cholesterol and aneurysm expansion, but it is plausible that statins might have a beneficial effect on aneurysm expansion through their pleiotropic effects which include anti-inflammatory activity and MMP

inhibition [Kalyanasundaram *et al* 2006; Evans *et al* 2007; Abisi *et al* 2008; Kajimoto *et al* 2009; Schweitzer *et al* 2010]. Pre-clinical and small clinical studies suggested that statins may limit aneurysm expansion but these encouraging results have not been borne out in larger clinical studies [Heart Protection Study Collaborative Group 2002; Kalyanasundaram *et al* 2006; Schouten *et al* 2006; Heart Protection Study Collaborative Group 2007; Forsdahl *et al* 2009; Karlsson *et al* 2009a; Golledge *et al* 2010; Hurks *et al* 2010; Sweeting *et al* 2010; Thompson *et al* 2010a]. There are no randomised controlled trials of statins in AAA. The UK heart protection study showed no reduction in requirement for aneurysm surgery amongst patients taking statins [Heart Protection Study Collaborative Group 2002].

Following some hopeful results in animal models both beta-adrenoceptor blockers (β-blockers) and ACE inhibitors have been assessed in clinical studies [Slaiby *et al* 1994]. However, whilst retrospective studies suggested that β-blockers may reduce AAA expansion, two randomised clinical trials of propranolol failed to show a beneficial effect and were hampered by the poor tolerability of propranolol treatment which led to poor compliance [Wilmink *et al* 2000; Propranolol Aneurysm Trial Investigators 2002]. Similarly, although ACE inhibitor use was found to be lower in patients admitted with ruptured AAA (n=3,379) compared to patients with non-ruptured AAA (n=11,947) in a retrospective study, the effects of ACE inhibitors on AAA expansion in prospective clinical studies have been variable [The UK Small Aneurysm Trial Participants 1998; Hackam *et al* 2006; Sweeting *et al* 2010; Thompson *et al* 2010a].

There are no randomised controlled trials of anti-platelet therapy in AAA, primarily because the strong evidence for prevention of atherosclerotic clinical events would make such a study in AAA patients unethical. In AAA, ILT is biologically active and may play an important role in aneurysm disease progression. Rationale for a direct aneurysm-related benefit for anti-platelet therapy lies in the limitation of thrombus volume and activity. It is also thought that inflammatory mediators released into the circulation from the ILT may activate and destabilise atherosclerotic plaque at a distant site increasing the risk of other cardiovascular events.

Chlamydia pneumoniae may play a role in the development of AAA and as a result it has been proposed that macrolide and tetracycline antibiotics may be effective in limiting AAA expansion [Karlsson *et al* 2000]. In a small clinical study (n=247) azithromycin did not reduce AAA growth rate [Karlsson *et al* 2009b]. Doxycycline, probably acting through inhibition of MMP activity rather than through an antibiotic mechanism, reduced aneurysm expansion in rodent models of AAA and reduced MMP activity in human aortic tissue samples obtained during surgical aneurysm repair [Curci *et al* 1998; Curci *et al* 2000; Longo *et al* 2002; Lindeman *et al* 2009]. In a small clinical study AAA growth rate was reduced by doxycycline and there are two ongoing randomised controlled trials [Mosorin *et al* 2001].

Other novel targets include the cyclooxygenase-2 (COX-2) pathway and the c-Jun N-terminal kinase (JNK) pathway [King *et al* 2006]. In mice, inhibition of the JNK pathway resulted in aneurysm regression and restoration of normal architecture [Yoshimura *et al* 2005; Kajimoto *et al* 2009]. Oxidative stress is central to the

pathology of AAA and patients with AAA have lower levels of the antioxidant vitamin E [Dubick *et al* 1987; Sakalihasan *et al* 1996; Dubick *et al* 1999; Tornwall *et al* 2001; Gavrila *et al* 2005]. However, amongst patients with AAA (n=181) considered as a subgroup of a larger clinical trial of vitamin E supplementation there was no apparent clinical benefit [Tornwall *et al* 2001].

At the present time there is no evidence to support the use of any pharmacological agent to suppress aneurysm expansion or reduce the risk of rupture. However, recognising the prevalence of atherosclerotic disease in the aneurysm population, standard secondary prevention measures should be instituted to reduce the risk of myocardial infarction, stroke and other cardiovascular events [Kertai *et al* 2004a; Kertai *et al* 2004b; Schouten *et al* 2005]. Development of a drug to slow or even reverse aneurysm expansion could revolutionise the management of patients with small- and medium-sized aneurysms, but pursuit of such an agent is challenging. Rodent models (e.g. abluminal $CaCl_2$ application, elastase infusion, angiotensin II/apoliprotein E (ApoE)) produce a dilated aorta but do not replicate the complexity of human aneurysm disease, and translation of pre-clinical research findings to the clinical setting is uncertain. In clinical studies results are confounded by the prevalence of atherosclerotic disease and consequent use of cardiovascular drugs by many patients. Assessment of efficacy in clinical studies is challenged by follow-up duration and the use of preventative surgery for large aneurysms, which precludes the use of rupture as an isolated endpoint.

The use of intermediate measures to determine drug efficacy is highly attractive, both to titrate treatment in individual patients and in the pharmaceutical industry as part of clinical trials. To this end a number of serum biomarkers have been investigated, but none have shown sufficient sensitivity and specificity [Golledge *et al* 2008]. Recently, cellular and molecular imaging technologies have allowed biological processes to be probed *in vivo*. Such a method of monitoring disease progression and effects of pharmacological intervention would be highly attractive.

Open surgical and endovascular intervention

Both open surgical repair and EVAR are effective at preventing rupture in patients with large aneurysms. Open repair has been the gold standard for the treatment of large AAA and remains an acceptable option with proven durability [Hallett *et al* 1997; Conrad *et al* 2007]. The EVAR-1 trial (n=1,082) compared EVAR (n=543) with open repair (n=539) in patients with large AAA (≥ 5.5 cm) considered to be fit for either procedure [Brown *et al* 2004]. Endovascular aneurysm repair was associated with a lower procedural mortality than open repair (1.7% *versus* 4.7%) [EVAR Trial Participants 2005]. These data are consistent with the results of other randomised controlled trials and registry data [Prinssen *et al* 2004; Schermerhorn *et al* 2008; Lederle *et al* 2009]. At 4 years the AAA-related mortality remained lower in the EVAR group (3.5% *versus* 6.3%), however the all-cause mortality was similar for both groups (18.4% *versus* 20.2%) and the complication rate (41% *versus* 9%) and re-intervention rate (20% *versus* 6%) were higher in the EVAR group [EVAR Trial Participants 2005]. By 10 years the early AAA-related event free survival advantage in favour of EVAR had been lost (AAA-free survival 93% in both groups)

and there was no difference in overall survival (54% in both groups) [Greenhalgh *et al* 2010]. The catch-up in mortality has been attributed to a combination of cardiovascular deaths and endograft ruptures in the EVAR group [Greenhalgh *et al* 2010**;** Brown *et al* 2011]. There was no difference in health-related quality of life measures at 4 years and 10 years, and EVAR was more expensive than open repair (£13,257 *versus* £9,946) [EVAR Trial Participants 2005; Greenhalgh *et al* 2010].

The EVAR-2 trial [Brown *et* al 2010] showed that in patients considered not fit for open surgery, compared to no intervention, EVAR reduced AAA-related mortality at 4 years (14% *versus* 19%) but did not improve all-cause mortality (66% *versus* 62%). In this group EVAR had a much higher mortality rate than was observed for patients in the EVAR arm of the EVAR-1 trial (7.3% *versus* 1.7%) [EVAR Trial Participants 2005].

1.6.3 AAA SURVEILLANCE

Once diagnosed, patients with intact, asymptomatic AAA are enrolled in an ultrasound-based surveillance programme that involves serial measurements of the maximum anteroposterior diameter of the aneurysm [Hirsch *et al* 2006]. Data from two large studies, the United States Aneurysm Detection and Management study (USADAM, n=1136) and the United Kingdom Small Aneurysm Trial (UKSAT, n=1090), have informed the diameter threshold for consideration of elective intervention in surveillance patients [The UK Small Aneurysm Trial Participants 1998; Lederle *et al* 2002b]. Both studies compared continued surveillance with immediate surgery for AAA with diameter 4-5.5 cm and concluded that there was no

survival benefit for immediate surgery in this group of patients. A threshold of 5.5 cm is therefore considered the appropriate time to intervene [Hirsch *et al* 2006].

However, whilst the risk of rupture increases with diameter (Lederle *et al* 2002a; Mofidi *et al* 2007; Thompson *et al* 2010b], the absolute diameter of the aneurysm is not the sole determinant of the risk of rupture [Di Martino *et al* 2006]. One in 14 screen-detected aneurysms <5.5 cm in diameter rupture within 3 years of detection, and up to one-fifth of ruptured AAA are less than 5.5 cm in diameter [Darling *et al* 1977; Nicholls *et al* 1998; Thompson *et al* 2010b]. Furthermore, many patients present with AAA with diameters considerably greater than 5.5 cm without prior symptoms or rupture [Lederle *et al* 2002a; Powell *et al* 2008]. Aneurysms commonly exhibit a staccato growth pattern and historical growth rates may not correlate with future expansion [Kurvers *et al* 2004].

It appears that the reliance upon diameter alone to predict rupture is inadequate, failing to take into account the biology of the disease and other factors associated with increased rupture risk such as gender and co-morbidities. The number of patients under long-term surveillance will increase as AAA screening commences since up to 90% of patients with screen-detected aneurysms have an aortic diameter of less than 5.5 cm. There is therefore an urgent clinical need for a better method of predicting aneurysm rupture in order that preventative open surgical and endovascular interventions can be targeted appropriately. In addition to measurement of aneurysm dimensions, the ability to probe the biological processes affecting the

aortic wall is likely to be critical to developing an improved method of assessing rupture risk.

1.7 CELLULAR AND MOLECULAR IMAGING

Standard clinical imaging of cardiovascular disease has provided detailed anatomical and morphological information focusing on the presence of stenoses and calcification. In atherosclerotic disease it has become evident that additional information concerning plaque biology would be useful to predict cardiovascular events. In the coronary arteries it is recognised that acute clinical events more often originate from rupture of plaques that, as a result of outward remodelling, did not encroach on the vessel lumen [Libby 1995]. Indeed elective angioplasty of fixed stenosing plaques improves symptoms of angina but does not reduce the incidence of myocardial infarction or death [Boden *et al* 2007].

The term ‘vulnerable plaque’ has been coined to describe the atheromatous plaque at risk of rupture with distinctive pathological features that include a thin fibrous cap, high macrophage density, a large lipid core and a reduction in the number of VSMC [Naghavi *et al* 2003]. Analogous to the concept of the vulnerable plaque, AAA at risk of rupture have been described as featuring hotspots of biological activity involving neovascularisation, inflammation and proteolytic degradation of the ECM of the aortic wall. These hotspots represent weakened areas of the aortic wall and are thought to be sites of potential aneurysm expansion and rupture. Consistent with the

stacatto growth pattern of AAA, these hotspots are dynamic in nature [Kurvers *et al* 2004; Vega de Ceniga *et al* 2008].

With recent innovations in cellular and molecular imaging, these high-risk histological features, along with a number of key biological processes, are viewed as possible imaging targets for the detection of vulnerable plaques *in vivo*. Whilst the majority of work in this area has focused on atherosclerotic disease, such techniques would be eminently translatable for use in aneurysm disease.

Using cellular or molecular imaging methods to target these hotspots would provide real-time information on the metabolic and biological activity within the aortic wall. With this insight it may be possible to predict more accurately the risk of aneurysm expansion and rupture for an individual patient. Furthermore such a technique would facilitate the development and assessment of novel pharmacological interventions to limit or reverse aneurysm expansion.

1.8 IMAGING MODALITIES

A range of imaging modalities exists including MRI, single photon emission computed tomography (SPECT), positron emission tomography (PET), ultrasound scanning (USS), and fluorescence and bioluminescence imaging (Table 1.1). Of these, PET has attracted the greatest attention for use in the clinical setting. Positron emission tomography provides picomolar chemical sensitivity and when used in conjunction with computed tomography (PET-CT), yields 3-dimensional spatial

information. However spatial resolution remains inferior to MRI, and PET-CT involves a significant dose of ionising radiation. Furthermore PET radiotracers have a limited half-life limiting the duration of follow-up to a few hours. Single photon emission computed tomography utilises lower energy gamma-emitting radiotracers such as indium-111 and technetium-99m. It is also hampered by low spatial resolution. Ultrasound scanning avoids ionising radiation and can be used with microbubble contrast agents, but is highly operator-dependent and spatial resolution is limited.

TABLE 1.1 Comparison of imaging modalities

	Spatial resolution	**Chemical sensitivity**	**Quantifiable?**	**Ionising radiation?**	**Operator dependent ?**	**Clinical potential**
MRI	Excellent (μm)	Low (nanomolar)	Semi	No	No	Good
PET-CT	Poor (mm)	High (picomolar)	Yes	Yes	No	Good
Optical	Poor (mm)	High (picomolar)	Yes	No	No	Poor
SPECT	Poor (mm)	Low (nanomolar)	Yes	Yes	No	Good
Ultrasound	Moderate (mm)	Low	Semi	No	Yes	Good

MRI - Magnetic resonance imaging; PET-CT - Positron emission tomography-computed tomography; SPECT - Single photon emission computed tomography.

Green fluorescent protein (GFP) and cyan fluorescent protein (CFP) are amongst a range of fluorescent and near infrared fluorescent (NIRF) proteins used in

fluorescence imaging along with reporter genes such as luciferase which converts luciferin to a fluorescent marker. Yielding picomolar sensitivity and information on cell viability, fluorescence is excellent in the pre-clinical setting. Unfortunately the limited penetration, which even for NIRF agents is restricted to a few centimetres, means that it is of limited use in large animals and humans.

Magnetic resonance imaging offers excellent 3-dimensional, sub-millimetre resolution and distinct soft tissue contrast. Its avoidance of ionising radiation makes it suitable for serial imaging studies. The longevity of some MRI contrast agents allows a prolonged follow-up of several days.

1.9 IMAGING TARGETS

Putative imaging targets include a range of pathophysiological processes and features. Endothelial damage is a key initiating event in cardiovascular diseases and has been assessed using both optical and magnetic resonance imaging [Nahrendorf *et al* 2006]. Neovascularisation is ubiquitous in AAA and is concentrated around sites of aneurysm rupture. Gadolinium-enhanced MRI can assess neovascularisation in vascular tissue in humans and a novel PET ligand for the pro-angiogenic integrin $\alpha_v\beta_3$ has been used in an atherosclerotic mouse model [Kerwin *et al* 2003; Laitinen *et al* 2009]. Inflammation is central to atherosclerotic and aneurysm disease. Phagocytic activity of macrophages has been demonstrated using ultrasmall superparamagnetic particles of iron oxide (USPIO) and MRI scanning. USPIO accumulate in rupture-prone rather than stable atherosclerotic plaques, and statin

therapy reduces both USPIO uptake and inflammation [Kooi *et al* 2003; Trivedi *et al* 2003; Tang *et al* 2009]. Uptake of USPIO has also been shown in AAA in pre-clinical models and in small clinical studies [Tang *et al* 2009; Turner *et al* 2009; Sadat *et al* 2011].

The PET radiotracer ^{18}F-fluorodeoxyglucose (^{18}F-FDG) is a glucose analogue that is taken up by cells but accumulates in a phosphorylated form as it is not a suitable substrate for glycolysis and further metabolism. Its accumulation in cells and tissues indicates metabolic activity, and in vascular tissue ^{18}F-FDG uptake correlates with the degree of inflammation [Rudd *et al* 2007]. In atherosclerotic disease ^{18}F-FDG uptake predicts acute plaque events, correlates with cardiovascular risk factors and is reduced with statin therapy [Rominger *et al* 2009; Rudd *et al* 2009; Wasselius *et al* 2009]. ^{18}F-FDG also accumulates in the wall of AAA but does not correlate clearly with AAA diameter or predict aneurysm expansion in small clinical studies [Reeps *et al* 2008; Kotze *et al* 2009; Reeps *et al* 2009a; Kotze *et al* 2011]. ^{18}F-FDG uptake was higher in patients with acute symptoms and correlated with histological evidence of aneurysm instability [Reeps *et al* 2008].

Probes have been developed for other pathways including MMP activity, VSMC apoptosis and oxidative stress, but are not yet available for clinical use [Fujimoto *et al* 2008; Zhang *et al* 2008; DeLeo *et al* 2009; Laufer *et al* 2009].

1.10 CHOICE OF USPIO-ENHANCED MRI TO INVESTIGATE ANEURYSM DISEASE

High resolution MRI provides excellent soft tissue contrast and can distinguish different components of atherosclerotic plaque including the lipid-rich necrotic core, fibrous cap and calcification [Cai *et al* 2005]. Standard gadolinium-enhanced MRI can also identify the fibrous cap and thrombus in AAA [Kramer *et al* 2004] Furthermore, MRI is safe and avoids ionising radiation making it suitable for serial imaging studies as would be required for monitoring inflammatory activity in AAA.

Discussed in detail below, USPIO are part of a novel group of MRI contrast agents capable of providing additional functional information beyond the anatomical data obtained using blood pool agents. USPIO are biodegradable, safe and do not affect cell viability or function. These agents have been used to assess inflammation in atherosclerotic plaques and several small studies have demonstrated their uptake in AAA but have not correlated this with clinical events. A further advantage of these agents is their current clinical availability. USPIO-enhanced MRI is a promising approach to evaluating dynamic inflammatory processes in AAA.

1.11 SUPERPARAMAGNETIC PARTICLES OF IRON OXIDE

Superparamagnetic particles of iron oxide (SPIO) constitute a novel class of MRI contrast agents. Possessing intense superparamagnetism, SPIO are detectable at

much lower concentrations than standard gadolinium-based MRI contrast agents [Zhang *et al* 2005]. Beyond the anatomical data provided by blood pool contrast agents, these agents can also yield additional biological and functional information. Taken up by macrophages both *in vitro* and *in vivo*, these nanoparticles accumulate at sites of tissue inflammation and have the potential to be used to investigate a range of inflammatory disease processes. In the clinical setting, such agents have already been used in conjunction with gadolinium for double contrast MRI studies of the liver where they are taken up by Kuppfer cells [Bellin *et al* 1998; Semelka and Helmberger 2001]. Furthermore, iron oxide nanoparticles can be used to label cells *ex vivo* and may be suitable for *in vivo* cell tracking studies that, if successful, would be a tremendous asset for advancing the development of cell therapies [Arbab *et al* 2004b]. The availability of these agents has therefore opened up a new sphere of possibilities for MRI.

These agents divide into two classes based on particle size due to the influence that diameter has on their behaviour. SPIO have a diameter in the region of 80-150 nm. Examples of SPIO include ferumoxide (Endorem, Guerbet, France) and ferucarbotran (Resovist, Bayer-Schering Pharma, Germany). USPIO are less than 50 nm in diameter and include ferumoxtran-10 (Sinerem, Guerbet, France). It should be noted that the quoted hydrodynamic particle size includes the polymeric coating, whilst the iron core itself is generally in the region of 4-7 nm regardless of overall particle diameter. In addition to size, the behaviour and distribution of different SPIO preparations are principally determined by the coating and surface charge of the particles.

The iron oxide core is manufactured by co-precipitation of magnetite crystals from an aqueous solution of ferrous (Fe^{2+}) and ferric (Fe^{3+}) salts [Laurent *et al* 2008]. Magnetite (Fe_3O_4) is also termed ferrous-ferric oxide, reflecting the presence of iron in two oxidation states within the same molecule. Under aerobic conditions, magnetite is gradually oxidised to maghaemite (Fe_2O_3) and iron nanoparticle preparations generally consist of a mixture of the two. Particle size can be modified within a reasonably tight range by modifying the conditions of co-precipitation including temperature, pH and the ratio of ferric and ferrous salts.

The magnetic core is then coated to stabilise the iron oxide crystal structure and prevent agglomeration and sedimentation. The coating may modulate the magnetic properties of the particles through a quenching effect. Importantly the surface coating is critical in determining the biological behaviour of the particles. A range of coatings has been described including dextran (e.g. ferumoxide, ferumoxtran-10), carboxydextran (e.g. ferubarbotran), starch, polyethylene glycol, alpha hydroxyacids (e.g. citrate-coated VSOP C184) and amino acids. The coating may be neutral, anionic or cationic, and ionic coatings appear to increase cellular particle uptake [Fleige *et al* 2002]. Clearly the nature of the coating also determines the suitability of the nanoparticle preparation for translational and clinical use.

1.11.1 CELLULAR UPTAKE OF SPIO AND USPIO

Cellular uptake of SPIO and USPIO occurs through a variety of mechanisms and is influenced amongst other things by cell type as well as particle size and coating

[Koval *et al* 1998]. Phagocytosis and receptor-mediated endocytosis are prominent in the uptake of larger SPIO particles, whilst pinocytosis appears to be important for uptake of USPIO. Scavenger receptors are involved in the internalisation of anionic and larger particles by macrophages. Scavenger receptor blockade by polysaccharides (e.g. fucoidin) or polynucleotides (e.g. poly-inosinic acid) reduces the uptake of both ferumoxides and ferumoxtran-10. Colchicine blocks non-specific pinocytosis and thereby inhibits uptake of dextran-coated but not citrate-coated iron nanoparticles [Moore *et al* 1997]. Conversely inhibition of phagocytosis through cytochalasin beta blockade of the cytoskeleton inhibited citrate- but not dextran-coated nanoparticle uptake [Fleige *et al* 2002]. Within the cell, particles accumulate in phagolysosomes [Muller *et al* 2007].

Particle internalisation is increased in activated macrophages stimulated by IL-4 and IFNγ [Rogers and Basu 2005]. There is conflicting evidence regarding the effect of statins on iron nanoparticle uptake, with one study showing inhibition of uptake by lovastatin and a second study showing no effect of atorvastatin [Rogers and Basu 2005; Muller *et al* 2008].

The avidity of particle uptake determines the circulating half-life of different iron nanoparticle contrast agents. SPIO are large enough to be recognised and rapidly taken up by Kuppfer cells in the reticuloendothelial system. Significantly higher concentrations are observed in the spleen and lymph nodes than in the liver. SPIO therefore accumulate in the liver and spleen following intravenous administration and have a relatively short plasma half-life in the region of 2-6 hours in humans.

Indeed this property is utilised when SPIO are used for the detection of malignant lesions in the liver [Bellin *et al* 1998; Semelka and Helmberger 2001].

In contrast, USPIO escape immediate recognition and persist for longer in the circulation [Corot *et al* 2006]. Ferumoxtran-10, for example, has a circulating half-life of 16-24 hours in humans and slowly accumulates at sites of inflammation allowing its use for vessel wall and lymphatic imaging [Corot 2007].

Whilst following administration SPIO and USPIO accumulate predominantly in the lymphoreticular system, accumulations are also observed in macrophages within the lung parenchyma and around the airway,but probably not in concentrations high enough to affect their overall bioavailability [Tsuchiya et al 2011]. In the absence of inflammation, USPIO and SPIO do not accumulate in the kidneys, gastrointestinal tract or great vessels [Tsuchiya et al 2011].

1.11.2 METABOLISM

A major advantage of using dextran-coated iron nanoparticles is that they are fully biodegradable with no long-term toxicity. Cellular iron content reduces from 72 hours onwards, probably through a combination of the dilution effect of cell division and recycling of iron content out of the cell [Sun *et al* 2005]. The former is more prominent in rapidly dividing cells such as stem cells whilst professional scavengers such as macrophages return iron to the body's general iron pool. The use of ferumoxtran-10 containing the radioisotopes ^{59}Fe and ^{14}C reveals the fate of iron nanoparticles *in vitro* [Corot 2007]. Under acidic conditions within macrophage

lysosomes, USPIO particles are degraded and become soluble within 4 days of administration. The dextran coating undergoes renal excretion and 89% has been eliminated after 8 weeks. The iron component of the nanoparticles enters the body's iron pool, being incorporated into haemoglobin, myoglobin and other iron-containing macromolecular complexes. Iron is excreted very slowly in the faeces: only 20% is excreted 3 months after administration.

1.11.3 BIODEGRADABILITY AND BIOCOMPATIBILITY

On a cellular level *in vitro* exposure of cells to iron nanoparticles and labelling with approximately 10-20 pgFe/cell generally has no adverse effects on cell viability. This has been shown in a wide variety of cell types including monocytes, THP-1 cells, T lymphocytes, mesenchymal stem cells (MSC), adipose-derived stem cells, neural precursor cells, endothelial progenitor cells and embryonic stem cells [Arbab *et al* 2004b; Arbab *et al* 2005; Au *et al* 2009; Cohen *et al* 2009; Farrell *et al* 2009; Hu *et al* 2009; Mai *et al* 2009; Wang *et al* 2009]. Normal differentiation of stem cells into cardiac myocytes, osteocytes, adipocytes and skeletal myocytes has been demonstrated, and there is no impairment of monocyte differentiation into macrophages and dendritic cells [Arbab *et al* 2004b; Arbab *et al* 2005; Au *et al* 2009; Wang *et al* 2009]. However chondrocyte differentiation of MSC may be impaired, although interestingly the behaviour of differentiated chondrocytes exposed to SPIO is unaffected [Bulte *et al* 2004; Farrell *et al* 2009]. Morphology, phenotype, migratory capacity, cytokine secretion and immunomodulatory activity are preserved in a range of cell types. Despite the overwhelming majority of studies finding no adverse cellular effects, there are a few reports of functional effects of

SPIO-labelling [Bulte *et al* 2004; Schäfer *et al* 2007; Schäfer *et al* 2009]. It is worth recognising the diversity in cell labelling protocols employed across these studies, including differences in the nature of transfection agents, which may explain such findings.

There is some evidence that SPIO-labelling promotes MSC proliferation, possibly through enhanced peroxidase activity, however the majority of studies have shown no effect on cell proliferation. Following cellular ingestion, part of the SPIO load is taken up by lysosomes. In this acidic environment, the dextran coating of the nanoparticle is degraded and a proportion of the iron oxide liberated may dissociate releasing Fe^{2+} that can generate reactive oxygen species through the Fenton reaction. Indeed even intact iron nanoparticles have a degree of intrinsic peroxidase-like activity through which they deplete cytoplasmic levels of H_2O_2**,** tending to promote cell proliferation and reduce apoptosis. Cells protect themselves against the potential harmful effects of Fe^{2+} by sequestering free iron into ferritin complexes. Increased cytoplasmic iron concentration decreases expression of the transferrin receptor (CD71) in many cell types but increases it in monocytes and erythrocytes [Pawelczyk *et al* 2006]. Indeed SPIO-labelling is known to upregulate expression of the transferrin receptor [Pawelczyk *et al* 2006; Schäfer *et al* 2007]. The transferrin receptor is associated with regulation of cell proliferation and differentiation. However it would appear that monocytes/macrophages, as professional scavengers, have an excellent capacity to deal with ingested iron and resist the potentially toxic effects [Pawelczyk *et al* 2006]. It is interesting that in the clinical setting chronic exposure of macrophages to iron, as occurs in chronic venous ulceration, polarises

macrophages towards the pro-inflammatory M1 phenotype which may inhibit ulcer healing [Sindrilaru *et al* 2011]. This effect is not seen in *ex vivo* exposure of cells to iron nanoparticles *in vitro*. Differences in response may be due to the chronicity of exposure and surrounding tissue cytokine mileau.

1.11.4 SAFETY PROFILE

Intravenous administration of SPIO and USPIO is very well tolerated with few clinical side-effects. The incidence of side-effects is reduced if administration is by slow intravenous infusion of a dilute suspension of iron oxide nanoparticles. One thousand six hundred and sixty-three patients received Sinerem as part of a series of 37 studies looking at its use for lymph node imaging in patients with cancer [Bonnemain 2008]. Of these, seven patients (0.004%) had a serious adverse event thought to be related directly to the administration of Sinerem and one patient died (0.0006%). Adverse events affected approximately half of patients in these studies of which 86% were mild-moderate in their severity and settled if the infusion was slowed or stopped. The rate of side-effects was significantly higher if Sinerem was administered as a concentrated bolus; if given as a dilute infusion far fewer adverse events were encountered. The most common adverse events were back pain (3.3%), headache (2.9%), pruritus (2.5%), urticaria (2.4%), nausea (2.3%), flushing (1.9%), warm feeling (1.7%) erythema (1.6%), rash (1.4%), chest pain (1.3%) and upper abdominal pain (1.2%). In summary administration of dextran-associated iron

nanoparticle preparations is safe with a very low incidence of serious adverse events and an acceptable rate of minor or self-limiting side-effects [Bernd *et al* 2009].

1.11.5 POTENTIAL USES

The SPIO preparations ferumoxide (Endorem, Guerbet, France) and ferucarbotran (Resovist, Bayer-Schering Pharma, Germany) have been used with gadolinium routinely in the clinical setting for double-contrast MRI studies of the liver [Bellin *et al* 1998; Semelka and Helmberger 2001]. The iron nanoparticles are taken up by Kuppfer cells and cause a reduction in the signal intensity in normal liver, rendering pathological areas such as tumours, which are largely devoid of macrophages, more obvious. By increasing the conspicuity of such lesions, metastases as small as 2-3 mm have been detected.

Other applications for iron nanoparticle-based agents are largely experimental and include their use as blood pool contrast agents, for *ex vivo* labelling of cells for *in vivo* cell tracking studies and in inflammation imaging.

(1) *Blood Pool Agent*

As blood pool contrast agents, USPIO have a number of potential advantages over standard gadolinium-based agents. USPIO contrast agents have a longer circulating half-life and reduced extravasation from the blood pool into the interstitium. This renders them suitable for both first-pass and particularly for equilibrium-phase perfusion studies, and they have been applied to angiographic imaging of vascular tumours [Robert *et al* 2005; Bremerich *et al* 2007]. However the requirement for

ultrashort echo time (TE) sequences and venous contamination are drawbacks. Additionally the use of USPIO negates the risk of nephrogenic systemic fibrosis (NSF), a rare and irreversible complication of gadolinium-containing contrast media occurring particularly in patients with severe renal dysfunction [Thomsen 2006; Sadowski *et al* 2007].

(2) ***Inflammation Imaging***

USPIO also have the potential for imaging inflammation and tissue-resident macrophages *in vivo*. USPIO-enhanced MRI increases the sensitivity and specificity of detection of lymph node metastases, particularly in non-FDG avid tumours such as prostate cancer. Other applications have included imaging macrophage activity in transplant allograft rejection, stroke, multiple sclerosis, soft tissue inflammation and the pancreas in early type I diabetes [Hauger *et al* 2000; Kaim *et al* 2003; Lutz *et al* 2004; Dousset *et al* 2006; Jander *et al* 2007; Wu *et al* 2009; Gaglia *et al* 2010].

In atherosclerotic plaque, following intravenous administration of USPIO, changes in signal intensity on T2 weighted (T2W) imaging have been shown to correlate with macrophage density [Morishige *et al* 2010]. USPIO-enhanced MRI can distinguish stable from unstable carotid plaques and treatment with atorvastatin reduced USPIO uptake and plaque inflammation [Kooi *et al* 2003; Trivedi *et al* 2006; Tang *et al* 2008a; Tang *et al* 2009]. USPIO accumulate in the aortae of hypercholesterolaemic rabbits. USPIO also concentrate in human AAA, but the distribution of USPIO

within the aneurysm is unknown and no correlation has been made with aneurysm expansion or rupture [Tang *et al* 2009; Sadat *et al* 2011]. A correlation has been shown between USPIO-MRI and ^{18}F-FDG PET-CT in carotid plaque assessment suggesting that both modalities are indicating the same biological process [Tang *et al* 2008b].

(3) *Cell Labelling*

Finally, SPIO have been used to label a variety of cell types *ex vivo* for *in vivo* cell tracking studies.

1.12 *IN VIVO* CELL TRACKING USING SPIO-LABELLING AND MRI

There is increasing interest in the possibility of using cell-based therapies to treat a wide range of diseases. The ability to track cells to a target site following delivery is highly desirable for the further development of cell-based treatments. There are a number of candidate modalities for this purpose, but SPIO-labelling and tracking of cells using MRI has emerged as a leading option. Advantages include excellent anatomical detail, high sensitivity and avoidance of ionising radiation, which is important when serial imaging studies are required.

1.12.1 CELL LABELLING

When injected directly intravenously, SPIO are rapidly taken up by macrophages in the reticuloendothelial system and are therefore unsuitable to be used to image tissue inflammation. However, this avidity of uptake by mononuclear cells has been exploited for cell labelling. Transfection agents have been used to enhance SPIO uptake and include poly-L-lysine (PLL), human immunodeficiency virus transactivator of transcription (HIV-Tat) peptide and mechanical measures such as electroporation. Arbab and colleagues have described a method of labelling cells with SPIO (Endorem) using protamine sulphate to optimise its uptake [Arbab *et al* 2004b]. This cationic transfection agent both enhances cell-nanoparticle electrostatic interactions, and initiates agglomeration of the iron oxide nanoparticles into ferumoxide-protamine complexes promoting recognition and uptake by cells. A particular advantage of this method of cell labelling is that it is potentially Good Manufacturing Practice (GMP) compliant since both Endorem and protamine sulphate are approved for use in humans. As described above, labelling in this way is non-toxic to mononuclear cells.

Pre-clinical studies

The potential of SPIO cell tracking was initially demonstrated in a range of animal models. Following direct injection in the target organ, MRI scanning was used to track labelled cells to a site of injury, tumour or inflammation in the brain, spinal cord, knee joint and heart [Kraitchman *et al* 2003; Chang *et al* 2008; Jing *et al* 2008; Cohen *et al* 2009; Hu *et al* 2009]. SPIO-labelled cells have been tracked to the kidney following renal arterial administration in a rat model of renal ischaemia [Jung *et al* 2009]. SPIO-labelled MSC injected subcutaneously along with breast cancer

cells in mice were detected in local tumours and distant pulmonary metastases [Loebinger *et al* 2009].

More recently cells have been tracked following systemic intravenous administration. SPIO-labelled MSC transplanted via the tail vein homed to de-endothelialised common carotid artery in splenectomised rats [Cao *et al* 2009]. In a mouse glioma model, SPIO-labelled cells tracking to the tumour was observed following intravenous administration [Anderson *et al* 2005]. Neural precursor cells tracked to the ischaemic rat brain [Song *et al* 2009]. Tracking of SPIO-labelled cardiomyocyte-like cells to the injured canine myocardium was confirmed on histology and SPECT scanning, but not using 1.5 tesla (T) MRI [Kraitchman *et al* 2005; Kim *et al* 2009]. It was suggested that MRI did not have the sensitivity to detect small numbers of cells.

Clinical studies

Following intra-nodal injection in patients with locally advanced malignant melanoma with nodal spread, SPIO- and ^{111}In-labelled autologous dendritic cells were tracked to regional lymph nodes using both MRI and scintigraphy [de Vries *et al* 2005]. Magnetic resonance imaging was found to be more sensitive than scintigraphy for cell detection, and MRI provided superior anatomical detail. Cells were detected in small numbers (1.5×10^5 cells) using MRI.

In a patient with a traumatic brain injury, SPIO-labelled cells were injected around the site of the injury using stereotactic surgery. A second patient received unlabelled

cells. Labelled but not unlabelled cells migrated and produced a hypointense signal around the injured brain [Zhu *et al* 2006].

Finally SPIO-labelled pancreatic islet cells were administered into the portal vein of insulin-dependent diabetic patients [Toso *et al* 2008]. The labelled cells were visualised on MRI scanning as hypointense lesions within the liver, but there was no correlation with the number of cells administered. Transplantation was successful in achieving independence from insulin in all patients, indicating conservation of cell function despite SPIO-labelling.

Successful tracking of SPIO-labelled cells to a target site following intravenous administration has not yet been reported.

1.13 MAGNETIC RESONANCE IMAGING OF SPIO

SPIO can be detected with standard, clinically available MRI sequences. Application of an excitatory radiofrequency pulse flips the net magnetisation vector (NMV) into the transverse plane creating a current in the receiver coil that constitutes the signal. The signal is expected to decay exponentially with time and this decay process is described by a constant called the T2* value.

Superparamagnetic contrast agents such as SPIO induce local magnetic field inhomogeneities leading to a rapid loss of phase-coherence amongst spinning magnetic nuclei following application of a radiofrequency pulse. This results in more

rapid decay of signal intensity over time corresponding to a shortening of the T2 and T2* relaxation times and a sharp reduction in the T2* value. On the resulting images, a profound reduction in the signal intensity is evident on T2W and particularly T2*W images, and tissues in which SPIO accumulate appear dark on T2W and T2*W studies. SPIO also have a T1 shortening effect that is most obvious at low concentrations whilst at higher concentrations T2* susceptibility effects predominate [Canet *et al* 1993; Torabi *et al* 2004].

Gradient echo sequences have a lower signal-to-noise ratio and inferior spatial resolution when compared to standard spin echo sequences, however their exquisite sensitivity to iron accumulation is advantageous for SPIO imaging. Using a multi echo sequence the signal intensity is sampled serially at increasing echo times allowing calculation of the T2* value ($S(t)=S(0)\exp-(t/T2^*)$). Changes in signal intensity on T2W or T2*W imaging, and changes in T2* value or its inverse R2* ($T2^*=1/R2^*$), may be used to assess iron accumulation.

1.13.1 CHALLENGES OF QUANTIFICATION OF IRON IN TISSUES

T2* and R2* values correlate with hepatic and cardiac iron concentration in sickle cell and thalassaemia patients with transfusion-related iron overload [Anderson *et al* 2001; Wood *et al* 2005; Storey *et al* 2007]. A linear, concentration-dependent increase in R2 and R2* values has been observed for both free SPIO and SPIO-labelled cells in *in vitro* agarose phantoms [Kuhlpeter *et al* 2007].

Interestingly, for free SPIO the R2* values are only slightly longer than the corresponding R2 values at a given concentration of iron, but if SPIO are compartmentalised within cells the effect on T2* decay is more pronounced and R2* values are much longer. Differences have also been noted amongst different cell types, presumably related to the way that iron is stored within the cell [Rad *et al* 2007]. These differences are observed because, when SPIO particles are clustered together, the magnitude of their magnetic properties is similar to that expected from the overall size of the cluster rather than the sum of their individual volumes [Tanimoto *et al* 2001]. There may also be an element of magnetic co-operativity between particles. Consequently, in accordance with the static dephasing regime theory, the susceptibility effect of clustered SPIO is exaggerated and much greater than the sum of the effect of individual particles [Tanimoto *et al* 2001; Bowen *et al* 2002]. As a result of this phenomenon, true quantification of SPIO in tissues is challenging since interpretation depends upon the context in which the particles are imaged.

Spatial resolution is critical to the detection of SPIO. A partial volume effect occurs if the size of the signal deficit induced is much smaller than the size of the voxel, reducing the sensitivity to detect SPIO. Furthermore, when clustered, SPIO exhibit a 'blooming effect' in which the spatial extent of the magnetic effect of the cluster extends substantially beyond the size of the cluster itself. This can make precise localisation of SPIO accumulation in tissues challenging, but has the advantage of increasing the sensitivity. With sufficient spatial resolution, single cell imaging of

cells labelled with micron-sized particles of iron oxide (MPIO) has been reported [Heyn *et al* 2006; Shapiro *et al* 2006].

1.13.2 APPROACHES TO SPIO DETECTION IN HUMANS

There are a number of reported methods for assessing SPIO accumulation in tissues. Images may be observed for signal deficits which is straight-forward but purely qualitative and open to operator bias [Zhu *et al* 2006].

Trivedi *et al* used small, manually-drawn regions of interest (ROI) to sample carotid arterial plaque and compared changes in signal intensity normalised to the signal intensity of adjacent sternocleidomastoid muscle [Trivedi *et al* 2006]. This approach is susceptible to observer bias and does not sample the whole vessel leading to the possibility of missing focal USPIO accumulation. Furthermore, it does not account for the T1 effects of USPIO and assumes that the signal intensity in adjacent muscle is unchanged by USPIO administration, which may not hold true due to the prolonged half-life of USPIO in the blood pool.

In their assessment of carotid plaque, Tang *et al* adopted a quadrant approach to reduce observer bias and allow the entire plaque to be sampled [Tang *et al* 2009]. This did, however, compromise spatial resolution such that focal USPIO accumulation may have been masked. This approach also precluded localisation of USPIO uptake to different components of the plaque.

The advantage of using T2* or R2* values rather than signal intensity to detect USPIO accumulation is that, in theory, it is a tissue property which should be independent of repetition time (TR), echo time and flip angle as well as the T1 effects of USPIO which would affect signal intensity values. If the absolute signal intensity or T2* value following USPIO administration is used rather than the change (pre minus post), other sources of signal deficit such as haemorrhage and calcification may confound data interpretation. Even if the latter approach is used, signal dropout due to calcification and haemorrhage may mask signal changes resulting from USPIO uptake.

A range of positive contrast sequences is being developed to improve tissue detection of SPIO agents but at present none of these sequences is commercially available [Seppenwoolde *et al* 2003; Mani *et al* 2006; Stuber *et al* 2007; Eibofner *et al* 2010].

Some uncertainties still exist around the interpretation of USPIO data. For example the exact mechanism by which USPIO enters tissues and cells is unclear. It may be that increased capillary permeability allows USPIO to leak out into the interstitium where upon it is ingested by tissue resident macrophages. Alternatively monocytes/macrophages in the blood stream may ingest the USPIO particles and transport them to the site of inflammation. Precisely which aspects of the inflammatory process USPIO-enhancement indicates is therefore a subject of debate. The specificity of USPIO-enhancement beyond the first 72 hours is also unclear.

Regardless of these outstanding questions and challenges, the potential of SPIO and USPIO contrast agents to probe biological processes *in vivo* is without doubt exciting. Recognising this, a pragmatic and semi-quantitative approach to data analysis would be highly desirable.

1.14 SUMMARY

Prediction of aneurysm expansion and rupture amongst patients under surveillance for AAA is challenging and reliance upon diameter measurements alone appears to be inadequate. Hotspots of biological activity are thought to represent weakened areas of the aortic wall at risk of expansion and rupture. Evolving cellular and molecular imaging techniques open up the possibility of using these hotspots as imaging targets to identify unstable aneurysms at risk of rupture. USPIO-enhanced MRI scanning can detect cellular inflammation with excellent spatial resolution and may be a useful investigative tool for assessing AAA. Accessing the biological processes involved in AAA would be useful for developing and monitoring the effects of novel pharmacological interventions for aneurysm disease.

Iron oxide nanoparticles can also be used to label cells for *in vivo* cell tracking studies. Capability to do this would be extremely useful for the further development and assessment of cell-based therapies for a wide range of diseases.

1.15 AIMS AND HYPOTHESES

The aim of this thesis is to investigate the role of magnetic resonance imaging with superparamagnetic particles of iron oxide with relevance to the cardiovascular system. Specifically, we will develop data acquisition and image analysis methodology for the detection of focal iron accumulation in tissues. We will then apply these techniques to the detection of inflammation in the aortic wall in patients with abdominal aortic aneurysms using USPIO-enhanced MRI, and correlate the findings with clinical disease progression. We will also develop a GMP compliant method of labelling cells *ex vivo* with SPIO for clinical cell tracking. We will assess the safety of administration of SPIO-labelled cells in humans, and determine the feasibility of imaging SPIO-labelled cells at a target site using clinical MRI scanning.

The following novel hypotheses will be addressed:

1. Changes in T2* value on clinical MRI scanning can be used to detect focal iron accumulation in tissues (*Chapter 3*).
2. USPIO-enhanced MRI can be used to detect inflammation in the wall of AAA and predict aneurysm expansion (*Chapter 4*).
3. Peripheral blood mononuclear cells (PBMC) can be labelled with SPIO *ex vivo* under GMP compliant conditions without affecting cell viability or function (*Chapter 5*).
4. Local and systemic administration of SPIO-labelled PBMC in humans is safe and SPIO-labelled cells can be detected at a target site using clinical magnetic resonance imaging (*Chapter 6*).
5. SPIO-labelled PBMC can be tracked to an inflammatory focus in humans following systemic intravenous administration (*Chapter 6*).

CHAPTER 2

METHODOLOGY

2.1. GENERAL

2.1.1 ETHICAL AND REGULATORY CONSIDERATIONS

All studies were undertaken with the approval of the Lothian Local Research Ethics Committee or Scotland A Research Ethics Committee. The Medicines and Healthcare Products Regulatory Agency (MHRA) approved the use of the MRI contrast agent Sinerem (Guerbet, France) to investigate patients with AAA as a Clinical Trial of an Investigational Medicinal Product (CTIMP). All studies were conducted in accordance with the Declaration of Helsinki. Studies were registered on the public website www.clinicaltrials.gov (NCT00794092; NCT00972946; NCT01169935).

2.1.2 SUBJECT RECRUITMENT

All participants gave written informed consent before participating in the study. An information sheet was provided electronically and participants' general practitioners were informed in writing.

2.1.3 PATIENTS WITH ABDOMINAL AORTIC ANEURYSMS

Patients with AAA with aortic diameter >4.0 cm on ultrasound scanning were identified from the outpatient aneurysm surveillance database at the Royal Infirmary of Edinburgh.

Patients who were under the age of 40 years old were excluded from participating in the study since we were interested in degenerative aneurysms rather than those

secondary to other conditions such as connective tissue disorders. Patients who were pregnant, and those who had active systemic inflammatory or malignant disease, renal dysfunction (estimated glomerular filtration rate (eGFR) <25 mL/min), hepatic cirrhosis (Child-Pugh score B or C), recent surgical procedure or a contraindication to MRI scanning were also excluded from the study.

2.1.4 HEALTHY VOLUNTEERS

Healthy volunteers (aged >18 years) were recruited by local advertisement through the University of Edinburgh.

Volunteers were excluded from participation in the study on the basis of the presence of any of the following: renal dysfunction (eGFR <25 mL/min), hepatic dysfunction (Child-Pugh score B or C), positive virology screen, pregnancy, breast feeding, blood dyscrasia, anaemia (Hb <12 g/dL), iron storage disorder, active malignancy, chronic inflammatory condition, history of or risk factors for protamine allergy, intercurrent illness, recent surgical procedure and contraindication to MRI scanning.

2.1.5 TUBERCULOSIS CONTACTS

Participants known to have a positive Mantoux test response, but not suffering from active tuberculosis, were identified from the Royal Infirmary of Edinburgh Department of Respiratory Medicine database of such patients. All known tuberculosis contacts are invited to the respiratory clinic for clinical assessment including a Mantoux test, a blood test and a chest radiograph. We included subjects

who had had a positive Mantoux test but had no symptoms or radiological features of tuberculosis.

Subjects were also excluded from participating in the study if they had renal dysfunction (eGFR <25 mL/min), hepatic dysfunction (Child-Pugh score B or C), positive virology screen, pregnancy, breast feeding, blood dyscrasia, anaemia (Hb <12 g/dL), iron storage disorder, active malignancy, chronic inflammatory condition, history of or risk factors for protamine allergy, intercurrent illness, recent surgical procedure or a contraindication to MRI scanning.

2.2 *EX VIVO* LABELLING OF PERIPHERAL BLOOD MONONUCLEAR CELLS WITH SPIO

2.2.1 CELL PROCUREMENT

Venesection

For *in vitro* laboratory work, whole venous blood (up to 240 mL) was obtained from a vein in the antecubital fossa using a large 17-gauge butterfly needle. Blood was collected into 50 mL tubes (Becton Dickinson Biosciences, USA) with 4 mL of the anticoagulant citrate per 40 mL of whole blood. Up to ~2×10^8 PBMC can be obtained from 250 mL of whole blood.

Where cells were to be processed for autologous reinfusion, blood was collected in the Cell Separator Unit of the Royal Infirmary of Edinburgh by connecting a 16-gauge cannula to a closed-circuit connection system containing citrate.

Apheresis

To achieve higher cell numbers, the process of apheresis, selective collection of specific blood components, was used. This process is used routinely in clinical practice, with applications including, plasma exchange, peripheral blood stem cell donations and red blood cell exchanges. A COBE Spectra apheresis machine (Gambro BCT, Lakewood, CO) was used according to the manufacturer's instructions. The manufacturer's standard validated protocol for donor lymphocyte collection (SOP No. 00 513 008: Donor Lymphocyte Collection, COBE Spectra Operator's Manual) was followed.

In brief, whole blood anticoagulated with citrate was drawn continuously from a peripheral vein into a rotating centrifuge. Blood components were separated on the basis of their density with red blood cells accumulating towards the outside and plasma on the inside of the chamber. The PBMC layer, which contains monocytes and leucocytes, was harvested between the two. The flow rate was manipulated to vary the position of the PBMC layer with relation to the collection port, and these adjustments were guided by regular comparison of the colour of the harvested product to a validated chart by the operating nurse. This optimised the purity of collection, minimising the degree of contamination by other blood components. The remaining blood components were continuously returned to the circulation through a second point of venous access such that at any point in time not more than 260 mL of the circulating volume was extracorporeal. Participants were observed for signs of

hypocalcaemia secondary to citrate toxicity and were treated by oral calcium replacement.

A 90-minute collection typically yielded approximately 100-150 mL of apheresis product containing of the order of 1-5 × 10^9 PBMC.

2.2.2 CELL PREPARATION AND LABELLING

Mononuclear cell isolation from whole blood or apheresis product

Whole blood or apheresis product was diluted 1:1 in phosphate buffered saline (PBS) and mononuclear cells were isolated by Ficoll (Histopaque) density gradient separation (400 g, 40 min). The mononuclear cell layer was harvested and washed twice in PBS.

Arbab protocol for labelling cells with SPIO

Arbab *et al* described a method for labelling cells with SPIO using protamine sulphate as a transfection agent to enhance its uptake [Arbab *et al* 2004]. SPIO (Endorem, Guerbet, France) was diluted to a concentration of 100 μg/mL in phenol red free Roswell Park Memorial Institute (RPMI) medium (Sigma Aldrich). Protamine sulphate (ProSulf, CP pharmaceuticals) was added (5 μg/mL) and SPIO-protamine complexes were allowed to form for 10 minutes. The mononuclear cell pellet was re-suspended in the SPIO-protamine suspension with a final cell concentration of 4 × 10^6 cells/mL and incubated at 37°C for 3 hours in 5% CO_2. The cell suspension was further diluted to a final SPIO concentration of 50 μg/mL and

incubated overnight. At the end of the incubation period, the cells were washed two or three times in RPMI until the supernatant was clear.

Edinburgh protocol

Guided by *in vitro* assays of cell viability and function, the Arbab protocol was adapted for clinical scale labelling of PBMC under GMP compliant conditions generating the Edinburgh protocol (Chapter 5). Implementation of the Edinburgh protocol in a GMP facility is outlined in full in the standard operating procedure in **Appendix 1.**

In brief, the mononuclear cell pellet was re-suspended in the volume of 0.9% saline required to give a cell concentration of 4×10^6 cells/mL. One hundred μg/mL of SPIO (Endorem) and 4 μg/mL of protamine sulphate were added directly into the cell suspension. The cells were transferred immediately in 250 mL polypropylene tubes (Becton Dickinson Biosciences, USA) to a roller mixer and were incubated at room temperature for 2 hours.

For clinical studies, cell preparation and labelling was undertaken in the GMP compliant Scottish National Blood Transfusion Service Tissue Services laboratory. Consistent with GMP regulations, sterility testing was integrated into each step of the protocol. At the end of the incubation period, the cell number was ascertained and the cell suspension was transferred to a low-adherence bag (Cryocyte, Baxter) for reinfusion.

2.3 *IN VITRO* EVALUATION OF CELLULAR EFFECTS OF SPIO-LABELLING

2.3.1 IMMUNOMAGNETIC SEPARATION OF MONOCYTES FROM PERIPHERAL BLOOD MONONUCLEAR CELLS

Using indirect magnetic labelling, monocytes were isolated from PBMC for assessment of cellular iron content and migratory capacity. This technique involves indirect immunomagnetic labelling of non-monocytes (including T cells, B cells, NK **c**ells and basophils) using a cocktail of biotin-conjugated antibodies (CD3, CD7, CD16, CD19, CD56, CD123, Glycophorin A) and magnetic anti-biotin Microbeads (Monocyte Isolation Kit II, Miltenyi Biotec).

Peripheral blood mononuclear cells were centrifuged (300 g for 10 min), the supernatant was aspirated entirely and the cell pellet was resuspended in 30 μL per 10^7 cells of buffer (PBS, 0.5% bovine serum albumin, 2 mM ethylenediaminetetraacetic acid (EDTA)). Ten μL of FcR blocking reagent and 10 μL of biotin-antibody cocktail per 10^7 cells were added and the mixture was incubated for 10 minutes at 4°C. Thirty μL of buffer and 20 μL of anti-biotin microbeads per 10^7 cells were added and the mixture was incubated for 15 minutes at 4°C. Cells were washed in 2 mL of buffer and centrifuged at 300 g for 10 minutes before being re-suspended in 500 μL of buffer. A magnetic-activated cell sorting (MACS) column was placed in a magnetic field (1.5T) and primed with 3 mL of buffer. Cells were passed through a pre-separation filter (pore size 100 μm) into the column and the effluent containing the monocytes was collected. Non-monocytes

were retained within the column. Flow cytometry confirmed the monocyte purity to be approximately 90%.

2.3.2 QUANTIFICATION OF CELLULAR IRON CONTENT

Cellular iron content was assessed using the Ferrozine assay. 10^5 monocytes were lysed for 10 minutes in 100 μL of 1% triton. One hundred μL of iron-releasing reagent (a freshly mixed solution of equal volumes of 1.4 M HCl and 4.5% $KMnO_4$ in distilled water) was added and the tubes were incubated at 60°C for 2 hours to release protein-bound iron (e.g. haemoglobin, ferritin). The mixture was then cooled to room temperature and 30 μL of the iron detection reagent was added (6.5 nM Ferrozine, 6.5 mM Neocuprine, 2.5 M ammonium acetate and 1 M ascorbic acid in distilled water). After 30 minutes, 280 μL of the resulting solution was transferred to a 96-well plate.

In order to determine the actual iron content of the test solutions a standard curve was generated using solutions of known concentration of $FeCl_3$ in 10 mM HCl (range 0-300 μM). One hundred μL of 50 nM NaOH and 100 μL of the iron detection reagent were added to 100 μL of the iron standard solution. After 30 minutes, 280 μL of the solution was transferred to the 96-well plate. A plate reader was used to measure the light absorbance at 490 nm. The iron content was expressed in pg of iron per cell.

2.3.3 CELL VIABILITY

Cells were allowed to adhere for 1 hour in 24-well tissue culture plates (10^6 cells/well; 37°C; 5% CO_2) following which the medium was harvested and exchanged for fresh Iscove's modified Dulbecco's medium (IMDM) supplemented with penicillin (100 U/mL), streptomycin (100 U/mL) and 10% autologous serum. This prevented continued uptake of SPIO and avoided interference of excess SPIO with the assays.

Flow cytometry: annexin V-binding and propidium iodide (PI) staining

Cells were harvested for analysis at 1, 24 and 72 hours using 0.25% trypsin and EDTA**.** Cell suspensions were incubated for 10 minutes on ice in annexin V-binding buffer (Hank's balanced salt solution (HBSS) containing 5 mM $CaCl_2$) with FITC-annexin V. Propidium iodide (PI**;** final concentration 2 μg/mL) was added to the cell suspension/annexin V-binding buffer mixture for 1 minute prior to analysis using a FACSCalibur flow cytometer (Becton Dickinson Biosciences, USA) equipped with CellQuest data analysis software.

Annexin V binds to phosphatidylserine expressed at the surface of cells in the early phase of apoptosis, and PI staining indicates permeability of the cell membrane in necrotic cells and cells in the late phase of apoptosis. Cells that were negative for both annexin V-binding and PI staining were classed as viable. The percentage of cells positive for annexin V-binding, PI staining, or both were combined to give an overall percentage of cytotoxicity.

Lactate dehydrogenase assay

The potential cytotoxicity of SPIO-labelling was also assessed using a lactate dehydrogenase (LDH) assay **(**Roche, Diagnostics Ltd, UK) according to the manufacturer's instructions. Lactate dehydrogenase is ubiquitous in all cells, is released following cell membrane damage and can be used to measure cytoxicity. Lactate dehydrogenase catalyses the conversion of lactate to pyruvate and in doing so reduces NAD+ to NAD/H^+. In the assay, in the presence of H^+, the tetrazolium salt (yellow) is converted to formazan (red) and this colour change is detectable using spectrophotometry. This test has the sensitivity to detect LDH release from as few as 500 cells per well of a 96-well plate.

After 24, 48 or 72 hours supernatants were collected for LDH measurement. Remaining cells were lysed and LDH was measured in the cell lysates in order to calculate the total LDH activity. The LDH activity in the supernatant as a percentage of the total (supernatant plus lysed cells) was calculated to give the percentage cytotoxicity.

2.3.4 QUANTIFICATION OF CYTOKINE RELEASE

The concentration of the inflammatory cytokines IL-1b, IL-6, IL-8, IL-10, IL-12p70, and TNF released from cells post labelling was measured using a cytometric bead array kit (Human Inflammatory Cytokine Kit; Becton Dickinson Biosciences, USA) according to the manufacturer's instructions. The limit of detection for this test was cytokine-specific: IL-1β 7.2 pg/mL, IL-6 2.5 pg/mL, IL-10 3.3 pg/mL, TNF 3.7 pg/mL and IL-12p70 1.9 pg/mL. Within the concentration range tested, the

cytometric bead array kit has acceptable precision with intra-assay coefficient of variation (CV; standard deviation divided by the mean) of 4-9% and inter-assay CV of 4-13%.

Labelled and unlabelled cells were plated as described above for 24, 48 and 72 hours. Cell supernatants were harvested and stored (-70°C) for batch analysis. Each sample (25 μL) was incubated (3 hours; room temperature; protected from light) with the mixed Human Inflammation Capture Bead suspension (25 μL) in a round-bottomed 96-well tissue culture plate. Analysis was performed by FACSArray cytometer (Becton Dickinson Biosciences, USA) equipped with FACSArray data analysis software. The concentration of each cytokine was calculated from a standard curve generated from the Human Inflammation Standards provided.

2.3.5 MIGRATORY CAPACITY

Labelled and unlabelled MACS-purified monocytes were loaded into the upper chamber (2.5×10^5 cells/well) of a modified Boyden chamber (Transwell polycarbonate inserts; 5 μm pore size, 24-well plates; Corning Costar, USA). Cells were allowed to migrate for 2 hours (37°C with 5% CO_2) through the microporous membrane into the lower chamber containing 600 μL RPMI with and without the chemokine human MCP-1; Recombinant Human CCL2/MCP-1, (R&D Systems; 50 ng/mL). Cells that had actively migrated through the membrane and adhered to its underside were fixed (100% methanol; 10 min) and stained with DiffQuik™ physiological stain as well as with the Prussian blue stain for iron. Transmigration

was quantified by counting the number of cells present in five randomly selected high power light microscopy fields (x40).

2.4 HISTOPATHOLOGICAL PROCESSING

2.4.1 CYTOSPIN PREPARATIONS

Cells (~10^4 cells) were cyto-centrifuged (300 rpm; 3 min) onto glass microscope slides. Resultant slides were fixed in methanol (100%; 1 min) and stained appropriately.

2.4.2 TISSUE SAMPLES

Whole tissue samples were fixed in ample 4% paraformaldehyde for at least 24 hours, dehydrated in progressively more concentrated alcohol solutions (70-100% ethanol), washed with xylene and embedded in paraffin wax. Slices of the tissue specimen (typically 5 μm thick) were mounted onto glass slides. In preparation for staining, the paraffin wax was removed by washing twice in xylene. Samples were then rehydrated in progressively weaker alcohol concentrations (100-70%) and rinsed in distilled water before staining.

2.4.3 DIFFQUIK™ PHYSIOLOGICAL STAIN

Diffquick stain (modified Romanowsky stain) provided cytoplasmic detail. Air-dried ethanol-fixed slides were exposed to Diffquick solution 1 (eosinophilic) for 30 seconds followed by Diffquick solution 2 (basophilic) and allowed to air-dry. Monocyte nuclei stained violet and the cytoplasm stained sky blue.

2.4.4 PRUSSIAN BLUE STAIN

Cellular iron uptake was confirmed by Prussian blue staining of tissue or cytospin preparations. Slides were stained with a freshly mixed solution of 5% potassium ferrocyanide and 5% hydrochloric acid for 15 minutes. Having allowed the slides to dry completely they were counter stained with Nuclear Fast Red (Sigma Aldrich, UK) prior to observation by light microscopy. Perl's Prussian blue stain causes iron to appear bright/dark blue.

2.5 *IN VITRO* MRI PHANTOM STUDIES

To mimic vascular tissue, phantoms were generated using 50 mL 0.15% agarose gel with 0.11 mM gadolinium EDTA [Walker *et al* 1989]. In brief, 0.16 g gadolinium chloride was dissolved in 10 mL deionised water. 0.32 g EDTA was dissolved in 10 mL deionised water, combined with the gadolinium chloride and diluted further to 500 mL. 0.75 g agarose was added and 0.1 M sodium hydroxide was added dropwise, titrating the pH to approximately 7.5 to allow full dissolution and achieve physiological pH conditions. The resulting agarose/$GdCl_3$/EDTA mixture was heated in a water bath at 90ºC for 1 hour before distribution into 50 mL tubes.

Two different preparations of superparamagnetic iron oxide nanoparticles stabilised with dextran and citrate were incorporated into these phantoms: ferumoxide (Endorem, Guerbet, France; SPIO; mean hydrodynamic particle diameter 80-150 nm) and ferumoxtran (Sinerem, Guerbet, France; USPIO; mean hydrodynamic

particle diameter 10-30 nm). In addition, using the Edinburgh protocol, human mononuclear cells were labelled with Endorem (100 μg/mL) in the presence of protamine sulphate (4 μg/mL) in 0.9 % saline for 2 hours at room temperature. Free USPIO, free SPIO or SPIO-labelled cells were added to the partially cooled gel in a range of concentrations. Phantoms were placed in a water bath and scanned using a 3T clinical MRI scanner.

2.6 MAGNETIC RESONANCE IMAGING CONTRAST AGENTS

2.6.1 SUPERPARAMAGNETIC PARTICLES OF IRON OXIDE

Two different SPIO contrast agents were used. SPIO are predominantly strong negative T2W and T2*W contrast agents, but also have weak positive T1 enhancement at low concentrations. Both SPIO preparations consisted of dextran-coated superparamagnetic iron oxide nanoparticles stabilised with dextran and citrate.

Endorem

Ferumoxide (Endorem, Guerbet, France) consisted of iron oxide particles with a mean hydrodynamic particle diameter 80-150 nm. Supplied as an aqueous suspension (11.2 mg Fe/mL) it was used for *ex vivo* labelling of PBMC.

Sinerem

Ferumoxtran (Sinerem, Guerbet, France) contains USPIO with a mean hydrodynamic particle diameter of 10-30 nm. As such, USPIO escape immediate

recognition by the reticuloendothelial system and can be used for imaging tissue inflammation. Indeed we have used Sinerem for the detection of inflammation in AAA. Supplied as a dry powder, it was first reconstituted in 10 mL of 0.9% saline and then the weight-adjusted dose of 2.6 mg/kg was diluted further in 100 mL of 0.9% saline. The resulting USPIO suspension was administered through a filter as a slow infusion over 30 minutes through a peripheral 20-gauge intravenous cannula.

Gadolinium

Gadolinium is a paramagnetic contrast agent that causes positive enhancement on T1W images. The gadolinium-based agent Dotarem (0.5 mmol/mL Gd-DOTA; Guerbet, France) was supplied as a liquid and administered intravenously using a power injector at a dose of 0.2 mL/kg bodyweight.

2.7 MAGNETIC RESONANCE IMAGING

The principles of magnetic resonance imaging are discussed further in **Appendix 2**.

2.7.1 RELAXATION

When exposed to the external magnetic field (B_0) of the MRI scanner, protons align with an orientation parallel (low-energy state) or anti-parallel (high-energy state) to B_0. A radiofrequency pulse is applied as a result of which a proportion of protons gain energy and the NMV is deflected away from the static magnetic field (B_0) into the transverse plane. Coherent (in phase) transverse magnetisation induces a current constituting the signal in the receiver coil. At the end of the radiofrequency pulse, the

NMV tends to relax and realign with B_0**.** Recovery of longitudinal magnetisation occurs as a proportion of protons in the high-energy state return to the low-energy state by emitting some of the energy (photons) that they had gained from the radiofrequency pulse (i.e. T1 recovery). The second component of relaxation is loss of coherent transverse magnetisation as spinning nuclei transfer energy amongst each other leading to loss of phase-coherence (i.e. T2 decay).

T2* decay is the loss of phase-coherence through a combination of T2 decay (due to spin-spin interactions) and small local magnetic field inhomogeneities. The T2* value is always shorter than the T2 value.

2.7.2 MRI SEQUENCES

Spin echo sequences

T1W and T2W turbo spin echo sequences were used to acquire detailed anatomical data. Spin echo sequences have a relatively long acquisition time but have a high signal-to-noise ratio and give excellent anatomical definition. A 90^o radiofrequency pulse is applied flipping the NMV into the transverse plane. As a result of T2* decay, the precessing protons begin to dephase immediately and phase-coherence is lost rapidly. To compensate for T2* decay, a further 180^o rephasing radiofrequency pulse is applied at a time t (where t=TE/2), which reverses the direction of the NMV. The signal is sampled at a time $2t$ (where $2t$=TE) when phase-coherence has been regained.

Gradient echo sequences

Gradient echo sequences were used to detect SPIO accumulation. A gradient magnetic field is induced at an angle to B_0 and interacts with the main magnetic field such that the composite field strength varies along the axis of B_0. Protons in different parts of the magnetic field are therefore exposed to different field strengths and precess at different frequencies. Gradual dephasing of coherent transverse magnetisation occurs and protons are rephased by application of a second gradient. The signal induced in the receiver coil at this point is called the gradient echo.

Compared to images acquired using spin echo sequences, gradient echo sequences have a poorer signal-to-noise ratio but are acquired much more quickly. There is no compensation for T2* decay and gradient echo sequences are therefore highly sensitive to the magnetic field inhomogeneities induced by SPIO.

Multi echo gradient echo sequences

In a multi echo gradient echo sequence the signal is sampled at multiple echo times following a radiofrequency pulse. Compared to acquiring the echoes using separate radiofrequency pulses, the use of a multi echo sequence reduces the acquisition time and, because the echoes are collected only milliseconds apart, avoids the need to register sequential images to each other for further analysis.

2.7.3 DATA ANALYSIS:

Following a radiofrequency pulse sequence, the signal decays exponentially with increasing echo time. Both endogenous iron and SPIO induce local magnetic field inhomogeneities. Rapid dephasing of coherent transverse magnetisation occurs and the signal intensity decays more rapidly in the presence of SPIO. As a result, tissues in which SPIO accumulate appear dark on T2W and particularly T2*W images. SPIO also have a T1 shortening effect that is most obvious at low concentrations, whilst at higher concentrations T2* susceptibility effects predominate [Canet *et al* 1993; Torabi *et al* 2004]. These T1 effects may confound data interpretation data if analysis is based on measurement of signal intensity at a single echo time.

The rate of decay of signal intensity is determined by the decay constant the T2* value calculated by the equation $S(t)=S(0)\exp-(t/T2^*)$, where $S(t)$ is the signal intensity at time t, and S(0) is the signal intensity at time 0. The rate of decay of signal intensity with echo time is increased in the presence of SPIO with a corresponding reduction in T2* value. Changes in T2* value and its inverse the R2* value ($T2^*=1/R2^*$) have been exploited for the detection of endogenous iron accumulation such as occurs in haemochromatosis and transfusion-related iron overload in patients with thalassaemia major. Using multi echo sequences, a reduction in T2* value or an increase in R2* value is observed in the myocardium and the liver in patients with systemic iron overload [Anderson *et al* 2001; Wood *et al* 2005; Storey *et al* 2007].

The advantage of using T2* or R2* for analysis is that these measures are independent of tissue effects and the T1 effects of SPIO.

Registration

T2W images have excellent discrimination of the lumen, thrombus, aortic wall and surrounding tissues.

T2*W sequences have less distinct soft tissue contrast but are exquisitely sensitive to the effects of USPIO accumulation. To allow comparison of serial imaging studies and to utilise the strengths of both of these image weightings, the T2W and T2*W images were co-registered.

Registration was performed using a semi-automatic 3-dimensional rigid voxel registration protocol utilising a normalised mutual information algorithm (Analyze, Mayo Clinic). The T2W images acquired on the first study visit were designated as the baseline images to which all other images were registered. T2*W images (first echo) were registered to the corresponding T2W images acquired on the same day. Subsequent T2W images were registered to the baseline T2W images. The use of multi echo T2*W sequences obviated the need for registration of individual echoes to each other since they were acquired only milliseconds apart. Where echoes were acquired separately they were registered together as described above.

T2* and R2* value calculation

A Gaussian filter was applied to the individual echoes to minimise noise corruption of the raw data. Using a multi echo T2*W sequence or by careful registration of separately-acquired echoes, the T2* or R2* value was calculated on a single voxel basis. For each voxel position, a plot of the natural log of the signal intensity *versus* the corresponding echo time was produced with the negative inverse gradient giving the T2* value. The R2* value was calculated using the negative gradient. A straight line was fitted to the four data points using a standard least squares method. The coefficient of determination (r^2) and the sum of squared deviations due to error (SSE) were used to exclude data that did not have an acceptable straight line fit. The thresholds for r^2 and SSE were determined experimentally by examining a subset of the data (Matlab, The Mathworks Inc, USA).

Data presentation

Data were then presented as T2* or R2* maps where the magnitude of each voxel represented the T2* or R2* value. Where appropriate, data were also presented using ΔT2* maps where each voxel represented the change in T2* value following the administration of the contrast agent. A colour scale was used to facilitate qualitative data interpretation. T2*W sequences are sensitive not only to the presence of iron but also to other sources of artefact. Where possible the repeatability of the T2* value measurement in the absence of SPIO or USPIO was established and used to define a threshold above which any changes in T2* could be attributed with confidence to SPIO or USPIO accumulation.

Regions of interest were defined on anatomical T1W or T2W images, applied to the T2* or R2* maps and used to compare data quantitatively.

2.7.4 STATISTICAL ANALYSIS

The Bland and Altman method was used to evaluate the repeatability of the T2* measurements [Bland and Altman 1986]. Continuous data were compared with a two-tailed Student *t*-test, whilst paired continuous data were compared with a two-tailed paired Student *t*-test. Continuous data with multiple timepoints were compared using a one-way analysis of variance (ANOVA) with repeated measures and Tukey's or Bonferroni's post-test comparison. Categorical data were anlaysed using Chi-squared test with cross-tabulation. Analyses were performed using Statistical Package for the Social Sciences (SPSS), Minitab or GraphPad Prism (GraphPad Software, USA) where appropriate. In each case statistical significance was taken as two-sided $P < 0.05$.

CHAPTER 3

ASSESSMENT OF TISSUE ACCUMULATION OF SUPERPARAMAGNETIC PARTICLES OF IRON OXIDE USING MAGNETIC RESONANCE IMAGING

3.1 SUMMARY

Contrast agents containing SPIO have been used for clinical MRI of vascular inflammation and *in vivo* cell tracking. However data acquisition and analysis of the resulting data pose a number of challenges. The aims of this study were to use *in vitro* phantoms and a population of patients undergoing USPIO imaging of AAA to define data acquisition and image analysis methodology to assess SPIO accumulation in tissues based on changes in T2* value. *In vitro,* USPIO, SPIO and SPIO-labelled cells produced a concentration-dependent reduction in T2 and T2* in agarose phantoms. Thirty-seven patients with asymptomatic aortic aneurysms >4.0 cm in diameter were recruited. Repeatability of T2* value measurement was determined in eight patients. Twenty-nine patients underwent MRI scanning before and 24-36 hours after administration of USPIO. T2- and multi echo T2*W sequences were performed in a 3T MRI scanner. USPIO accumulation was assessed using the decay constant for signal intensity over time: the T2* value. Based on repeatability data, thresholds for absolute change (45 ms) and per cent change (59%) in T2* values were defined for the detection of SPIO in tissues informing colour scale map data presentation. Per cent changes in T2* value were highly discriminatory for detecting and quantifying USPIO accumulation in tissues with heterogeneous background T2* values.

In summary we have defined a robust semi-quantitative image acquisition and data analysis algorithm for the detection of SPIO accumulation that has extensive application for clinical imaging of cellular inflammation and *in vivo* cell tracking.

3.2 INTRODUCTION

Superparamagnetic particles of iron oxide form a class of MRI contrast agents possessing much stronger paramagnetism than standard gadolinium-based agents. This intense paramagnetism renders SPIO exquisitely sensitive contrast agents that can be detected at very low concentrations. However, the analysis of the resulting data presents a number of challenges and a pragmatic solution is required if the potential of these agents is to be realised.

SPIO have been used to label a variety of cell types and to track cells *in vivo* using MRI [Arbab *et al* 2004; de Vries *et al* 2005a; de Vries *et al* 2005b; Arbab *et al* 2006; Zhu *et al* 2006; Toso *et al* 2008b]. The ability to track cells, such as stem cells, would be an important tool for the further development of novel cell-based therapies, allowing the identification of cells reaching and remaining in the intended target therapeutic site. Small enough to escape immediate recognition by the reticuloendothelial system, USPIO can be used to study cellular inflammation within tissues [Corot *et al* 2007]. Inflammation is critical in the pathogenesis of many conditions including atherosclerosis and aneurysm disease. In preliminary clinical MRI studies, USPIO accumulated in vulnerable and ruptured carotid plaques but not stable plaques [Kooi *et al* 2003; Trivedi *et al* 2006; Tang *et al* 2009]. Magnetic resonance imaging with USPIO is therefore a promising method of detecting cellular inflammation and plaque instability.

Image analysis for published clinical studies using SPIO has typically involved the inspection of images for a reduction in signal intensity consistent with iron accumulation. Beyond a simple dichotomisation for the presence or absence of iron, it would be attractive to achieve a more objective semi-quantitative assessment of SPIO accumulation. The calculation of the T2* value is one such approach and is possible using standard clinical T2*W sequences commonly used for the assessment of tissue iron overload [Kirk *et al* 2009]. However, the acquisition parameters used require optimisation for SPIO detection at 3T since the reduction in T2* value caused by SPIO accumulation is greater at higher field strengths [Anderson *et al* 2001; Storey *et al* 2007]. In patients with systemic iron overload, this technique estimates the global iron burden within tissues including the liver and myocardium. In contrast, when SPIO are used for clinical cell tracking studies or the identification of cellular inflammation, additional spatial detail is required to describe subtle regional variations in the distribution of iron within different tissue components with heterogeneous baseline T2* values. Thus, assessing focal SPIO uptake and changes in T2* value on a heterogeneous background presents many challenges.

The aims of this study were to develop and define 3T protocols to detect SPIO accumulation, and to develop a robust image analysis methodology that would allow assessment of SPIO accumulation in different tissue components and regions. We here describe the development of these methods in the context of a study using USPIO to detect aortic wall cellular inflammation in patients with AAA.

3.3 MATERIALS AND METHODS

3.3.1 PHANTOMS

To mimic vascular tissue, phantoms were generated using 50 mL 0.15% agarose gel with 0.11 mM gadolinium EDTA [Walker *et al* 1989]. Two different preparations of superparamagnetic iron oxide nanoparticles stabilised with dextran and citrate were incorporated into these phantoms: ferumoxide (Endorem, Guerbet, France; SPIO; mean hydrodynamic particle diameter 80-150 nm) and ferumoxtran (Sinerem, Guerbet, France; USPIO; mean hydrodynamic particle diameter 10-30 nm) respectively. In addition, human mononuclear cells were labelled with SPIO according to the Edinburgh protocol. Free USPIO, free SPIO or SPIO-labelled cells were added to the gel in a range of concentrations.

Phantoms were placed in a water bath and scanned using a 3T Siemens Magnetom Verio MRI scanner (Siemens, Erlangen, Germany) with a 12-channel receive head matrix coil. A T2W spin echo sequence was applied to a 5 mm coronal slice with a TR of 4000 ms (to avoid T1 saturation effects) and multiple echo time values ranging from 7.7 to 250 ms. A T2*W multi gradient echo sequence with TR of 4000 ms and echo times of 4.9, 7.7, 10.5 and 13.3 ms was applied to the same slice. Values for T2 and T2* were calculated from regression of log signal intensity *versus* echo time (Minitab version 16, USA).

3.3.2 CLINICAL STUDIES

Patients (n=37) with asymptomatic AAA (4.0-9.0 cm) were recruited from the AAA surveillance programme at the Royal Infirmary in Edinburgh between August 2009 and July 2010. All patients had an asymptomatic AAA with diameter >4.0 cm on ultrasound scanning. Eight patients were recruited to obtain repeatability data for baseline T2* measurement in the absence of USPIO and twenty-nine patients were recruited to receive the USPIO contrast agent.

3.3.3 CONTRAST AGENT ADMINISTRATION

The weight-adjusted dose (2.6 mg/kg) of Sinerem (Guerbet, France) was diluted in 100 mL of 0.9% sodium chloride and administered as a slow infusion over 30 minutes.

3.3.4 MAGNETIC RESONANCE IMAGING

Magnetic resonance imaging was undertaken in a clinical whole-body 3T Siemens Magnetom Verio MRI scanner (Siemens, Erlangen, Germany) using a combination of body and spine matrix coil elements to optimise image acquisition in the abdominal aorta.

Coronal and sagittal breath-held T2W HASTE localiser sequences were used to define the extent of the aneurysm and plan slice positions for subsequent scans. A respiratory-gated electrocardiogram-triggered axial T2W turbo spin echo sequence was used to acquire detailed anatomical data (TR/TE 2R-R intervals/72 ms; flip angle 180°; matrix 192 × 256; field of view 400 × 400 mm; slice width 5 mm). A

multi gradient echo T2*W sequence (TE 4.9, 7.7, 10.5, 13.3 ms; TR 133 ms; flip angle 15°; matrix 192 × 256; field of view 400 × 400 mm; slice width 5 mm) was used to acquire images of the aneurysm with slice positions corresponding to those of the T2W images. T2W images give excellent discrimination of the boundaries between the flow lumen, thrombus, wall and surrounding tissues. T2*W sequences, have less distinct soft tissue contrast, but are exquisitely sensitive to the effects of USPIO accumulation. The echo times for the T2*W sequences were selected such that fat and water were in phase for each echo to minimise phase shift artefact and subsequent errors in T2* calculation. The field of view used for both sequences was typically 400 × 400 mm, but was adjusted for larger subjects to minimise phase wrap artefacts.

For the eight patients recruited to determine the repeatability of T2* measurements, the aneurysm was sampled over five adjacent slices. Sequences were repeated up to three times. A T2W sequence was applied and T2*W sequences were acquired (run 1) and repeated (run 2). The study subject then came out of the scanner and got off the table before returning immediately to undergo a repeat scan to simulate the pre-and post-contrast acquisitions in patients receiving USPIO. The localiser sequences were repeated and slice positions were selected to match those used in runs 1 and 2 using the position in relation to the vertebral bodies to guide slice placement. The T2W and T2*W sequences (run 3) were then repeated.

In the twenty-nine patients recruited to receive USPIO, MRI scanning was performed before and 24-36 hours after the administration of the contrast agent. T2W and T2*W sequences were applied to the entire extent of the aneurysm. With reference to position in relation to the vertebral bodies, axial slice positions on the post-contrast scan were matched to those used for the pre-contrast scan.

For calculation of the T2* value, the signal intensity was sampled at four echo times within the multi echo sequence. For accurate T2* value calculation, it is important that the signal intensity is always higher than the background noise, even at the longest echo time [Miller and Joseph 1993]. If, following administration of the contrast agent, the signal intensity decays to the level of the noise, the reduction in T2* value may be underestimated and the sensitivity to detect USPIO accumulation is reduced. To confirm the appropriate selection of echo times in the multi echo sequence, a ROI was selected to measure the mean signal intensity at each echo time in areas of high and low USPIO uptake in a subset (n=6) of the post-USPIO scans, and in corresponding areas of the pre-contrast scans. The noise level was calculated according to Edelstein's approximation as 1/0.66 times the standard deviation of the signal intensity in extracorporeal air free from artefact [Edelstein *et al* 1984].

3.3.5 REGISTRATION

T2W images give excellent discrimination of the boundaries between the flow lumen, thrombus, aortic wall and surrounding tissues (Figure 3.1) [Kramer *et al* 2004]. T2*W sequences have less distinct soft tissue contrast but are exquisitely

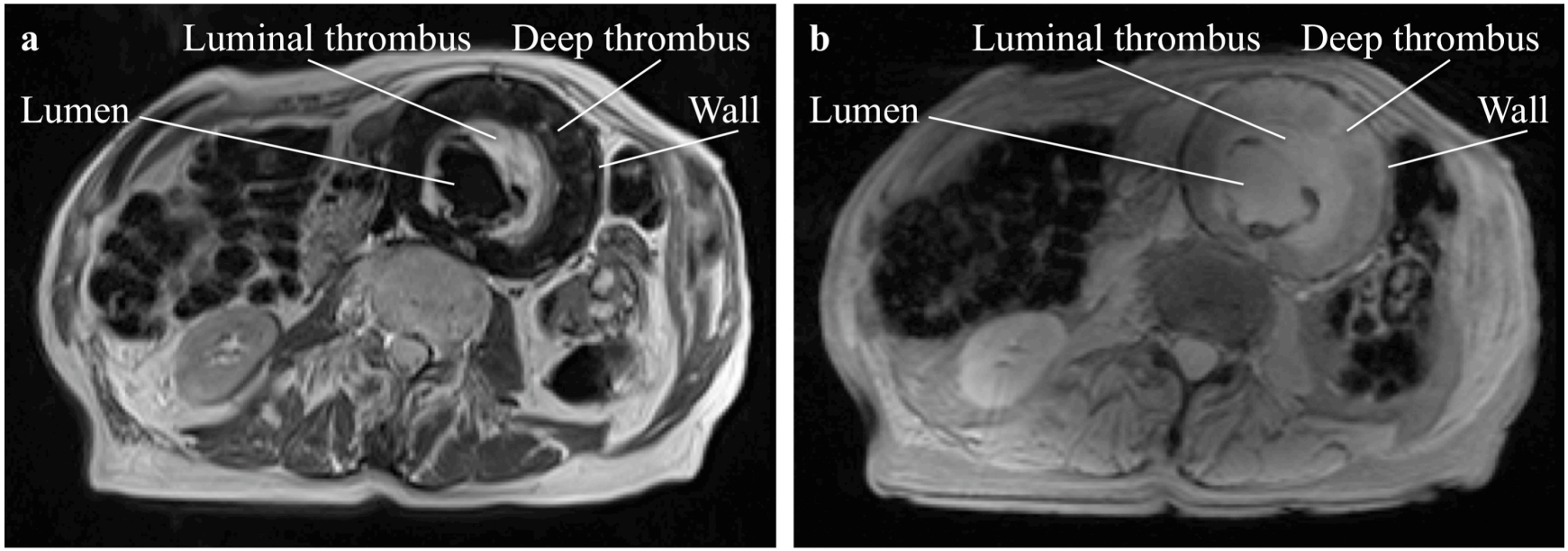

Figure 3.1 T2W image **(a)** and T2*W image **(b)** with echo time of 4.9 ms. The different components of the aneurysm are clearly seen on both images but the T2W image has superior soft tissue contrast.
T2W - T2 weighted.

sensitive to the effects of USPIO accumulation. To utilise the strengths of both of these image weightings, the T2W and T2*W images were co-registered. Subsequent images were registered to the base image using a well-established semi-automatic rigid 3-dimensional voxel registration protocol (Analyze, Mayo Clinic) utilising a normalised mutual information algorithm [Studholme, 1998]. The use of a multi echo T2*W sequence avoided the need to register the individual echoes for T2* map generation. The first echo (TE 4.1 ms) was used for registration since it provided the best structural definition.

Registration of the entire imaging volume was found to compromise the quality of registration of the aorta itself due to bowel and abdominal wall motion. Therefore, to minimise the contribution of bowel and abdominal wall motion within this algorithm, a region for registration was selected to include the aorta, vertebrae and spinal musculature, which remain fairly static during the respiratory cycle, but exclude the more mobile abdominal wall and bowel as far as possible. Following the initial automatic step, registration was further optimised manually where necessary following visual inspection of a blend of the two images. The registration process generated a transformation matrix that was applied to the original images to align them with the pre-contrast T2W image. The transformed images were used for the remainder of the image analysis procedure.

3.3.6 IMAGE ANALYSIS

At 3T, the predominant effect of SPIO accumulation is to induce small local magnetic field inhomogeneities resulting in rapid dephasing of coherent transverse magnetisation. In the presence of SPIO, the rate of decay of signal is increased with a corresponding reduction in T2*. The T2* value is the decay constant for the exponential decay of signal intensity with increasing echo time. Since SPIO contrast agents have T1 as well as T2/T2* effects, comparison was made between the pre- and post-contrast T2* value, rather than using the signal intensity at a single echo time thereby negating the positive signal enhancement caused by the T1 shortening effect. From the four individual echoes in the multi echo T2*W sequence, a T2* map was generated in which each voxel represented the T2* value calculated by the equation $S(t)=S(0)\exp-(t/T2^*)$, where $S(t)$ is the signal intensity at time t, and $S(0)$ is the signal intensity at time 0.

A 3 x 3 voxel Gaussian filter was applied to the individual echoes to minimise the effect of noise on subsequent image processing steps. Then, for each voxel position a plot of the natural log of the signal intensity *versus* the corresponding echo time was produced with the negative inverse gradient giving the T2* value. A straight line was fitted to the four data points using a standard least squares method. The coefficient of variation and the SSE were used to exclude data that did not have an acceptable straight line fit. The thresholds for r^2 (>0.4) and SSE (<0.2) were determined experimentally by examining a subset of the data (Matlab, The Mathworks Inc, USA).

A ROI, including the aortic wall and ILT but excluding the lumen, was drawn on the T2W base image and applied to the transformed T2* maps. The change in T2* value may be expressed as the absolute change or as the per cent change relative to the baseline T2* value. Given the anticipated heterogeneity of baseline T2* of different plaque components [Kramer *et al* 2004], we assessed both absolute change and per cent change in T2* for vascular imaging using USPIO.

3.3.7 OUTPUT IMAGE GENERATION

The absolute or per cent change in T2* was displayed using colour scale maps. SPIO agents result in negative contrast on T2*W MRI, and a reduction in T2* value on a T2* map, both of which are difficult to detect by visual inspection of grey-scale images. Presentation of data using a hot-cold (red-blue) colour scale map retains spatial information alongside quantitative T2* data to facilitate data interpretation. The repeatability data were used to define the colour scale by establishing a threshold for ΔT2* above which a change could be attributed to SPIO accumulation.

3.3.8 STATISTICAL ANALYSIS

The Bland and Altman method was used to evaluate the repeatability of the T2* measurements [Bland and Altman 1986]. Statistical analysis using Minitab was performed where appropriate with two-tailed Student *t*-test and statistical significance was taken as two-sided $P < 0.05$.

3.4 RESULTS

3.4.1 PHANTOMS

There was a concentration-dependent reduction in both T2 and T2* values with increasing concentrations of USPIO, SPIO and SPIO-labelled cells (Figure 3.2).

3.4.2 CLINICAL STUDIES

Thirty-seven patients with aneurysm diameter 4.0-9.0 cm were recruited to the trial of whom 29 received the USPIO contrast agent. There were no side-effects relating to the administration of the USPIO contrast agent which was generally well tolerated.

The excellent soft tissue contrast on high-resolution T2W imaging of the aorta at 3T allowed ready discrimination of the different components (lumen, wall and thrombus) for the majority of the aneurysm volume (Figure 3.1). The use of 5 mm thick slices enabled coverage of the entire aneurysm, but in a few patients with particularly tortuous regions of vasculature (e.g. aneurysm neck and iliac bifurcation), there was a partial volume effect that compromised distinction of the outer wall from surrounding tissues and required the use of thinner slices. Elsewhere the outer wall of the vessel was generally readily identified since the interface with visceral fat gave high contrast. However delineation of the vessel wall was more difficult if the wall was particularly thin or was adjacent to other structures, such as the vena cava or vertebral column that provided less contrast. Excellent registration was achieved for slices in the main body of the aneurysm in all but one of the

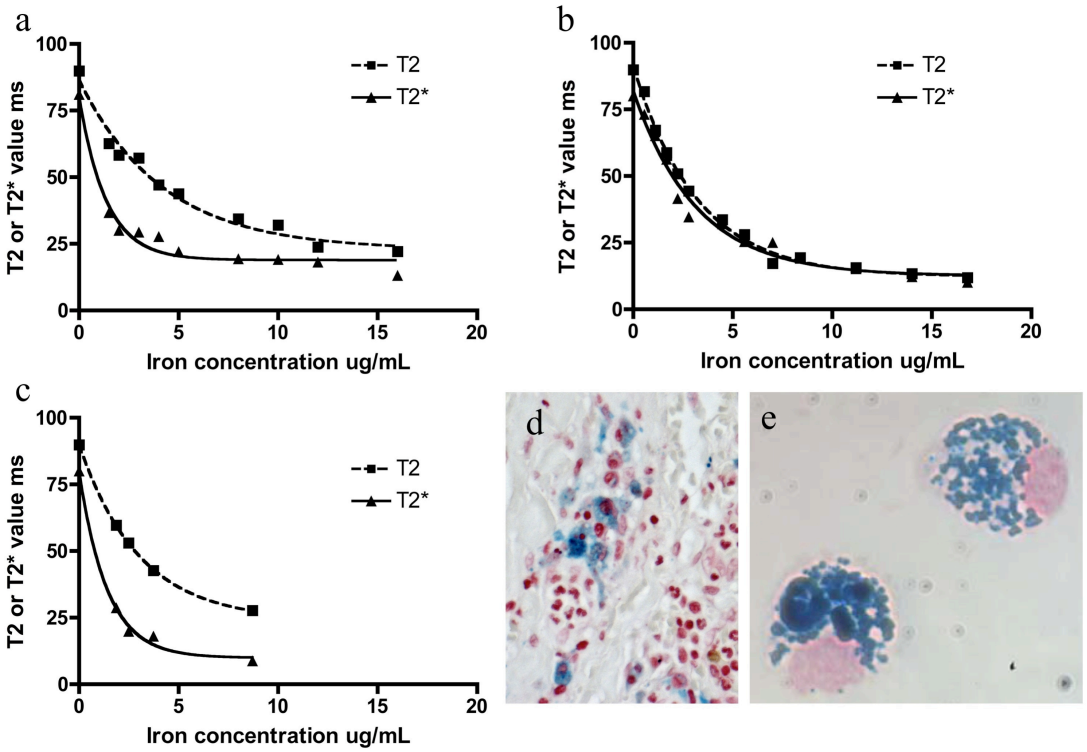

Figure 3.2 Change in T2 and T2* with increasing iron concentration for free USPIO **(a)**, free SPIO **(b)** and SPIO-labelled cells **(c)**. Histology of the aortic wall from a patient with an abdominal aortic aneurysm showing intracellular USPIO uptake and accumulation (blue; Perl's iron stain x100) **(d)**. Cytospin of mononuclear cells following *ex vivo* labelling with SPIO showing intracellular iron accumulation (blue; Perl's iron stain x100) **(e)**.
A dose-dependent reduction in both T2 and T2* was observed for free USPIO, SPIO and SPIO-labelled cells. For free SPIO, at a given concentration of iron, T2 and T2* were similar. In contrast, when SPIO was compartmentalised within cells, the effect on T2* was greater than the effect on the T2, consistent with the induction of local magnetic field inhomogeneities by clustered SPIO. For phantoms with SPIO-labelled cells, T2 was higher and T2* was lower than for phantoms containing the equivalent concentration of free SPIO.
USPIO - Ultrasmall superparamagnetic particles of iron oxide; SPIO - Superparamagnetic particles of iron oxide.

patients. This patient moved slightly during scanning although acceptable registration was still achievable by registering each slice separately.

3.4.3 T2* CALCULATION

For accurate estimation of the T2* value, multiple data points were obtained by sampling the signal intensity at several echo times (Figure 3.3). It is important that the signal intensity at the longest echo time is higher than the background noise both pre- and post-contrast administration to avoid underestimation of the T2* value [Miller and Joseph 1993]. We have avoided this potential noise corruption of the T2* value calculation by using a multi echo sequence with a maximum echo time of 13.3 ms such that, even in regions with the highest USPIO uptake, the mean signal intensity at the longest echo time (13.3 ms) was 109.5 ± 26.1 ms: well above the mean noise level of 0.88 ms. Less than 10% of the data did not have an acceptable straight line fit and were excluded from the T2* map.

Repeatability and threshold of T2*

The repeatability of the measurement of the T2* value was determined by comparison of data from two T2*W sequences (run 1 *versus* run 2) performed in quick succession without moving the patient. This analysis was performed on a voxel-by-voxel basis with a total of 24,698 data points, of which 1.1% were affected by artefact and discarded. Using the Bland and Altman method [Bland and Altman 1986], there was a mean bias of -0.21 ms and standard deviation of the difference of 16.4 ms.

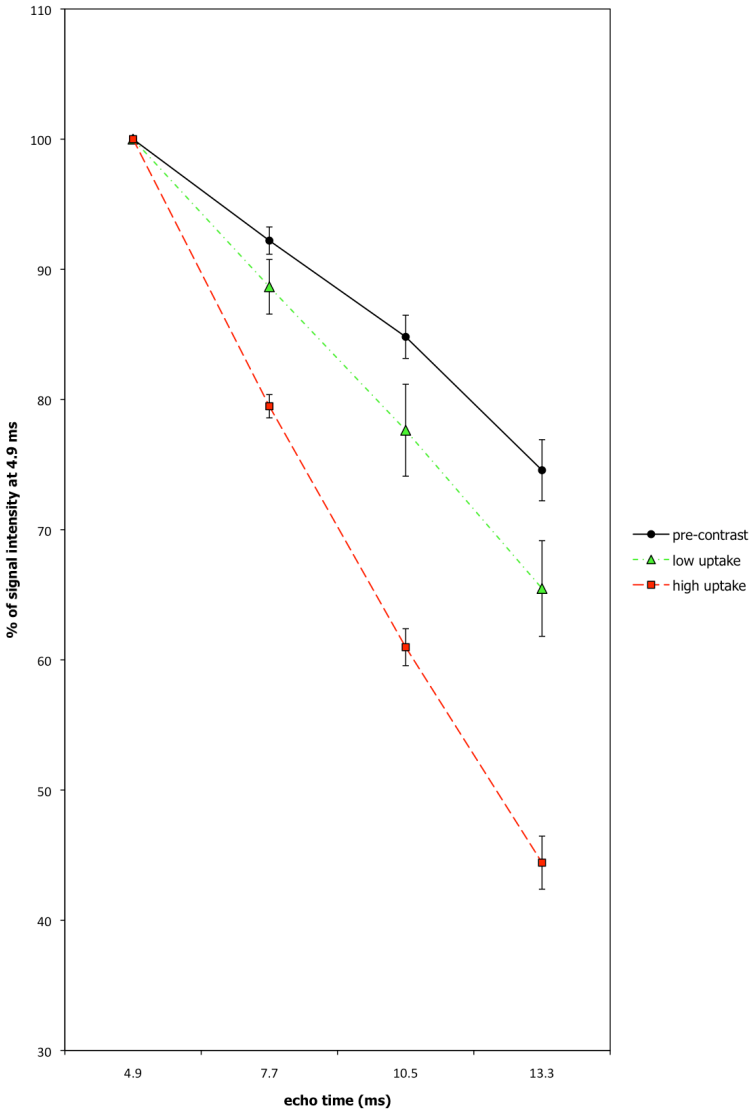

Figure 3.3 Signal intensity as percentage of first echo time (TE=4.9 ms) within the multi echo sequence of pre-contrast and post-contrast images in areas of high and low USPIO uptake. The signal intensity decays more rapidly where there is high USPIO uptake, but even at the longest echo time (TE=13.3 ms), the signal intensity is well above the noise level (0.88 ms). T2* values for pre-contrast, low uptake and high uptake were 28.8, 19.8 and 10.5 ms respectively.
TE - Echo time; USPIO - Ultrasmall superparamagnetic particles of iron oxide.

We wanted to assess the between-scan variability in T2* in the absence of USPIO in order to establish a threshold above which an observed ΔT2* could be attributed to USPIO accumulation. For each patient in the reproducibility series, the T2* value was measured (run 1) and repeated (run 3) having moved the patient out of the scanner, repositioned the patient and repeated the localiser sequences. The absolute change and per cent change in T2* value between run 1 and run 3 were calculated for each voxel giving an indication of the composite variability in T2* value resulting from the measurement itself and from registration. The 95th percentile value for the absolute and per cent ΔT2* was calculated for individual patients and averaged for all eight patients giving an absolute threshold of 45.0 ms and relative threshold of 59.1% for ΔT2* values.

USPIO and change in T2*

The change in T2* value may be expressed as the absolute or per cent change from the baseline value. The frequency distribution for the absolute ΔT2* values was similar for those who did or did not receive USPIO although, as anticipated, it did show a small rightward shift of 19 ms ($P < 0.0001$) for those receiving USPIO (Figure 3.4). In contrast, there was a marked non-uniform shift in frequency distribution with USPIO when considering the per cent ΔT2* (Figure 3.4). A focal area of USPIO uptake is difficult to distinguish on a colour map of absolute ΔT2* but is clearly seen on a per cent ΔT2* colour map (Figure 3.5). There is a reduction in signal intensity in the same area on the post-USPIO T2*W scans but this is more obvious when the same data are displayed as a colour map.

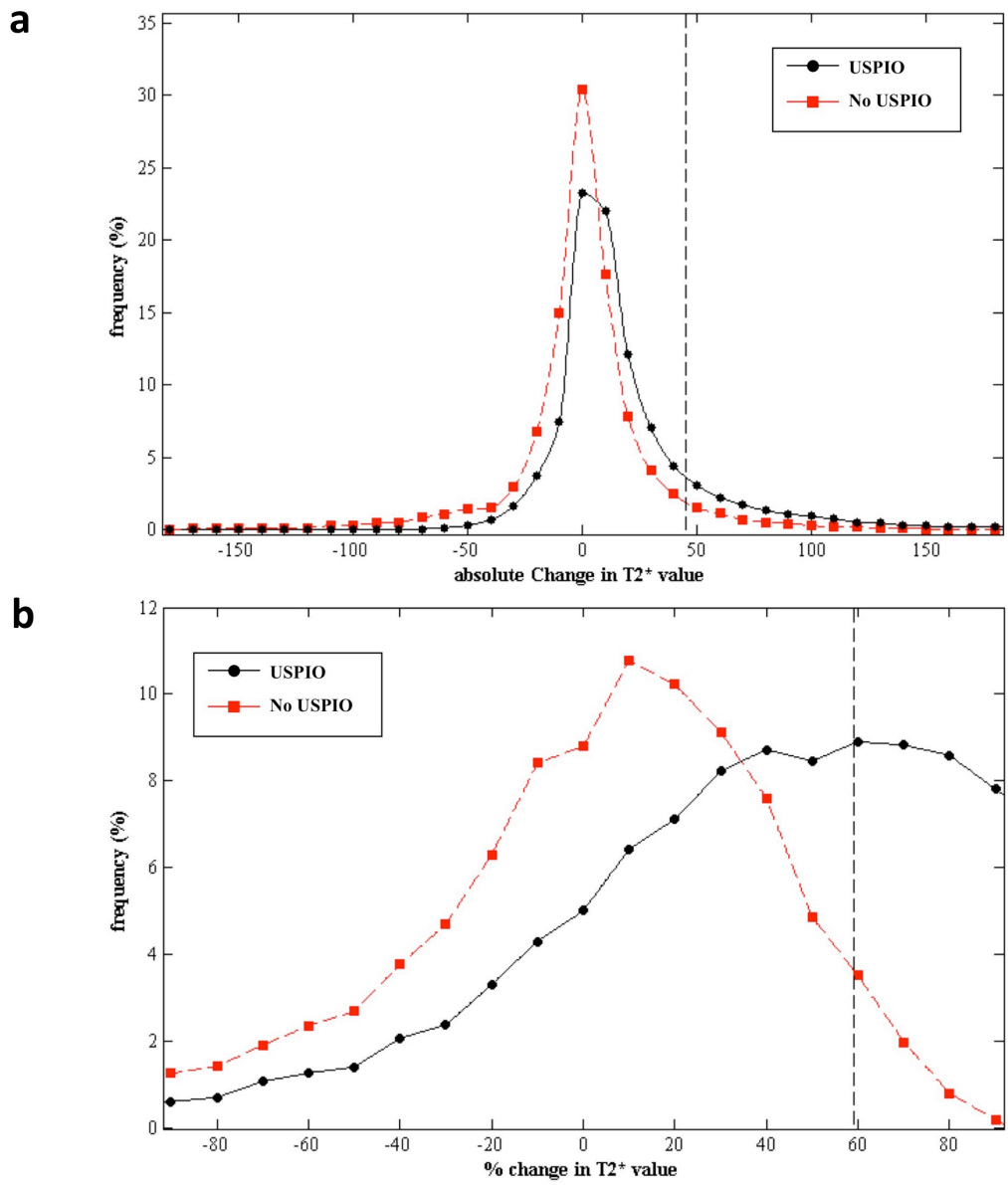

Figure 3.4 T2*W sequences were performed (run 1) and repeated (run 3) having moved the patient out of the scanner, repositioned the patient and repeated the localiser sequences. The absolute change and per cent change in T2* between run 1 and run 3 were calculated for each voxel giving an indication of the composite variability in T2* resulting from the measurement itself and from registration. **(a) Absolute Change in T2*:** Frequency of voxels with absolute change in T2* for patients who did or did not receive USPIO. The upper 95% threshold of change in T2* in the absence of USPIO was 45 ms. **(b) Per cent Change in T2*:** Frequency of voxels with per cent change in T2* for patients who did or did not receive USPIO. The upper 95% threshold of per cent change in T2* in the absence of USPIO was 59%.
T2*W - T2* weighted; USPIO - Ultrasmall superparamagnetic particles of iron oxide.

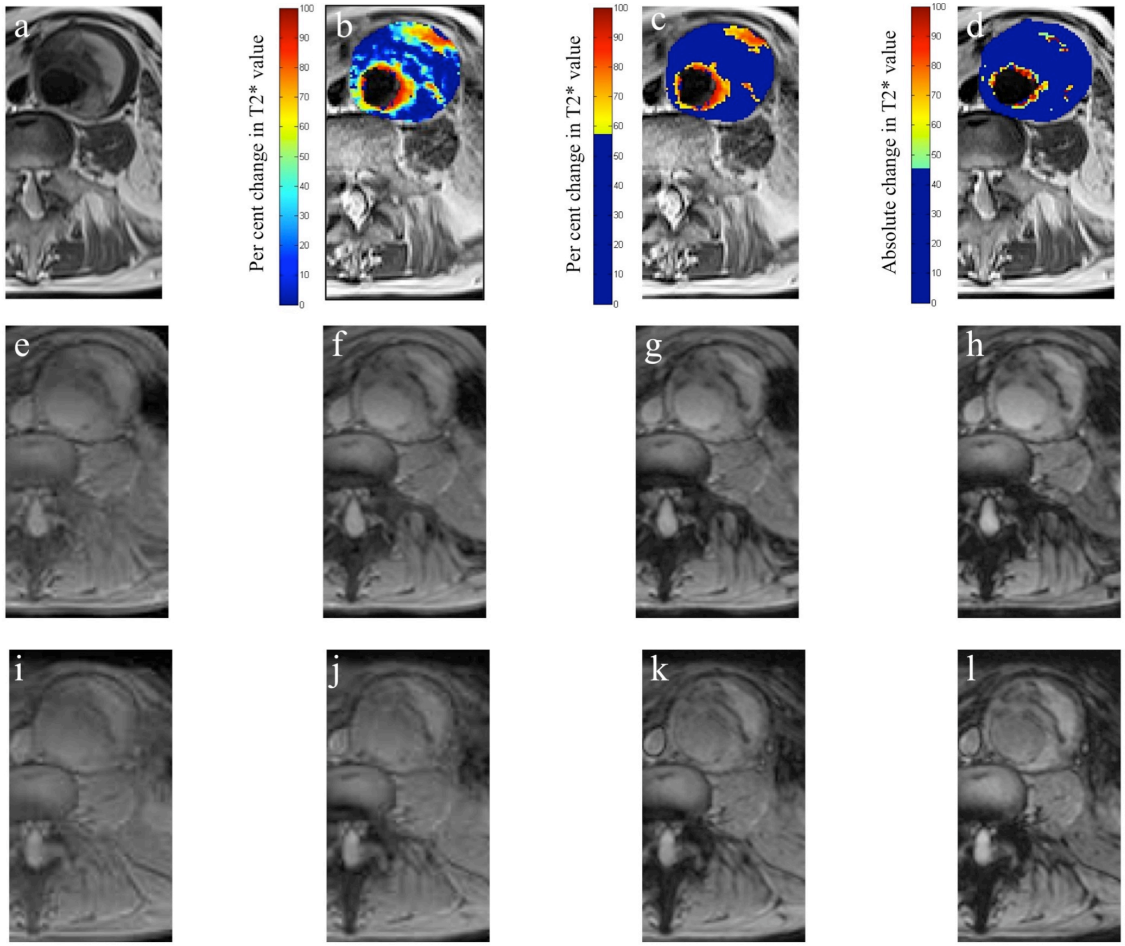

Figure 3.5 Patient with focal uptake of USPIO in the anterior wall of the aneurysm. (a) T2W anatomical image, **(b)** colour map of the per cent change in T2*, **(c)** colour map of the per cent change in T2* with a threshold of 59%, and **(d)** colour map of the absolute change in T2* with a threshold of 45 ms. **(e)-(h)** Pre-USPIO T2*W images with echo times of 4.9, 7.4, 10.7, 13.3 ms. **(i)-(l)** Post-USPIO T2*W images with echo times of 4.9, 7.4, 10.7, 13.3 ms.
USPIO - Ultrasmall superparamagnetic particles of iron oxide; T2W - T2 weighted

3.5 DISCUSSION

We have defined a robust semi-quantitative method for the detection of iron nanoparticle accumulation in humans using 3T MRI. Using precise tissue registration and per cent change in T2* (ΔT2*), we can identify USPIO accumulation against a highly heterogeneous tissue background. This technique is highly sensitive to the magnitude and spatial distribution of SPIO, and holds major promise as an *in vivo* method of detecting cellular inflammation and tracking SPIO-labelled cells.

We used ΔT2* following contrast administration to evaluate SPIO accumulation semi-quantitatively because SPIO have some T1 as well as T2/T2* effects that could confound data interpretation if signal intensity measures are used. Analysis of data in previous clinical studies employing USPIO has been largely qualitative and used dichotomous assessments of signal voids or reductions in signal intensity in the target tissue relative to control tissue (e.g. adjacent muscle or fat) at a single echo time [de Vries *et al* 2005b; Zhu *et al* 2006; Toso *et al* 2008a; Tang *et al* 2009]. Our method has the major advantage that it is objective and calibrated against repeatability data rather than assuming that the signal intensity of control tissue is unchanged by SPIO administration. We have shown a correlation between iron concentration and T2* for USPIO, SPIO and SPIO-labelled cells in phantom studies, and a linear correlation exists between iron concentration and the R2* value (R2*=1/T2*) [Kuhlpeter *et al* 2007; Rad *et al* 2007]. The R2* value also correlates with hepatic iron concentration in patients with transfusion-related hepatic iron

overload. However, quantification of iron concentration in tissues can be challenging and it is worth considering that the relationship between R2 and R2* values may not be linear in situations where cells are present in large clumps as the effect of iron nanoparticles on the magnetic field is magnified in this scenario [Bowen *et al* 2002].

Rather than look at a single T2* value, we chose to scan patients before and after USPIO administration so that signal voids resulting from USPIO accumulation could be distinguished from calcification and other artefacts. Relaximetry-based methods, such as T2* mapping, depend on resolution and can be subject to partial volume effects if the voxel size is much larger than the spatial extent of the magnetic influence of the SPIO particles. If image analysis depends on visual inspection for signal deficits alone, this can lead to false negatives [Toso *et al* 2008b]. Conversely, the very high susceptibility of clustered SPIO particles causes a concentration-dependent 'blooming' artefact where the magnetic effects of the SPIO particles extends well beyond the area occupied by the particles themselves. This effect is more pronounced at 3T and may lead to overestimation of the spatial extent of SPIO uptake. Compared to 1.5T MRI, 3T MRI offers improved signal-to-noise ratio, greater spatial resolution and higher sensitivity for detecting low concentrations of iron with additional benefits including improved signal-to-noise ratio and greater spatial resolution.

In the presence of high concentrations of iron, the signal intensity decays very rapidly such that at the shortest echo time the signal intensity is of a similar magnitude to the background noise. In this situation the data become categorical for

the presence or absence of iron as the T2* value cannot be calculated. We found that 3T MRI is ideally suited to USPIO imaging of AAA since tissue iron concentrations were within the quantitative range. We selected the echo times for the multi echo T2*W sequences such that even at the longest echo time the signal intensity was considerably greater than the background noise enabling quantitative analysis.

We showed that in the aortic wall and in other tissues with heterogeneous baseline T2* values, the use of per cent ΔT2* was more discriminatory than absolute ΔT2* for the detection of USPIO accumulation. On the basis of T2* repeatability measurements, we were able to define a threshold based on the 95th percentile of the per cent ΔT2*. This enabled us to attribute large changes in T2* to the accumulation of USPIO rather than to artefactual changes in T2*.

Registration is a critical part of the analysis process for focal SPIO uptake. With precise anatomical detail and a voxel size of 1.4 x 1.4 mm, we achieved excellent and robust registration, retaining single voxel spatial resolution. This allowed us to determine whether SPIO uptake was within the wall or the thrombus. However a multivoxel grid could be applied in situations where fine resolution is not essential or registration is sub-optimal. For AAA, we would advocate the use of thinner slices in tortuous areas to avoid partial volume effects and improve delineation of ROI and registration.

The use of a colour map rather than numeric data to present ΔT2* is advantageous since important spatial information is retained alongside the quantitative data for

ΔT2*. It also overcomes the difficulty of identifying areas of uptake of SPIO that cause signal voids on standard grey-scale T2*W images. Observer interpretation of colour maps and inter-observer agreement are facilitated by application of a threshold of significance for per cent ΔT2* as described above.

The method described here is not fully quantitative and this is the main limitation of this technique. This is because the magnetic effects of iron nanoparticles is dependent not only on their concentration but also on the homogeneity of their distribution. Further phantom and *in vivo* tissue work may clarify this further. However we believe that this semi-quantitative approach does enable the use of SPIO and USPIO for a range of clinical applications. The process could be streamlined by the development of semi-automatic methods for image registration and hotspot detection.

Towards improved detection of iron in tissues, a number of novel positive contrast imaging sequences has been proposed including susceptibility-weighted imaging, ultrashort echo time sequences, selective radiofrequency pulse methods (such as Inversion Recovery with ON-resonant water suppression, IRON) and off-resonance imaging [Seppenwoolde *et al* 2003; Mani *et al* 2006; Stuber *et al* 2007; Eibofner *et al* 2010]. A major advantage of the method described here, however, is the use of commercially available imaging sequences and image analysis techniques that are suitable for current clinical use.

For cell tracking studies, single cell imaging has been proposed as a way of improving quantification [Heyn *et al* 2006; Shapiro *et al* 2006]. Cells are typically labelled with MPIO and signal voids, each representing a single MPIO-labelled cell, are counted automatically. However, whilst this has been achieved in pre-clinical rodent models, a field strength of 7T is probably required to achieve sufficient resolution (200 x 200 μm in-plane) in humans to detect single cells reliably. Furthermore clinical scale cell tracking studies use up to 10^9 cells and this method is not immediately translatable for clinical use.

In conclusion, recognising both the great potential of SPIO contrast agents and the challenges of analysing the resulting data, we have defined a semi-quantitative image analysis algorithm for the detection of SPIO accumulation that has extensive application for imaging cellular inflammation and for *in vivo* cell tracking studies.

CHAPTER 4

MAGNETIC RESONANCE IMAGING

OF ABDOMINAL AORTIC ANEURYSMS USING

ULTRASMALL SUPERPARAMAGNETIC PARTICLES OF IRON OXIDE

4.1 SUMMARY

Abdominal aortic aneurysms are a major cause of death. Prediction of aneurysm expansion and rupture is challenging and currently relies on the simple measure of aneurysm diameter. Using magnetic resonance imaging, we aimed to assess whether areas of cellular inflammation correlated with the rate of AAA expansion. Stable patients (n=29; 27 male; aged 70 ± 5 years) with asymptomatic AAA (4.0-6.6 cm) were recruited from a surveillance programme and imaged using a 3T MRI scanner before and 24-36 hours after administration of USPIO**.** The change in T2* value on T2*W imaging was used to detect accumulation of USPIO within the AAA. Histological examination of aneurysm tissue confirmed co-localisation and uptake of USPIO in areas with macrophage infiltration. Patients with distinct mural uptake of USPIO had a 3-fold higher growth rate (n=11, 0.66 cm/yr; P=0.020) than those with no (n=6, 0.22 cm/yr) or non-specific USPIO uptake (n=8, 0.24 cm/yr) despite having similar aneurysm diameters (5.4 ± 0.6, 5.1 ± 0.5 and 5.0 ± 0.5 cm respectively; P >0.05). In one patient with an inflammatory aneurysm, there was a strong and widespread uptake of USPIO extending beyond the aortic wall. In conclusion, uptake of USPIO in AAA identifies cellular inflammation and appears to distinguish those patients with more rapidly progressive AAA expansion. This technique holds major promise as a new method of risk-stratifying patients with AAA that extends beyond the simple anatomical measure of aneurysm diameter.

4.2 INTRODUCTION

Abdominal aortic aneurysms have a prevalence of 5% in men over the age of 65 years and acute rupture is associated with a mortality rate of 65-85%. Abdominal aortic aneurysms are responsible for 2-3% of deaths in men aged ≥65 years and account for over 15,000 deaths annually in the United States [Ashton *et al* 2002]. Open surgical or endovascular intervention to prevent rupture is considered when the perceived risk of rupture outweighs the risk of procedural complications with a diameter threshold of 5.5 cm being considered the appropriate time to intervene [The UK Small Aneurysm Trial Participants 1998; Lederle *et al* 2002b; Hirsch *et al* 2006]. However, up to one-fifth of ruptured AAA are less than 5.5 cm in diameter [Darling *et al* 1977], and many patients present with AAA diameters considerably greater than 5.5 cm without prior symptoms or rupture [Powell *et al* 2008]. Apart from the simple measurement of aneurysm diameter, there are currently no methods of predicting which patients with AAA are at risk of further aneurysm growth and rupture. We therefore need better methods to guide preventative intervention in these patients.

Aortic aneurysms arise when the aortic wall develops excessive medial neovascularisation, infiltration of macrophages and lymphocytes, and irreversible proteolytic degradation and remodelling of the ECM. These pathological processes do not affect the aorta uniformly but are focal in nature with mural neovascularisation, inflammation and MMP activity occurring at sites of low tensile strength [Vallabhaneni *et al* 2004] and AAA rupture [Thompson *et al* 1996;

Choke *et al* 2006; Wilson *et al* 2006]. These areas of increased biological activity within the aortic aneurysm wall are therefore putative targets for novel imaging techniques.

Magnetic resonance imaging is emerging as a useful investigative tool for cardiovascular disease that can distinguish the different atherosclerotic plaque components, such as the lipid-rich core and areas of calcification [Cai *et al* 2005]. Standard gadolinium-based MRI identifies areas of thrombus formation and fibrosis in AAA [Kramer *et al* 2004]. Recently a novel class of MRI contrast agents containing SPIO has been developed that provides additional biological and functional information through the detection of cellular inflammation within tissues. USPIO, with particle sizes in the range 10-30 nm, escape immediate recognition by the reticuloendothelial system and persist for longer in the bloodstream allowing them to be used to assess the accumulation of macrophages within vascular and lymphatic tissues [Harisinghani *et al* 2003; Kooi *et al* 2003; Trivedi *et al* 2006 Heesakkers *et al* 2008; Tang *et al* 2009]. Current preparations are biodegradable and safe for clinical administration [Bourrinet *et al* 2006; Muller *et al* 2007; Bernd *et al* 2009].

USPIO accumulate in the aortae of hypercholesterolaemic rabbits [Ruehm *et al* 2001] and in murine models of AAA [Turner *et al* 2009]. In humans, USPIO accumulate in ruptured or rupture-prone carotid plaques rather than stable plaques [Kooi *et al* 2003; Trivedi *et al* 2006], and treatment with atorvastatin reduces both inflammation and USPIO uptake in carotid plaques [Tang *et al* 2009]. USPIO also

accumulate in AAA but to date no correlation has been made with clinical disease progression [Sadat *et al* 2011].

The aims of this study, therefore, were to determine whether USPIO uptake could be used to detect areas of cellular inflammation within the wall of the AAA, and to determine whether USPIO uptake patterns correlate with aneurysm growth rates.

4.3 METHODS

4.3.1 SUBJECTS

Patients with an AAA with a diameter of greater than 4.0 cm on ultrasound examination of the aorta were recruited from the outpatient aneurysm surveillance programme.

Demographic and clinical data, including past medical history and medications, were obtained through patient interview and source hospital records. Patients were being monitored in the aneurysm surveillance programme involving serial ultrasound-based measurements of the maximum anteroposterior diameter of the AAA, usually at 6-monthly intervals. Scans were undertaken by accredited clinical vascular scientists with interobserver CV of aortic diameter measurements of 3.5% in our laboratory [Wilson *et al* 2000]. Due to the staccato growth pattern of AAA and need for a contemporary measurement [Kurvers *et al* 2004], the annual growth rate was determined from two ultrasound scans performed 6 months apart, with one conducted before and the other after the MRI examination.

4.3.2 CONTRAST AGENT ADMINISTRATION

The weight-adjusted dose of USPIO (Sinerem, Guerbet, France) 2.6 mg/kg was diluted in 100 mL of 0.9% saline and administered through a filter as a slow intravenous infusion over 30 minutes.

4.3.3 MAGNETIC RESONANCE IMAGING

Participants underwent MRI in a whole body 3T Siemens Magnetom Verio scanner (Siemens, Erlangen, Germany) before and 24-36 hours [Trivedi *et al* 2004] after administration of the contrast agent. Routine clinical coronal and sagittal breath-held T2W multislice HASTE localiser sequences were used to identify the position and extent of the aneurysm following which a respiratory-gated, electrocardiogram-triggered T2W turbo spin echo sequence was used to acquire detailed anatomical data (TR/TE 2R-R intervals/72 ms; flip angle 180°; matrix 192 × 256; field of view 400 × 400 mm; slice width 5 mm). A multi echo, gradient echo T2*W sequence (TE 4.9, 7.7, 10.5, 13.3 ms; TR 133 ms; flip angle 15°; matrix 192 × 256; field of view 400 × 400 mm; slice width 5 mm) was used to acquire axial images of the entire aneurysm with slice positions corresponding to those of the T2W images.

The echo times for the T2*W sequences were selected such that fat and water were in phase for each echo to minimise phase shift artefact and errors in T2* measurements. The field of view used for both sequences was typically 400 × 400 mm, but was adjusted for larger subjects to minimise phase wrap artefacts. T2W images give excellent discrimination of the boundaries between the flow

lumen, thrombus, wall and surrounding tissues. T2*W sequences, have less distinct soft tissue contrast, but are exquisitely sensitive to the effects of USPIO accumulation. At the post-contrast scan, slice positions were selected to match those of the pre-contrast scan as closely as possible by reference to the vertebral bodies.

In a subset of nineteen patients, T1W images were acquired before and 5 minutes after the bolus administration of 0.2 mL/kg of gadolinium (Dotarem, Guerbet Pharmaceuticals, France) using a turbo spin echo acquisition (TR/TE 1 R-R interval/28 ms; flip angle 180°; matrix 192 × 256; field of view 400 × 400 mm; slice width 5 mm). Gadolinium-enhanced sequences were performed after the baseline T2W and T2*W sequences were acquired, 2 hours before USPIO administration and approximately 24 hours before the post-USPIO MRI scan. Since gadolinium has a plasma half-life in the region of 2 hours and, unlike USPIO, is not readily taken up into the intracellular compartment, USPIO-enhancement is unlikely to have been affected by pre-administration of gadolinium.

4.3.4 IMAGE ANALYSIS

In order that the soft tissue discrimination of the T2W images could be used to complement the iron sensitivity of the T2*W images, and to allow direct comparison of the pre- and post-contrast data, all the images were registered to the pre-contrast T2W image using a semi-automatic rigid 3-dimensional voxel registration protocol (Analyze, Mayo Clinic). Bowel and abdominal wall motion were found to compromise registration of the aorta itself and this was minimised by excluding these structures from the volume for registration as far as possible. A ROI encompassing

the aortic wall and thrombus but excluding the flow lumen was drawn on each slice of the pre-contrast T2W image. The four echoes in the multi echo T2*W sequence were combined to generate a T2* map, in which the data represented the T2* value for each voxel. The T2* value is the decay constant for the exponential decay of signal intensity with time. In the presence of USPIO, the signal decays more rapidly due to local field inhomogeneities and the T2* value is reduced. A 3 x 3 voxel Gaussian filter was applied to the individual echoes to reduce noise, and experimentally-determined thresholds for r^2 (r^2 >0.4) and SSE <0.2 were used to exclude data that did not have an acceptable straight line fit when ln signal intensity (SI) was plotted against echo time.

The previously delineated ROI was applied to the T2* maps that had been registered to the pre-contrast T2W scan. The per cent change in T2* value (%ΔT2*) following the administration of USPIO was calculated on a voxel-by-voxel basis and displayed on a colour scale (%ΔT2*= (T2* value scan 1 - T2* value scan 2)/(T2* value scan 1) x 100). From the 95th percentile of the %ΔT2* value observed in a group of patients not receiving USPIO, we have established a threshold of significance for %ΔT2* of 59% above which an observed change in T2* value can be attributed to USPIO uptake. All voxels with values for %ΔT2* below this threshold appear blue on the colour map whilst voxels above this threshold appear on a yellow-red colour scale. This facilitates data interpretation and minimises observer bias.

To assess the gadolinium-enhancement on T1W images, the pre- and post-contrast images were registered to the pre-contrast T2W image. The previously delineated

ROI was applied to the T1 images. The per cent change in signal intensity was calculated (%Δ SI) on a voxel-by-voxel basis and displayed on a colour scale (%Δ SI= (SI scan 2 - SI scan 1)/(SI scan 1) x 100). By convention, an increase in signal intensity of more than 50% of the baseline value was taken to be significant.

4.3.5 CLASSIFICATION OF ANEURYSMS

Cellular inflammation is an important pathological process in the development of AAA with the associated proteolytic degradation of the aortic wall representing the key step leading to AAA expansion and rupture. We were interested to see whether aneurysm expansion rate is increased in aneurysms with USPIO uptake in (i) the aortic wall or (ii) the associated thrombus. Therefore, two independent observers, blinded to the patient demographics, and aneurysm diameter and growth rate, reviewed the colour map images and classified them into three clear pre-defined groups according to their appearance:

Group 1 – no mural or thrombus USPIO uptake except isolated periluminal T2* enhancement occurring immediately adjacent to, and in continuity with, the lumen.
Group 2 – diffuse USPIO uptake that was distinct from the periluminal thrombus and the aortic wall.
Group 3 – focal areas (with at least 10 contiguous voxels) of USPIO uptake within the aortic wall of the aneurysm distinct from periluminal area and thrombus.

Differences in classification were resolved by consensus.

4.3.6 HISTOLOGY

For patients undergoing open surgical repair within 48 hours of USPIO administration, samples of aortic wall were obtained from the arteriotomy site on the anterior aspect of the aneurysm sac. Samples were fixed in formalin, embedded in paraffin, sectioned and stained to look at the architecture (haematoxylin and eosin, and elastin van Gieson) and USPIO accumulation (Prussian blue). The distribution of macrophages was assessed by immunohistochemical staining for macrophages (mouse, anti-human CD68 monoclonal antibody; DAKO).

4.3.7 STATISTICAL ANALYSIS

The data were normally distributed. Continuous data were compared with one-way ANOVA with Tukey's post-test comparison (Minitab) and categorical data were analysed using Chi-squared test with cross-tabulation (SPSS). Statistical significance was taken as two-sided $P < 0.05$.

4.4 RESULTS

4.4.1 PATIENTS

Twenty-nine patients (27 male) were recruited into the trial with a mean age of 70 ± 5 years and mean AAA diameter of 5.2 cm (range 4.0-6.6 cm). All aneurysms were fusiform and confined to the abdominal aorta. One patient had an inflammatory aneurysm with ureteric obstruction and a raised erythrocyte sedimentation rate of 100 mm/hour (reference range 1-10 mm/hour). The remaining patients were asymptomatic. As anticipated, patients had a range of cardiovascular risk factors and

co-morbidities (Table 4.1). During the study period, four patients underwent open surgical repair of their AAA (two in group 1 and two in group 3), two patients were treated by EVAR (one in group 2 and one in group 3) and one patient in group 3 died of a ruptured aneurysm having been assessed and considered unfit for operative intervention. It was not possible to calculate a growth rate for four patients (one in group 1, one in group 2 and two in group 3) who had only a single diameter measurement, either because they proceeded straight to surgery or had only recently presented to the surveillance programme.

4.4.2 USPIO ADMINISTRATION

The administration of USPIO was well tolerated with no significant adverse events. There was a relatively even distribution of patients within the three categories of USPIO uptake (Table 4.1). Patients in the three groups were similar in terms of age, sex, use of medications, initial aneurysm diameter and all co-morbidities except hypertension (P=0.024). In patients undergoing open surgical AAA repair, histology confirmed the accumulation of USPIO that co-located with immunohistochemical staining for CD68-positive macrophages (Figure 4.1). Iron deposits were not seen in control tissue from a patient with an aneurysmal aorta who had not received USPIO (Figure 1).

4.4.3 MAGNETIC RESONANCE IMAGING WITH USPIO

Patients had between 10 and 20 slices to cover the entire aneurysm with a total of 351 slices for analysis. Registration within the main body of the aneurysm was excellent for all scans although 9.7 ± 1.4% of the data were discarded due to poor

straight-line fit when ln SI was plotted against echo time. Classification of AAA according to USPIO uptake (Figure 4.2) was consistent and reproducible with

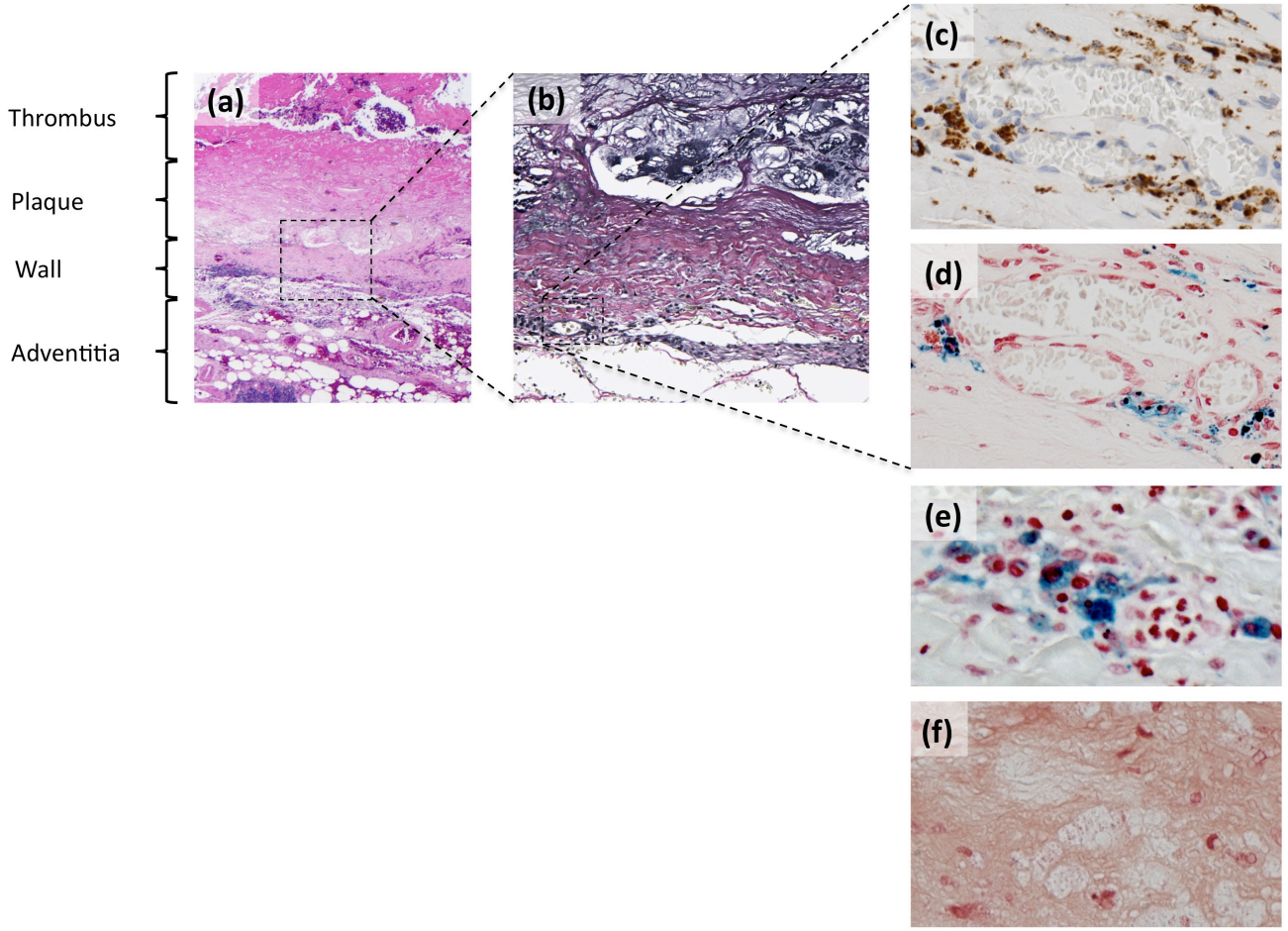

Figure 4.1 Representative histological sections of the aortic wall. (a) Haematoxylin and eosin (x20) of the full thickness of the aortic wall including atherosclerotic plaque, adherent thrombus and peri-adventitial fatty tissue. **(b)** Elastin van Gieson stain (x100) of the aortic wall showing complete destruction of the normal wall structure including fibrosis (collagen; pink) of the media and adventitia and virtual absence of intact medial elastic fibres (black). **(c)** Prussian blue staining for iron demonstrating co-localisation of CD68-postive macrophages (x400; brown) with **(d)** USPIO particles (x400; blue). **(e)** High power (x1000) Prussian blue staining showing intra-cytoplasmic accumulation of USPIO within macrophages. **(f)** Prussian blue stain of aneurysmal aorta in a patient not receiving USPIO showing no evidence of iron accumulation.
CD - Cluster of differentiation; USPIO - Ultrasmall superparamagnetic particles of iron oxide

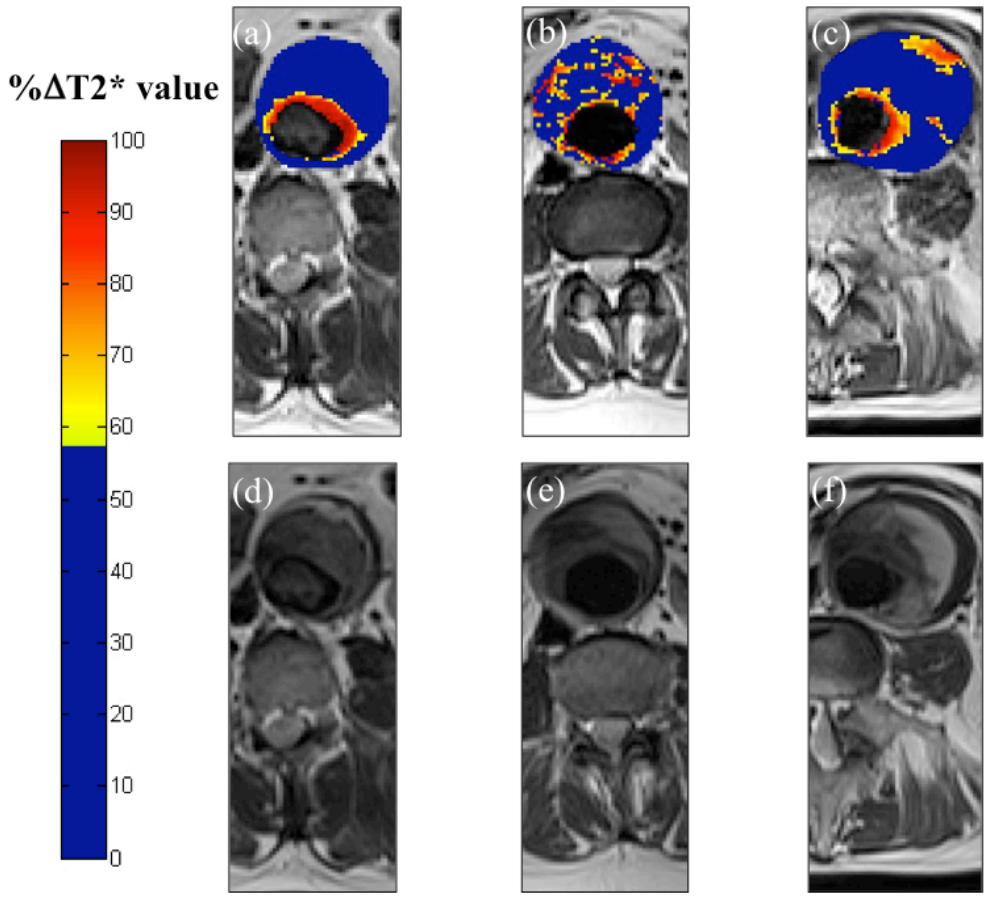

Figure 4.2 Colour maps **(a-c)** showing representative abdominal aortic aneurysm (AAA) slices from patients in each of the three groups alongside the corresponding T2W anatomical images **(d-f)**. The colour scale represents the magnitude of the change in T2* value with blue indicating minimal change and red indicating a large change in T2* value. We have previously defined the threshold above which changes in T2* value can be attributed to USPIO accumulation. Only changes in T2* value above the threshold are presented on the graduated (yellow-red) colour scale, whilst data below the threshold appear blue. A distinctive pattern is seen for each patient group: **(a)** group 1 shows a large change in T2* value only in the periluminal area; **(b)** group 2, diffuse patchy changes in T2* throughout the intraluminal thrombus, but no distinct focal area of USPIO uptake affecting the aortic wall; and **(c)** group 3, discrete focal area of USPIO uptake involving the wall of the AAA that is distinct from the periluminal region - this patient subsequently died suddenly from presumed ruptured AAA.
T2W - T2 weighted; USPIO - Ultrasmall superparamagnetic particles of iron oxide.

excellent inter-observer agreement and a kappa statistic of 0.89. There appeared to be no differences in USPIO uptake whether or not patients had received pre-administration of gadolinium.

The effect of USPIO accumulation is to accelerate dephasing of transverse magnetisation resulting in rapid loss of signal with increasing echo time and hence a reduction in the decay constant, the T2* value. The magnitude of the change in T2* value was encoded for each voxel with a large reduction in T2* value reflecting a greater accumulation of USPIO. We have previously defined a threshold (59%) above which the change in T2* value can be attributed to USPIO accumulation rather than variability of the measurement. In all patients, there was non-specific USPIO uptake in the periluminal region consistent with transition of the particles from the blood pool (Figure 4.2). Interestingly the same region of the thrombus enhanced rapidly on T1W MRI with gadolinium (Figure 4.3). In group 3, in addition to the presence of focal areas of USPIO uptake (at least 10 contiguous voxels), there was a higher proportion of USPIO positive voxels in the aortic wall compared to the other two groups ($P < 0.0001$) supporting the correct classification of patients into the three groups (Figure 4.4a).

Patients with distinct focal areas of increased USPIO uptake in the wall of the aneurysm (group 3) had aneurysm growth rates that were 3-fold higher than patients without (group 1) or with non-specific (group 2) uptake of USPIO ($P=0.020$; Figure 4.4b). Interestingly, there was no difference in baseline aneurysm diameter

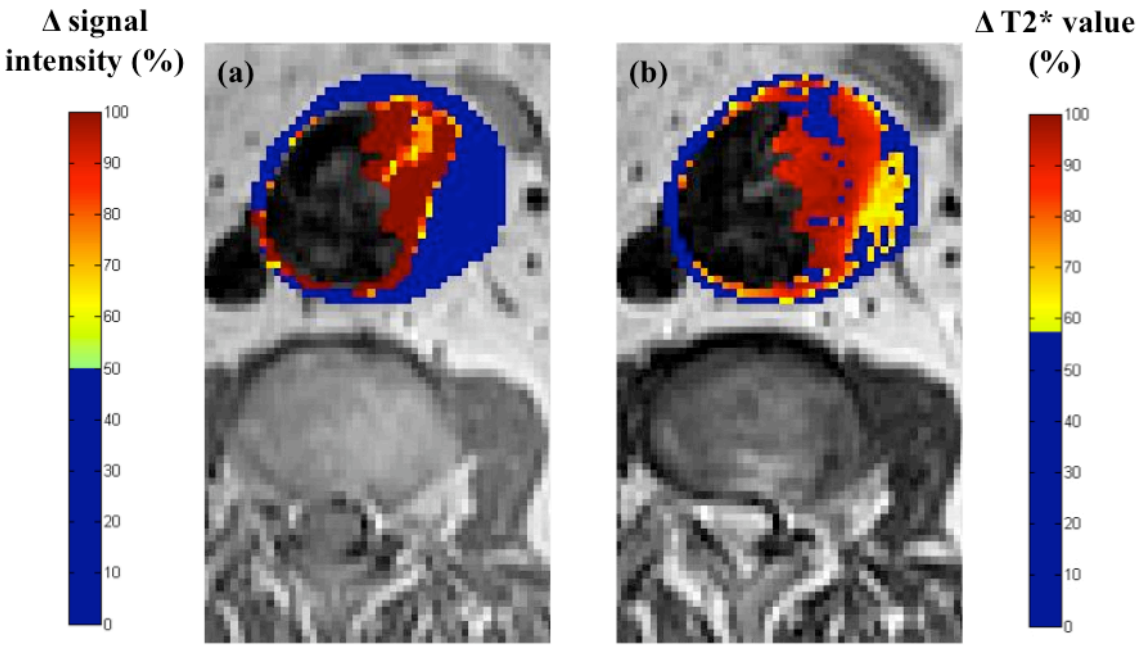

Figure 4.3 The blood pool contrast agent gadolinium **(a)** enhances only the periluminal halo region of the thrombus and the fibrous cap. USPIO-enhancement **(b)** is seen not only in the periluminal halo but also in the deep layer of the thrombus and in the aortic wall.
USPIO - Ultrasmall superparamagnetic particles of iron oxide.

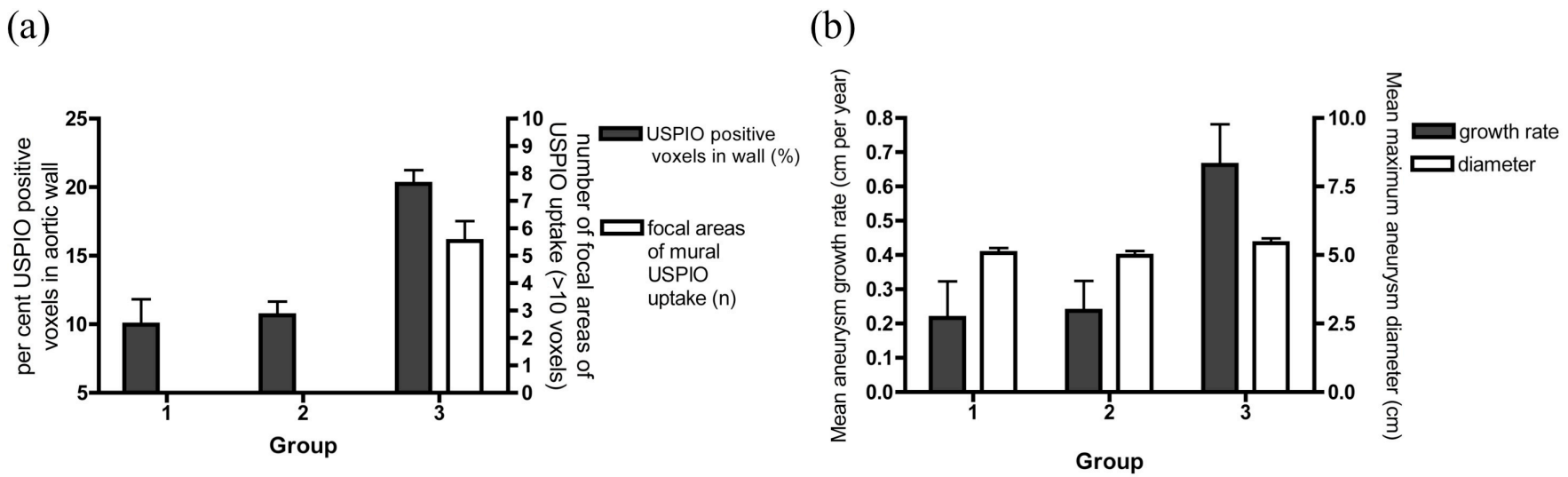

Figure 4.4 **(a)** Per cent USPIO positive voxels in the aortic wall (solid bars) and focal areas of increased USPIO uptake (open bars). USPIO positive voxels were higher in group 3 compared to the other two groups (P <0.001). **(b)** Relationship of diameter and growth rate with patient group. Initial aneurysm diameters (open bars) are similar for the three groups, but the aneurysm growth rates (solid bars) are higher for patients in group 3 (0.66 cm/yr) compared to those in groups 1 (0.22 cm/yr) and 2 (0.24 cm/yr; P=0.020).
USPIO - Ultrasmall superparamagnetic particles of iron oxide.

across the three groups (Figure 4b). The percentage of USPIO positive voxels in the aortic wall correlated with the AAA growth rate (r=0.46; P=0.028).

One patient in group 3 had an inflammatory aneurysm; a specific subtype of AAA characterised by systemic inflammation, a thickened, fibrosed aortic wall, and fibrosis and inflammation extending beyond the aorta into surrounding tissues. This produced a unique change in T2* pattern with intense USPIO uptake extending beyond the wall of the AAA (Figure 4.5).

4.5 DISCUSSION

We have shown for the first time that uptake of USPIO in AAA identifies cellular inflammation and appears to distinguish those patients with more rapidly progressive AAA expansion. This technique holds major promise as a new method of risk-stratifying patients with AAA that extends beyond the simple anatomical measure of aneurysm diameter.

We have used a smart contrast agent that consists of 20 nm dextran-coated iron oxide nanoparticles. Following intravenous administration, these USPIO circulate within the blood pool with a long half-life and are engulfed by macrophages. They accumulate at sites of cellular inflammation at sufficient concentrations to cause signal changes on MRI. As a result of their superparamagnetic properties, they induce local field inhomogeneities leading to rapid dephasing of the transverse magnetisation of spinning protons and thus loss of coherent signal. Whilst these

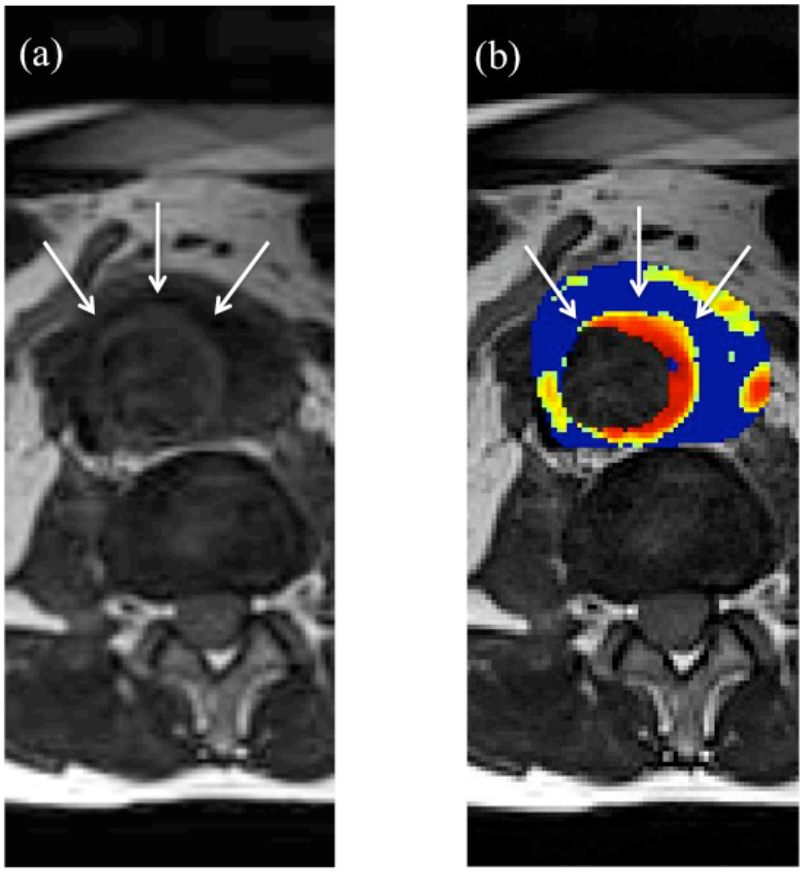

Figure 4.5 **(a)** Distinctive appearance of an inflammatory abdominal aortic aneurysm (AAA) on T2W imaging. Arrows indicate the aortic wall. **(b)** Regions with a large per cent change in T2* value are present outwith the aortic wall showing inflammation extending into surrounding tissues as is typical of an inflammatory AAA (see colour scale; Figure 2). This patient had ureteric obstruction and an erythrocyte sedimentation rate of >100 mm/hr (reference range 1-10 mm/hr).
T2W - T2 weighted.

agents exhibit T1 relaxivity, the predominant extravascular effect of USPIO at 3T is to cause a dropout of signal on T2W and especially T2*W images [Corot 2007]. Due to the mixed T1 and T2/T2* effects of USPIO, we chose to measure their effect on the rate of exponential signal decay by calculating the decay constant, T2* value, from the signal intensities at four echo times rather than relying on the signal intensity at a single echo time. This proved to be a highly sensitive technique and variations in the change of T2* value identified areas of cellular inflammation that were confirmed on subsequent histological examination of aneurysm tissue obtained at the time of open surgery.

Within the study population, we observed distinct patterns of spatial variation in the change of T2* value and were able to divide patients into three groups on this basis. Patients in group 1 had a high change in T2* value only in the periluminal aspect of the aneurysm: this 'halo effect' being a constant finding in all study patients. Intraluminal thrombus is a consistent feature of AAA and usually has a laminar appearance with the mural component having been deposited first and subsequent growth of the thrombus occurring by further deposition of fibrin, platelets and red blood cells on the inner luminal aspect [Touat *et al* 2006]. The universal finding of a large change in T2* value in the periluminal region of the aneurysm is therefore likely to reflect trapping of USPIO in fresh potentially gelatinous thrombus that is typically friable and highly cellular because of its close proximity to flowing blood [Adolph *et al 1*997]. It was interesting to observe that this region also enhanced rapidly with gadolinium, consistent with a less selective and more generalised uptake of contrast agents in this region. A previous study using the larger SPIO particles

(80-150 nm) demonstrated their accumulation in the luminal layer of aortic thrombus, resulting in an MRI signal that correlated with histological evidence of leucocyte infiltration (CD68 and CD66b) and levels of MMP [Nchimi *et al* 2010]. As acknowledged by the authors, these large SPIO particles are not well suited to vascular tissue imaging due to their short plasma half-life that limits their sensitivity for detecting vessel wall inflammation.

The second group of patients had a heterogeneous pattern of change in T2* signal within the thrombus but no uptake in the aortic wall. The role of the thrombus in aneurysm expansion and rupture is uncertain [Adolph *et al* 1997; Vorp *et al* 2001; Kazi *et al* 2005]. Some macrophages are present deep within the thrombus, but alternatively this signal pattern may reflect USPIO within the canaliculi that traverse the thrombus, conducting fluid, small molecules and, to a certain extent, cells from the lumen towards the aortic wall [Adolph *et al* 1997]. This pattern of USPIO uptake and inflammation within the thrombus is of uncertain significance but interestingly did not appear to be associated with accelerated aneurysm growth.

In the third group of patients, we found one or more distinct focal areas of inflammation involving the wall itself and spatially distinct from the periluminal halo. This finding was associated with an increased growth rate compared to patients without mural USPIO uptake. This high growth rate (0.66 cm/yr) is clinically significant since the average aneurysm growth in screened populations is 0.26 cm/yr and growth rates >0.2 cm/yr are associated with increased AAA-related events [Lederle *et al* 2002a; Brady *et al 20*04; Thompson *et al* 2010]. We are unable to

exclude the possibility that differences in the incidence of hypertension amongst patients in the three groups influenced AAA growth rate, however this seems unlikely since the groups with the highest (group 2) and lowest (group 1) incidence of hypertension had similarly low growth rates. In patients with ruptured AAA, histology of the aneurysm wall has shown areas of increased biological activity and these correlate with a reduction in aortic wall tensile strength [Thompson *et al* 1996; Vallabhaneni *et al* 2004; Choke *et al* 2006; Wilson *et al* 2006]. It would be interesting to determine whether, in patients with AAA and abdominal pain of uncertain aetiology, USPIO imaging could distinguish between those with impending rupture and those with non-AAA related abdominal pain. Finally, whether this pattern of USPIO uptake in AAA may prove to be a marker for future AAA-related events is unclear and requires a large prospective study.

Existing techniques for surveillance of AAA and estimation of risk of rupture rely solely upon diameter measurements, but clinical data from aneurysm screening and surveillance programmes suggest that there is considerable scope to improve on this. Of those aneurysms detected by screening that are less than 5.5 cm in diameter, one in 14 will rupture over the following 3 years [Thompson *et al* 2010] and together account for up to one-fifth of all ruptured AAA [Darling *et al* 1977]. However, simply reducing the diameter threshold for intervention would not improve mortality [The UK Small Aneurysm Trial Participants 1998; Lederle *et al* 2002b]. Furthermore, small aneurysms exhibit a bimodal distribution for growth with half remaining small and only half continuing to grow [Thompson *et al* 2010]. Having been shown to reduce AAA-related mortality by 53%, aneurysm screening is being

introduced in many countries across the world [Ashton *et al* 2002; Screening for abdominal aortic aneurysm 2005]. However, screening considerably increases the number of patients under long-term surveillance, and only around 30% of these patients will require future intervention [Ashton *et al* 2002; Thompson *et al* 2010]. Taken together, these observations support a need for a more sophisticated and individualised method of predicting clinical events in patients with AAA so that screening, surveillance and intervention can be targeted at high-risk patients, reducing the overall economic cost and decreasing morbidity and mortality. We believe USPIO imaging represents a logical and important new approach that has the potential to address these major unmet clinical needs.

The conclusions drawn from these results are limited by the small number of patients and the limited duration of clinical follow-up. In succession to these interesting pilot results, a large prospective clinical trial with a longer duration of follow-up would be required to confirm the findings of the present study and assess the role of MRI and USPIO in the prediction of AAA-related clinical events. This would also enable a more sophisticated three-dimensional CT- or MRI-based assessment of growth and its relationship to areas of USPIO uptake. Serial examinations would provide further information regarding the optimum time for imaging, the time course of particle clearance and the dynamics of inflammatory hotspots with time. Further modifications of the image acquisition protocol such as reduction in slice thickness and omission of the interslice gap would improve the spatial resolution of the colour maps.

In conclusion we have demonstrated that assessment of USPIO uptake with MRI can be used to detect focal hotspots of inflammation in asymptomatic AAA, and that mural USPIO uptake is associated with more rapid expansion of AAA. If successful this technique has a number of potential highly relevant clinical applications that include informing selection of patients for intervention to prevent rupture, rationalisation of AAA screening resources to target high-risk patients, and application as a biomarker to investigate the utility of novel therapeutic interventions for AAA.

CHAPTER 5

DEVELOPMENT OF A GOOD MANUFACTURING PRACTICE COMPLIANT PROTOCOL FOR LABELLING HUMAN MONONUCLEAR CELLS FOR MAGNETIC RESONANCE CELL TRACKING IN MAN

5.1 SUMMARY

The ability to track cells non-invasively to a target site using magnetic resonance imaging would have a wide range of clinical applications including for inflammatory cell tracking to investigate disease biology and as an adjunct to cell-based therapies to determine the distribution of cells following their administration. A laboratory method has been described previously allowing cells to be labelled *ex vivo* with a MRI contrast agent containing SPIO using protamine sulphate to enhance cellular uptake. This method has here been translated successfully into a GMP compliant protocol for clinical scale SPIO-labelling of human mononuclear cells. SPIO-labelling was efficient and did not affect cell viability, cytokine release or migratory capacity *in vitro*. Furthermore, SPIO-labelled cells were visualised *in vitro* using a 3T clinical MRI scanner. This is therefore a promising investigative tool for clinical cell tracking studies in humans.

5.2 INTRODUCTION

Stem cell and other cell-based therapies have emerged over recent years as potential novel treatment options for a wide range of diseases [Perin *et al* 2004; Wollert *et al* 2004; Fuchs *et al* 2006; Gyongyosi *et al* 2008; Gyongyosi *et al* 2009; Yousef *et al* 2009]. Ensuring the delivery of a sufficient number of cells to the target site is critical to the development and assessment of these therapies. A number of methods have been proposed for tracking cells *in vivo* but their translation into the clinical setting has been hampered for a number of reasons including limitations of the

imaging modality in humans and failure of reagents to comply with GMP standards: a pre-requisite for clinical use.

By virtue of its high spatial resolution, excellent soft tissue contrast and avoidance of ionising radiation, MRI is ideally suited to human cell tracking studies. Magnetic resonance imaging contrast agents consisting of dextran-coated SPIO are available for use in humans and are in routine clinical use for liver imaging. SPIO possess intense superparamagnetism causing a profound reduction in signal intensity on T2- and particularly T2*W imaging. SPIO are readily taken up by macrophages, are not toxic to cells and are biodegradable *in vivo* [Arbab *et al* 2005; Ju *et al* 2006; Neri *et al* 2008; Farrell *et al* 2009; Hu *et al* 2009; Wang *et al* 2009].

An effective method has been described for incorporating SPIO into phagocytic cells using protamine sulphate as a polycationic transfection agent to enhance its uptake through electrostatic interactions [Arbab *et al* 2004]. Since both SPIO (Endorem) and protamine sulphate are approved for human use, this method is potentially suitable for labelling cells for clinical studies.

The aims of this study were (i) to translate this scientific method into a GMP compliant protocol for clinical scale labelling of human PBMC and (ii) to confirm normal cell viability and function of labelled cells.

5.3 METHODS

5.3.1 OPTIMISATION OF SPIO CELL LABELLING METHODOLOGY AND TRANSLATION INTO A GMP COMPLIANT CLINICAL SCALE PROTOCOL

Using the method described by Arbab *et al* [Arbab *et al* 2004] as a starting point, the Edinburgh protocol was established for clinical scale labelling of human mononuclear cells with SPIO under GMP compliant conditions. In order to guide the method-development process, the *in vitro* labelling efficiency, viability and function of labelled cells were determined following each iteration of the protocol.

Initially, processing of high cell numbers had caused problems with cell clumping and loss of a substantial proportion of cells was encountered. In addition there was a requirement to adapt the Arbab method for use in the GMP setting and to condense the protocol such that cells could be procured and processed for reinfusion on the same working day. Particular considerations for the translation of a laboratory method into a GMP protocol include suitability of reagents and vessels for human use, access to an appropriate facility that meets GMP requirements, and suitability of the protocol to be performed in a reproducible way by a number of operators in different facilities.

5.3.2 ENDOREM AND PROTAMINE CONCENTRATIONS

In pursuit of a protocol that would minimise cell clumping, maximise cell yield and maintain SPIO uptake, a number of permutations of the Endorem concentration (10-1000 μg/mL), protamine concentration (0-40 μg/mL) and their ratio were

explored. We also investigated the timing of addition of Endorem and protamine to the cell suspension.

5.3.3 LABELLING MEDIUM AND LABELLING CONTAINER

Monocytes exhibit plastic adherence and a proportion of cells were lost during incubation as they became stuck to the receptacle in which labelling took place. We therefore evaluated a range of vessels in which to contain the cell suspension for the labelling process, and compared a static incubation period with continuous agitation. With a view to enabling cells to be infused in the medium in which they were labelled, comparison was made of labelling in 0.9% saline rather than cell culture medium, and the influence of divalent ions (Ca^{2+} and Mg^{2+}) on cell adhesion and SPIO uptake was evaluated.

5.3.4 LABELLING DURATION

To accommodate the proposed MRI scanning schedule for the clinical studies, it was desirable to make cells available for reinfusion during the afternoon. We therefore looked to modify the Arbab protocol in the following ways: (i) reduction of labelling time to 2 hours; (ii) cells labelled and then stored overnight for reinfusion the following day; (iii) cells stored overnight and labelled the following day; and (iv) cells labelled overnight (~16 hours).

5.3.5 FINAL EDINBURGH PROTOCOL FOR LABELLING MONONUCLEAR CELLS WITH SPIO

Venous blood was collected into citrate yielding 1-5 × 10^8 PMBC. A leucapheresis machine (COBE Spectra, Gambro BCT, USA) was used to collect 1-5 × 10^9 PBMC. Peripheral blood mononclear cells were isolated by density-gradient separation and suspended in 0.9% saline (4 × 10^6 cells/mL). Cells were labelled with SPIO according to the Edinburgh protocol. In brief, Endorem (100 μg/mL; Guerbet, France) and protamine sulphate (4 μg/mL; Prosulf) were added to the cell suspension and incubated at room temperature for 2 hours with continuous agitation.

5.3.6 EFFECT OF SPIO-LABELLING ON CELL VIABILITY AND FUNCTION

SPIO uptake

Prussian blue staining of methanol-fixed cytospin preparations confirmed cellular SPIO uptake. Granularity (side scatter) of CD14+ cells was examined by flow cytometry as a surrogate marker of nanoparticle internalisation. Monocytes were isolated from the PBMC population by immunomagnetic separation and the cellular iron content of the resulting purified monocytes was determined using the Ferrozine assay (Sigma, UK).

Cell viability

SPIO-labelled and unlabelled cells were harvested at 1, 24 and 72 hours, exposed to FITC-annexin V and PI, and analysed by flow cytometry. The percentages of cells positive for annexin V-binding, PI staining, or both were combined to give the

percentage cytotoxicity. Viability was also assessed at 24, 48 and 72 hours using a LDH assay (Roche Diagnostics Ltd, UK).

Cytokine release

The concentration of the pro-inflammatory cytokines released from cells 24, 48 and 72 hours post labelling was measured using a cytometric bead array kit (Becton Dickinson, Biosciences**,** USA).

Migratory capacity

Monocytes were isolated from the PBMC population by immunomagnetic separation. Labelled and unlabelled purified monocytes (2.5×10^5 cells/well) were allowed to migrate for 2 hours through a microporous (5 μm) membrane (Corning Costar, USA) towards 0 or 50 ng/mL of recombinant human MCP-1 (R&D Systems, UK). Transmigration was quantified by counting the cells adherent to the undersurface of the membrane.

5.3.7 MAGNETIC RESONANCE IMAGING

Phantoms mimicking the magnetic properties of vascular tissue were constructed using 50 mL of 0.15% agarose with 0.11 nM gadolinium EDTA. Labelled cells were added to phantoms in a range of concentrations. Phantoms were placed in a water bath and scanned using a 3T Siemens Magnetom Verio MRI scanner (Siemens, Erlangen, Germany) with a 12-channel receive head matrix coil. A T2W spin echo sequence was applied to a 5 mm coronal slice with a TR of 4000 ms (to avoid T1 saturation effects) and multiple echo time values ranging from 7.7-250 ms. A T2*W

multi gradient echo sequence with TR of 4000 ms and echo times of 4.9, 7.7, 10.5 and 13.3 ms was applied to the same slice. Values for R2 and R2* were calculated from regression of log signal intensity *versus* echo time (Minitab version 16, USA).

5.3.8 STATISTICAL ANALYSIS

Where appropriate data were analysed by unpaired two-tailed Student *t*-test. Two-sided $P < 0.05$ was regarded as statistically significant.

5.4 RESULTS

5.4.1 DEVELOPMENT OF A GMP COMPLIANT PROTOCOL FOR LABELLING HUMAN MONONUCLEAR CELLS WITH SPIO

By adapting and optimising the method described by Arbab *et al* [Arbab *et al* 2004], the Edinburgh protocol was established for clinical scale labelling of human mononuclear cells with SPIO under GMP compliant conditions.

Processing of the high number of cells required for clinical cell tracking studies according to the Arbab protocol caused problems with cell clumping (Figure 5.1a and b) which appeared to be multifactorial and resulted in the loss of a substantial proportion of cells.

Similar to the Arbab protocol, concentrations of 100 μg/mL of Endorem and 4 μg/mL protamine sulphate were found to be optimal. Adding Endorem and protamine directly into the cell suspension avoided the formation of large Endorem

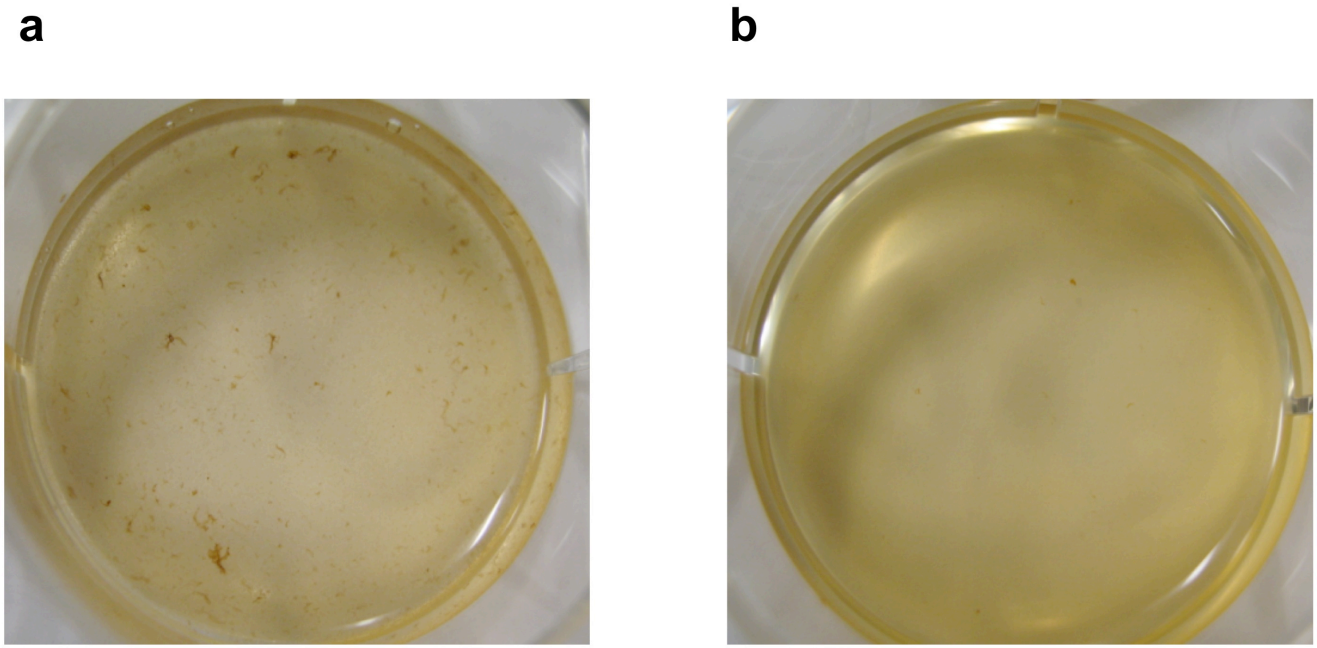

Figure 5.1 Cell clumping. Labelling a high number of cells by the original Arbab method **[Arbab *et al* 2004]** resulted in significant clumping **(a)**. However when cells were labelled according to the Edinburgh protocol, which has been optimised for processing cells on a clinical scale, cells remained in a single-cell suspension **(b)**.

protamine complexes that occurs when the two are mixed in the absence of cells, and which promote clumping when cells are then added. Continuous agitation using a roller-mixer avoided gravitational sedimentation during incubation, exposing all cells to SPIO uniformly and reducing clumping. To minimise plastic adherence and facilitate the use of a roller-mixer, cells were labelled in a 250 mL polypropylene conical tube (Falcon, Becton Dickinson, Biosciences, USA). It was confirmed that cells could be labelled at room temperature without affecting SPIO uptake and there was therefore no requirement for an incubator within the GMP facility.

When cells were labelled in suspension, SPIO became cell-associated almost immediately, initially adhering to the outer surface of the cell and subsequently being incorporated into the cell during the remainder of the incubation period. In contrast to the situation when cells are labelled whilst adherent or when allowed to settle out of suspension, almost no free SPIO remained at the end of the incubation period if continuous agitation was employed. There was therefore little to be gained by washing cells at the end of the labelling period since virtually no free iron remained to be removed, and this had the added benefit of avoiding centrifugation which markedly promotes clumping of SPIO-labelled cells. To allow cells to be infused in the medium in which they were labelled, cells were incubated in 0.9% saline rather than cell culture medium and this did not affect SPIO uptake. The omission of divalent ions (Ca^{2+} and Mg^{2+}) did not affect iron uptake and may have contributed to the reduction in clumping by inhibiting integrin-mediated cell adhesion.

Storage of cells overnight, either before or after labelling, resulted in excessive clumping. Additionally, overnight exposure to SPIO resulted in increased toxicity. However, the labelling duration could be reduced to 2 hours without affecting SPIO uptake and preserving cells in pristine condition. By procuring cells early in the morning, it was therefore possible to make labelled cells available for reinfusion in the middle of the afternoon allowing studies to be undertaken within a clinically acceptable timeframe.

Throughout the optimisation process, attention was directed at the reagents and vessels tested to ensure that they met GMP requirements. In addition, the final protocol was thoroughly tested in the GMP facility confirming that is was highly compatible with GMP regulations and suitable for use by a variety of operators according to a comprehensive Standard Operating Procedure **(Appendix 1**).

5.4.2 *IN VITRO* EVALUATION OF THE EFFECT OF SPIO-LABELLING ON CELL VIABILITY AND FUNCTION

It is important that the behaviour of SPIO-labelled mononuclear cells remains unchanged in terms of cell viability and function so that the results of *in vivo* cell tracking studies reflect accurately the biological processes being observed. The results presented below represent the findings in cells labelled according to the optimised Edinburgh protocol.

Confirmation of SPIO uptake

Prussian blue staining of labelled cells demonstrated intracellular accumulation of iron nanoparticles (Figure 5.2a). Although the entire PBMC population, including both lymphocytes and monocytes, was exposed to SPIO, SPIO uptake was predominantly confined to the phagocytic monocytes. The mean iron content of labelled monocytes was 18 ± 3 pg/cell compared to 1 ± 0.3 g/cell for unlabelled cells. Flow cytometric analysis showed that CD14-labelled monocytes exhibited greater side scatter following SPIO-labelling indicating increased granularity and SPIO uptake (Figure 5.2b and c).

Assessment of cytotoxicity

SPIO-labelling had no effect on cellular release of inflammatory cytokines (Figure 5.3). Cell viability was assessed by flow cytometric detection of PI staining and binding of FITC-conjugated annexin V. Cells that were negative for both annexin V-binding and PI staining were classified as viable. The percentages of cells positive for annexin V-binding, PI staining, or both were combined to give an overall percentage of cytotoxicity. Viability of labelled and unlabelled cells was equivalent up to 72 hours post labelling (Figure 5.4a). Due to the possibility that the electrostatic effects of protamine sulphate may have affected membrane permeability, we also looked at cellular release of LDH and confirmed that SPIO-labelling did not affect viability of cells cultured for up to 72 hours post labelling (Figure 5.4b).

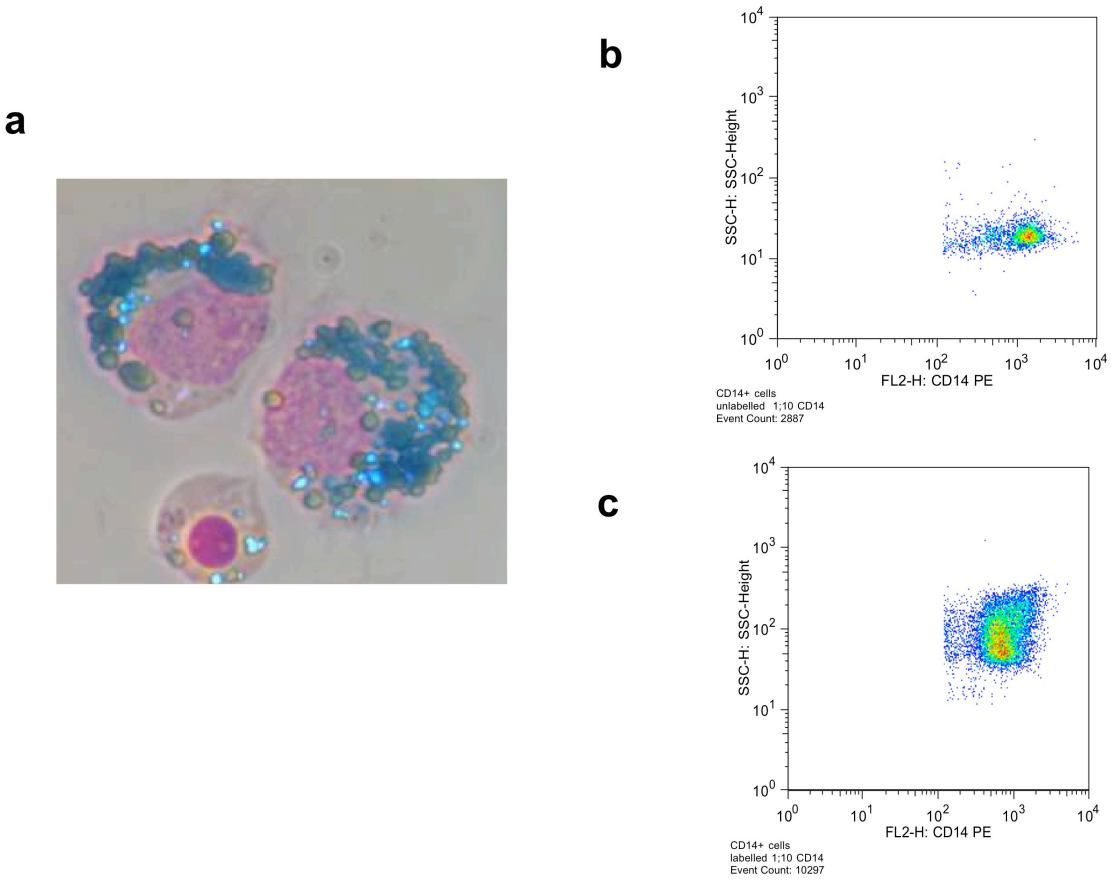

Figure 5.2 Cellular uptake of SPIO. (a) Cytospin preparation of peripheral blood mononuclear cells labelled with SPIO. Iron nanoparticles are seen within the cytoplasm but excluded from the nucleus, indicating that the SPIO is intracellular rather than adherent to the cell surface. **(b)** CD14 positive cells (monocytes) increased their side scatter following SPIO labelling **(c)** indicating increased granularity and SPIO internalisation.
SSC - Side scatter; FL - Fluorescence parameter; CD - Cluster of differentiation; PE - Phycoerythrin; SPIO - Superparamagnetic particles of iron oxide.

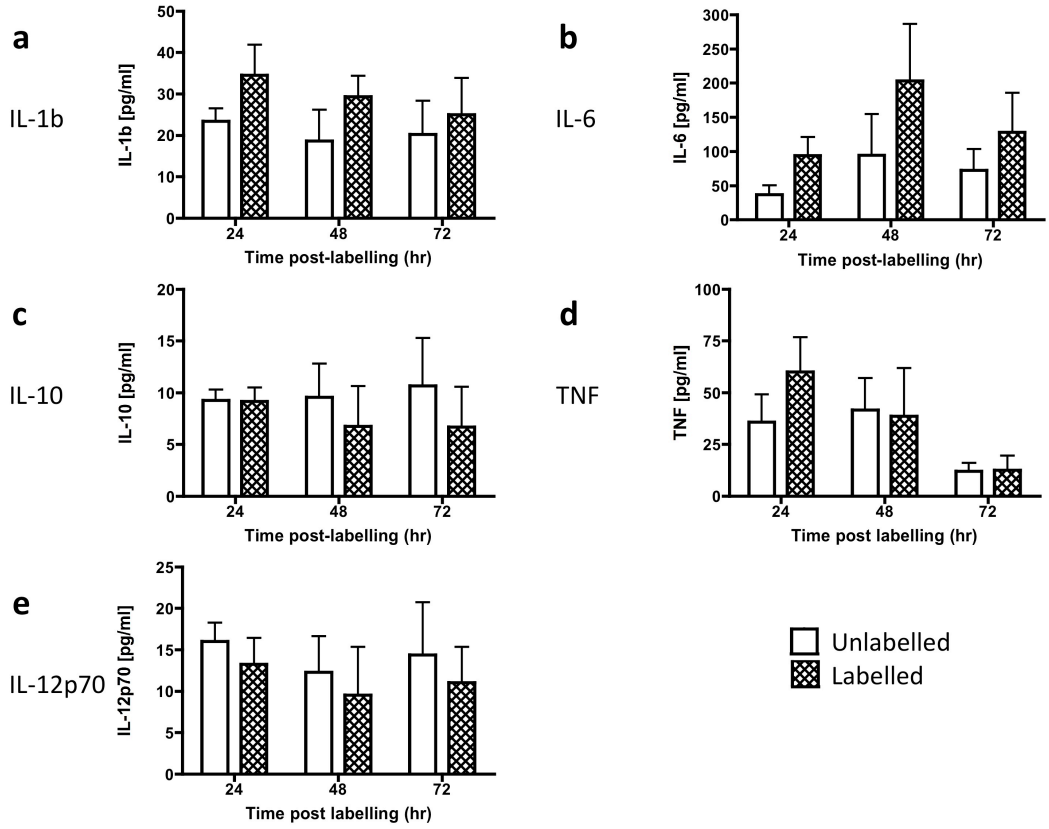

Figure 5.3 Effect of SPIO-labelling on cytokine release. SPIO-labelling did not affect the cytokine (IL-1, IL-6, IL-10, TNF, IL-12p70) release profile up to 72 hours post-labelling ($P > 0.05$ for all cytokines at all timepoints; n=4).
IL - Interleukin; TNF - Tumour necrosis factor; SPIO - Superparamagnetic particles of iron oxide.

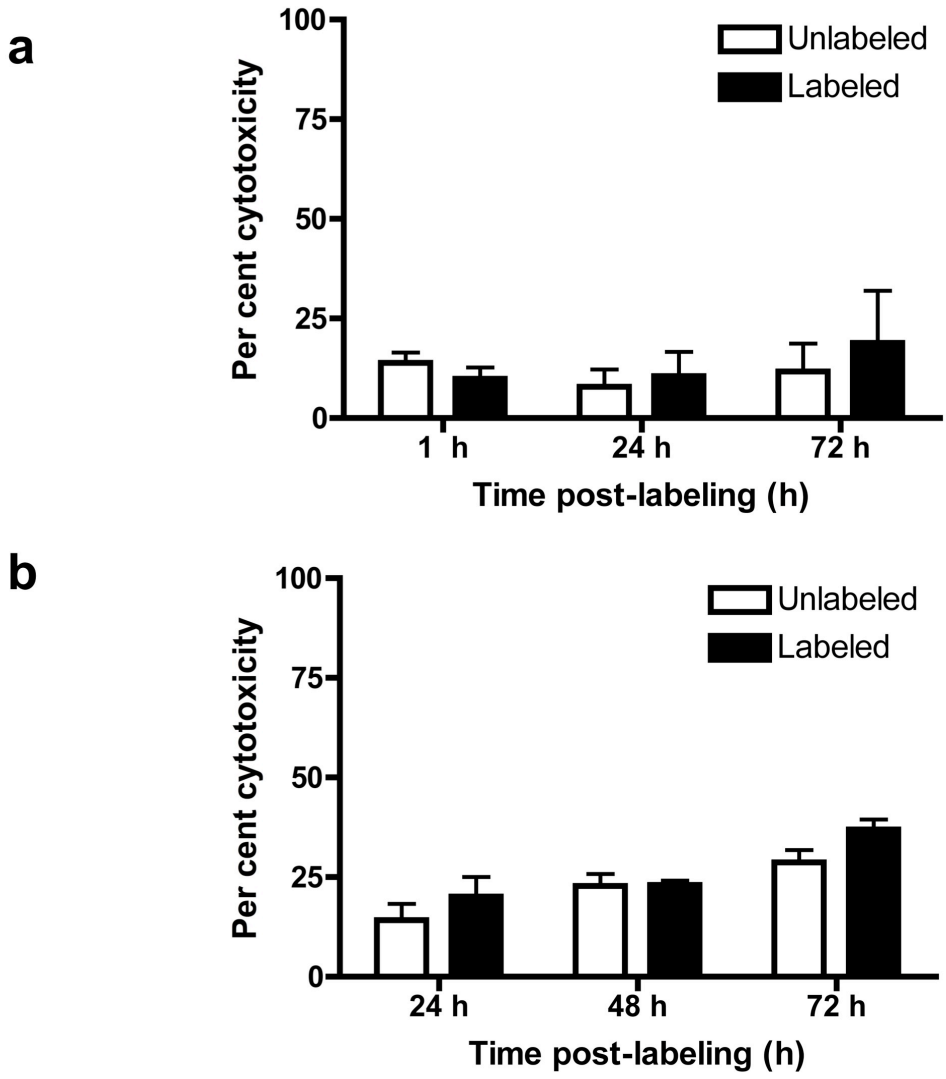

Figure 5.4 Effect of SPIO-labelling on cell viability. Labelling mononuclear cells with SPIO had no effect on cell viability measured either by flow cytometric analysis of annexin V binding in combination with PI staining (a) or a colorimetric assay for LDH release **(b)**. There was no difference in viability between labelled and unlabelled cells at any timepoint investigated ($P > 0.05$ for both methods at all timepoints; n=3).
SPIO - Superparamagnetic particles of iron oxide; PI - Propidium iodide; LDH - Lactate dehydrogenase.

Effect of SPIO-labelling on chemotaxis

Because cell tracking studies are critically dependent on the ability of labelled cells to migrate to the target site, we examined the ability of labelled and unlabelled monocytes to migrate towards a chemotactic stimulus MCP-1 *in vitro*. When the original Arbab method was used to label a high number of cells, clumps formed and cells failed to migrate, even in the presence of MCP-1. However cells labelled according to the Edinburgh protocol remained as a single cell suspension and migrated in equivalent numbers to unlabelled cells (164 ± 10 SPIO-labelled cells *versus* 139 ± 20 unlabelled cells at 50 ng/mL MCP-1; P=0.29). Prussian blue staining confirmed the presence of SPIO in the cytoplasm of migrating labelled cells (Figure 5.5a-g).

5.4.3 MRI SCANNING *IN VITRO*

SPIO-labelled cells were detectable *in vitro* using a clinical MRI scanner and cellular iron concentration exhibited a linear relationship with R2* value (Figure 5.6).

5.5 DISCUSSION

In this study, we have demonstrated, for the first time, that human mononuclear cells can be labelled with SPIO under GMP compliant conditions without affecting cell viability or function. Furthermore, the resulting labelled cells can be visualised *in vitro* at clinically relevant field strengths.

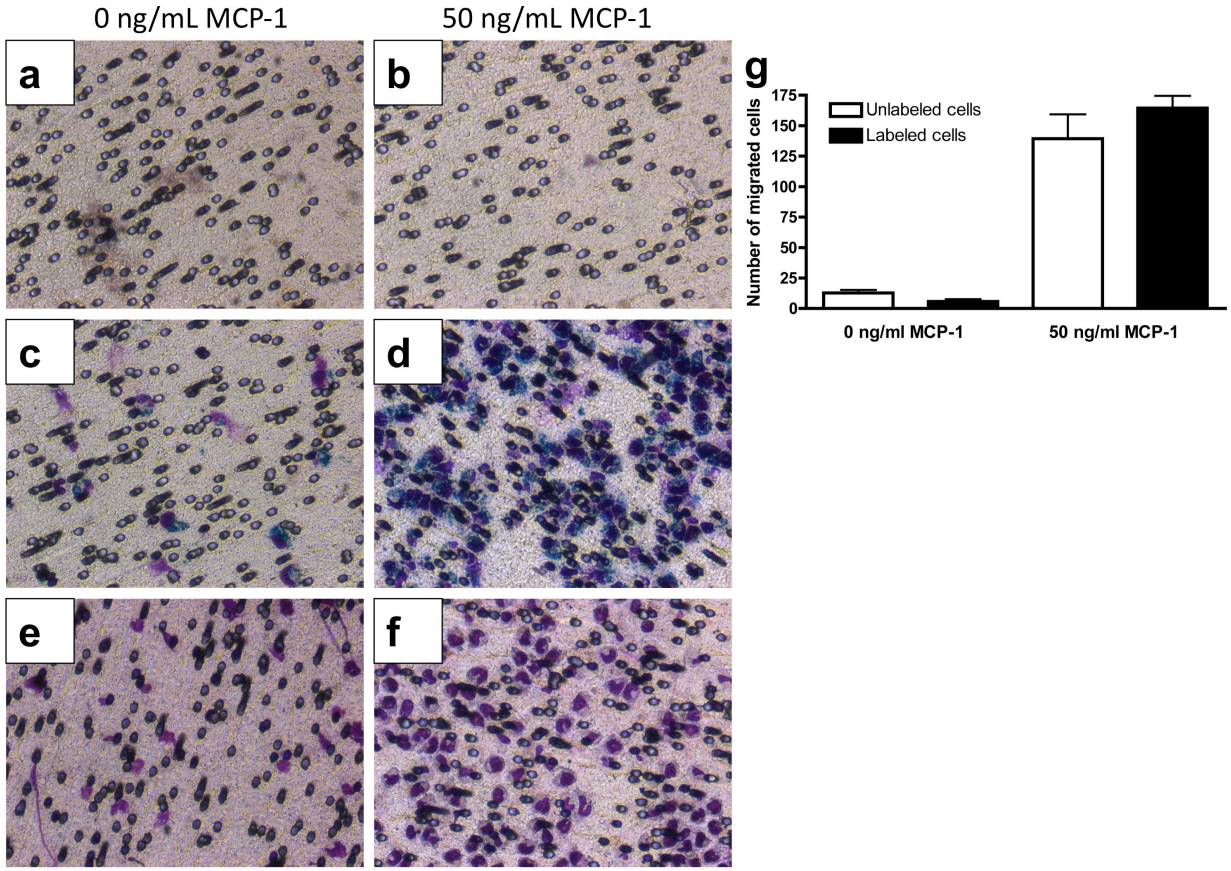

Figure 5.5 Effect of SPIO-labelling on chemotaxis. In an *in vitro* migration assay cells were allowed to migrate through a 5 μm microporous membrane towards 0 or 50 ng/mL of the chemokine human recombinant monocyte chemoattractant protein (MCP-1). Migrated cells adhered to the undersurface of the membrane and were stained with DiffQuik™ physiological stain (staining nuclei purple) and counterstained with Prussian blue causing SPIO particles carried in the cytoplasm to appear dark blue. Comparison was made of cells labelled according to the original protocol, which clumped and were unable to migrate **(a and b)**, with cells labelled according to the Edinburgh protocol **(c and d)** that remained in single cell suspension and migrated in equivalent numbers to unlabelled cells **(e and f)**. Quantification of chemotaxis **(g)** demonstrated that SPIO-labelling did not affect migratory capacity compared to unlabelled cells ($P > 0.05$ for both 0 and 50 ng/mL MCP-1; n=6).
SPIO - Superparamagnetic particles of iron oxide; MCPI-1 - Monocyte chemoattractant protein-1.

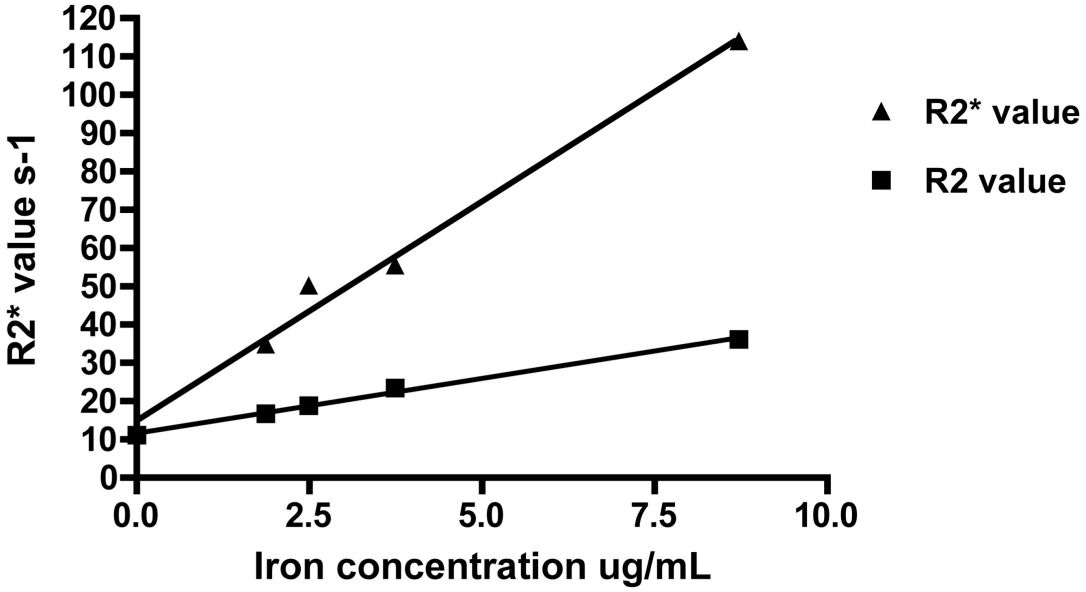

Figure 5.6 ***In vitro*** **agarose phantoms.** SPIO-labelled cells were introduced into agarose phantoms and scanned using T2W and T2*W sequences in a 3T clinical MRI scanner. There was a linear relationship between increasing iron concentration and R2* value.
SPIO - Superparamagnetic particles of iron oxide; T2W - T2 weighted; 3T - 3 Tesla.

It is essential that techniques for labelling cells for cell tracking studies do not impair cell function. There are several mechanisms through which SPIO might logically be expected to affect cell viability and function. However it would appear that monocytes and macrophages, as professional scavengers, have an excellent capacity to deal with ingested iron and resist the potentially toxic effects [Pawelczyk *et al* 2006]. The majority of studies have shown preservation of both viability and function following SPIO-labelling of a variety of cell types including mesenchymal, haematopoietic, neural and adipose-derived stem cells [Arbab et *al* 2005; Ju *et al* 2006; Neri *et al* 2008; Farrell *et al* 2009; Hu *et al* 2009; Wang *et al* 2009], with only a few reporting adverse effects and one showing increased proliferation of SPIO-labelled mesenchymal stem cells [Bulte *et al* 2004; Kostura *et al* 2004; Huang *et al* 2009]. These studies employed a range of cell labelling protocols, including differences in the nature of transfection agents, which may explain such findings.

We have demonstrated *in vitro* that viability and cytokine production are unaffected in PBMC labelled with SPIO according to the Edinburgh protocol. We were also able to demonstrate *in vitro* that SPIO-labelled PBMC exhibit normal migration towards the chemokine MCP-1 in a modified Boyden chamber. This is in contrast to others who have demonstrated *in vitro* migration in response to Regulated on Activation, Normal T-cell Expressed and Secreted (RANTES) but loss of MCP-1-dependent migration in SPIO-labelled monocyte-like cells from the THP-1 cell line [Janic *et al* 2008].

Whilst we have demonstrated no evidence of short-term toxicity (up to 72 hours) in SPIO-labelled PBMC, we have not assessed longer-term effects. In addition we have only assessed the effects of SPIO-labelling within an *in vitro* culture system and we have not assessed the potential toxic effects of introducing SPIO-labelled cells into tissues *in vivo*.

Finally we have demonstrated that cells labelled with SPIO are detectable *in vitro* using a clinical MRI scanner. The magnetic effects of SPIO are dependent on the field strength of the external magnetic field. There is a linear relationship between R2* value and field strength, and R2* values at 3T are approximately double the corresponding value at 1.5T [Storey *et al* 2007]. Magnetic resonance imaging using a higher field strength of 3T therefore offers increased sensitivity to detect iron accumulation as well as improved signal-to-noise ratio. However, at very high tissue iron concentrations the signal intensity may decay very rapidly so that even with short echo time intervals achieved through single echo acquisitions the iron concentration lies beyond the quantifiable range at 3T.

The production of cell-based products for use in humans must be consistent with GMP requirements and is regulated under recent directives issued by the European Union and the Food and Drug Administration (FDA). Considerations include the suitability of reagents, receptacles, equipment and facilities used during the preparation of cell-products for human use. It is essential that basic scientists, clinical researchers and technicians liaise regarding these guidelines throughout the protocol

development and implementation stages to ensure that the final protocol is compliant with these regulations.

Small numbers of samples have been used to assess the effects of SPIO cell labelling on cell viability and function *in vitro*. Furthermore, the toxicity of SPIO labelling has only been assessed for up to 72 hours *in vitro* and cells may respond differently when exposed to SPIO for a more prolonged period of time *in vivo* when influenced by other cell types and the surrounding cytokine milieu. This requires further evalution before more solid conclusions can be drawn regarding the cellular effects of SPIO labelling. Further phantom work may help to clarify the effects of SPIO size, iron concentration, cell type and cell aggregation on signal change and facilitate interpretation of the resulting imaging data. Future targeted agents may allow more specific cell labelling.

In conclusion, this study has defined a GMP compliant protocol by which human mononuclear cells can be labelled with SPIO on a clinical scale and no adverse effects on cell viability or function were observed. We have also demonstrated the feasibility of imaging cells *in vitro* at clinical field strengths. This therefore represents a highly promising technique for clinical cell tracking studies.

CHAPTER 6

IN VIVO MONONUCLEAR CELL TRACKING USING SUPERPARAMAGNETIC PARTICLES OF IRON OXIDE IN HUMANS

6.1 SUMMARY

Cell therapy is an emerging and exciting potential novel treatment option for a wide range of diseases and the success of such therapies depends on the delivery of cells to their target site. However, monitoring and tracking cells to ensure tissue delivery and engraftment is a critical step in establishing clinical and therapeutic efficacy. We have previously demonstrated that human mononuclear cells can be labelled with SPIO for clinical cell tracking studies under GMP compliant conditions without affecting cell viability or function. The safety of both intramuscular and intravenous administration of SPIO-labelled cells is demonstrated, with cells readily identifiable *in vivo* for at least 7 days using magnetic resonance imaging. We also show that SPIO-labelled mononuclear cells track to the reticuloendothelial system as well as an iatrogenic inflammatory focus in healthy human volunteers. SPIO-labelling for magnetic resonance cell tracking therefore appears to be a safe, feasible and potentially widely applicable technique that has major potential for a range of clinical applications including monitoring cellular inflammatory responses and tracking of delivered cells in cell therapies.

6.2 INTRODUCTION

Considerable interest surrounds stem cell and other cell-based therapies which have emerged as potential novel treatment options for a wide range of diseases including acute myocardial infarction and severe heart failure [Perin *et al* 2004; Wollert *et al* 2004; Fuchs *et al* 2006; Gyongyosi *et al* 2009; Yousef *et al* 2009]. The ability to

track cells to the intended target therapeutic site non-invasively would be a key development for the assessment of these therapies as they continue to evolve.

Radio imaging techniques, such as scintigraphy and PET, can be sensitive but offer poor spatial resolution, expose patients to ionising radiation and have the added disadvantage that radiotracers have a short half-life, limiting the duration of follow-up. However MRI offers excellent spatial resolution and soft tissue contrast whilst avoiding ionising radiation.

SPIO are part of a novel group of MRI contrast agents available for clinical use. SPIO induce local magnetic field inhomogeneities causing rapid dephasing of spinning protons and shortening of the T2* relaxation time. Compared to paramagnetic agents such as gadolinium, SPIO are detectable at much lower concentrations and are readily taken up by resident macrophages in the reticuloendothelial system. SPIO are biodegradable *in vivo*, and we (Chapter 5) and others have shown that they are not toxic to a variety of cell types *in vitro* [Arbab *et al* 2005; Ju *et al* 2006; Neri *et al* 2008; Farrell *et al* 2009; Hu *et al* 2009; Wang *et al* 2009].

We have also demonstrated that human PBMC can be labelled with SPIO under GMP compliant conditions without affecting cell viability or function, and the resulting SPIO-labelled cells can be imaged *in vitro* in a 3T clinical MRI scanner. Importantly, however, the safety of intravenous administration of SPIO-labelled cells in humans has yet to be demonstrated, and would be critical for the development and

FDA approval of novel cell tracking agents for clinical use. Furthermore, whilst SPIO-labelled cells have been tracked to a target site following local administration, this has not previously been achieved following systemic administration of cells.

We therefore aimed to (i) confirm the safety of both local and intravenous administration of labelled cells and (ii) track intravenously administered SPIO-labelled cells *in vivo* in humans.

6.3 METHODS

6.3.1 SUBJECTS

Healthy volunteers aged >18 years were recruited by advertisement. Participants underwent a standard health assessment, including virology screening, to confirm suitability to participate in the study. Participants known to have a positive Mantoux test response were identified from the Department of Respiratory Medicine database of such patients.

6.3.2 CELL PREPARATION AND LABELLING

Blood was collected by venesection into citrate or by leucapheresis (COBE Spectra, Gambro BCT, USA) to yield approximately $1\text{-}5 \times 10^8$ or $1\text{-}5 \times 10^9$ PBMC respectively.

In the Scottish National Blood Transfusion Service GMP facility, PBMC were isolated by density-gradient separation and labelled with SPIO according to the

optimised Edinburgh protocol. In brief, PBMC were suspended in 0.9% saline (4×10^6 cells/mL) and incubated with SPIO (100 μg/mL; Endorem, Guerbet, France) and protamine sulphate (4 μg/mL; Prosulf) at room temperature for 2 hours with continuous agitation. Cells were provided for reinfusion in a low-adherence bag (Cryocyte, Baxter, UK).

6.3.3 INTRAMUSCULAR ADMINISTRATION

Having shown that cells can be imaged in *in vitro* agarose phantoms**,** and before proceeding to systemic cell tracking studies, we wanted to demonstrate the feasibility of imaging labelled cells in humans at clinically relevant field strengths. Six healthy volunteers each received three 2 mL intramuscular thigh injections of SPIO alone, SPIO-labelled autologous PBMC and unlabelled autologous PBMC, following which they underwent imaging in a 1.5T MRI scanner immediately and at 7 days.

6.3.4 PHASED-DOSING PROTOCOL: SAFETY OF INTRAVENOUS ADMINISTRATION OF SPIO-LABELLED CELLS

In order to establish the safety of intravenous administration of SPIO-labelled cells, we undertook a phased-dosing study in which two volunteers each received six increasing doses of SPIO-labelled autologous PBMC (10^4-10^9 cells) over four study visits. Cell infusions were carried out in a Clinical Research Facility with non-invasive physiological monitoring (pulse oximetry, non-invasive blood pressure and temperature) and nurse observation during cell reinfusion and the subsequent observation period. Cells were administered through a giving set with a 200 μm macroaggregate filter. Each cell infusion lasted 30-60 minutes (depending on

volume) and was followed by a 60-minute observation period after which a further infusion of cells was commenced or the participant was discharged.

Blood was sampled at each visit before reinfusion and one hour post-infusion of labelled cells. Blood was drawn into citrate and EDTA tubes for full blood count, routine biochemistry and coagulation parameters including prothrombin time, activated partial thromboplastin time, fibrinogen and D-dimer. Participants were contacted within one week of the study visit to confirm that there had been no delayed adverse effects following administration of labelled cells.

6.3.5 Intravenous administration of SPIO-labelled cells for cell tracking

Twelve further healthy volunteers were recruited and received a low dose of SPIO-labelled autologous PBMC obtained from a 250 mL venesection (~1-5 × 10^8 cells; n=6) or a high dose of cells obtained from a standard leucapheresis collection (~1-5 × 10^9 cells; n=6). Intravenous cell infusions were carried out and blood samples were obtained as described above. These participants underwent MRI scanning in a 3T scanner before and 2, 24, 48 and 168 hours following administration of cells.

6.3.6 Mantoux test

A local cutaneous inflammatory response was induced in the thigh of healthy volunteers using the Mantoux test: an intradermal injection of 2 units of tuberculin purified protein derivative (PPD). In previously exposed individuals, tuberculin PPD stimulates a type IV delayed, cell-mediated hypersensitivity reaction involving an

influx of neutrophils initially (~6 hours), and subsequently of monocytes (12-48 hours) and lymphocytes (12-96 hours) into the dermal skin layer [Vukmanovic-Stejic *et al* 2006; Kumar *et al* 2007]. Twenty-four hours after the Mantoux test, participants underwent a standard leucapheresis collection and later the same day received an infusion of SPIO-labelled autologous PBMC. T2 and T2*W imaging was performed before and 2, 24 and 48 hours following the administration of cells. A skin biopsy was obtained from the site of the Mantoux test 96 hours following administration of cells (120 hours after the Mantoux test), fixed in 4% paraformaldehyde and stained with Prussian blue.

6.3.7 MAGNETIC RESONANCE IMAGING

Volunteers receiving cells intramuscularly underwent MRI scanning of the thigh in a 1.5T Phillips scanner using a T2W sequence with a long echo time (137 ms).

Volunteers undergoing intravenous infusion were scanned using a 3T Magnetom Verio scanner (Siemens, Erlangen, Germany). Routine localiser sequences were applied following which T2W (TE 87 ms; TR 1800 ms; matrix 256 × 192; field of view 380 × 285 mm) and T2*W (multi echo TE 4.1-22.1 ms; TR 100 ms; flip angle 15°; matrix 282 × 512; field of view 282 × 410 mm; slice width 5 mm) sequences were used to acquire axial images of the upper abdomen.

T1W (3D VIBE; TE/TR 2.0/5.5 ms; matrix 416 × 416; field of view 210 × 210 mm; slice width 5 mm) and T2*W (2D multislice gradient echo; TE 9.8, 12.3, 14.8 ms;

TR 120.0 ms; matrix size 312 × 384; field of view 203 × 250 mm; slice width 5 mm) images of the thigh were acquired following Mantoux testing.

6.3.8 IMAGE ANALYSIS

Following local administration of SPIO or cells, T2W axial images of the thigh were inspected qualitatively for evidence of a change in signal intensity.

Following systemic administration of SPIO-labelled cells, transaxial abdominal images were analysed on the basis of the R2* value. The T2* value is the decay constant for the decay of signal intensity with increasing echo time, and its inverse the R2* value (T2*=1/R2*) has been used to evaluate tissue iron concentration [Wood *et al* 2005].

The use of all six echo times to calculate the R2* value was validated by selecting ROI at each echo time and plotting signal intensity against echo time**.** Even at longer echo times the signal was clearly distinct from the background noise level and exponential decay of signal intensity with time was confirmed. Therefore a six echo R2* map was generated. Regions of interest were selected on the initial 4.1 ms echo time image taking care to avoid major blood vessels and motion artefact. Five regions of consistent size (0.5 cm^2) were selected in the spleen, liver, skeletal muscle (control) and background noise, and were copied to the corresponding R2* map. Relationship to distinctive anatomical features was used to ensure that the regions chosen were consistent amongst scans from each of the five study visits.

For cell tracking to the site of the Mantoux test, higher resolution was required to allow visualisation of the skin and subcutaneous tissue. The individual echoes were acquired separately and had to be registered together for R2* map generation using in-house software. Regions of interest were selected in the inflamed skin, normal unaffected skin (control), skeletal muscle (control), liver and spleen at each timepoint.

6.3.9 STATISTICAL ANALYSIS

Blood results and physiological monitoring data were compared by paired two-tailed Student *t*-test. T2* MRI data were analysed by repeated-measures, one-way ANOVA with post-test Bonferroni correction (GraphPad Prism, GraphPad Software, USA). Two-sided $P<0.05$ was regarded as statistically significant.

6.4 RESULTS

6.4.1 CLINICAL STUDIES

Intramuscular administration

Injections were performed successfully in all participants without complication. A signal deficit was observed at the site of administration of SPIO alone and SPIO-labelled cells (Figure 6.1a and b). Whilst an oedematous change was noted at the site of injection of unlabelled cells, no dropout of signal was seen (Figure 6.1c). These findings were consistent for all six participants and persisted for at least 7 days.

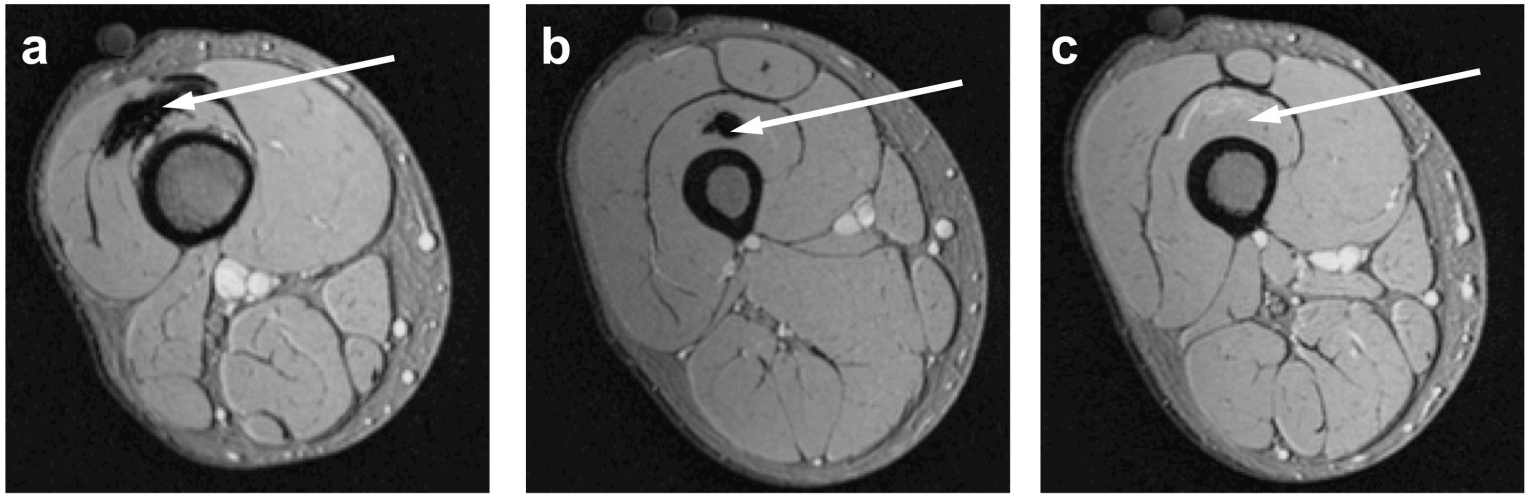

Figure 6.1 MRI scanning following intramuscular administration of cells. T2W imaging of the thigh following intramuscular administration of labelled cells. A signal deficit is seen in relation to injection of SPIO alone **(a)** and SPIO-labelled cells **(b)** but not unlabelled cells **(c)**. These findings were consistent for all six participants and persisted for 7 days.
MRI - Magnetic resonance imaging; T2W - T2 weighted; SPIO - Superparamagnetic particles of iron oxide.

Safety of intravenous administration of SPIO-labelled cells

In the phased-dosing study, all cell infusions in both participants were well tolerated with no early or late clinical side-effects. A further twelve volunteers then received a low dose of SPIO-labelled autologous PBMC obtained from a 250 mL venesection ($2.03 \pm 0.18 \times 10^8$ cells; mean ± standard error of the mean (SEM); n=6) or a high dose of SPIO-labelled autologous PBMC obtained from a standard leucapheresis collection ($2.23 \pm 0.51 \times 10^9$ cells; n=6). Cell infusions had no effect on heart rate, blood pressure or temperature (Table 6.1).

Although the problem of macroscopic cell clumping had been obviated using the Edinburgh protocol, labelled cells were administered through a macroaggregate filter and we aimed to demonstrate that there were no clinically significant microembolic events associated with cell administration. Peripheral perfusion, monitored continuously by digital pulse oximetry during and for an hour after cell infusion, was unaffected. To ensure further that labelled cells did not have a procoagulant effect *in vivo*, blood was sampled for prothrombin time, activated partial thromboplastin time and fibrinogen concentration before and after cell infusion, and D-dimer concentration was measured after cell infusion. Infusion of SPIO-labelled cells did not affect any coagulation variable, and there were no clinically significant effects on routine clinical haematological and biochemical variables (Table 6.2).

MRI scanning

Following administration of labelled cells, the signal intensity was reduced in the liver and spleen on T2- (Figure 6.2) and T2*W imaging. There was a

TABLE 6.1 Non-invasive physiological monitoring parameters before and at the end of infusion of 1-5 x 10^9 PBMC SPIO-labelled cells (n=12)

	Mean pre-infusion	Mean post-infusion	P
Systolic blood pressure (mmHg)	127	123	0.10
Diastolic blood pressure (mmHg)	75	74	0.72
Heart rate (beats per minute)	69	67	0.16
Temperature (°C)	36.8	36.9	0.27
Oxygen saturations on air (per cent)	99	99	0.81

PBMC - Peripheral blood mononuclear cells; SPIO - Superparamagnetic particles of iron oxide.

TABLE 6.2 Haematological, biochemical and coagulation variables before and after infusion of 1-5 x 10^9 SPIO-labelled cells (n=12)

	Normal range	Mean pre-infusion	Mean post-infusion	P
Haemoglobin (g/L)	115 - 165	136 ± 5	132 ± 4	0.07
White blood count (x10^9/L)	4.0 - 11.0	7.1 ± 1.1	7.5 ± 0.6	0.68
Platelets (x10^9/L)	150 - 350	237 ± 19	230 ± 18	0.35
Prothrombin time (s)	10.5 - 13.5	11 ± 0	12 ± 0	0.19
Activated partial thromboplastin time (s)	26 - 36	30 ± 0	30 ± 0	0.59
Fibrinogen (g/L)	1.5 - 4	2.8 ± 0.2	2.7 ± 0.2	0.09
D-Dimer (ng/mL)	0 - 230	-	114 ± 22	-
Urea (mmol/L)	2.5 - 6.6	4.4 ± 0.3	4.5 ± 0.2	0.84
Creatinine (μmol/L)	60 - 120	68 ± 3	68 ± 3	0.87
Sodium (mmol/L)	135 - 145	140 ± 0	140 ± 0	0.40
Potassium (mmol/L)	3.6 - 5.0	4.1 ± 0.1	4.0 ± 0.1	0.22
TCO_2 (mmol/L)	20 - 30	26 ± 1	28 ± 1	0.16
Bilirubin (μmol/L)	3 - 16	12 ± 2	11 ± 1	0.31
Alanine amino transferase (U/L)	10 - 55	20 ± 2	21 ± 2	0.53
Alkaline phosphatase (U/L)	40 - 125	70 ± 7	68 ± 7	0.88

SPIO - Superparamagnetic particles of iron oxide.

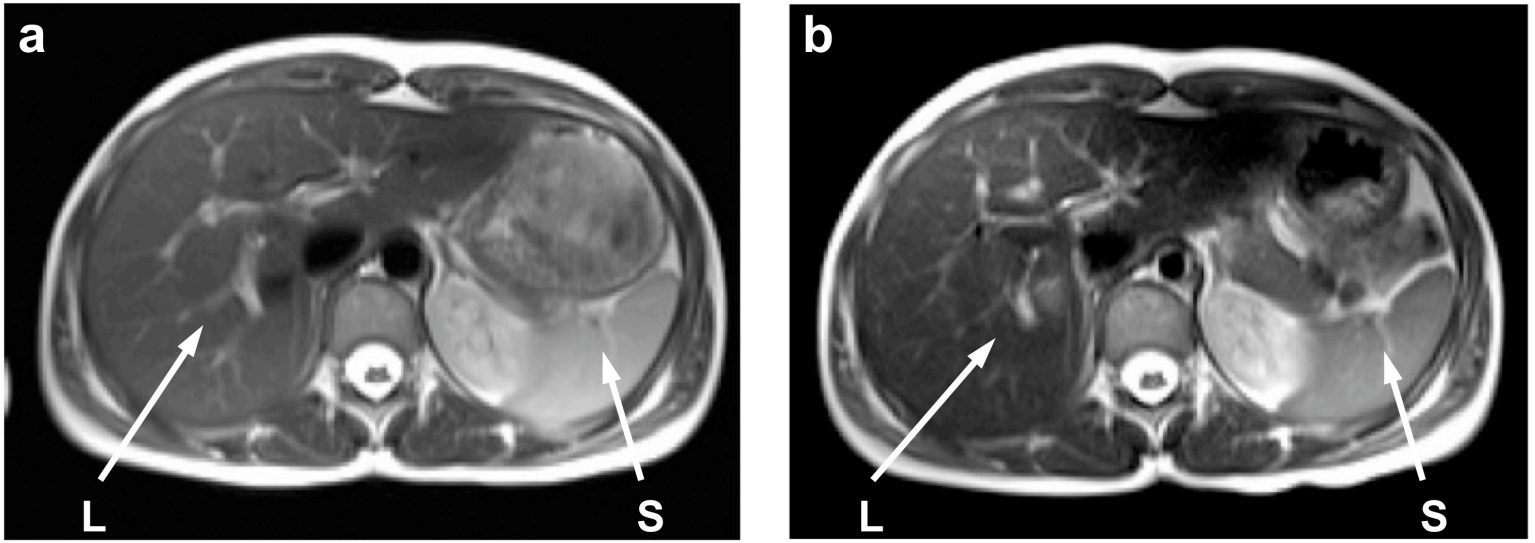

Figure 6.2 MRI scanning of the upper abdomen following systemic administration of cells. T2 weighted transaxial slice through the upper abdomen before **(a)** and after **(b)** intravenous administration of SPIO-labelled cells. Signal intensity is reduced in the liver (L) and spleen (S) following administration of cells.
MRI - Magnetic resonance imaging; SPIO - Superparamagnetic particles of iron oxide.

marked increase in R2* value in the liver and in the spleen ($P < 0.001$) following the administration of cells (Figure 6.3) reflecting the dose-dependent accumulation of SPIO-labelled cells at these sites. There was no change in the R2* value in skeletal muscle (negative control) and the background noise level remained constant.

6.4.2 CELL TRACKING TO AN INFLAMMATORY FOCUS

At 24 and 48 hours, an increase in the R2* value was observed in the inflamed skin ($P < 0.001$) as well as the liver and the spleen but not the adjacent normal skin or skeletal muscle ($P > 0.05$; Figure 6.4a-h). A skin biopsy was obtained from the site of the Mantoux test 96 hours following administration of cells (120 hours after the Mantoux test) and stained with Prussian blue. Occasional iron-laden cells were observed in the inflamed skin consistent with the diminishing monocyte and macrophage cell numbers by this stage in a type IV hypersensitivity response (Figure 6.5a-c). In a participant who had a negative response to the Mantoux test, there was no change in R2* following the administration of SPIO-labelled cells (Figure 6.6).

6.5 DISCUSSION

We have shown that intravenous administration of SPIO-labelled cells is safe, and that cells can be visualised *in vivo* at clinically relevant field strengths following either local or systemic administration. Importantly SPIO-labelled cells can be tracked to a site of iatrogenic focal inflammation in healthy human volunteers. This technique therefore has the potential to track the distribution, time course and fate of

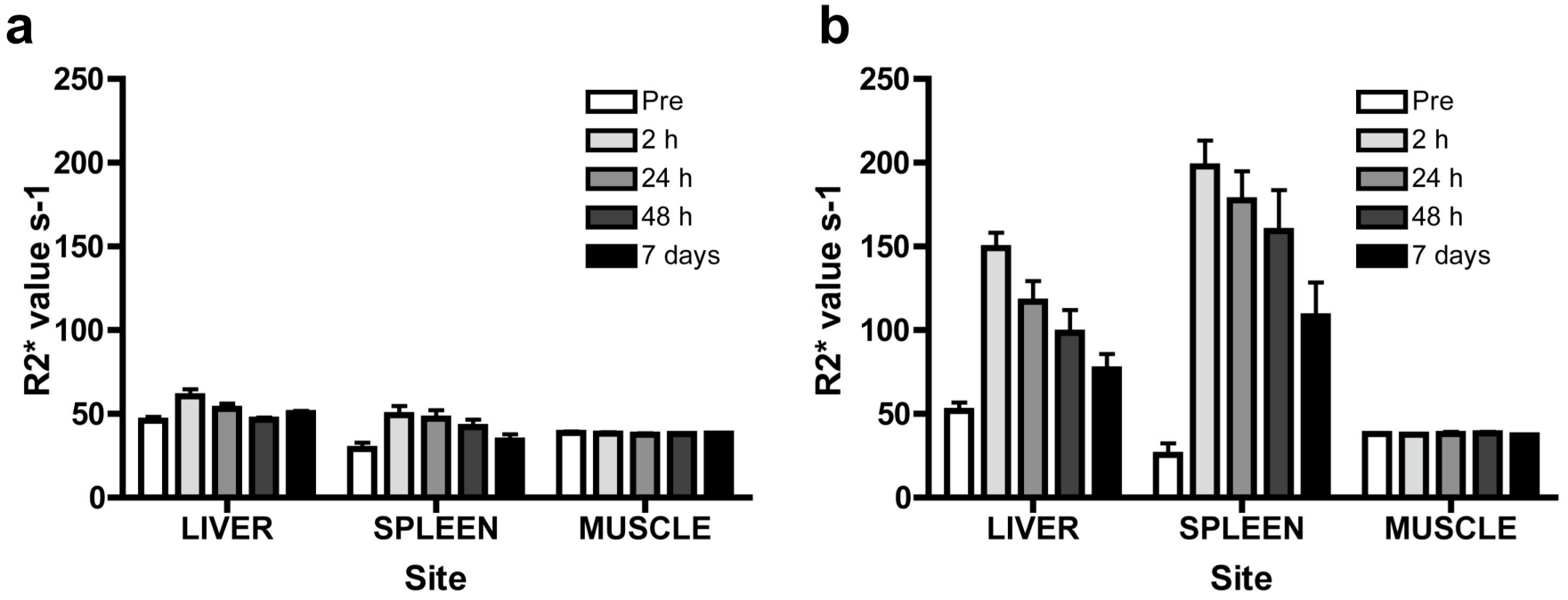

Figure 6.3 Change in R2* value in the reticuloendothelial system following administration of SPIO labelled cells. Change in R2* value from baseline 2 hr, 24 hr, 48 hr and 7 days following intravenous administration of a low dose (**a;** 1-5 × 10^8 PBMC; n=6) or a high dose (**b**; 1-5 × 10^9 PBMC; n=6) of SPIO-labelled cells. An increase in R2* value is seen in the spleen ($P < 0.0001$) and liver ($P < 0.0001$) but not skeletal muscle (control, $P > 0.05$).
PMBC - Peripheral blood mononuclear cells; SPIO - Superparamagnetic particles of iron oxide.

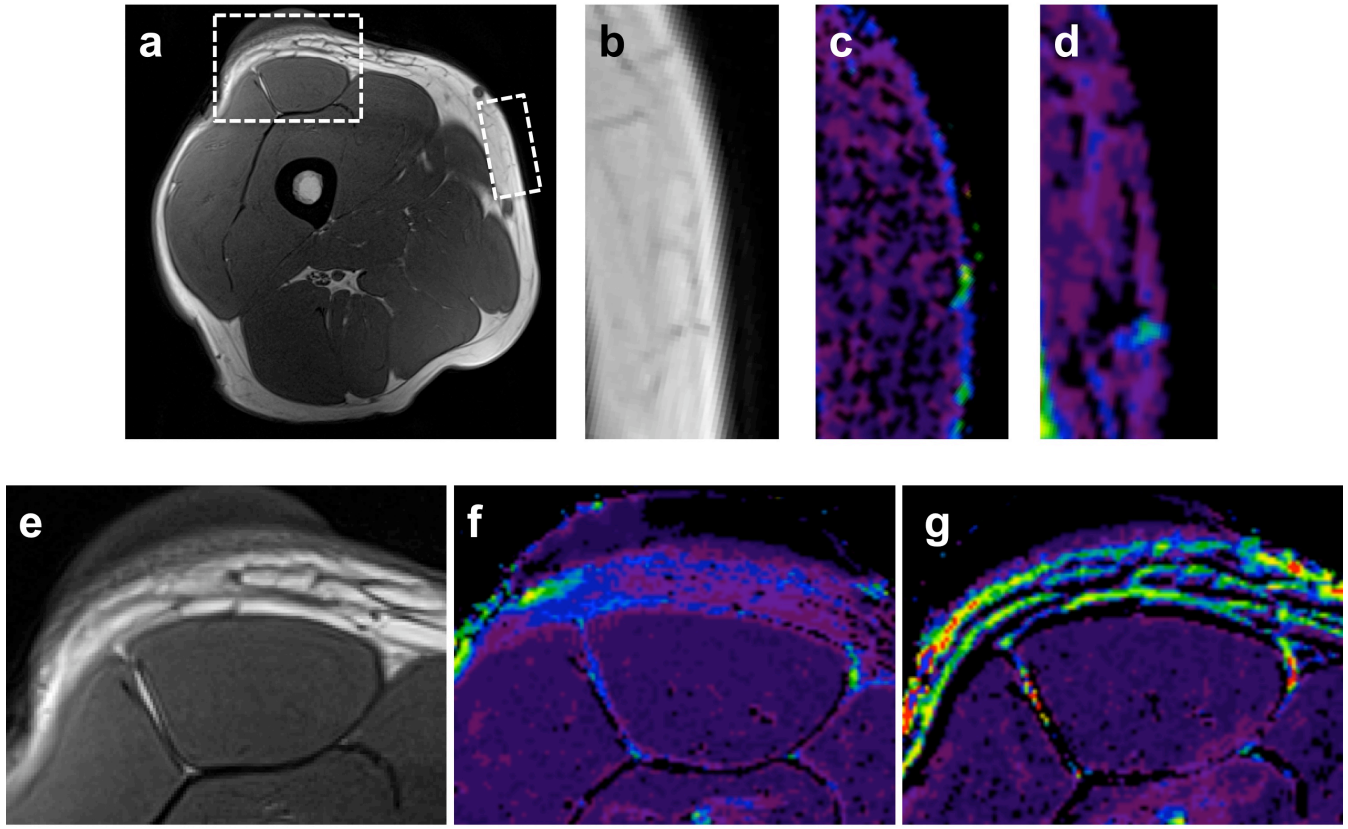

Figure 6.4 **(a)** T1W axial image of the thigh 24 hr following the Mantoux test. A thick layer of aqueous jelly was applied to the skin to avoid artefact that would otherwise occur at the interface between the outer layer of skin and the surrounding air. **(b)** A magnified area of normal unaffected skin and subcutaneous tissue on the medial aspect of the thigh. R2* maps before **(c)** and after **(d)** infusion of SPIO-labelled cells show no change in R2* value in normal skin and subcutaneous tissue following cell administration. The skin and subcutaneous tissue thickens in the region of the Mantoux test on the anterior thigh **(e)**. Corresponding R2* maps of this inflamed skin **(f)** show a marked increase in R2* value following the administration of SPIO-labelled cells **(g)**.
T1W - T1 weighted; SPIO - Superparamagnetic particles of iron oxide

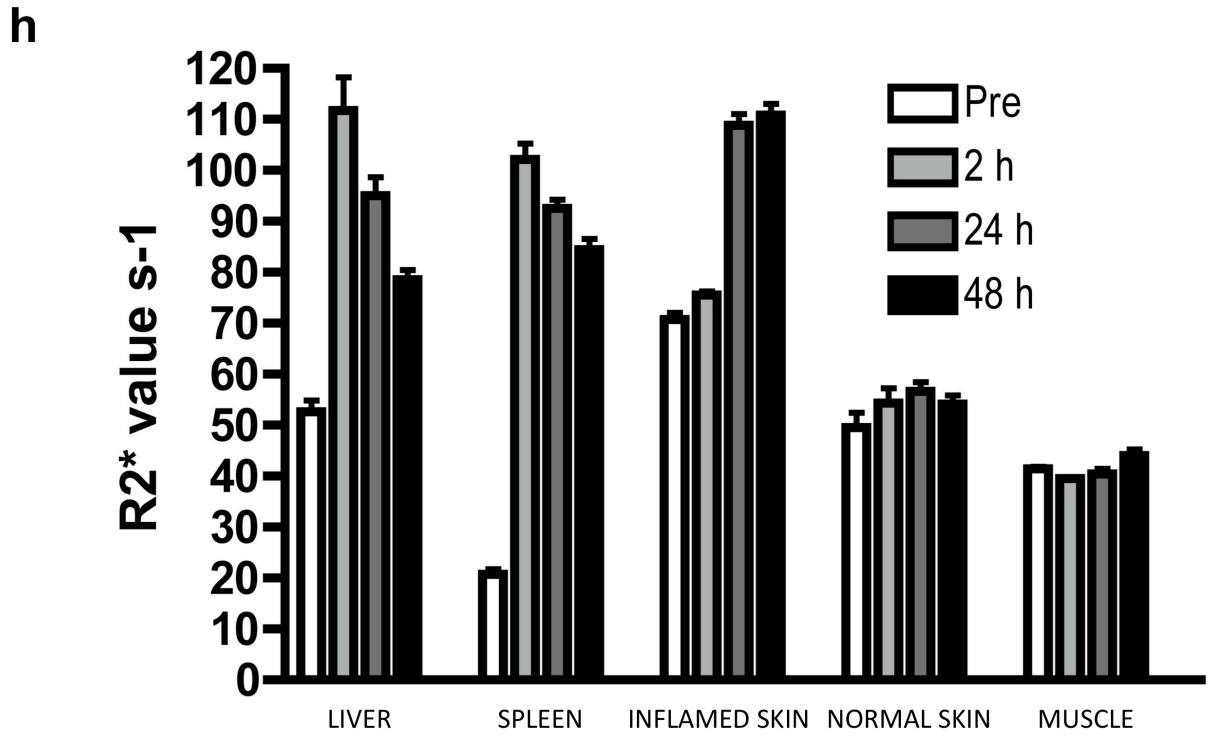

Figure 6.4. Cell tracking to a region of cutaneous inflammation. (h) Consistent with accumulation of SPIO-labelled cells, a significant increase in R2* value is observed 24 and 48 hr after cell administration in inflamed skin in the region of the Mantoux test ($P < 0.0001$) as well as in the liver and the spleen ($P < 0.0001$), but not in unaffected normal skin or skeletal muscle (control; $P > 0.05$).
SPIO - Superparamagnetic particles of iron oxide.

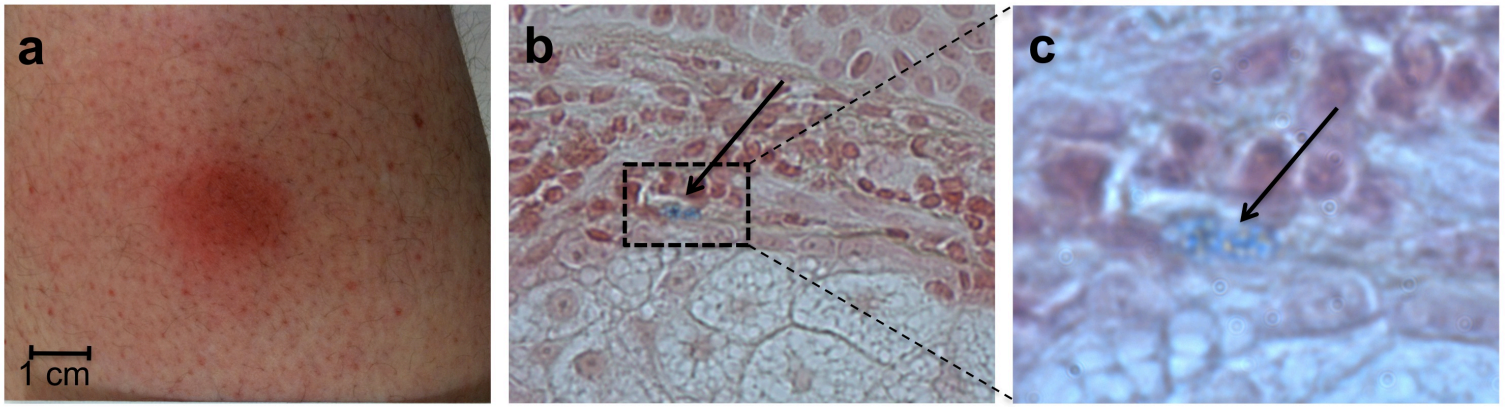

Figure 6.5 Accumulation of SPIO-labelled cells at the site of the Mantoux test. The strongly positive cutaneous response to the Mantoux test is clearly visible in the anterior thigh **(a)**. SPIO-loaded cells are seen on Prussian blue staining of a skin biopsy from this area 96 hr following cell infusion **(b and c)**.
SPIO - Superparamagnetic particles of iron oxide.

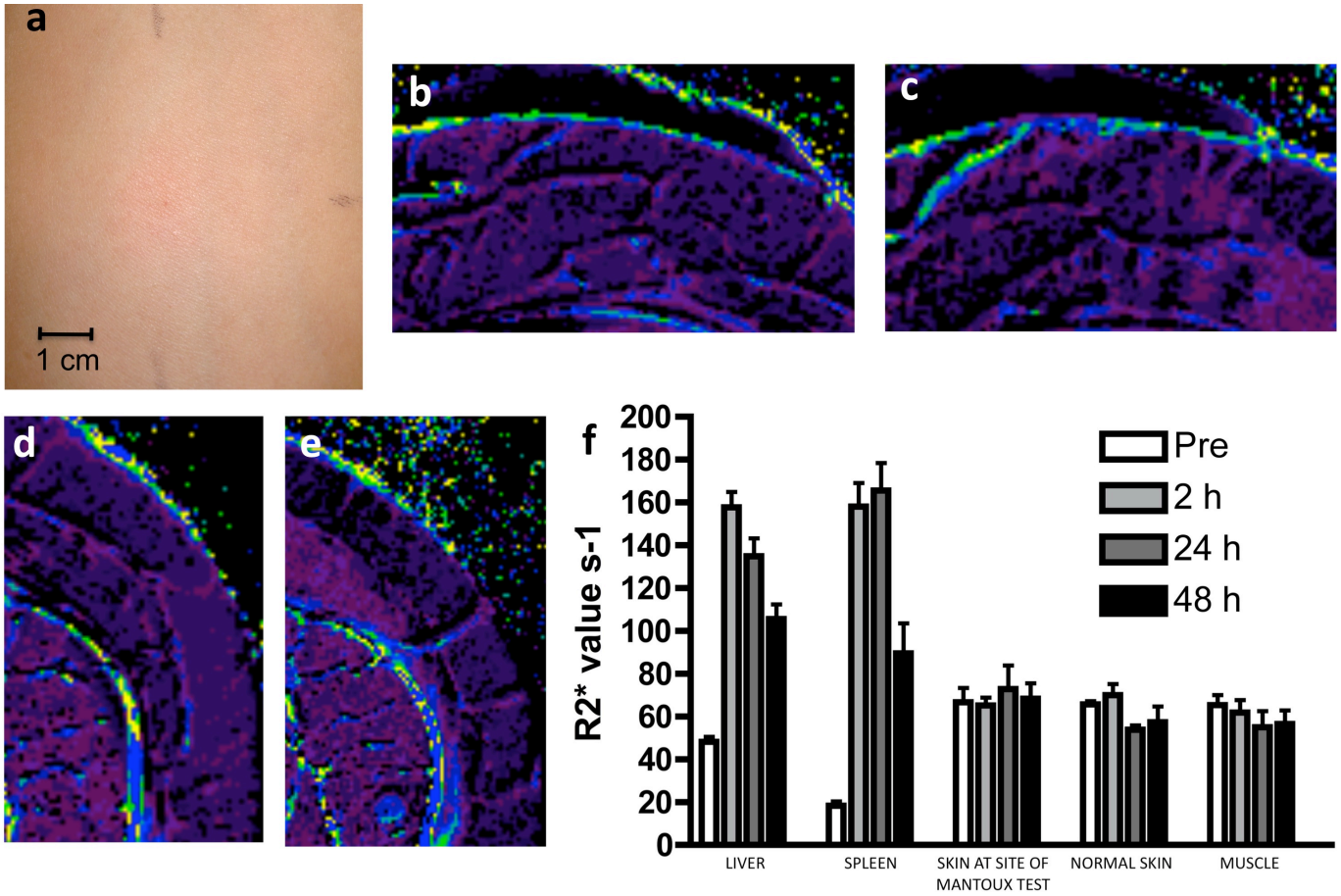

Figure 6.6 (a) There is no evidence of an inflammatory response at the site of the Mantoux test. R2* maps before **(b)** and after **(c)** infusion of SPIO-labelled cells show no change in R2* value in skin and subcutaneous tissue at the site of the Mantoux test following cell administration. Similarly, R2* maps before **(d)** and after **(e)** infusion of SPIO-labelled cells show no change in R2* value in skin and subcutaneous tissue at the control site (medial thigh) following cell administration. **(f)** The R2* value increased significantly in the liver and spleen ($p<0.0001$, all time points) but not in the skin at the site of the Mantoux test, normal skin or skeletal muscle ($p>0.05$, all timepoints) following the administration of SPIO-labelled cells.
SPIO - Superparamagnetic particles of iron oxide.

cells administered systemically as part of cell therapy: a critical component of the development of cellular therapeutic strategies, and ultimately of monitoring the success of treatment.

It is essential that techniques for labelling cells for cell tracking studies do not impair cell viability or function and we have previously shown that human PBMC can be labelled with SPIO under GMP compliant conditions without affecting cell viability, cytokine release or migratory capacity *in vitro*. Importantly we have also shown for the first time that intravenous administration of SPIO-labelled cells in humans is safe. Although several SPIO agents have been approved for intravenous administration, the FDA has not approved the intravenous administration of cells into which SPIO has been incorporated *ex vivo*. These safety data are therefore critical for the further development and subsequent FDA approval of novel SPIO-based cell tracking agents, facilitating translation into the clinical setting.

Several recent publications have reported tracking of labelled cells to a site of inflammation following both local and systemic administration in the pre-clinical setting [Kraitchman *et al* 2003; Anderson *et al* 2005; Cao *et al* 2009a; Cao *et al* 2009b; Kim *et al* 2009; Loebinger *et al* 2009; Song *et al* 2009]. Migration of cells to a target site has also been demonstrated in humans following local administration. de Vries and colleagues labelled human dendritic cells with USPIO (particle size 20 nm), injected them directly into peripheral lymph nodes in patients with melanoma and demonstrated their migration to regional lymph nodes on MRI scanning and histology of surgical resection specimens [de Vries *et al* 2005].

SPIO-labelled pancreatic islet cells have been detected in the liver following portal venous administration and SPIO-labelled MSC have been tracked to the site of injury following intracerebral injection in a patient with a traumatic brain injury [Zhu *et al* 2006; Toso *et al* 2008]. However this is the first report of successful tracking of SPIO-labelled cells to a target site following systemic intravenous administration. This finding substantially broadens the potential applications for SPIO-labelled cell tracking.

We have shown that at clinically relevant field strengths, it is readily possible to image ~10^8 mononuclear cells (containing ~1-5 × 10^7 monocytes) following local or intravenous administration, and others have imaged as few as 1.5 × 10^5 cells in a target site following local delivery of 7.5 × 10^6 cells [de Vries *et al* 2005]. If there was any concern regarding the effect of SPIO-labelling on the likely success of cell-based treatments, it would therefore be possible to label a small but representative proportion of the total number of cells given, allowing visualisation of the fate and distribution of cells, but leaving the majority of cells for engraftment or other desired function. Alternatively, if the purpose of cell tracking was not therapeutic but, for example, to observe inflammatory cell tracking, a much higher dose of labelled cells could be administered to increase the sensitivity for detecting labelled cells in the target site. We have demonstrated that 1-5 × 10^9 SPIO-labelled autologous PBMC can be given safely: 100-fold greater than the dose needed for detection on MRI scanning.

It is acknowledged that whilst MRI can detect accumulation of SPIO-labelled cells at a target site, further quantification of cell number is currently challenging. This is because clustering of iron nanoparticles magnifies their magnetic effects, confounding attempts at quantification. However, novel positive imaging sequences may address this issue in the future. Furthermore, using this method of cell labelling it is not clear whether cells at the target site remain viable nor whether the SPIO remains intracellular. Further work is required to establish the duration of specificity of SPIO accumulation in tissues to indicate the continued presence of delivered cells at the target site. In the future, antibody or enzyme conjugated SPIO may yield additional information regarding cell viability and behaviour within tissues. It would also be important to define the time course of SPIO clearance from tissues if serial administration of cells was considered. Larger studies are needed to confirm the role of SPIO in cell tracking studies.

In conclusion, we have demonstrated the feasibility of imaging SPIO-labelled cells in humans at clinical MRI field strengths following local or systemic administration. This technology for *in vivo* cell tracking is widely applicable for monitoring cell therapy and a range of other applications including leucocyte trafficking.

CHAPTER 7

CONCLUSIONS AND FUTURE DIRECTIONS

7.1 BACKGROUND

Inflammation is central to the pathophysiology of cardiovascular disease. In atherosclerotic plaque, high macrophage density is a feature of vulnerability and correlates with risk of plaque rupture and clinical events [Naghavi *et al* 2003]. Similarly, in abdominal aortic aneurysm disease, hotspots of neovascularisation, inflammation and proteolytic activity are thought to represent regions of the aneurysm wall prone to further expansion and rupture [Thompson *et al* 1996; Vallabhaneni *et al* 2004; Choke *et al* 2006; Wilson *et al* 2006]. However, current cardiovascular imaging methods look only at plaque and aneurysm morphology and are unable to assess lesion vulnerability on the basis of inflammatory and other biological activity.

Cell-based therapies may have the potential to contribute to regeneration following injury, and stabilise or even regress cardiovascular disease. When evaluating their efficacy, it would be advantageous to be able to determine the proportion of cells reaching and remaining in the intended target therapeutic site. However this is not currently feasible in clinical studies due to lack of a suitable method.

Beyond the definition of anatomical structure that traditional imaging methods offer, novel cellular and molecular imaging techniques aim to allow the non-invasive assessment of biological activity within tissues. Superparamagnetic particles of iron oxide are part of a novel class of MRI contrast agents and are taken up by phagocytic cells including monocytes and macrophages [Corot *et al* 2007]. USPIO have been

used to distinguish stable from ruptured and rupture-prone atherosclerotic plaques and to demonstrate a reduction in macrophage activity in carotid plaques following the institution of statin therapy [Kooi *et al* 2003; Trivedi *et al* 2006; Tang *et al* 2009]. Uptake of USPIO in AAA has been reported as an incidental finding but has not been correlated with disease progression [Sadat *et al* 2011]. SPIO have been used to label cells for *in vivo* cell tracking studies. In pre-clinical studies, SPIO-labelled cells have been tracked to a target site following both local and systemic administration. In humans, whilst cell tracking has been demonstrated following local administration close to the target tissue, the ability to track cells following systemic administration would increase vastly the range of potential applications of this technique.

Using two distinct approaches, we have assessed the potential of SPIO to probe inflammatory activity in cardiovascular disease. Firstly we have investigated USPIO-enhanced MRI to assess inflammation and its relationship to disease progression in patients with AAA. Secondly we have developed a method of labelling cells with SPIO *ex vivo* for clinical cell tracking studies. To facilitate this work we first developed the necessary image acquisition and data analysis methodology.

7.2 SUMMARY OF THESIS FINDINGS

7.2.1 CHANGES IN T2* VALUE ON CLINICAL MRI SCANNING CAN BE USED TO DETECT FOCAL IRON ACCUMULATION IN TISSUES

Whilst SPIO are promising as smart contrast agents, image acquisition and data analysis presents a number of issues that require to be addressed if SPIO are to be used to their full potential for cardiovascular imaging. Data analysis for existing studies often involves the inspection of images for a reduction in signal intensity at the target site. Alternatively, ROI have been used to assess signal changes but this compromises spatial resolution. We aimed to address this issue by developing a robust, semi-quantitative method for detecting SPIO accumulation in tissues.

Using a multi gradient echo T2*W sequence we have assessed SPIO accumulation in tissues by looking at changes in T2* and R2* values, and applied this methodology for USPIO imaging of AAA and SPIO cell tracking in a variety of tissues. By applying a threshold based on repeatability data for calculation of the T2* value in vascular tissue, we have been able to distinguish USPIO accumulation from artefactual changes in T2* value. However, the differential magnetic effects of clustered *versus* homogeneously distributed SPIO makes accurate quantification of tissue iron concentration challenging. Development and availability of novel positive contrast imaging sequences will be required for fully quantitative assessment of SPIO accumulation in tissues.

With tissue-specific calibration, this methodology could be adapted for SPIO-MRI of a range of organs and tissues, and for a variety of applications.

7.2.2 USPIO-ENHANCED MRI CAN BE USED TO DETECT INFLAMMATION IN THE WALL OF ABDOMINAL AORTIC ANEURYSMS AND PREDICT ANEURYSM EXPANSION

AAA affects 5% of men over the age of 65 and causes up to 8,000 deaths annually in the United Kingdom [Ashton *et al* 2002]. The vast majority of these deaths occur as a result of aortic rupture, which has a mortality rate of 65-85%. Currently, maximum aneurysm diameter is used to assess risk of rupture, however, diameter is not the only determinant of rupture. Up to 20% of ruptured AAA have a diameter less than 5.5 cm, the threshold above which risk of rupture increases considerably and preventative intervention is considered [Darling *et al* 1977]. Furthermore, many patients have much larger aneurysms that are asymptomatic and appear stable. With the implementation of aneurysm screening, the number of patients under surveillance is likely to increase considerably and an improved method of rupture prediction is required to determine more accurately the patients requiring surgical or endovascular intervention [Ashton *et al* 2002].

In aneurysm disease, the aortic wall is affected by intense areas of biological activity including neovascularisation, inflammation and degradation of the extracellular matrix by MMP. These biological hotspots are thought to be regions of the aortic wall at risk of aneurysm expansion and rupture. We have shown that USPIO-enhanced MRI can detect aortic wall inflammation [Richards *et al* 2011]. This was corroborated by histological examination of aortic wall tissue samples taken from

patients undergoing open surgical repair of their AAA shortly after participating in the study. USPIO particles were found to collocate with macrophages; indeed on high power views the USPIO particles were identified within the macrophage cytoplasm.

Furthermore, USPIO uptake and inflammation in the aneurysm wall appeared to predict accelerated aneurysm expansion and USPIO-MRI is therefore a promising method of identifying patients with AAA at risk of further expansion and rupture. We intend to conduct a larger longitudinal study to confirm these findings. Assessment of biological activity within aortic aneurysms may also be useful for developing and monitoring the response to novel pharmacological interventions.

7.2.3 SPIO-LABELLING DOES NOT AFFECT VIABILITY OR FUNCTION OF PERIPHERAL BLOOD MONONUCLEAR CELLS

The success of cell-based therapies is contingent upon the delivery of an adequate number of cells to the target therapeutic site, however this is challenging to ascertain in human studies. For the further development and evaluation of cell-based therapies it would be advantageous to have a method of determining the proportion of infused cells reaching the target site and we have investigated cell tracking using SPIO-labelled cells.

A GMP compliant protocol was defined for clinical scale labelling of human mononuclear cells with SPIO for use in clinical cell tracking studies. The viability, cytokine release pattern and migratory capacity of the resulting SPIO-labelled cells

were similar to unlabelled cells. This was important so that the observed distribution of SPIO-labelled cells could be extrapolated to the behaviour of mononuclear cells *in vivo*. We also showed that SPIO-labelled cells could be visualised in *in vitro* agarose phantoms in a clinical MRI scanner. This preliminary work and method development established a basis for subsequent healthy volunteer cell tracking studies.

7.2.4 LOCAL AND SYSTEMIC ADMINISTRATION OF SPIO-LABELLED PERIPHERAL BLOOD MONONUCLEAR CELLS IN HUMANS IS SAFE

We have shown that both local and systemic administration of up to 10^9 SPIO-labelled cells in humans is safe. This is an important finding since the FDA has been hesitant to approve the administration of SPIO-labelled cells in humans due to lack of available safety data. This in turn has limited commercial interest in developing suitable agents for clinical cell tracking hampering further developments in this field. Establishing the safety of SPIO-labelled cells is therefore important to enable further research into the development of novel SPIO-based cell labelling agents and tracking methods. It is our hope that the accumulation of relevant safety data will allow clinical trials to proceed.

7.2.5 SPIO-LABELLED PBMC CAN BE TRACKED TO AN INFLAMMATORY FOCUS IN HUMANS FOLLOWING SYSTEMIC INTRAVENOUS ADMINISTRATION

We have shown that SPIO-labelled cells can be visualised at a target site in humans using a clinical MRI scanner following both local and systemic administration. Furthermore, we have shown that SPIO-labelled cells can be tracked to an experimental inflammatory focus in the skin of healthy human volunteers. Following

cell administration, changes in R2* value in the target site indicated cell accumulation in the inflamed skin and SPIO-labelled cells were also detected on histological examination of skin biopsies. No change in R2* value was observed in normal skin. Thus MRI detection of SPIO-labelled cells has sufficient sensitivity to enable clinical cell tracking and this is the first demonstration of successful magnetic resonance cell tracking in humans following systemic administration of cells. This technology has a broad range of potential clinical applications. As well as monitoring the success of cell-based therapies SPIO cell tracking may allow the investigation of inflammatory processes and activity through dynamic leucocyte trafficking. These findings also support the use of SPIO as reporters for novel cell tracking agents.

Having shown the feasibility of using SPIO-based cell tracking methods to determine the distribution of cells following infusion, it would be important to extend this technique to achieve specific labelling of a range of cell types further broadening the potential applications.

7.3 FUTURE DIRECTIONS

A number of questions and ideas have arisen as a result of the studies described within this thesis and we hope to address some of these issues with further studies.

7.3.1 USPIO-MRI TO ASSESS CLINICAL OUTCOMES FOR PATIENTS UNDER SURVEILLANCE FOR AAA

Ruptured AAA has an extremely high mortality and is the 13th leading cause of death

in the United Kingdom. In this preliminary study we have demonstrated that MRI with USPIO can detect aortic wall inflammation and appears to predict accelerated aneurysm expansion. Following on from these exciting pilot results, we intend to undertake a large, longitudinal study with the aim of establishing definitive proof of clinical efficacy and the size of effect of using USPIO uptake identified on MRI to predict disease progression in patients with AAA. This would include prediction not just of growth as a surrogate risk factor for rupture, but also of actual clinical events including rupture and requirement for surgical repair. In a prospective, observational, single-centre cohort study, we will recruit two hundred and twenty-eight patients with AAA (anteroposterior diameter >40 mm) from the clinical surveillance programme. At baseline, the AAA of each subject will be imaged with (i) an ultrasound scanner as part of standard clinical care, (ii) a 3T MRI scanner before and 24-36 hours after administration of 4.0 mg/kg of USPIO (ferumoxytol), and (iii) a 320-multidetector CT scanner with contrast enhancement. Thereafter, subjects will be followed-up every 6 months with clinical and ultrasound scanning as part of the clinical surveillance programme. At 2 years, a repeat CT scan will be performed to assess 3-dimensional growth of the aneurysm.

The primary research question of the study will be whether mural aortic uptake of USPIO predicts the composite endpoint of aneurysm rupture or need for elective surgical repair. Secondary endpoints will include aneurysm growth rate and clinical events including aneurysm rupture, aneurysm repair and aneurysm-related mortality. If successful we anticipate that USPIO-MRI could become a useful clinical tool of major benefit to patients under surveillance for AAA.

7.3.2 CORRELATION BETWEEN INFLAMMATORY ACTIVITY AND BIOMECHANICAL FORCES IN AAA

Evidence that regions of the aneurysm wall featuring intense biological activity are weakened and prone to further expansion and rupture is the basis of using USPIO-MRI to predict clinical disease progression. Biomechanical modelling can identify areas of the aortic wall exposed to particularly high tissue stresses and, when used in conjunction with USPIO-MRI, may improve further our ability to distinguish patients at increased risk of AAA expansion and rupture. Furthermore, biomechanical factors may be important in initiating and perpetuating inflammation in vascular tissue. Through collaboration with our medical physics colleagues we will use the CT and MRI 3D datasets collected as part of the longitudinal study described above to explore the relationship between biomechanical and biological factors in AAA pathophysiology, expansion and rupture.

7.3.3 CORRELATION BETWEEN USPIO-MRI AND PET-CT WITH FLUORODEOXYGLUCOSE (^{18}F-FDG) AND SODIUM FLUORIDE (^{18}F-NAF) FOR THE ASSESSMENT OF INFLAMMATORY ACTIVITY IN CARDIOVASCULAR DISEASE

Of the imaging modalities currently available, PET-CT with FDG is the best established for the assessment of inflammation in the cardiovascular system. FDG uptake has been shown to correlate with tissue macrophage density in carotid atherosclerotic plaque, and FDG uptake is greater in symptomatic atherosclerotic plaques [Davies *et al* 2007; Rudd *et al* 2007]. However, little is known of the correlation between USPIO uptake and FDG uptake. USPIO accumulation is reliant

upon macrophage phagocytosis, whilst FDG assesses cellular metabolic activity. A small study of two patients has shown similar uptake patterns for USPIO and FDG in carotid atherosclerotic plaque, suggesting that both modalities indicate similar disease processes [Tang *et al* 2008b]. We plan to extend this comparison by scanning patients with AAA. This will allow us to compare FDG and USPIO uptake in aneurysmal disease in the abdominal aorta, and by selecting an area of adjacent thoracic aorta we will be able to assess atherosclerotic disease in the same patients.

^{18}F-NaF is an alternative PET ligand that is incorporated into hydroxyapatite crystals in bone and has been used to detect areas of new bone formation and active calcification. Calcification is a feature of advanced atherosclerotic disease and 'spotty'calcification is recognised as an imaging marker for plaque vulnerability. Our group has recently shown the potential of ^{18}F-NaF for cardiovascular imaging. ^{18}F-NaF uptake correlated with disease severity in patients with aortic stensosis and a correlation was observed between coronary artery ^{18}F-NaF uptake and the Framingham cardiovascular risk score [Dweck *et al* 2012]. Interestingly, ^{18}F-NaF uptake occurred at the periphery of FDG-avid areas, suggesting that its uptake may indicate the early phase of inflammation. We propose to investigate ^{18}F-NaF uptake as a marker of inflammation and vulnerability in symptomatic carotid atherosclerotic disease as well as in AAA, and to assess its use for stratifying cardiovascular event risk in these patients.

7.3.4 USE OF USPIO-MRI TO ASSESS INFLAMMATORY ACTIVITY FOLLOWING MYOCARDIAL INFARCTION

Beyond aneurysm disease we have looked to apply the image acquisition and data analysis methodology developed for USPIO-MRI to assess inflammatory activity in other cardiovascular tissues and diseases. Following reperfusion of an infarct-related coronary artery, the myocardium subtended by it may recover rapidly or become apoptotic/necrotic. Recruitment of monocytes to the affected area is important for myocardial healing and remodelling, but excessive or disordered inflammatory activity may have deleterious effects.

We are currently using USPIO-MRI to assess inflammatory activity following myocardial infarction and primary coronary intervention and have generated some interesting preliminary results (Figure 7.1). If successful we hope to establish the relationship between the inflammatory response and infarct size, and to assess the effects of pharmacological intervention to limit myocardial inflammation using USPIO-MRI.

7.3.5 USE OF ANTIBODY-TARGETTED SUPERPARAMAGNETIC MICROBEADS FOR *IN VIVO* CELL TRACKING

Cell tracking has a wide range of potential clinical applications. Using SPIO and protamine sulphate we were able to label phagocytic cells for clinical cell tracking studies and successfully tracked intravenously delivered SPIO-labelled cells to an experimental inflammatory focus in healthy human volunteers. However, it would be attractive to be able to achieve specific labelling of a range of cell types including

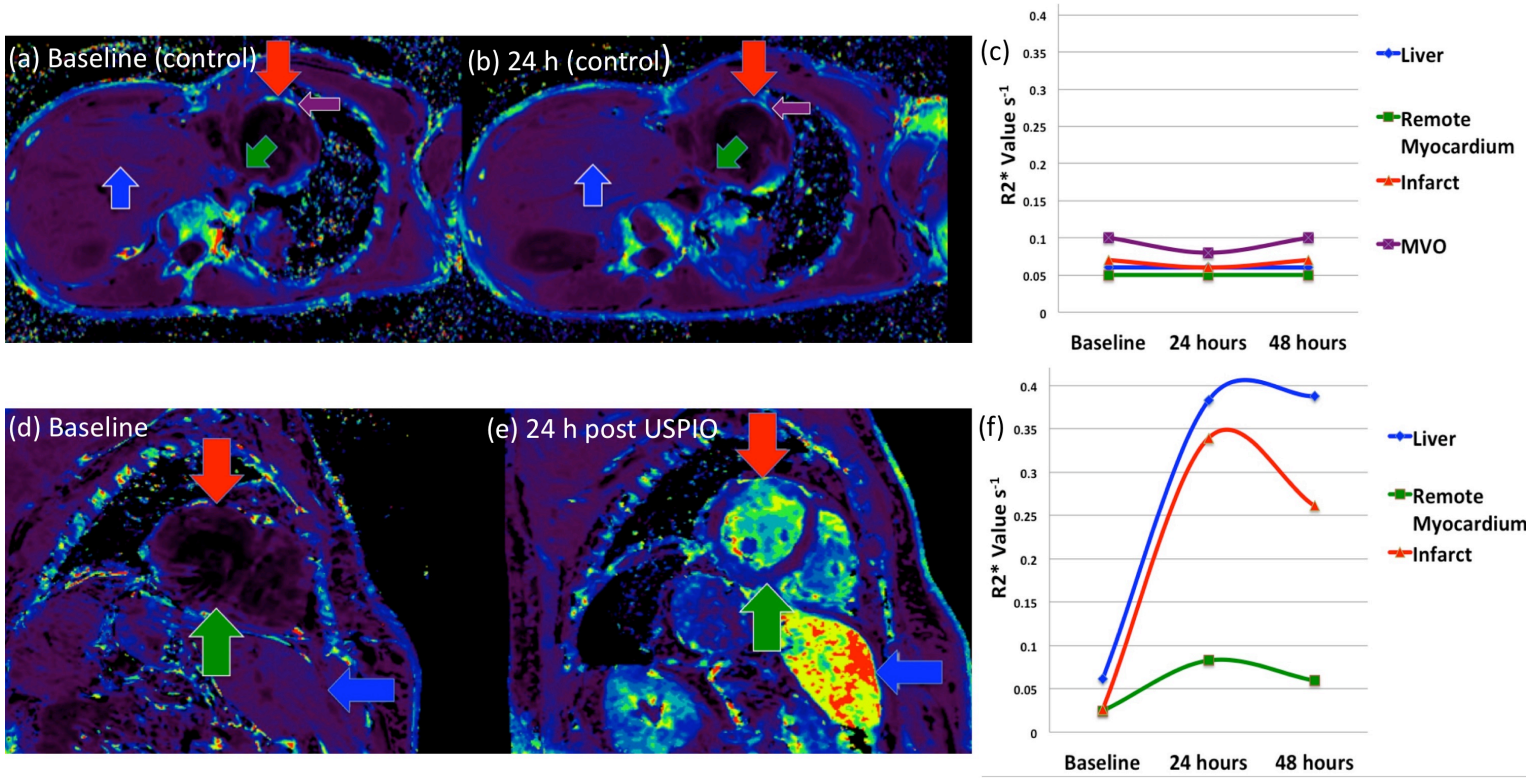

Figure 7.1 USPIO uptake in the myocardium following myocardial infarction and primary coronary revascularisation. Following myocardial infarction and primary coronary revascularisation, patients (n=10) underwent MRI scanning immediately before and 24 and 48 hours after administration of USPIO. A further group of patients (n=6) acted as controls and did not receive USPIO. Colour maps indicate the R2* value before and after USPIO administration. Regions of interest were drawn on the following areas indicated by coloured arrows: red=infarct; purple=microvascular obstruction (if present); green=myocardium remote from infarct; blue=liver. In control patients no difference in R2* value was observed in any of these areas at baseline **(a)** and at 24 hours **(b)**. This was confirmed on qualitative analysis **(c)**. In patients receiving USPIO, compared to baseline **(d)** the R2* value was increased in the infarcted myocardium **(e)** (from 0.041 ± 0.012 s^{-1} at baseline to 0.155 ± 0.045 s^{-1} ($p < 0.001$) and 0.124 ± 0.035 s^{-1} ($p < 0.05$) at 24 and 48 h respectively). As expected the R2* value was also increased in the liver following USPIO administration. Intriguingly, following USPIO administration, a small change in R2* value was observed in the myocardium remote from the infarct **(f)**.
USPIO - Ultrasmall superparamagnetic particles of iron oxide; MRI - Magnetic resonance imaging.

non-phagocytes. This would allow tracking of cells including stem cells, and in addition would allow investigation of specific aspects of cellular inflammatory activity *in vivo*.

There now exists the possibility to label cells using targeted antibody-coupled superparamagnetic iron dextrose microbeads (Miltenyi Biotech). These GMP grade microbeads have been developed and used extensively within the field of cell therapy for isolation of a variety of cell types. There are a number of potential advantages to labelling cells using microbeads rather than SPIO. The processing time is significantly reduced since the isolation and labelling steps are combined. To encourage uptake of SPIO into cells, a transfection agent must be used (e.g. protamine sulphate) which can lead to cell clumping. Furthermore, using antibody-targeted microbeads discrete cell populations can be labelled whereas Endorem is taken up non-specifically by any cell with phagocytic capacity. Finally non-phagocytic cells can readily be labelled using antibody-targeted microbeads.

When microbeads are used for immunomagnetic separation of different cell types, the aim is to achieve highly specific cell surface labelling with the minimum number of microbeads required to separate labelled from unlabelled cells in a magnetic separation column. We have modified this method to maximise cellular iron uptake by encouraging microbead phagocytosis, and in the first instance intend to use *in vitro* MRI phantoms to assess the potential for visualisation and translation into the clinical setting.

7.4 CLINICAL PERSPECTIVE

With strong evidence for a relationship between biological activity and cardiovascular events, the use of molecular imaging to assess pathophysiological processes is an enticing concept for improving risk stratification in patients with cardiovascular diseases. This in turn could enable individualised pharmacological therapy and risk factor control for high-risk individuals, which may be a more effective way to reduce the risk of cardiovascular events. There is also considerable interest in cellular and molecular imaging modalities from the pharmaceutical industry since these may provide intermediate measures for the assessment of efficacy of novel drugs and therapeutic targets.

In aneurysm disease, it would be beneficial to have an improved method of assessing risk of aneurysm rupture to facilitate decision-making regarding the necessity and urgency of surgical or endovascular intervention. If shown to predict aneurysm rupture, MRI scanning with USPIO could address this need for more accurate risk stratification. In particular there may be patients with AAA smaller than the current threshold of 5.5 cm who are identified as being at increased risk of rupture using USPIO-MRI but who would not currently be considered for intervention. Furthermore, patients with large AAA whose aneurysm appears to be stable with little inflammatory activity may be spared surgery and its associated risks. In patients with AAA presenting with abdominal pain and tenderness it can be difficult to distinguish whether the symptoms indicate an aneurysm at risk of imminent rupture or whether the symptoms are explained by an alternative pathology. USPIO-MRI

may be useful in this group of patients to determine whether urgent aneurysm surgery is required.

By assessing inflammatory activity in the aneurysm wall, MRI with USPIO may also be a useful way of assessing novel pharmacological agents in aneurysm disease both in terms of assessing their efficacy at the drug development stage, and to monitor and titrate dose on an individual patient basis.

Regenerative medicine and cell-based therapies may become important treatment options to limit and even reverse cardiovascular and other diseases. Currently, the results of clinical trials can be difficult to interpret because there is no method of establishing the proportion of cells retained in the target therapeutic site following infusion. We have shown that using MRI, SPIO-labelled cells can be tracked to an experimental inflammatory focus *in vivo* following systemic administration. In the field of cell therapy, SPIO cell labelling could enable the proportion of cells reaching the target site to be determined non-invasively following administration. This would be critical for the assessment of the success of such cell-based therapies.

In summary we have demonstrated the current use and future potential of SPIO in cardiovascular disease. USPIO allow correlation between biological activity and clinical disease progression in abdominal aortic aneurysm disease, and may become an invaluable clinical tool for the assessment of these patients. SPIO cell labelling enables clinical inflammatory cell tracking which has the potential to be a huge asset

as an investigative tool for assessing inflammatory activity *in vivo* and as a clinical tool to monitor the distribution of cells given as part of cell therapy.

REFERENCES

Abisi S, Burnand KG, Humphries J, Waltham M, Taylor P, Smith A. Effect of statins on proteolytic activity in the wall of abdominal aortic aneurysms. *Br J Surg* 2008;**95**(3):333-337.

Adam DJ, Mohan IV, Stuart WP, Bain M, Bradbury AW.. Community and hospital outcome from ruptured abdominal aortic aneurysm within the catchment area of a regional vascular surgical service. *J Vasc Surg* 1999;**30**(5):922-928.

Adolph R, Vorp DA, Steed DL, Webster MW, Kameneva MV, Watkins SC. Cellular content and permeability of intraluminal thrombus in abdominal aortic aneurysm. *J Vasc Surg* 1997;**25**(5):916-926.

Anderson LJ, Holden S, Davis B *et al*. Cardiovascular T2-star (T2*) magnetic resonance for the early diagnosis of myocardial iron overload. *Eur Heart J* 2001;**22**(23):2171-2179.

Anderson SA, Glod J, Arbab AS *et al*. Noninvasive MR imaging of magnetically labeled stem cells to directly identify neovasculature in a glioma model. *Blood* 2005;**105**(1):420-425.

Arbab AS, Jordan EK, Wilson LB, Yocum GT, Lewis BK, Frank JA. In vivo trafficking and targeted delivery of magnetically labeled stem cells. *Hum Gene Ther* 2004a;**5**(4):351-360.

Arbab AS, Yocum GT, Kalish H *et al*. Efficient magnetic cell labeling with protamine sulfate complexed to ferumoxides for cellular MRI. *Blood* 2004b;**104**(4):1217-1223.

Arbab AS, Yocum GT, Rad AM *et al*. Labeling of cells with ferumoxides-protamine sulfate complexes does not inhibit function or differentiation capacity of hematopoietic or mesenchymal stem cells. *NMR in Biomedicine* 2005;**18**(8):553-559.

Arbab AS, Pandit SD, Anderson SA *et al.* Magnetic resonance imaging and confocal microscopy studies of magnetically labeled endothelial progenitor cells trafficking to sites of tumor angiogenesis. *Stem Cells* 2006;**24**(3):671-678.

Ashton HA, Buxton MJ, Day NE *et al*. The Multicentre Aneurysm Screening Study (MASS) into the effect of abdominal aortic aneurysm screening on mortality in men: a randomised controlled trial. *Lancet* 2002;**360**(9345):1531-1539.

Au K-W, Liao S-Y, Lee Y-K *et al*. Effects of iron oxide nanoparticles on cardiac differentiation of embryonic stem cells. *Biochem Biophys Res Commun* 2009;**379**(4):898-903.

Bellin MF, Roy C, Kinkel K *et al.* Lymph node metastases: safety and effectiveness of MR imaging with ultrasmall superparamagnetic iron oxide particles- initial clinical experience. *Radiology* 1998;**207**(3):799-808.

Bernd H, De Kerviler E, Gaillard S, Bonnemain B. Safety and tolerability of ultrasmall superparamagnetic iron oxide contrast agent: comprehensive analysis of a clinical development program. *Invest Radiol* 2009;**44**(6):336-342.

Bjornheden T, Levin M, Evaldsson M, Wiklund O. Evidence of hypoxic areas within the arterial wall in vivo. *Arterioscler Thromb Vasc Biol* 1999;**19**(4):870-876.

Bland JM and Altman DG. Statistical methods for assessing agreement between two methods of clinical measurement. *Lancet* 1986;**1**(8476):307-310.

Boden WE, O'Rourke RA, Teo KK *et al*. Optimal Medical Therapy With or Without sPCI for Stable Coronary Disease *N Engl J Med* 2007;**356**:1503-1516.

Bonnemain BG. *Sinerem Investigator's Brochure*, France 2008.

Bourrinet P, Bengele HH, Bonnemain B *et al*. Preclinical safety and pharmacokinetic profile of ferumoxtran-10, an ultrasmall superparamagnetic iron oxide magnetic resonance contrast agent. *Invest Radiol* 2006;**41**(3):313-324.

Bowen CV, Zhang X, Saab G, Gareau PJ, Rutt BK. Application of the static dephasing regime theory to superparamagnetic iron-oxide loaded cells. *Magn Reson Med* 2002;**48**(1):52-61.

Bradbury AW, Makhdoomi KR, Adam DJ, Murie JA, Jenkins AM, Ruckley CV. Twelve-year experience of the management of ruptured abdominal aortic aneurysm. *Br J Surg* 1997;**84**(12):1705-1707.

Brady AR, Fowkes FG, Greenhalgh RM, Powell JT, Ruckley CV, Thompson SG. Risk factors for postoperative death following elective surgical repair of abdominal aortic aneurysm: results from the UK Small Aneurysm Trial. On behalf of the UK Small Aneurysm Trial participants. *Br J Surg* 2000;**87**(6):742-749.

Brady AR, Thompson SG, Fowkes FG, Greenhalgh RM, Powell JT. Abdominal aortic aneurysm expansion: risk factors and time intervals for surveillance. *Circulation* 2004;**110**(1):16-21.

Bremerich J, Bilecen D, Reimer P. MR angiography with blood pool contrast agents. *Eur Radiol* 2007;**17**(12):3017-3024.

Brown LC, Powell JT. Risk factors for aneurysm rupture in patients kept under ultrasound surveillance. UK Small Aneurysm Trial Participants. *Ann Surg* 1999;**230**(3):289-296; discussion 296-287.

Brown LC, Epstein D, Manca A, Beard JD, Powell JT, Greenhalgh RM. The UK Endovascular Aneurysm Repair (EVAR) trials: design, methodology and progress. *Eur J Vasc Endovasc Surg* 2004;**27**(4):372-381.

Brown LC, Thompson SG, Greenhalgh RM, Powell JT. Incidence of cardiovascular events and death after open or endovascular repair of abdominal aortic aneurysm in the randomized EVAR trial 1. *Br J Surg* 2011;**98**:935-942

Bruemmer D, Collins AR, Noh G *et al*. Angiotensin II-accelerated atherosclerosis and aneurysm formation is attenuated in osteopontin-deficient mice. *J Clin Invest* 2003;**112**(9):1318-1331.

Bulte JWM, Kraitchman DL, Mackay AM, Pittenger MF. Chondrogenic differentiation of mesenchymal stem cells is inhibited after magnetic labeling with ferumoxides. *Blood* 2004;**104**(10):3410-3412; author reply 3412-3413.

Cai J, Hatsukami TS, Ferguson MS *et al*. In vivo quantitative measurement of intact fibrous cap and lipid-rich necrotic core size in atherosclerotic carotid plaque: comparison of high-resolution, contrast-enhanced magnetic resonance imaging and histology. *Circulation* 2005;**112**(22):3437-3444.

Canet E, Revel D, Forrat R *et al*. Superparamagnetic iron oxide particles and positive enhancement for myocardial perfusion studies assessed by subsecond T1-weighted MRI. *Magn Reson Imaging* 1993;**11**(8):1139-1145.

Cao AH, Shi HJ, Zhang Y, Teng GJ. In vivo tracking of dual-labeled mesenchymal stem cells homing into the injured common carotid artery. *Anat Rec (Hoboken)* 2009;**292**(10):1677-1683.

Chang NK, Jeong YY, Park JS *et al.* Tracking of neural stem cells in rats with intracerebral hemorrhage by the use of 3T MRI. *Korean J Radiol* 2008;**9**(3):196-204.

Choke E, Cockerill G, Wilson WR *et al*. A review of biological factors implicated in abdominal aortic aneurysm rupture. *Eur J Vasc Endovasc Surg* 2005;**30**(3):227-244.

Choke E, Cockerill GW, Dawson J *et al*. Hypoxia at the site of abdominal aortic aneurysm rupture is not associated with increased lactate. *Ann N Y Acad Sci* 2006a;**1085**:306-310.

Choke E, Thompson MM, Dawson J *et al.* Abdominal aortic aneurysm rupture is associated with increased medial neovascularization and overexpression of proangiogenic cytokines. *Arterioscler Thromb Vasc Biol* 2006b;**26**(9):2077-2082.

Cohen M, Muja N, Fainstein N, Bulte J, Ben-Hur T. Conserved fate and function of ferumoxides-labeled neural precursor cells in vitro and in vivo. *J Neurosci Res* 2009;**88**:936-944 (2010).

Conrad MF, Crawford RS, Pedraza JD *et al*. Long-term durability of open abdominal aortic aneurysm repair. *J Vasc Surg* 2007;**46**(4):669-675.

Corot AC, Port M, Guilbert I *et al*. Superparamagnetic Contrast Agents. In: Modo MMJ and Bulte JWM, eds. Molecular and Cellular MR Imaging: CRC Press 2007: p60-78.

Corot C, Robert P, Idee JM, Port M. Recent advances in iron oxide nanocrystal technology for medical imaging. *Adv Drug Deliv Rev* 2006;**58**(14):1471-1504.

Coutard M, Touat Z, Houard X, Leclercq A, Michel JB. Thrombus versus wall biological activities in experimental aortic aneurysms. *J Vasc Res* 2010;**47**(4):355-366.

Curci JA, Mao D, Bohner DG *et al*. Preoperative treatment with doxycycline reduces aortic wall expression and activation of matrix metalloproteinases in patients with abdominal aortic aneurysms. *J Vasc Surg* 2000;**31**(2):325-342.

Curci JA, Petrinec D, Liao S, Golub LM, Thompson RW. Pharmacologic suppression of experimental abdominal aortic aneurysms: acomparison of doxycycline and four chemically modified tetracyclines. *J Vasc Surg* 1998;**28**(6):1082-1093.

Darling RC, Messina CR, Brewster DC, Ottinger LW. Autopsy study of unoperated abdominal aortic aneurysms. The case for early resection. *Circulation* 1977;**56**(3 Suppl):II161-164.

Davies JR, Izquierdo-Garcia D, Rudd JH *et al*. FDG-PET can distinguish inflamed from non-inflamed plaque in an animal model of atherosclerosis. *Int J Cardiovasc Imaging* 2010;**26**(1):41-48.

Dawson J, Cockerill G, Choke E, Loftus I, Thompson MM. Aortic aneurysms as a source of circulating interleukin-6. *Ann N Y Acad Sci* 2006;**1085**:320-323.

Dawson J, Cockerill GW, Choke E, Belli AM, Loftus I, Thompson MM. Aortic aneurysms secrete interleukin-6 into the circulation. *J Vasc Surg* 2007;**45**(2):350-356.

de Vries IJM, Lesterhuis WJ, Barentsz JO *et al*. Magnetic resonance tracking of dendritic cells in melanoma patients for monitoring of cellular therapy. *Nat Biotechnol* 2005;**23**(11):1407-1413.

DeLeo MJ, 3rd, Gounis MJ, Hong B, Ford JC, Wakhloo AK, Bogdanov AA, Jr. Carotid artery brain aneurysm model: in vivo molecular enzyme-specific MR imaging of active inflammation in a pilot study. *Radiology* 2009;**252**(3):696-703.

Deng GG, Martin-McNulty B, Sukovich DA *et al*. Urokinase-type plasminogen activator plays a critical role in angiotensin II-induced abdominal aortic aneurysm. *Circ Res* 2003;**92**(5):510-517.

Devereux RB, Roman MJ. Aortic disease in Marfan's syndrome. *N Engl J Med* 1999;**340**(17):1358-1359.

Di Martino ES, Bohra A, Vande Geest JP, Gupta N, Makaroun MS, Vorp DA. Biomechanical properties of ruptured versus electively repaired abdominal aortic aneurysm wall tissue. *J Vasc Surg* 2006;**43**(3):570-576; discussion 576.

Dousset V, Brochet B, Deloire MS *et al*. MR imaging of relapsing multiple sclerosis patients using ultra-small-particle iron oxide and compared with gadolinium. *AJNR Am J Neuroradiol* 2006;**27**(5):1000-1005.

Dubick MA, Hunter GC, Casey SM, Keen CL. Aortic ascorbic acid, trace elements, and superoxide dismutase activity in human aneurysmal and occlusive disease. *Proc Soc Exp Biol Med* 1987;**184**(2):138-143.

Dubick MA, Keen CL, DiSilvestro RA, Eskelson CD, Ireton J, Hunter GC. Antioxidant enzyme activity in human abdominal aortic aneurysmal and occlusive disease. *Proc Soc Exp Biol Med* 1999;**220**(1):39-45.

Dweck MR, Jones C, Joshi NV *et al*. Assessment of valvular calcification and inflammation by positron emission tomography in patients with aortic stenosis. *Circulation* 2012;**125**(1):76-86.

Edelstein WA, Bottomley PA, Pfeifer LM. A signal-to-noise calibration procedure for NMR imaging systems. *Med Phys* 1984;**11**(2):180-185.

Eibofner F, Steidle G, Kehlbach R, Bantleon R, Schick F. Positive contrast imaging of iron oxide nanoparticles with susceptibility-weighted imaging. *Magn Reson Med* 2010;**64**(4):1027-38.

Ejiri J, Inoue N, Tsukube T *et al*. Oxidative stress in the pathogenesis of thoracic aortic aneurysm: protective role of statin and angiotensin II type 1 receptor blocker. *Cardiovasc Res* 2003;**59**(4):988-996.

Eliason JL, Hannawa KK, Ailawadi G *et al*. Neutrophil depletion inhibits experimental abdominal aortic aneurysm formation. *Circulation* 2005;**112**(2):232-240.

Engstrom G, Borner G, Lindblad B, Janzon L, Lindgarde F. Incidence of fatal or repaired abdominal aortic aneurysm in relation to inflammation-sensitive plasma proteins. *Arterioscler Thromb Vasc Biol* 2004;**24**(2):337-341.

Erdozain OJ, Pegrum S, Winrow VR, Horrocks M, Stevens CR. Hypoxia in abdominal aortic aneurysm supports a role for HIF-1alpha and Ets-1 as drivers of matrix metalloproteinase upregulation in human aortic smooth muscle cells. *J Vasc Res* 2010;**48**(2):163-170.

Erentug V, Bozbuga N, Omeroglu SN *et al*. Rupture of abdominal aortic aneurysms in Behcet's disease. *Ann Vasc Surg* 2003;**17**(6):682-685.

Evans J, Powell JT, Schwalbe E, Loftus IM, Thompson MM. Simvastatin attenuates the activity of matrix metalloprotease-9 in aneurysmal aortic tissue. *Eur J Vasc Endovasc Surg* 2007;**34**(3):302-303.

EVAR Trial Participants. Endovascular aneurysm repair versus open repair in patients with abdominal aortic aneurysm (EVAR trial 1): randomised controlled trial. *Lancet* 2005;**65**(9478):2179-2186.

Farrell E, Wielopolski P, Pavljasevic P *et al*. Cell labelling with superparamagnetic iron oxide has no effect on chondrocyte behaviour. *Osteoarthr Cartil* 2009;**17**(7):958-964.

Fleige G, Seeberger F, Laux D *et al*. In vitro characterization of two different ultrasmall iron oxide particles for magnetic resonance cell tracking. *Invest Radiol* 2002;**37**(9):482-488.

Fleming C, Whitlock EP, Beil TL, Lederle FA. Screening for abdominal aortic aneurysm: a best-evidence systematic review for the U.S. Preventive Services Task Force. *Ann Intern Med* 2005;**142**(3):203-211.

Folkesson M, Silveira A, Eriksson P, Swedenborg J. Protease activity in the multi-layered intra-luminal thrombus of abdominal aortic aneurysms. *Atherosclerosis* 2011;**218**(2):294-299.

Forsdahl SH, Singh K, Solberg S, Jacobsen BK. Risk factors for abdominal aortic aneurysms: a 7-year prospective study: the Tromso Study, 1994-2001. *Circulation* 2009;**119**(16):2202-2208.

Freestone T, Turner RJ, Coady A, Higman DJ, Greenhalgh RM, Powell JT. Inflammation and matrix metalloproteinases in the enlarging abdominal aortic aneurysm. *Arterioscler Thromb Vasc Biol* 1995;**15**(8):1145-1151.

Fuchs S, Kornowski R, Weisz G *et al*. Safety and feasibility of transendocardial autologous bone marrow cell transplantation in patients with advanced heart disease. *Am J Cardiol* 2006;**97**(6):823-829.

Fujimoto S, Hartung D, Ohshima S *et al.* Molecular imaging of matrix metalloproteinase in atherosclerotic lesions: resolution with dietary modification and statin therapy. *J Am Coll Cardiol* 2008;**52**(23):1847-1857.

Gaglia JL, Guimaraes AR, Harisinghani M *et al*. Noninvasive imaging of pancreatic islet inflammation in type 1A diabetes patients. *J Clin Invest* 2011;**121**(1):442-445.

Gasser TC, Martufi G, Auer M, Folkesson M, Swedenborg J. Micromechanical characterization of intra-luminal thrombus tissue from abdominal aortic aneurysms. *Ann Biomed Eng* 2009;**38**(2):371-379.

Gavrila D, Li WG, McCormick ML *et al*. Vitamin E inhibits abdominal aortic aneurysm formation in angiotensin II-infused apolipoprotein E-deficient mice. *Arterioscler Thromb Vasc Biol* 2005;**25**(8):1671-1677.

General Register Office for Scotland Mortality Statistics 2008.

Geng YJ, Henderson LE, Levesque EB, Muszynski M, Libby P. Fas is expressed in human atherosclerotic intima and promotes apoptosis of cytokine-primed human vascular smooth muscle cells. *Arterioscler Thromb Vasc Biol* 1997;**17**(10):2200-2208.

Georgakarakos E, Ioannou CV, Volanis S, Papaharilaou Y, Ekaterinaris J, Katsamouris AN. The influence of intraluminal thrombus on abdominal aortic aneurysm wall stress. *Int Angiol* 2009;**28**(4):325-333.

Gillum RF. Epidemiology of aortic aneurysm in the United States. *J Clin Epidemiol* 1995;**48**(11):1289-1298.

Giusti B, Rossi L, Lapini I *et al*. Gene expression profiling of peripheral blood in patients with abdominal aortic aneurysm. *Eur J Vasc Endovasc Surg* 2009;**38**(1):104-112.

Golledge J, Clancy P, Jamrozik K, Norman PE. Obesity, adipokines, and abdominal aortic aneurysm: Health in Men study. *Circulation* 2007a;**116**(20):2275-2279.

Golledge J, Muller J, Shephard N *et al*. Association between osteopontin and human abdominal aortic aneurysm. *Arterioscler Thromb Vasc Biol* 2007b;**27**(3):655-660.

Golledge J, Tsao PS, Dalman RL, Norman PE.. Circulating markers of abdominal aortic aneurysm presence and progression. *Circulation* 2008;**118**(23):2382-2392.

Golledge J, Cullen B, Moran C, Rush C. Efficacy of simvastatin in reducing aortic dilatation in mouse models of abdominal aortic aneurysm. *Cardiovasc Drugs Ther* 2010;**24**(5-6):373-378.

Greenhalgh RM, Brown LC, Powell JT, Thompson SG, Epstein D, Sculpher MJ. Endovascular versus open repair of abdominal aortic aneurysm. *N Engl J Med* 2010;**362**(20):1863-1871.

Grootenboer N, Bosch JL, Hendriks JM, van Sambeek MR. Epidemiology, aetiology, risk of rupture and treatment of abdominal aortic aneurysms: does sex matter? *Eur J Vasc Endovasc Surg* 2009;**38**(3):278-284.

Grote K, Flach I, Luchtefeld M *et al.* Mechanical stretch enhances mRNA expression and proenzyme release of matrix metalloproteinase-2 (MMP-2) via NAD(P)H oxidase-derived reactive oxygen species. *Circ Res* 2003;**92**(11):e80-86.

Gyongyosi M, Blanco J, Marian T *et al*. Serial noninvasive in vivo positron emission tomographic tracking of percutaneously intramyocardially injected autologous porcine mesenchymal stem cells modified for transgene reporter gene expression. *Circ Cardiovasc Imaging* 2008;**1**(2):94-103.

Gyongyosi M, Lang I, Dettke M *et al*. Combined delivery approach of bone marrow mononuclear stem cells early and late after myocardial infarction: the MYSTAR prospective, randomized study. *Nat Clin Pract Cardiovasc Med* 2009;**6**(1):70-81.

Hackam DG, Thiruchelvam D, Redelmeier DA. Angiotensin-coverting enzyme inhibitors and aortic rupture: a population-based case-control study. *Lancet* 2006;**368**(9536):659-665.

Hallett JW, Jr., Marshall DM, Petterson TM *et al*. Graft-related complications after abdominal aortic aneurysm repair: reassurance from a 36-year population-based experience. *J Vasc Surg* 1997;**25**(2):277-284; discussion 285-276.

Hans SS, Jareunpoon O, Balasubramaniam M, Zelenock GB. Size and location of thrombus in intact and ruptured abdominal aortic aneurysms. *J Vasc Surg* 2005;**41**(4):584-588.

Harisinghani MG, Barentsz J, Hahn PF *et al*. Noninvasive detection of clinically occult lymph-node metastases in prostate cancer. *N Engl J Med* 2003;**348**(25):2491-2499.

Haug ES, Skomsvoll JF, Jacobsen G, Halvorsen TB, Saether OD, Myhre HO. Inflammatory aortic aneurysm is associated with increased incidence of autoimmune disease. *J Vasc Surg* 2003;**38**(3):492-497.

Hauger O, Delalande C, Deminiere C *et al*. Nephrotoxic nephritis and obstructive nephropathy: evaluation with MR imaging enhanced with ultrasmall superparamagnetic iron oxide-preliminary findings in a rat model. *Radiology* 2000;**217**(3):819-826.

Heart Protection Study Collaborative Group. MRC/BHF Heart Protection Study of cholesterol lowering with simvastatin in 20,536 high-risk individuals: a randomised placebo-controlled trial. *Lancet* 2002;**360**(9326):7-22.

Heart Protection Study Collaborative Group. Randomized trial of the effects of cholesterol-lowering with simvastatin on peripheral vascular and other major vascular outcomes in 20,536 people with peripheral arterial disease and other high-risk conditions. *J Vasc Surg* 2007;**45**(4):645-654; discussion 653-644.

Heesakkers RA, Hovels AM, Jager GJ *et al*. MRI with a lymph-node-specific contrast agent as an alternative to CT scan and lymph-node dissection in patients with prostate cancer: a prospective multicohort study. *Lancet Oncol* 2008;**9**(9):850-856.

Henderson EL, Geng YJ, Sukhova GK, Whittemore AD, Knox J, Libby P. Death of smooth muscle cells and expression of mediators of apoptosis by T lymphocytes in human abdominal aortic aneurysms. *Circulation* 1999;**99**(1):96-104.

Heyn C, Ronald JA, Mackenzie LT *et al*. In vivo magnetic resonance imaging of single cells in mouse brain with optical validation. *Magn Reson Med* 2006;**55**(1):23-29.

Hirsch AT, Haskal ZJ, Hertzer NR *et al*. ACC/AHA 2005 Practice Guidelines for the management of patients with peripheral arterial disease (lower extremity, renal, mesenteric, and abdominal aortic): a collaborative report from the American Association for Vascular Surgery/Society for Vascular Surgery, Society for Cardiovascular Angiography and Interventions, Society for Vascular Medicine and Biology, Society of Interventional Radiology, and the ACC/AHA Task Force on Practice Guidelines. *Circulation* 2006;**113**(11):e463-654.

Hishikawa K, Oemar BS, Yang Z, Luscher TF. Pulsatile stretch stimulates superoxide production and activates nuclear factor-kappa B in human coronary smooth muscle. Circ Res 1997;**81**(5):797-803.

Hobbs SD, Claridge MW, Quick CR, Day NE, Bradbury AW, Wilmink AB. LDL cholesterol is associated with small abdominal aortic aneurysms. *Eur J Vasc Endovasc Surg* 2003;**26**(6):618-622.

Houard X, Touat Z, Ollivier V *et al*. Mediators of neutrophil recruitment in human abdominal aortic aneurysms. *Cardiovasc Res* 2009;**82**(3):532-541.

Hu S, Zhang J, Hu X *et al*. In vitro labeling of human umbilical cord mesenchymal stem cells with superparamagnetic iron oxide nanoparticles. *J Cell Biochem* 2009;**108**(2):529-535.

Huang D-M, Hsiao J-K, Chen Y-C *et al*. The promotion of human mesenchymal stem cell proliferation by superparamagnetic iron oxide nanoparticles. *Biomaterials* 2009;**30**(22):3645-3651.

Hurks R, Hoefer IE, Vink A *et al*. Different effects of commonly prescribed statins on abdominal aortic aneurysm wall biology. *Eur J Vasc Endovasc Surg* 2010;**39**(5):569-576.

Jaffer FA, O'Donnell CJ, Larson MG *et al*. Age and sex distribution of subclinical aortic atherosclerosis: a magnetic resonance imaging examination of the Framingham Heart Study. *Arterioscler Thromb Vasc Biol* 2002;**22**(5):849-854.

Jander S, Schroeter M, Saleh A. Imaging inflammation in acute brain ischemia. *Stroke* 2007;**38**(2 Suppl):642-645.

Janic B, Iskander ASM, Rad AM, Soltanian-Zadeh H, Arbab AS. Effects of ferumoxides-protamine sulfate labeling on immunomodulatory characteristics of macrophage-like THP-1 cells. *PLoS ONE* 2008;**3**(6):e2499.

Jing XH, Yang L, Duan XJ *et al*. In vivo MR imaging tracking of magnetic iron oxide nanoparticle labeled, engineered, autologous bone marrow mesenchymal stem cells following intra-articular injection. *Joint Bone Spine* 2008;**75**(4):432-438.

Johansen K and Koepsell T. Familial tendency for abdominal aortic aneurysms. *J Am Med Assoc* 1986;**256**(14):1934-1936.

Johansson G and Swedenborg J. Ruptured abdominal aortic aneurysms: a study of incidence and mortality. *Br J Surg* 1986;**73**(2):101-103.

Ju S, Teng G, Zhang Y, Ma M, Chen F, Ni Y. In vitro labeling and MRI of mesenchymal stem cells from human umbilical cord blood. *Magn Reson Imaging* 2006;**24**(5):611-617.

Jung SI, Kim SH, Kim HC *et al*. In vivo MR imaging of magnetically labeled mesenchymal stem cells in a rat model of renal ischemia. *Korean J Radiol* 2009;**10**(3):277-284.

Juvonen J, Juvonen T, Laurila A *et al*. Demonstration of Chlamydia pneumoniae in the walls of abdominal aortic aneurysms. *J Vasc Surg* 1997a;**25**(3):499-505.

Juvonen J, Surcel HM, Satta J *et al*. Elevated circulating levels of inflammatory cytokines in patients with abdominal aortic aneurysm. *Arterioscler Thromb Vasc Biol* 1997b;**17**(11):2843-2847.

Kaim AH, Jundt G, Wischer T *et al.* Functional-morphologic MR imaging with ultrasmall superparamagnetic particles of iron oxide in acute and chronic soft-tissue infection: study in rats. *Radiology* 2003;**227**(1):169-174.

Kajimoto K, Miyauchi K, Kasai T *et al*. Short-term 20-mg atorvastatin therapy reduces key inflammatory factors including c-Jun N-terminal kinase and dendritic cells and matrix metalloproteinase expression in human abdominal aortic aneurysmal wall. *Atherosclerosis* 2009;**206**(2):505-511.

Kalyanasundaram A, Elmore JR, Manazer JR *et al*. Simvastatin suppresses experimental aortic aneurysm expansion. J *Vasc Surg* 2006;**43**(1):117-124.

Karlsson L, Bergqvist D, Lindback J, Parsson H. Expansion of small-diameter abdominal aortic aneurysms is not reflected by the release of inflammatory mediators IL-6, MMP-9 and CRP in plasma. *Eur J Vasc Endovasc Surg* 2009a;**37**(4):420-424.

Karlsson L, Gnarpe J, Bergqvist D, Lindback J, Parsson H. The effect of azithromycin and Chlamydophilia pneumonia infection on expansion of small abdominal aortic aneurysms - a prospective randomized double-blind trial. *J Vasc Surg* 2009b;**50**(1):23-29.

Karlsson L, Gnarpe J, Naas J *et al*. Detection of viable Chlamydia pneumoniae in abdominal aortic aneurysms. *Eur J Vasc Endovasc Surg* 2000;**19**(6):630-635.

Kazi M, Thyberg J, Religa P *et al*. Influence of intraluminal thrombus on structural and cellular composition of abdominal aortic aneurysm wall. *J Vasc Surg* 2003;**38**(6):1283-1292.

Kazi M, Zhu C, Roy J *et al*. Difference in matrix-degrading protease expression and activity between thrombus-free and thrombus-covered wall of abdominal aortic aneurysm. *Arterioscler Thromb Vasc Biol* 2005;**25**(7):1341-1346.

Kertai MD, Boersma E, Westerhout CM *et al.* A combination of statins and beta-blockers is independently associated with a reduction in the incidence of perioperative mortality and nonfatal myocardial infarction in patients undergoing abdominal aortic aneurysm surgery. *Eur J Vasc Endovasc Surg* 2004a;**28**(4):343-352.

Kertai MD, Boersma E, Westerhout CM *et al*. Association between long-term statin use and mortality after successful abdominal aortic aneurysm surgery. *Am J Med* 2004b;**116**(2):96-103.

Kerwin W, Hooker A, Spilker M *et al*. Quantitative magnetic resonance imaging analysis of neovasculature volume in carotid atherosclerotic plaque. *Circulation* 2003;**107**(6):851-856.

Kim U, Shin D, Park J *et al***.** Homing of adipose-derived stem cells to radiofrequency catheter ablated canine atrium and differentiation into cardiomyocyte-like cells. *Int J Cardiol* 2011;**146**(3):371-378.

King VL, Trivedi DB, Gitlin JM, Loftin CD. Selective cyclooxygenase-2 inhibition with celecoxib decreases angiotensin II-induced abdominal aortic aneurysm formation in mice. *Arterioscler Thromb Vasc Biol* 2006;**26**(5):1137-1143.

Kirk P, Roughton M, Porter JB *et al*. Cardiac T2* magnetic resonance for prediction of cardiac complications in thalassemia major. *Circulation* 2009;**120**(20):1961-1968.

Kniemeyer HW, Kessler T, Reber PU, Ris HB, Hakki H, Widmer MK. Treatment of ruptured abdominal aortic aneurysm, a permanent challenge or a waste of resources? Prediction of outcome using a multi-organ-dysfunction score. *Eur J Vasc Endovasc Surg* 2000;**19**(2):190-196.

Kontusaari S, Tromp G, Kuivaniemi H, Romanic AM, Prockop DJ. A mutation in the gene for type III procollagen (COL3A1) in a family with aortic aneurysms. *J Clin Invest* 1990;**86**(5):1465-1473.

Kooi ME, Cappendijk VC, Cleutjens KB *et al.* Accumulation of ultrasmall superparamagnetic particles of iron oxide in human atherosclerotic plaques can be detected by in vivo magnetic resonance imaging. *Circulation* 2003;**107**(19):2453-2458.

Kostura L, Kraitchman DL, Mackay AM, Pittenger MF, Bulte JWM. Feridex labeling of mesenchymal stem cells inhibits chondrogenesis but not adipogenesis or osteogenesis. *NMR in Biomedicine* 2004;**17**(7):513-517.

Kotze CW, Menezes LJ, Endozo R, Groves AM, Ell PJ, Yusuf SW. Increased metabolic activity in abdominal aortic aneurysm detected by 18F-fluorodeoxyglucose (18F-FDG) positron emission tomography/computed tomography (PET/CT). *Eur J Vasc Endovasc Surg* 2009;**38**(1):93-99.

Kotze CW, Groves AM, Menezes LJ *et al*. What is the relationship between (18)F-FDG aortic aneurysm uptake on PET/CT and future growth rate? *Eur J Nucl Med Mol Imaging* 2011;**38**(8)1493-1499.

Koval M, Preiter K, Adles C, Stahl PD, Steinberg TH. Size of IgG-opsonized particles determines macrophage response during internalization. *Exp Cell Res* 1998;**242**(1):265-273.

Kraitchman DL, Heldman AW, Atalar E *et al*. In vivo magnetic resonance imaging of mesenchymal stem cells in myocardial infarction. *Circulation* 2003;**107**(18):2290-2293.

Kraitchman DL, Tatsumi M, Gilson WD *et al*. Dynamic imaging of allogeneic mesenchymal stem cells trafficking to myocardial infarction. *Circulation* 2005;**112**(10):1451-1461.

Kramer CM, Cerilli LA, Hagspiel K, DiMaria JM, Epstein FH, Kern JA. Magnetic resonance imaging identifies the fibrous cap in atherosclerotic abdominal aortic aneurysm. *Circulation* 2004;**109**(8):1016-1021.

Kuhlpeter R, Dahnke H, Matuszewski L *et al.* R2 and R2* mapping for sensing cell-bound superparamagnetic nanoparticles: in vitro and murine in vivo testing. *Radiology* 2007;**245**(2):449-457.

Kumar V, Abbas AK, Fasto N, Mitchell R 2007. Robbins Basic Pathology 8th Edition.

Kurvers H, Veith FJ, Lipsitz EC *et al*. Discontinuous, staccato growth of abdominal aortic aneurysms. *J Am Coll Surg* 2004;**199**(5):709-715.

Lai CF, Seshadri V, Huang K *et al*. An osteopontin-NADPH oxidase signaling cascade promotes pro-matrix metalloproteinase 9 activation in aortic mesenchymal cells. *Circ Res* 2006;**98**(12):1479-1489.

Laitinen I, Saraste A, Weidl E *et al*. Evaluation of alphavbeta3 integrin-targeted positron emission tomography tracer 18F-galacto-RGD for imaging of vascular inflammation in atherosclerotic mice. *Circ Cardiovasc Imaging* 2009;**2**(4):331-338.

Laufer EM, Winkens MH, Narula J, Hofstra L. Molecular imaging of macrophage cell death for the assessment of plaque vulnerability. *Arterioscler Thromb Vasc Biol* 2009;**29**(7):1031-1038.

Laurent S, Forge D, Port M *et al*. Magnetic iron oxide nanoparticles: synthesis, stabilization, vectorization, physicochemical characterizations, and biological applications. *Chem Rev* 2008;**108**(6):2064-2110.

Laursen JB, Rajagopalan S, Galis Z, Tarpey M, Freeman BA, Harrison DG. Role of superoxide in angiotensin II-induced but not catecholamine-induced hypertension. *Circulation* 1997;**95**(3):588-593.

Lederle FA, Johnson GR, Wilson SE. Abdominal aortic aneurysm in women. *J Vasc Surg* 2001;**34**(1):122-126.

Lederle FA, Johnson GR, Wilson SE *et al*. Rupture rate of large abdominal aortic aneurysms in patients refusing or unfit for elective repair. *J Am Med Assoc* 2002a;**287**(22):2968-2972.

Lederle FA, Wilson SE, Johnson GR *et al*. Immediate repair compared with surveillance of small abdominal aortic aneurysms. *N Engl J Med* 2002b;**346**(19):1437-1444.

Lederle FA, Nelson DB, Joseph AM. Smokers' relative risk for aortic aneurysm compared with other smoking-related diseases: a systematic review. *J Vasc Surg* 2003;**38**(2):329-334.

Lederle FA, Freischlag JA, Kyriakides TC *et al*. Outcomes following endovascular vs open repair of abdominal aortic aneurysm: a randomized trial. *J Am Med Assoc* 2009;**302**(14):1535-1542.

Libby P. Molecular bases of the acute coronary syndromes. *Circulation* 1995;**91**(11):2844-2850.

Libby P. Inflammation in atherosclerosis. *Nature* 2002;**420**(6917):868-874.

Lindeman JH, Abdul-Hussien H, Schaapherder AF *et al*. Enhanced expression and activation of pro-inflammatory transcription factors distinguish aneurysmal from atherosclerotic aorta: IL-6- and IL-8-dominated inflammatory responses prevail in the human aneurysm. *Clin Sci (Lond)* 2008;**114**(11):687-697.

Lindeman JH, Abdul-Hussien H, van Bockel JH, Wolterbeek R, Kleemann R. Clinical trial of doxycycline for matrix metalloproteinase-9 inhibition in patients with an abdominal aneurysm: doxycycline selectively depletes aortic wall neutrophils and cytotoxic T cells. *Circulation* 2009;**119**(16):2209-2216.

Lindholt JS, Heegaard NH, Vammen S, Fasting H, Henneberg EW, Heickendorff L. Smoking, but not lipids, lipoprotein(a) and antibodies against oxidised LDL, is correlated to the expansion of abdominal aortic aneurysms. Eur *J Vasc Endovasc Surg* 2001;**21**(1):51-56.

Lindholt JS, Jorgensen B, Shi GP, Henneberg EW. Relationships between activators and inhibitors of plasminogen, and the progression of small abdominal aortic aneurysms. *Eur J Vasc Endovasc Surg* 2003;**25**(6):546-551.

Lindholt JS, Juul S, Fasting H, Henneberg EW. Preliminary ten year results from a randomised single centre mass screening trial for abdominal aortic aneurysm. *Eur J Vasc Endovasc Surg* 2006;**32**(6):608-614.

Lindholt JS and Shi GP. Chronic inflammation, immune response, and infection in abdominal aortic aneurysms. *Eur J Vasc Endovasc Surg* 2006;**31**(5):453-463.

Loebinger MR, Kyrtatos PG, Turmaine M *et al*. Magnetic resonance imaging of mesenchymal stem cells homing to pulmonary metastases using biocompatible magnetic nanoparticles. *Cancer Res* 2009;**69**(23):8862-8867.

Longo GM, Xiong W, Greiner TC, Zhao Y, Fiotti N, Baxter BT. Matrix metalloproteinases 2 and 9 work in concert to produce aortic aneurysms. *J Clin Invest* 2002;**110**(5):625-632.

Lum H and Roebuck KA. Oxidant stress and endothelial cell dysfunction. *Am J Physiol Cell Physiol* 2001;**280**(4):C719-741.

Lutz AM, Seemayer C, Corot C *et al*. Detection of synovial macrophages in an experimental rabbit model of antigen-induced arthritis: ultrasmall superparamagnetic iron oxide-enhanced MR imaging. *Radiology* 2004;**233**(1):149-157.

Mai X-L, Ma Z-L, Sun J-H, Ju S-H, Ma M, Teng G-J. Assessments of proliferation capacity and viability of New Zealand rabbit peripheral blood endothelial progenitor cells labeled with superparamagnetic particles. *Cell transplantation* 2009;**18**(2):171-181.

Mani V, Briley-Saebo KC, Itskovich VV, Samber DD, Fayad ZA. Gradient echo acquisition for superparamagnetic particles with positive contrast (GRASP): sequence characterization in membrane and glass superparamagnetic iron oxide phantoms at 1.5T and 3T. *Magn Reson Med* 2006;**55**(1):126-135.

Matsumura K, Hirano T, Takeda K *et al*. Incidence of aneurysms in Takayasu's arteritis. *Angiology* 1991;**42**(4):308-315.

Matusik P, Mazur P, Stepien E, Pfitzner R, Sadowski J, Undas A. Architecture of intraluminal thrombus removed from abdominal aortic aneurysm. *J Thromb Thrombolysis* 2010;**30**(1):7-9.

McCormick ML, Gavrila D, Weintraub NL. Role of oxidative stress in the pathogenesis of abdominal aortic aneurysms. *Arterioscler Thromb Vasc Biol* 2007;**27**(3):461-469.

Mehard WB, Heiken JP, Sicard GA. High-attenuating crescent in abdominal aortic aneurysm wall at CT: a sign of acute or impending rupture. *Radiology* 1994;**192**(2):359-362.

Meyers DG, Neuberger JS, He J. Cardiovascular effect of bans on smoking in public places: a systematic review and meta-analysis. *J Am Coll Cardiol* 2009;**54**(14):1249-1255.

Micheletta F, Natoli S, Misuraca M, Sbarigia E, Diczfalusy U, Iuliano L. Vitamin E supplementation in patients with carotid atherosclerosis: reversal of altered oxidative stress status in plasma but not in plaque. *Arterioscler Thromb Vasc Biol* 2004;**24**(1):136-140.

Miller AJ and Joseph PM. The use of power images to perform quantitative analysis on low SNR MR images. *Magn Reson Imaging* 1993;**11**(7):1051-1056.

Miller FJ, Jr., Sharp WJ, Fang X, Oberley LW, Oberley TD, Weintraub NL. Oxidative stress in human abdominal aortic aneurysms: a potential mediator of aneurysmal remodeling. *Arterioscler Thromb Vasc Biol* 2002;**22**(4):560-565.

Mofidi R, Goldie VJ, Kelman J, Dawson AR, Murie JA, Chalmers RT. Influence of sex on expansion rate of abdominal aortic aneurysms. *Br J Surg* 2007;**94**(3):310-314.

Moore A, Weissleder R, Bogdanov A, Jr. Uptake of dextran-coated monocrystalline iron oxides in tumor cells and macrophages. *J Magn Reson Imaging* 1997;**7**(6):1140-1145.

Morishige K, Kacher DF, Libby P *et al*. High-resolution magnetic resonance imaging enhanced with superparamagnetic nanoparticles measures macrophage burden in atherosclerosis. *Circulation* 2010;**122**(17):1707-1715.

Mosorin M, Juvonen J, Biancari F *et al*. Use of doxycycline to decrease the growth rate of abdominal aortic aneurysms: a randomized, double-blind, placebo-controlled pilot study. *J Vasc Surg* 2001;**34**(4):606-610.

Muller K, Skepper JN, Posfai M *et al*. Effect of ultrasmall superparamagnetic iron oxide nanoparticles (Ferumoxtran-10) on human monocyte-macrophages in vitro. *Biomaterials* 2007;**28**(9):1629-1642.

Muller K, Skepper JN, Tang TY *et al.* Atorvastatin and uptake of ultrasmall superparamagnetic iron oxide nanoparticles (Ferumoxtran-10) in human monocyte-macrophages: implications for magnetic resonance imaging. *Biomaterials* 2008;**29**(17):2656-2662.

Naghavi M, Libby P, Falk E *et al.* From vulnerable plaque to vulnerable patient: a call for new definitions and risk assessment strategies: Part I. *Circulation* 2003;**108**(14):1664-1672.

Nahrendorf M, Jaffer FA, Kelly KA *et al*. Noninvasive vascular cell adhesion molecule-1 imaging identifies inflammatory activation of cells in atherosclerosis. *Circulation* 2006;**114**(14):1504-1511.

Nchimi A, Defawe O, Brisbois D *et al*. MR imaging of iron phagocytosis in intraluminal thrombi of abdominal aortic aneurysms in humans. *Radiology* 2010;**254**(3):973-981.

Neri M, Maderna C, Cavazzin C *et al*. Efficient in vitro labeling of human neural precursor cells with superparamagnetic iron oxide particles: relevance for in vivo cell tracking. *Stem Cells* 2008;**26**(2):505-516.

Nicholls SC, Gardner JB, Meissner MH, Johansen HK. Rupture in small abdominal aortic aneurysms. *J Vasc Surg* 1998;**28**(5):884-888.

Office for National Statistics in England and Wales, Mortality Statistics 2008.

Paik D and Tilson MD. Neovascularization in the abdominal aortic aneurysm. Endothelial nitric oxide synthase, nitric oxide, and elastolysis. *Ann N Y Acad Sci* 1996;**800**:277.

Pawelczyk E, Arbab AS, Pandit S, Hu E, Frank JA. 2006. Expression of transferrin receptor and ferritin following ferumoxides-protamine sulfate labeling of cells: implications for cellular magnetic resonance imaging. *NMR in Biomedicine* 1996;**19**(5):581-592.

Perin EC, Dohmann HF, Borojevic R *et al*. Improved exercise capacity and ischemia 6 and 12 months after transendocardial injection of autologous bone marrow mononuclear cells for ischemic cardiomyopathy. *Circulation* 2004;**110**(11 Suppl 1):II213-218.

Polzer S, Gasser TC, Swedenborg J, Bursa J. The impact of intraluminal thrombus failure on the mechanical stress in the wall of abdominal aortic aneurysms. *Eur J Vasc Endovasc Surg* 2011;**41**(4):467-473.

Powell JT, Muller BR, Greenhalgh RM. Acute phase proteins in patients with abdominal aortic aneurysms. *J Cardiovasc Surg (Torino)* 1987;**28**(5):528-530.

Powell JT, Brown LC, Greenhalgh RM, Thompson SG. The rupture rate of large abdominal aortic aneurysms: is this modified by anatomical suitability for endovascular repair? *Ann Surg* 2008;**247**(1):173-179.

Prinssen M, Verhoeven EL, Buth J *et al*. A randomized trial comparing conventional and endovascular repair of abdominal aortic aneurysms. *N Engl J Med* 2004;**351**(16):1607-1618.

Propranolol Aneurysm Trial Investigators. Propranolol for small abdominal aortic aneurysms: results of a randomized trial. J Vasc Surg 2002;**35**(1):72-79.

Rad AM, Arbab AS, Iskander AS, Jiang Q, Soltanian-Zadeh H. Quantification of superparamagnetic iron oxide (SPIO)-labeled cells using MRI. *J Magn Reson Imaging* 2007;**26**(2):366-374.

Raghavan ML, Webster MW, Vorp DA. Ex vivo biomechanical behavior of abdominal aortic aneurysm: assessment using a new mathematical model. *Ann Biomed Eng* 1996;**24**(5):573-582.

Raghavan ML, Vorp DA, Federle MP, Makaroun MS, Webster MW. Wall stress distribution on three-dimensionally reconstructed models of human abdominal aortic aneurysm. *J Vasc Surg* 2000;**31**(4):760-769.

Rajagopalan S, Meng XP, Ramasamy S, Harrison DG, Galis ZS. Reactive oxygen species produced by macrophage-derived foam cells regulate the activity of vascular matrix metalloproteinases in vitro. Implications for atherosclerotic plaque stability. *J Clin Invest* 1996;**98**(11):2572-2579.

Rasmussen TE, Hallett JW, Jr., Schulte S, Harmsen WS, O'Fallon WM, Weyand CM. Genetic similarity in inflammatory and degenerative abdominal aortic aneurysms: a study of human leukocyte antigen class II disease risk genes. *J Vasc Surg* 2001;**34**(1):84-89.

Rasmussen TE, Hallett JW, Jr., Tazelaar HD *et al*. Human leukocyte antigen class II immune response genes, female gender, and cigarette smoking as risk and modulating factors in abdominal aortic aneurysms. *J Vasc Surg* 2002;**35**(5):988-993.

Reed D, Reed C, Stemmermann G, Hayashi T. Are aortic aneurysms caused by atherosclerosis? *Circulation* 1992;**85**(1):205-211.

Reeps C, Essler M, Pelisek J, Seidl S, Eckstein HH, Krause BJ. Increased 18F-fluorodeoxyglucose uptake in abdominal aortic aneurysms in positron emission/computed tomography is associated with inflammation, aortic wall instability, and acute symptoms. *J Vasc Surg* 2008;**48**(2):417-423; discussion 424.

Reeps C, Gee MW, Maier A *et al*. Glucose metabolism in the vessel wall correlates with mechanical instability and inflammatory changes in a patient with a growing aneurysm of the abdominal aorta. *Circ Cardiovasc Imaging* 2009a;**2**(6):507-509.

Reeps C, Pelisek J, Seidl S *et al*. Inflammatory infiltrates and neovessels are relevant sources of MMPs in abdominal aortic aneurysm wall. *Pathobiology* 2009b;**76**(5):243-252.

Richards JM, Semple SI, Macgillivray TJ *et al*. Abdominal aortic aneurysm growth predicted by uptake of ultrasmall superparamagnetic particles of iron oxide: a pilot study. *Circ Cardiovasc Imaging* 2011;**4**(3):274-281.

Robert P, Violas X, Santus R, Le Bihan D, Corot C. Optimization of a blood pool contrast agent injection protocol for MR angiography. *J Magn Reson Imaging* 2005;**21**(5):611-619.

Rogers WJ and Basu P. Factors regulating macrophage endocytosis of nanoparticles: implications for targeted magnetic resonance plaque imaging. *Atherosclerosis* 2005;**178**(1):67-73.

Rominger A, Saam T, Wolpers S *et al*. 18F-FDG PET/CT identifies patients at risk for future vascular events in an otherwise asymptomatic cohort with neoplastic disease. *J Nucl Med* 2009;**50**(10):1611-1620.

Roy J, Labruto F, Beckman MO, Danielson J, Johansson G, Swedenborg J. Bleeding into the intraluminal thrombus in abdominal aortic aneurysms is associated with rupture. *J Vasc Surg* 2008;**48**(5):1108-1113.

Rudd JH, Myers KS, Bansilal S *et al*. (18)Fluorodeoxyglucose positron emission tomography imaging of atherosclerotic plaque inflammation is highly reproducible: implications for atherosclerosis therapy trials. *J Am Coll Cardiol* 2007;**50**(9):892-896.

Rudd JH, Myers KS, Bansilal S *et al*. Relationships among regional arterial inflammation, calcification, risk factors, and biomarkers: a prospective fluorodeoxyglucose positron-emission tomography/computed tomography imaging study. *Circ Cardiovasc Imaging* 2009;**2**(2):107-115.

Ruehm SG, Corot C, Vogt P, Kolb S, Debatin JF. Magnetic resonance imaging of atherosclerotic plaque with ultrasmall superparamagnetic particles of iron oxide in hyperlipidemic rabbits. *Circulation* 2001;**103**(3):415-422.

Sadat U, Taviani V, Patterson AJ *et al*. Ultrasmall superparamagnetic iron oxide-enhanced magnetic resonance imaging of abdominal aortic aneurysms - a feasibility study. *Eur J Vasc Endovasc Surg* 2011;**41**(2):167-174.

Sadowski EA, Bennett LK, Chan MR *et al*. Nephrogenic systemic fibrosis: risk factors and incidence estimation. *Radiology* 2007;**243**(1):148-157.

Sakalihasan N, Pincemail J, Defraigne JO, Nusgens B, Lapiere C, Limet R. Decrease of plasma vitamin E (alpha-tocopherol) levels in patients with abdominal aortic aneurysm. *Ann N Y Acad Sci* 1996;**800**:278-282.

Sakthivel P, Shively V, Kakoulidou M, Pearce W, Lefvert AK. The soluble forms of CD28, CD86 and CTLA- constitute possible immunological markers in patients with abdominal aortic aneurysm. *J Intern Med* 2007;**261**(4):399-407.

Sandford RM, Bown MJ, London NJ, Sayers RD. The genetic basis of abdominal aortic aneurysms: a review. *Eur J Vasc Endovasc Surg* 2007**33**(4):381-390.

Santana MA and Rosenstein Y. What it takes to become an effector T cell: the process, the cells involved, and the mechanisms. *J Cell Physiol* 2003;**195**(3):392-401.

Satoh K, Nigro P, Matoba T *et al*. Cyclophilin A enhances vascular oxidative stress and the development of angiotensin II-induced aortic aneurysms. *Nat Med* 2009;**15**(6):649-656.

Schäfer R, Kehlbach R, Wiskirchen J *et al*. Transferrin receptor upregulation: in vitro labeling of rat mesenchymal stem cells with superparamagnetic iron oxide. *Radiology* 2007;**244**(2):514-523.

Schäfer R, Kehlbach R, Müller M *et al*. Labeling of human mesenchymal stromal cells with superparamagnetic iron oxide leads to a decrease in migration capacity and colony formation ability. *Cytotherapy* 2009;**11**(1):68-78.

Schermerhorn ML, O'Malley AJ, Jhaveri A, Cotterill P, Pomposelli F, Landon BE. Endovascular vs. open repair of abdominal aortic aneurysms in the Medicare population. *N Engl J Med* 2008;**358**(5):464-474.

Schonbeck U, Sukhova GK, Gerdes N, Libby P. T(H)2 predominant immune responses prevail in human abdominal aortic aneurysm. *Am J Pathol* 2002;**161**(2):499-506.

Schouten O, Kertai MD, Bax JJ *et al*. Safety of perioperative statin use in high-risk patients undergoing major vascular surgery. *Am J Cardiol* 2005;**95**(5):658-660.

Schouten O, van Laanen JH, Boersma E *et al.* Statins are associated with a reduced infrarenal abdominal aortic aneurysm growth. *Eur J Vasc Endovasc Surg* 2006;**32**(1):21-26.

Schweitzer M, Mitmaker B, Obrand D *et al*. Atorvastatin modulates matrix metalloproteinase expression, activity, and signaling in abdominal aortic aneurysms. *Vasc Endovascular Surg* 2010;**44**(2):116-122.

Screening for abdominal aortic aneurysm: recommendation statement. *Ann Intern Med* 2005;**142**(3):198-202.

Semelka RC, Helmberger TK. Contrast agents for MR imaging of the liver. *Radiology* 2001;**18**(1):27-38.

Seppenwoolde JH, Viergever MA, Bakker CJ. Passive tracking exploiting local signal conservation: the white marker phenomenon. *Magn Reson Med* 2003;**50**(4):784-790.

Shantikumar S, Ajjan R, Porter KE, Scott DJ. 2010 Diabetes and the abdominal aortic aneurysm. *Eur J Vasc Endovasc Surg* 2003;**39**(2):200-207.

Shapiro EM, Sharer K, Skrtic S, Koretsky AP. In vivo detection of single cells by MRI. *Magn Reson Med* 2006;**55**(2):242-249.

Sindrilaru A, Peters T, Wieschalka S *et al*. An unrestrained proinflammatory M1 macrophage population induced by iron impairs wound healing in humans and mice. *J Clin Invest* 2011;**121**(3):985-997.

Slaiby JM, Ricci MA, Gadowski GR, Hendley ED, Pilcher DB. Expansion of aortic aneurysms is reduced by propranolol in a hypertensive rat model. *J Vasc Surg* 1994;**20**(2):178-183.

Song M, Kim Y, Kim Y *et al.* MRI tracking of intravenously transplanted human neural stem cells in rat focal ischemia model. *Neurosci Res* 2009;**64**(2):235-239.

Speelman L, Schurink GW, Bosboom EM *et al*. The mechanical role of thrombus on the growth rate of an abdominal aortic aneurysm. *J Vasc Surg* 2010;**51**(1):19-26.

Stenbaek J, Kalin B, Swedenborg J. Growth of thrombus may be a better predictor of rupture than diameter in patients with abdominal aortic aneurysms. *Eur J Vasc Endovasc Surg* 2000;**20**(5):466-469.

Storey P, Thompson AA, Carqueville CL, Wood JC, de Freitas RA, Rigsby CK. R2* imaging of transfusional iron burden at 3T and comparison with 1.5T. *J Magn Reson Imaging* 2007;**25**(3):540-547.

Stuber M, Gilson WD, Schar M *et al.* Positive contrast visualization of iron oxide-labeled stem cells using inversion-recovery with ON-resonant water suppression (IRON). *Magn Reson Med* 2007;**58**(5):1072-1077.

Studholme C, Hawkes D, Hill D. A normalized entropy measure for multimodality image alignment. *Proc SPIE Medical Imaging* 1998;**3338**:132-143.

Sun J, Zhang J, Lindholt JS *et al*. Critical role of mast cell chymase in mouse abdominal aortic aneurysm formation. *Circulation* 2009;**120**(11):973-982.

Sun R, Dittrich J, Le-Huu M *et al*. Physical and biological characterization of superparamagnetic iron oxide- and ultrasmall superparamagnetic iron oxide-labeled cells: a comparison. *Invest Radiol* 2005;**40**(8):504-513.

Sweeting MJ, Thompson SG, Brown LC, Greenhalgh RM, Powell JT. Use of angiotensin converting enzyme inhibitors is associated with increased growth rate of abdominal aortic aneurysms. *J Vasc Surg* 2010;**52**(1):1-4.

Tamarina NA, McMillan WD, Shively VP, Pearce WH. Expression of matrix metalloproteinases and their inhibitors in aneurysms and normal aorta. *Surgery* 1997; **122**(2):264-271; discussion 271-262.

Tambyraja AL, Dawson R, Valenti D, Murie JA, Chalmers RT. Systemic inflammation and repair of abdominal aortic aneurysm. *World J Surg* 2007;**31**(6):1210-1214.

Tanaka S, Komori K, Okadome K, Sugimachi K, Mori R. Detection of active cytomegalovirus infection in inflammatory aortic aneurysms with RNA polymerase chain reaction. *J Vasc Surg* 1994;**20**(2):235-243.

Tang TY, Howarth SP, Li ZY *et al*. Correlation of carotid atheromatous plaque inflammation with biomechanical stress: utility of USPIO enhanced MR imaging and finite element analysis. *Atherosclerosis* 2008a;**196**(2):879-887.

Tang TY, Moustafa RR, Howarth SP *et al*. Combined PET-FDG and USPIO-enhanced MR imaging in patients with symptomatic moderate carotid artery stenosis. *Eur J Vasc Endovasc Surg* 2008b;**36**(1):53-55.

Tang TY, Howarth SP, Miller SR *et al*. The ATHEROMA (Atorvastatin Therapy: Effects on Reduction of Macrophage Activity) Study. Evaluation using ultrasmall superparamagnetic iron oxide-enhanced magnetic resonance imaging in carotid disease. *J Am Coll Cardiol* 2009;**3**(22):2039-2050.

Tanimoto A, Oshio K, Suematsu M, Pouliquen D, Stark DD. Relaxation effects of clustered particles. *J Magn Reson Imaging* 2001;**14**(1):72-77.

The Alpha-Tocopherol, Beta Carotene Cancer Prevention Study Group. The effect of vitamin E and beta carotene on the incidence of lung cancer and other cancers in male smokers. *N Engl J Med* 1994;**330**(15):1029-1035.

The UK Small Aneurysm Trial Participants. Mortality results for randomised controlled trial of early elective surgery or ultrasonographic surveillance for small abdominal aortic aneurysms. *Lancet* 1998;**352**(9141):1649-1655.

Thompson A, Cooper JA, Fabricius M, Humphries SE, Ashton HA, Hafez H. An analysis of drug modulation of abdominal aortic aneurysm growth through 25 years of surveillance. *J Vasc Surg* 2010a;**52**(1):55-61 e52.

Thompson AR, Cooper JA, Ashton HA, Hafez H. Growth rates of small abdominal aortic aneurysms correlate with clinical events. *Br J Surg* 2010b;**97**(1):37-44.

Thompson MM, Jones L, Nasim A, Sayers RD, Bell PR. Angiogenesis in abdominal aortic aneurysms. *Eur J Vasc Endovasc Surg* 1996;**11**(4):464-469.

Thompson RW, Holmes DR, Mertens RA *et al*. Production and localization of 92-kilodalton gelatinase in abdominal aortic aneurysms. An elastolytic metalloproteinase expressed by aneurysm-infiltrating macrophages. *J Clin Invest* 1995;**96**(1):318-326.

Thomsen HS. Nephrogenic systemic fibrosis: A serious late adverse reaction to gadodiamide. *Eur Radiol* 2006;**16**(12):2619-2621.

Torabi M, Aquino SL, Harisinghani MG. Current concepts in lymph node imaging. *J Nucl Med* 2004;**45**(9):1509-1518.

Tornwall ME, Virtamo J, Haukka JK, Albanes D, Huttunen JK. Alpha-tocopherol (vitamin E) and beta-carotene supplementation does not affect the risk for large abdominal aortic aneurysm in a controlled trial. *Atherosclerosis* 2001;**157**(1):167-173.

Toso C, Vallee J-P, Morel P *et al*. Clinical magnetic resonance imaging of pancreatic islet grafts after iron nanoparticle labeling. *Am J Transplant* 2008;**8**(3):701-706.

Touat Z, Ollivier V, Dai J *et al*. Renewal of mural thrombus releases plasma markers and is involved in aortic abdominal aneurysm evolution. *Am J Pathol* 2006;**168**(3):1022-1030.

Trivedi R, J UK-I, Gillard J. Accumulation of ultrasmall superparamagnetic particles of iron oxide in human atherosclerotic plaque. *Circulation* 2003;**108**(19):e140; author reply e140.

Trivedi RA, U-King-Im JM, Graves MJ *et al*. In vivo detection of macrophages in human carotid atheroma: temporal dependence of ultrasmall superparamagnetic particles of iron oxide-enhanced MRI. *Stroke* 2004;**35**(7):1631-1635.

Trivedi RA, Mallawarachi C, U-King-Im JM *et al*. Identifying inflamed carotid plaques using in vivo USPIO-enhanced MR imaging to label plaque macrophages. *Arterioscler Thromb Vasc Biol* 2006;**26**(7):1601-1606.

Tsuruda T, Kato J, Hatakeyama K *et al*. Adventitial mast cells contribute to pathogenesis in the progression of abdominal aortic aneurysm. *Circ Res* 2008;**102**(11):1368-1377.

Turner GH, Olzinski AR, Bernard RE *et al*. Assessment of macrophage infiltration in a murine model of abdominal aortic aneurysm. *J Magn Reson Imaging* 2009;**30**(2):455-460.

UK National Screening Committee. Essential elements in developing an abdominal aortic aneurysm (AAA) screening and surveillance programme Version 2.2. UK National Screening Committee: NHS abdominal aortic aneurysm screening programme 2010.

Vallabhaneni SR, Gilling-Smith GL, How TV, Carter SD, Brennan JA, Harris PL. Heterogeneity of tensile strength and matrix metalloproteinase activity in the wall of abdominal aortic aneurysms. *J Endovasc Ther* 2004;**11**(4):494-502.

Vega de Ceniga M, Gomez R, Estallo L, de la Fuente N, Viviens B, Barba A. Analysis of expansion patterns in 4-4.9 cm abdominal aortic aneurysms. *Ann Vasc Surg* 2008;**22**(1):37-44.

Vorp DA, Federspiel WJ, Webster MW. Does laminated intraluminal thrombus within abdominal aortic aneurysm cause anoxia of the aortic wall? *J Vasc Surg* 1996;**23**(3):540-541.

Vorp DA, Lee PC, Wang DH *et al*. Association of intraluminal thrombus in abdominal aortic aneurysm with local hypoxia and wall weakening. *J Vasc Surg* 2001;**34**(2):291-299.

Vukmanovic-Stejic M, Reed JR, Lacy KE, Rustin MH, Akbar AN. Mantoux Test as a model for a secondary immune response in humans. *Immunol Lett* 2006;**107**(2):93-101.

Wahlgren CM, Larsson E, Magnusson PK, Hultgren R, Swedenborg J. Genetic and environmental contributions to abdominal aortic aneurysm development in a twin population. *J Vasc Surg* 2010;**51**(1):3-7; discussion 7.

Walker DI, Bloor K, Williams G, Gillie I. Inflammatory aneurysms of the abdominal aorta. *Br J Surg* 1972;**59**(8):609-614.

Walker PM, Balmer C, Ablett S, Lerski RA. A test material for tissue characterisation and system calibration in MRI. *Phys Med Biol* 1989;**34**(1):5-22.

Wallinder J, Bergqvist D, Henriksson AE. Proinflammatory and anti-inflammatory cytokine balance in patients with abdominal aortic aneurysm and the impact of aneurysm size. *Vasc Endovascular Surg* 2009;**43**(3):258-261.

Wang DH, Makaroun M, Webster MW, Vorp DA. Mechanical properties and microstructure of intraluminal thrombus from abdominal aortic aneurysm. *J Biomech Eng* 2001;**123**(6):536-539.

Wang L, Deng J, Wang J *et al.* Superparamagnetic iron oxide does not affect the viability and function of adipose-derived stem cells, and superparamagnetic iron oxide-enhanced magnetic resonance imaging identifies viable cells. *Magn Reson Imaging* 2009;**27**(1):108-119.

Wasselius J, Larsson S, Sundin A, Jacobsson H. Assessment of inactive, active and mixed atherosclerotic plaques by 18F-FDG-PET; an age group-based correlation with cardiovascular risk factors. *Int J Cardiovasc Imaging* 2009;**25**(2):133-140.

Wilmink AB, Hubbard CS, Day NE *et al*. Effect of propranolol on the expansion of abdominal aortic aneurysms: a randomised study (abstract). *Br J Surg* 2000;**87**:499.

Wilson K, Whyman M, Hoskins P *et al*. The relationship between abdominal aortic aneurysm wall compliance, maximum diameter and growth rate. *Cardiovasc Surg* 1999;**7**(2):208-213.

Wilson KA, Hoskins PR, Lee AJ, Fowkes FG, Ruckley CV, Bradbury AW. Ultrasonic measurement of abdominal aortic aneurysm wall compliance: a reproducibility study. *J Vasc Surg* 2000;**31**(3):507-513.

Wilson KA, Lindholt JS, Hoskins PR, Heickendorff L, Vammen S, Bradbury AW. The relationship between abdominal aortic aneurysm distensibility and serum markers of elastin and collagen metabolism. *Eur J Vasc Endovasc Surg* 2001;**21**(2):175-178.

Wilson WR, Schwalbe EC, Jones JL, Bell PR, Thompson MM. Matrix metalloproteinase 8 (neutrophil collagenase) in the pathogenesis of abdominal aortic aneurysm. *Br J Surg* 2005;**92**(7):828-833.

Wilson WR, Anderton M, Schwalbe EC *et al*. Matrix metalloproteinase-8 and -9 are increased at the site of abdominal aortic aneurysm rupture. *Circulation* 2006;**113**(3):438-445.

Wolinsky H and Glagov S. Comparison of abdominal and thoracic aortic medial structure in mammals. Deviation of man from the usual pattern. *Circ Res* 1969;**25**(6):677-686.

Wollert KC, Meyer GP, Lotz J *et al*. Intracoronary autologous bone-marrow cell transfer after myocardial infarction: the BOOST randomised controlled clinical trial. *Lancet* 2004;**364**(9429):141-148.

Wood JC, Enriquez C, Ghugre N *et al*. MRI R2 and R2* mapping accurately estimates hepatic iron concentration in transfusion-dependent thalassemia and sickle cell disease patients. *Blood* 2005;**106**(4):1460-1465.

Wu YL, Ye Q, Sato K, Foley LM, Hitchens TK, Ho C. Noninvasive evaluation of cardiac allograft rejection by cellular and functional cardiac magnetic resonance. ***JACC*** *Cardiovasc Imaging* 2009;**2**(6):731-741.

Yoshimura K, Aoki H, Ikeda Y *et al*. Regression of abdominal aortic aneurysm by inhibition of c-Jun N-terminal kinase. *Nat Med* 2005;**11**(12):1330-1338.

Yousef M, Schannwell CM, Kostering M, Zeus T, Brehm M, Strauer BE. The BALANCE Study: clinical benefit and long-term outcome after intracoronary autologous bone marrow cell transplantation in patients with acute myocardial infarction. *J Am Coll Cardiol* 2009;**53**(24):2262-2269.

Zhang J, Schmidt J, Ryschich E, Mueller-Schilling M, Schumacher H, Allenberg JR. Inducible nitric oxide synthase is present in human abdominal aortic aneurysm and promotes oxidative vascular injury. *J Vasc Surg* 2003;**38**(2):360-367.

Zhang J, Nie L, Razavian M *et al*. Molecular imaging of activated matrix metalloproteinases in vascular remodeling. *Circulation* 2008;**118**(19):1953-1960.

Zhang Z, van den Bos EJ, Wielopolski PA *et al*. In vitro imaging of single living human umbilical vein endothelial cells with a clinical 3.0-T MRI scanner. ***MAGMA*** 2005;**18**(4):175-185.

Zhu J, Zhou L, XingWu F. Tracking neural stem cells in patients with brain trauma. *N Engl J Med* 2006;**355**(22):2376-2378.

APPENDIX 1

- TISS`UE SERVICES DIRECTORATE

STANDARD OPERATING PROCEDURE
ISSUE CONTROL SHEET

Document Details

Doc Number:	LIBS TSD 901 03	Number Of Pages	11
Supercedes:	TSD 901 02	Plus Appendices/ Worksheets:	4
Document Title:	Isolation of mononuclear cells from venesection blood collection, labelling cells with Supraparamagnetic Iron Oxide and preparation of the labelled cells for infusion.		
		Status(Final/ Training/ Draft))	FINAL
Initiating Dept.:	SE TISSUE BANK	**Written by**	**E.Forrest/A.Atkinson**

Document Authorisation/ Issue & Implementation

EFFECTIVE DATE: ISSUE DATE:

Document Issue Approved By: John Drain [Quality Manager]

Content Authorised By: Elaine Forrest [Departmental Manager]

Distribution Details

DEPARTMENT / SECTION	Copy No/Nos.	ISSUED BY	RECEIVED BY	DATE ISSUED
MASTERCOPY	M	John Drain		28th August 09
SE TISSUE BANK	1	John Drain		28th August 09
NSL (Anne Atkinson)	2	John Drain		28th August 09
CARDIOLOGY, RIE (Dr Richards	3	John Drain		28th August 09

Introduction

This document describes the procedure for isolation of Mononuclear Cells (MNC) from a venesection (whole) blood collection, labelling with Supraparamagnetic Iron Oxide (SPIO/Endorem) and preparation of the cells for infusion. All stages of the process to the point of final packaging of cells are performed aseptically within a Microbiological Safety Cabinet in the GMP Clean Room Facility (Grade A environment within a Grade B background). Clean Rooms 1 and 2 within the TS Laboratory area or the Stem Cell Development Clean Room within the TS Cellular Therapy Suite may be used for the process.

Changes from previous version:

Time for incubation of cells with Endorem on roller mixer reduced from 2 hours to 30 minutes, therefore all of procedure performed in single session in clean room. Amendments to SOP made accordingly.
Addition of option to issue 2ml aliquot of labelled cells for intramuscular injection where required.
Ficoll now poured into accuspin tubes.
Addition of method for cleaning sample racks, centrifuge and roller mixer.
Minor reformatting to improve clarity.

1. Health and Safety

Refer to the Departmental Health & Safety Manual for general health and safety policies and procedures.

2. Materials

2.1. Equipment

Lasair Particle Counter (if required)
Hettich Rotafix 32 Centrifuge & 4-place rotor
Roller mixer (Fisher Scientific MPR-465-010B)
Tube Sealer (Sebra: Model: Omni)
Bag Sealer (Astrapac: Model: SD 250)
Gilson Pipetting Aid
20μl /50-200μl /1,000μl Pipettes
Light Microscope and x10/x40 objectives
Improved Nebauer Haemocytometer & Coverslip
Staedler Fine Waterproof Marker
Sample Racks for Universal Containers and 225ml Containers
1 x Yellow Clinical Waste Bag
Calculator
Sterile 50ml Leucosep Containers (Greiner Bio-One Code:227290)

Sterile BD-Falcon 50ml Conical Tubes (Becton Dickinson Code: 352077)
Sterile BD-Falcon 225ml Conical Tubes (Becton Dickinson Code: 352075)
Sterile 3ml Pasteur Pipettes (VWR Code: 1612-1747)
Sterile 5ml Cellstar Serological Pipettes (Greiner Bio-One Code: 606180)
Sterile 25ml Cellstar Serological Pipettes (Greiner Bio-One Code: 760180)
Sterile 200μl Pipette Tips (Eppendorf Code: 154006)
Sterile 1ml Pipette Tips (Eppendorf Code: 323106)
Sterile Plasma Transfer Set (Baxter Code: VMC 2240)
Sterile 50ml Syringes (BD Code: 300866)
Sterile 2ml Syringes (BD Code: 300185)
Sterile Syringe Caps
Sterile Universal 13cm Filling Tube (Bunzl Healthcare Code: UN 888)
Sterile 500ml Cryocyte Freezing Containers (Baxter Code: R4R9955)
Sterile Origen O-Wraps (Quest Biomedical Code: 6ORW1430)
Sterile Scissors (In-House)
1.8ml Cryovials (Nunc Code: LW3434)
Sterile Drape (Molnlycke Healthcare Code: 700530)
Sterile Klercide 70/30 IPA Spray (Shield Medicare Code: 3035800)
Sterile Klerwipe 70% IPA Wipes –Sachet (Shield Medicare Code: 3036040)
Sterile Klerwipe 70% IPA Wipes – Pouch (Shield Medicare Code: 3035960)
Sterile Klerwipe Dry Wipe – Sachet (Shield Medicare Code: 3036060)
Sterile Klerwipe Biocide B Pouch Wipes (Shield Medicare Code: 3035900)
Sterile Microseal 3000 Polyester Wipes (Berkshire Code: 785000120S)
8 x 90mm TSA plates (Oxoid Code: PO0821B)
x 90mm SAB plates (Oxoid Code: PO 0410B)
x 55mm TSA + Lecithin + Tween Contact Plates (Oxoid Code: PO 0479D)
x Microbiology Sample Container Packs (Cherwell Code: 211987)
Venesection pack containing whole blood

2.2. Reagents

1 x 8ml ampoule Endorem (SPIO/Fe) (11.2mg/ml)(Guerbet:code 013873)[1]
1 x 5ml ampoule Protamine Sulphate 50mg in 5ml (10mg/ml) Wockhardt Code: FP3404 [2]
x 100ml Sterile Ficoll-Paque (GE Healthcare:code 17-5442-02)
1 x 1,000ml Sodium Chloride for Intravenous Infusion BP 0.9% w/w

Ordered and supplied by Cardiovascular Group
Ordered via NRIE Pharmacy

LIBS TSD 201:	Environmental Monitoring of the Clean Room Suite and Associated Areas
LIBS TSD 208:	Operation and Cleaning of Class II Microbiological Safety Cabinets
LIBS TSD 213:	Clothing procedure for entering the TS General Lab and Cleanroom Suite
LIBS TSD 217:	Introduction of Materials and Equipment into the General Laboratory and Clean Room and Disposal of Waste Materials
LIBS TSD 223:	Disposal of Clinical Waste
LIBS TSD 248:	Bacteriological Screening of Tissue Samples
LIBS TSD 307:	Operation of Sebra Tube Sealers
LIBS TSD 308:	Operation of Lasair Particle Counter
LIBS TSD 439:	Preparation of Cellular Therapy Product Labels
LIBS TSD 601:	Operation and Cleaning of Class II Microbiological Safety Cabinets in the Cellular Therapy Suite
LIBS TSD 603:	Clothing Procedure for Entering the Tissue Services Cellular Therapy Suite
LIBS TSD 604:	Introduction of Consumables, Reagents and Equipment into the Tissue Services Cellular Therapy Suite and Disposal of Waste Materials
LIBF TSD 602:	Venesection Collection: Isolation & SPIO Labelling of MNC: Clean Room Batch Record
LIBF TSD 603:	Venesection Collection: Isolation & SPIO Labelling of MNC: Cell Counts and Calculations

2.3. Documentation

Current versions of :

3. Staff

All staff undertaking this procedure must be appropriately trained and assessed.

4. Bacteriology Testing

Samples for bacteriology testing are taken into TSB & Thioglycollate broth from the following during the procedure:

Sample Type	Sample Size
Session 1:Venesection Sample	0.5ml
Session 1:Post Ficoll Supernatant	1ml
Session 1:Post Wash Supernatant	1ml
Session 2:Post Incubation Cell Suspension	1ml

4.1. Samples must be labelled with the donation number, date of sampling, sample type and processed as described in LIBS TSD 248.

4.2. A record of sterility samples taken throughout the procedure is made on LIBF TSD 602.

4.3. The Bacteriology Lab Book must be checked to ensure that all samples taken for sterility testing during the procedure are received by microbiology and logged correctly.

5. Preparation for Procedure in Clean Room

5.1. Prepare processing record with forms. Print blank labels for labelling final product.

5.2. If using the CTS Clean Room check that the clean room air pressure is within limits before entering the clean room. Record outcome on LIBF TSD 424.

5.3. If using TS Clean Room 1/2, check that clean room air pressures are within limits and that the Airnet Particle Monitoring system is operational before entering the clean room suite. Record outcome on LIBF TSD 602.

5.4. All reagents, materials & equipment are introduced to the transfer hatch as described in LIBS TSD 604/217.

6. Clean Room Procedure

6.1. Operator and assistant don cleanroom clothing as described in LIBS TSD 603/213 and enter the clean room.

6.2. Environmental monitoring for the procedure must be performed as described in LIBS TSD 201. Where require the Lasair Particle counter must be switched on as described in LIBS TSD 308.

6.3. Ensure the MSC is operating safely before proceeding. Record outcome on LIBF TSD 602. Clean the MSC as described in LIBS TSD 601/208. Record cleaning in appropriate cleaning record. Take Pre-Procedure contact plates from the MSC as described in LIBS TSD 201.

6.4. Ensure that the microscope is operating correctly before proceeding.

6.5. Clean the centrifuge, centrifuge buckets, inserts and lids with Sterile Klercide Biocide B wipes, leave for 5 minutes, then wipe all surfaces with Sterile IPA spray and dry with sterile dry wipes. Record cleaning in centrifuge cleaning record.

6.6. Clean the roller mixer with Sterile Klercide Biocide B wipes, leave for 5 minutes, then wipe all surfaces with Sterile IPA spray and dry with sterile dry wipes. Record cleaning in roller mixer cleaning record.

6.7. Clean the sample racks with Sterile Biocide B wipes, leave for 5 minutes, then wipe all surfaces with Sterile IPA spray and dry with sterile dry wipes.

6.8. Clean all pipettes with Sterile Klercide Biocide B wipes, leave for 5 minutes, then wipe all surfaces with Sterile IPA spray and dry with sterile dry wipes.

6.9. The assistant will unload the materials from the hatch, & pass the materials as required into the operator in the MSC as described in LIBS TSD 604/217. All consumable and reagent batch numbers must be recorded on LIBF TSD 602.

6.10. Check pack and product details before commencing:
Before proceeding, operator and assistant must check and confirm that:

Patient information, product details and donation number on pack label matches information on consent forms. Checks must be recorded on LIBF TSD 602.

6.11. Spray operator & assistant gloves with Sterile IPA before commencing procedure in MSC.

6.12. The assistant passes a sterile drape to the operator who prepares a sterile field in the MSC.

6.13. The assistant will then place environmental monitoring plates at the appropriate positions as described in LIBS TSD 201 and record the procedure start time on LIBF TSD 602.

6.14. **<u>Separate MNC from Whole Blood by Density Gradient Centrifugation using Ficoll.</u>**

6.14.1. **N.B All spikes and ports must be wiped with sterile alcohol wipes before connecting. All bottle/container necks must be wiped with sterile alcohol wipes before pouring.**

6.14.2. Pour approx. 18mls of ficoll-paque into the appropriate number of 50ml accuspin tubes. The number of accuspin tubes will depend on the volume of blood collected. The maximum amount of blood that can be processed is 280mls (8 x tubes @ 35mls/tube).

6.14.3. Place accuspin tubes in sample rack. Pass the accuspin tubes to the assistant**.**

6.14.4. Centrifuge the tubes for 30 secs @ 400g (2,000 r.p.m) to allow the ficoll to settle to the bottom of the tube. Wipe the accuspin tubes and rack with sterile alcohol wipes before transferring to operator.

6.14.5. Using a Pasteur pipette remove excess ficoll above the scinter and discard to waste.

6.14.6. Transfer blood from the venesection pack into a 225ml conical tube by cutting the tail of bag with sterile scissors and allowing the blood to pour into the tube.

6.14.7. Remove 1ml aliquot of venesection sample using a pasteur pipette for sterility testing as described in Section 5.0.

6.14.8. Carefully pour blood directly onto the scinter in the accuspin tubes. Distribute the blood evenly between the first 4 tubes, up to a maximum of 35mls of blood per tube.

6.14.9. Pass accuspin tubes to assistant. Centrifuge the accuspin tubes for 30 minutes @ 400g (2,000 r.p.m).

6.14.10. After 25 mins, repeat from 7.13.7 above for remaining tubes.

6.14.11. **The original pack must be retained to allow final product pack label checks.**

6.15. <u>Wash MNC x2 in Saline</u>.

6.15.1. Wipe the sample rack followed by the tubes with sterile alcohol wipes and return to the operator.

6.15.2. After centrifugation, the MNC form a distinct band at the sample/medium interface. Using a 25ml volumetric pipette, carefully remove supernatant to within 2cm of the mononuclear layer and discard the supernatant into a 225ml conical tube labelled **WASTE.**

6.15.3. Remove 2mls post ficoll supernatant using a pasteur pipette for sterility testing as described in Section 5.0.

6.15.4. Carefully remove the MNC layer at the interfaces, loosening any cells adhering to the walls of the tubes.

6.15.5. Distribute the MNC equally between 4 x 50ml universal containers.

6.15.6. Insert a plasma transfer set into the saline bag. Make up the volume in each tube to 50mls with saline. Replace the caps and invert the tubes three times. Pass MNC samples to assistant.

6.15.7. Centrifuge the MNC samples for 10 minutes @ 300g (1500 rpm). Wipe the sample rack followed by the tubes with sterile alcohol wipes and return to operator.

6.15.8. MNC will form a pellet at the base of the tube. Using a 25ml volumetric pipette initially, followed by a pastette carefully remove all supernatant from the cell pellet and discard the supernatant into the waste container.

6.15.9. Gently resuspend each of the pellets in 5-10mls of saline and pool the pellets into one 50ml tube. **Mix thoroughly and make up to an exact final volume of 30mls. N.B All volumes must be checked by the assistant.**

6.15.10. Remove 500µl of the cell suspension and place into a cryovial for cell counting. Label with date and donation number and prefix “Pre”.

6.15.11. Repeat wash procedure from 7.14.6 x1.

6.16. <u>Perform a Manual White Cell Count</u>

6.16.1. Perform a white cell count as described in Appendix 1.

6.16.2. All cell counts and calculations must be performed independently by the operator and assistant. Record calculations and results on LIBF TSD 603.

6.17. Calculate the Volume of Saline, Endorem and Protamine Sulphate to add to the Cells.

Note: The final volume of Endorem infused must not exceed 0.075mls/kg of recipient body weight and the final volume of cells infused must not exceed 500mls. If required, the volume of cells labelled initially must be adjusted to achieve this.

6.17.1. Saline is added to the cell suspension to achieve a final cell concentration of 4 x 10^6 cells/ml.

Example: If the total cell count is 200 x 10^6, then the total volume of saline required to be added to the cell pellet to achieve a final cell concentration of 4x10^6/ml will be:

$\frac{200 \times 10^6}{} = 50$ mls saline x10^6

6.17.2. Endorem is added to the cell suspension to give a final concentration of Fe: 100ug/ml. Endorem contains 11.2mg Fe/ml therefore 8.9µl of Endorem solution will contain 100µg Fe.

Example: For 50 mls of cell suspension at a concentration of 4 x 10^6/ml, 445µl (50 x 8.9µl) of Endorem is added. Ensure that the volume of endorem is within the limit of 0.075mls/kg of recipient body weight. (The recipient's current weight will be recorded on LIBF TSD 210)

Example: For a 60kg donor, the maximum amount of Endorem for infusion will be 60 x 0.075mls = 4.5mls.

Protamine Sulphate is added to the cell suspension to give a final concentration of Protamine: 4µg/ml. Protamine Sulphate contains 10mg Protamine/ml therefore 0.4µl of Protamine Sulphate will contain 4µg of Protamine.

Example: For 50 mls of cell suspension 20µl (50x0.4) of Protamine Sulphate is added.

6.17.3. Record calculations and results on LIBF TSD 603. All calculations must be performed independently by the operator and assistant.

6.18. Add Saline, Endorem and Protamine Sulphate to Cells

6.18.1. Spray operator & assistant gloves with Sterile IPA before continuing procedure in MSC.

6.18.2. Clean the roller mixer with sterile alcohol wipes and transfer into the MSC.

6.18.3. Wipe the sample rack followed by the tube with sterile alcohol wipes and return to the operator.

6.18.4. Remove 2mls post wash supernatant using a pasteur pipette for sterility testing as described in Section 5.0.

6.18.5. Remove all of the remaining supernatant from the cell pellet and discard the supernatant into the waste container.

6.18.6. Using a 25ml pipette, resuspend the pellet **initially** in **30mls** of saline and transfer suspension into a 225ml conical tube. Add required additional volume of saline to achieve final cell concentration of **4 x 10^6 cells/ml.** Mix the cell suspension.

6.18.7. Using a pipette, add the correct volume of Endorem directly to the cell suspension.

6.18.8. Using a pipette, add the correct volume of Protamine Sulphate directly to the cell suspension. Mix.

6.18.9. Record the final volume of suspension (including endorem and protamine) to the nearest ml on LIBF TSD 603.

6.18.10. **Place the tube immediately on the roller mixer. The cells are mixed at ambient room temperature for 30 minutes. Note the incubation start/finish time on LIBF TSD 602.**

6.19. **Perform a Manual White Cell Count**

Spray operator & assistant gloves with Sterile IPA before continuing procedure in MSC.

6.19.1. Using a pipette remove 500µl of the cell suspension and place into a cryovial for cell counting. Label with date and donation number and prefix “Post”.

6.19.2. Perform a white cell count as described in Appendix 1.

6.19.3. Operator and assistant must perform all cell counts and calculations independently. Record the results on LIBF TSD 603.

6.20. **Prepare Pack/Syringe labels with Patient and Product Details.**

6.20.1. All pack/syringe labels must be checked for accuracy independently by the operator and assistant against the original venesection pack label and the cell dose calculations on LIBF TSD 603.

6.21. **Package Cells for Infusion**

6.21.1. Spray operator & assistant gloves with Sterile IPA before continuing procedure in MSC.

6.21.2. The entire volume of cells remaining post incubation will be infused, but **must not exceed 500mls**. The cells are transferred into the required number of 500ml cryocyte containers depending on the final volume. If required a 2ml aliquot of labelled cells is prepared for intramuscular injection.

6.21.3. Remove 1ml post incubation cell suspension using a pasteur pipette for sterility testing as described in Section 5.0.

6.21.4. Remove 2ml aliquot of cell suspension (if required), cap with syringe cap. Pass to assistant.

6.21.5. Visually check the integrity of the cryocyte container and port and tubing closures. Do not use container if port and/or tubing closures are not in place or if the integrity of the container is compromised.

6.21.6. Close the roller clamps on 1 x male and 1 x female luer lines on each of the containers, leaving 1 x female line open to access the container. The roller clamps should be positioned on the line as near to the container as possible.

6.21.7. Using a sterile filling tube attached to a 50ml syringe, withdraw all remaining cell suspension and introduce the suspension into the cryocyte bag via the luer line.

6.21.8. Carefully remove excess air from the cryocyte container by applying gentle pressure to the pack until all the air in the container has been expelled and close the roller clamp on the line.

6.21.9. Clean the jaws and lever assembly of the Sebra Heat Sealer using a sterile alcohol wipe. Pass to the operator. Refer to LIBS TSD 307 for operating instructions for the Sebra Heat Sealer.

6.21.10. Dry the line and jaws of the sealer using a sterile lint free wipe. Ensure there is no fluid in the line (tap gently to return fluid to container if required).

6.21.11. Seal the line to the cryocyte container as close as possible to the container, ensuring that the seal is parallel to the plane of the container and centred on the tubing.

6.21.12. Make a 2nd seal 0.5cm above the 1st seal, but not above the height of the yellow D-rings.

6.21.13. Cut the middle of the 2nd seal using sterile blunt-ended scissors and discard the excess line. Do not pull the line ends to separate. This could cause a small hole in the seal compromising the sterility and integrity of the contents.

6.21.14. Check the integrity of the seals both visually and by inverting the container and applying gentle pressure. If there is any evidence of leakage, the contents of the container must be transferred to a fresh cryocyte container and resealed.

6.21.15. Pass the container to the assistant.

6.21.16. The sterile procedure is now complete. Operator and assistant must take finger plates as described in LIBS TSD 201.

6.22. <u>Label and Package Containers/Syringe</u>.

6.22.1. Place the correct identification label in the label pocket of the cryocyte bag. Operator and assistant must confirm contents of

label are accurate. Seal the label pocket x3 with the Sebra Tube Sealer.

6.22.2. Place the bag in an O-wrap outer bag and seal x1 using the bag sealer.

6.22.3. Wrap an identification label around the syringe and place the syringe in a 225ml conical tube. Label the outside of the conical tube with an identification label.

6.22.4. Place labelled containers/syringe in CR or Product Dispatch hatch.

6.23. The MSC must be cleaned as described in LIBS TSD 601/208 and “Post Clean “ contact plates taken.

6.24. The centrifuge, roller mixer, sample racks and pipettes must be cleaned post procedure as described in 7.5 -7.8.

6.25. All waste must be handled as described in LIBS TSD 604/223 and returned to the hatch for disposal.

6.26. Ensure all documentation is complete and signed by the operator/assistant before leaving the clean room.

6.27. Medical release and issue of the cells for infusion is described in LIBS TSD.

Appendix 1

Procedure for Manual White Cell Counting using the Improved Nebauer Counting Chamber

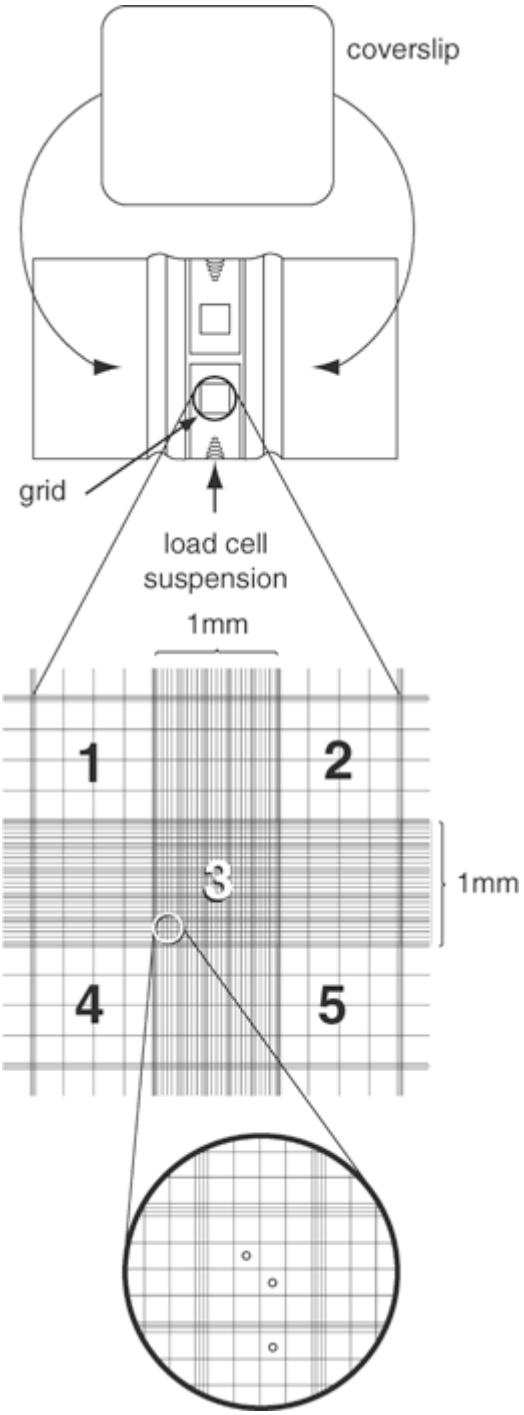

- Ensure that both the haemocytometer and coverslip are clean by wiping over with sterile alcohol wipe. Breathe on to the surface of the haemocytometer and quickly place the coverslip in position so that it is centred over the counting chamber.
- Gently, but firmly press down the coverslip, using a thumb placed either side, holding the haemocytometer firmly between both hands, until Newton's rings (refraction rings of light of a rainbow/oil slick colouration) are seen.
- Take up a 20µl of the cell suspension into the tip of a 100µl Gilson. Gently touch the tip against the side of the coverslip where it touches the base of the depression. Press down the plunger of the Gilson and a drop of the suspension will be drawn out of the pipette into the chamber and will fill one of the chambers.
- Ensure that the counting chamber is filled with a single action and that no fluid
  flows into the surrounding depression.
- It is important to carry out the following steps as quickly as possible to ensure that the chamber does not dry out:
- Place the haemocytometer under the microscope. Turn the microscope on and under low power (x5/x10) focus on the grid area of the counting chamber.
- The grid area can be seen to be formed of 9 large squares in a 3x3 grid. Each of these squares covers an area of $1mm^2$, which, with the depth of the chamber being 0.1mm, means that the volume of each large square is $0.1mm^3$.
- The central area of the grid (**3**) is made up of triple ruled lines that in the centre form a 5x5 grid of 25 squares with a total volume of $0.1mm^3$. Each of these 25 squares have an area of $0.04mm^2$ and a volume of $0.004mm^3$.
- Turn to the x40 objective and count the four corner and one central $0.04mm^2$ squares. Cells falling on the bordering triple lines should only be counted if they are on either the top or the left lines only. Exclude those touching the bottom and the right hand side lines.
- The most accurate count is achieved when 120-200 cells are counted. If there are more cells than this the suspension should be further diluted and counted again, noting the dilution factor in the calculation.
- If there are fewer cells turn the objective to x10 and count all 25 squares in the central grid.
- Count the cells and make a note of the count on LIBF TSD 603.
- The counts will be performed by two individuals and the mean of the two counts taken for calculation of cell concentration.

- **Calculate the number of cells using the following calculation:**

If you have counted 5 of the 25 squares in the central triple ruled grid the calculation will be as follows:

- The central triple ruled grid has a volume of 0.1mm^3. You have counted 5 squares, so to convert to the number of cells in 0.1mm^3, divide by 5 then multiply by 25.
- To convert from cells/ 0.1mm^3 to cells/ml, multiply by 10,000 and then by the dilution factor (if applicable).

$$\text{No of Cells/ml} = \frac{\text{Cell Count}}{5} \times 25 \times 10{,}000 \times \text{Dilution Factor}$$

If you have counted all 25 squares (0.1mm^3) in the central grid, to allow for a low density cell population the calculation will be:

- The central triple ruled grid has a volume of 0.1mm^3. To convert from cells/ 0.1mm^3 to cells/ml, multiply by 10,000 and then by the dilution factor (if applicable).

No of Cells /ml = Cell Count x 10,000 x Dilution Factor

Departmental Manager must consider staff training and re-training requirements associated with the introduction of this SOP; and initial as appropriate the statements below for its application within their department:

☐ **Training required for all staff in the department carrying out procedure.**

☐ **Familiarisation with SOP content required for staff trained and competent in the procedure.**

☐ **SOP held by dept. for information purposes only, staff signatures not required.**

Staff Names	Staff Signature	Date

APPENDIX 2

1.1 MAGNETIC RESONANCE IMAGING

1.1.1 ATOMIC STRUCTURE

Atoms are made up of a central cluster of nucleons in the nucleus surrounded by a cloud of orbiting, spinning electrons. The mass of an atom is concentrated in the nucleus which consists of particles called nucleons: protons which are positively charged and neutrons which have no charge. The mass number of an atom is the sum of the number of protons and neutrons. To maintain overall electrical neutrality, the number of electrons must be equal to the number of protons. The mass of an electron is negligible when compared to that of the nucleus.

1.1.2 MAGNETIC NUCLEI

Protons and neutrons spin about their own axis and have a paired nucleon which spins in the opposite direction. In most atoms, protons and neutrons are present in equal number so overall the spins of pairs of particles cancel each other out. Therefore, when considered as a whole, the nucleus has no net spin. In some atoms, however, the number of neutrons is one more or one fewer than the number of protons. In this situation the spin of one of the nucleons is unopposed conferring the property of angular momentum or spin to the atom. Such atoms are described as magnetically active and examples of these include hydrogen, carbon, nitrogen, oxygen, fluorine, sodium and phosphorous. Any of these nuclei can be utilised for magnetic resonance imaging (MRI). Hydrogen, which consists of a single proton, is most commonly used for *in vivo* imaging due to its relative abundance in the human body and large magnetic moment.

Magnetic nuclei (the electron cloud is ignored here) such as hydrogen are positively charged and possess angular momentum. According to the laws of electromagnetic induction, a moving, charged particle generates a magnetic field around it and is said to have a magnetic moment. In the absence of an external magnetic field the axes of different spinning protons are randomly orientated.

1.3 CLASSICAL AND QUANTUM MECHANICS

According to the laws of classical mechanics, in the presence of an external magnetic field (B_0), a proton experiences a torque force and tends to align its own field with that of the stronger external field. The proton is unable to align itself exactly and its own magnetic moment orbits around B_0. This phenomenon is called precession and is analogous to the wobbling of a spinning top (Figure A2.1). The precessional frequency is proportional to the field strength of B_0 and is described by the Larmor equation

$$\omega_0 = B_0 \times \lambda$$

where ω_0 is the precessional frequency, B_0 is the strength of the external magnetic field and λ is the gyromagnetic ratio (angular momentum/magnetic moment of a particular nucleus).

Under the laws of quantum mechanics, there are two states in which individual protons can align with B_0. Low-energy protons will align in approximately the same direction as the field (parallel or spin up) and high-energy protons will align in the opposite direction (anti-parallel or spin down) (Figure A2.2). Both of these states are stable but protons may swap between the two states by gaining or losing a photon.

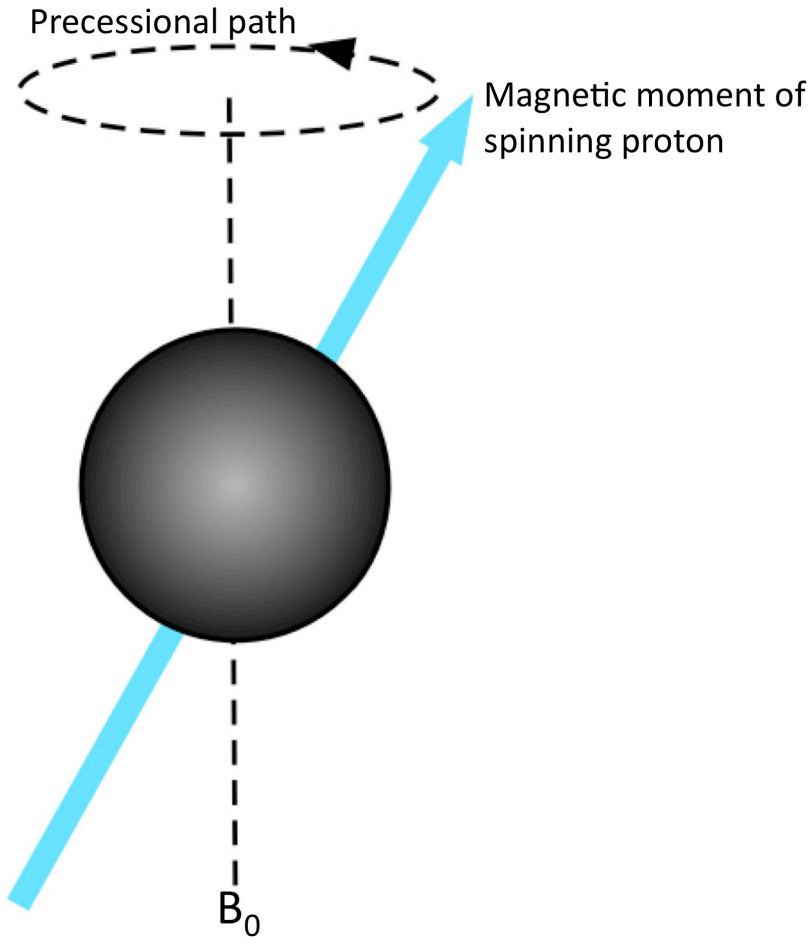

Figure A2.1 Precession
When an external magnetic field (B_0) is applied magnetic nuclei attempt to align with B_0, but do so incompletely and instead precess around it.

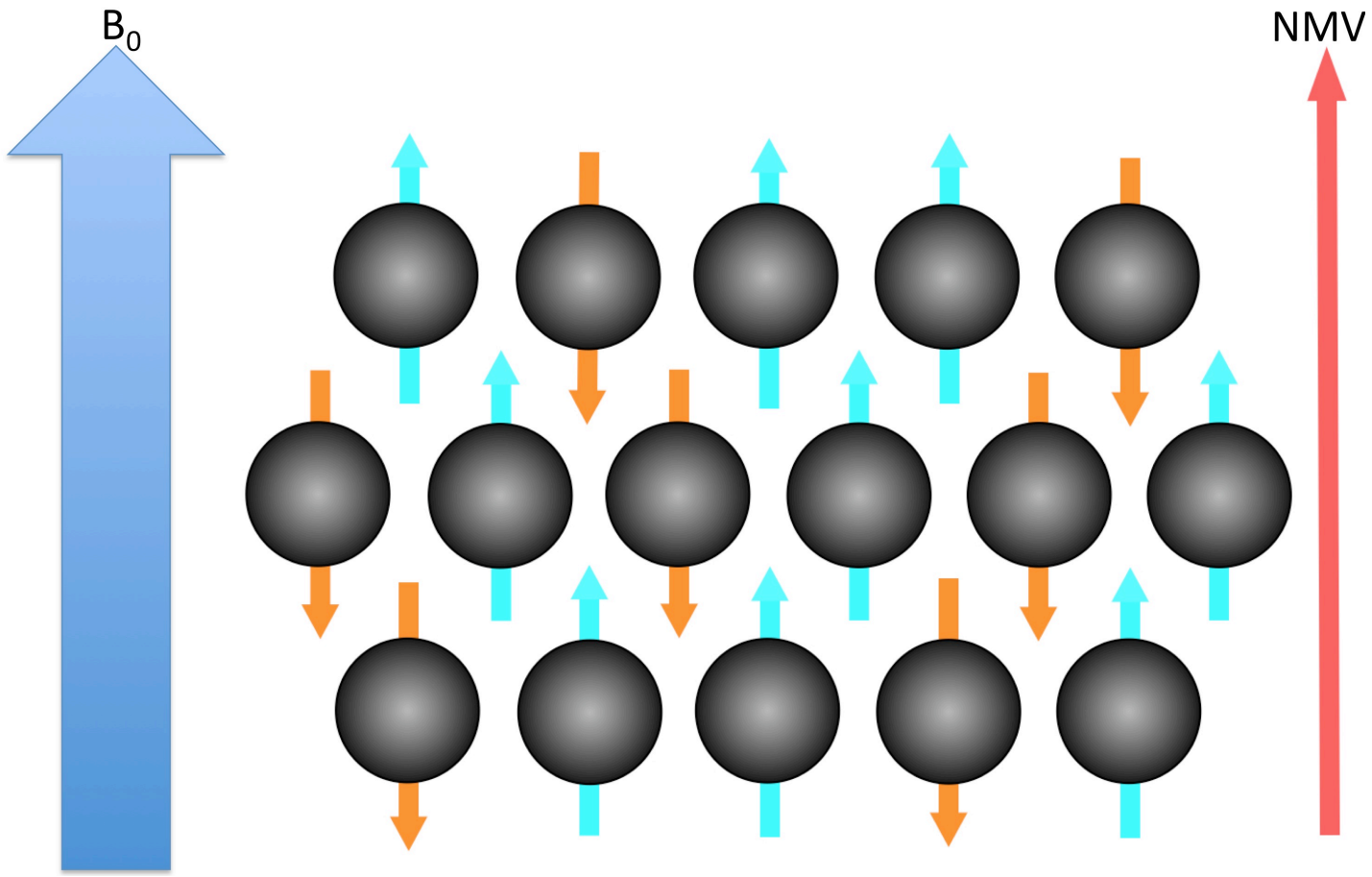

Figure A2.2 Quantum theory and energy levels
According to quantum theory, magnetic nuclei lie in either the low energy (spin up or parallel) state or in the high energy (spin down or anti-parallel) state. In the resting state a small excess of nuclei lie in the parallel state creating a small NMV in the same direction as B_0.
NMV - Net magnetisation vector; B_0 - External magnetic field.

The proportion of protons in each state depends on the temperature and the strength of the external field. At a higher temperature, a higher proportion of protons have sufficient energy to oppose B_0 and exist in the anti-parallel or spin down state. In clinical imaging, however, the temperature is not subject to manipulation and the only important factor is the external field strength.

When a patient lies in a clinical MRI scanner, the small majority of hydrogen protons aligning in the parallel direction generate the Net Magnetisation Vector (NMV or M_0), the size of which reflects the balance of protons in the parallel and anti-parallel states (Figure A2.2). As the strength of B_0 increases, fewer nuclei have enough energy to oppose the external field and more protons lie in the parallel or spin up state. The NMV is therefore of greater magnitude at higher field strengths and this explains why there is more signal when imaging in higher tesla MRI scanners.

Whilst individual protons behave in accordance with the laws of quantum theory, the average behaviour of a group of protons conforms to the laws of classical mechanics.

1.4 RESONANCE AND PHASE

Resonance occurs when particles are excited by energy of the same frequency as their own oscillation (i.e. the Larmor frequency). For protons precessing at clinical field strengths, the frequency of energy required to induce resonance is within the radiofrequency (RF) range of the electromagnetic spectrum. The exact frequency required for resonance is specific to individual MRI active atomic nuclei.

When protons are excited by a RF pulse, a proportion will gain sufficient energy to move into the high energy spin down or anti-parallel state (Figure A2.3). The effect on the NMV is deflection away from B_0. The angle between the NMV and B_0 is the flip angle. The flip angle depends on the size and duration of the RF pulse. The flip angle is more easily understood if a fixed frame is considered rather than a rotating frame (Figure A2.4).

Under the influence of an external magnetic field, protons precess at the same frequency but are out of phase with each other. The other effect of application of a resonant RF pulse is to cause all the protons to precess in phase. The concept of phase-coherence can be understood when compared to the hour hand of a clock (Figure A2.5). All over the world the hour hand takes 12 hours to complete a revolution of the clock face (i.e. they have the same frequency), but depending on which time-zone you are in the hour hand will be pointing at a different time (i.e. they are out of phase with each other). If, however, you consider all of the clocks in the same country, the hour hands will all be pointing to the same time (i.e. they are in phase). When all the protons are in phase they are said to have phase-coherence and the resulting MR signal is greater. When phase-coherence is lost the signal becomes indetectable.

1.5 TRANSVERSE MAGNETISATION AND SIGNAL

According to Faraday's Law of electromagnetic induction, a voltage is induced in a conductive coil placed in a fluctuating magnetic field. Because resonance causes the NMV to be deflected away from B_0 into the transverse plane and because the NMV

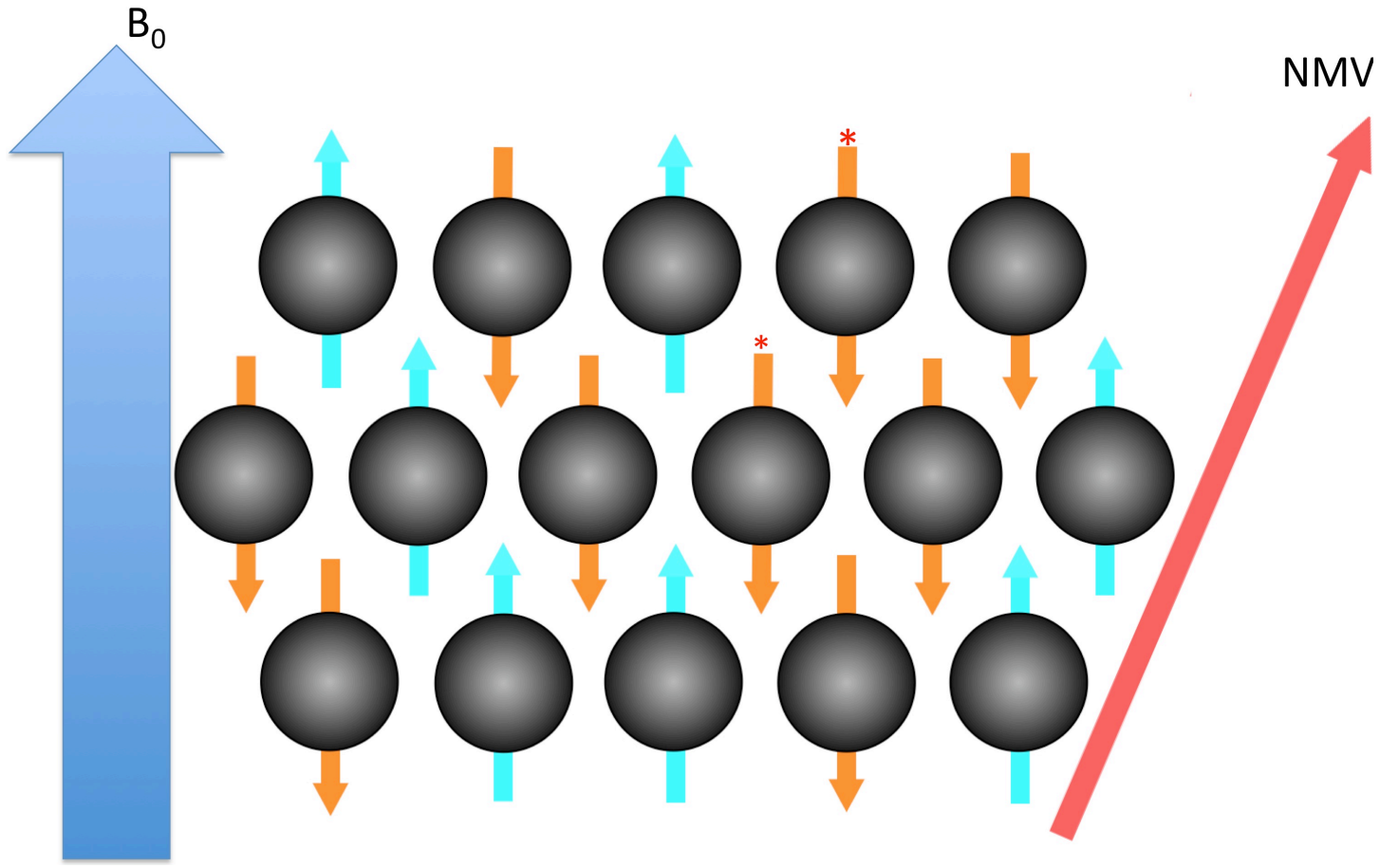

Figure A2.3 Resonance and transverse magnetisation
When the radiofrequency pulse is applied, resonance is induced. Some nuclei gain energy and move into the high energy state (*) deflecting the NMV into the transverse plane at an angle to B_0.
NMV - Net magnetisation vector; B_0 - External magnetic field.

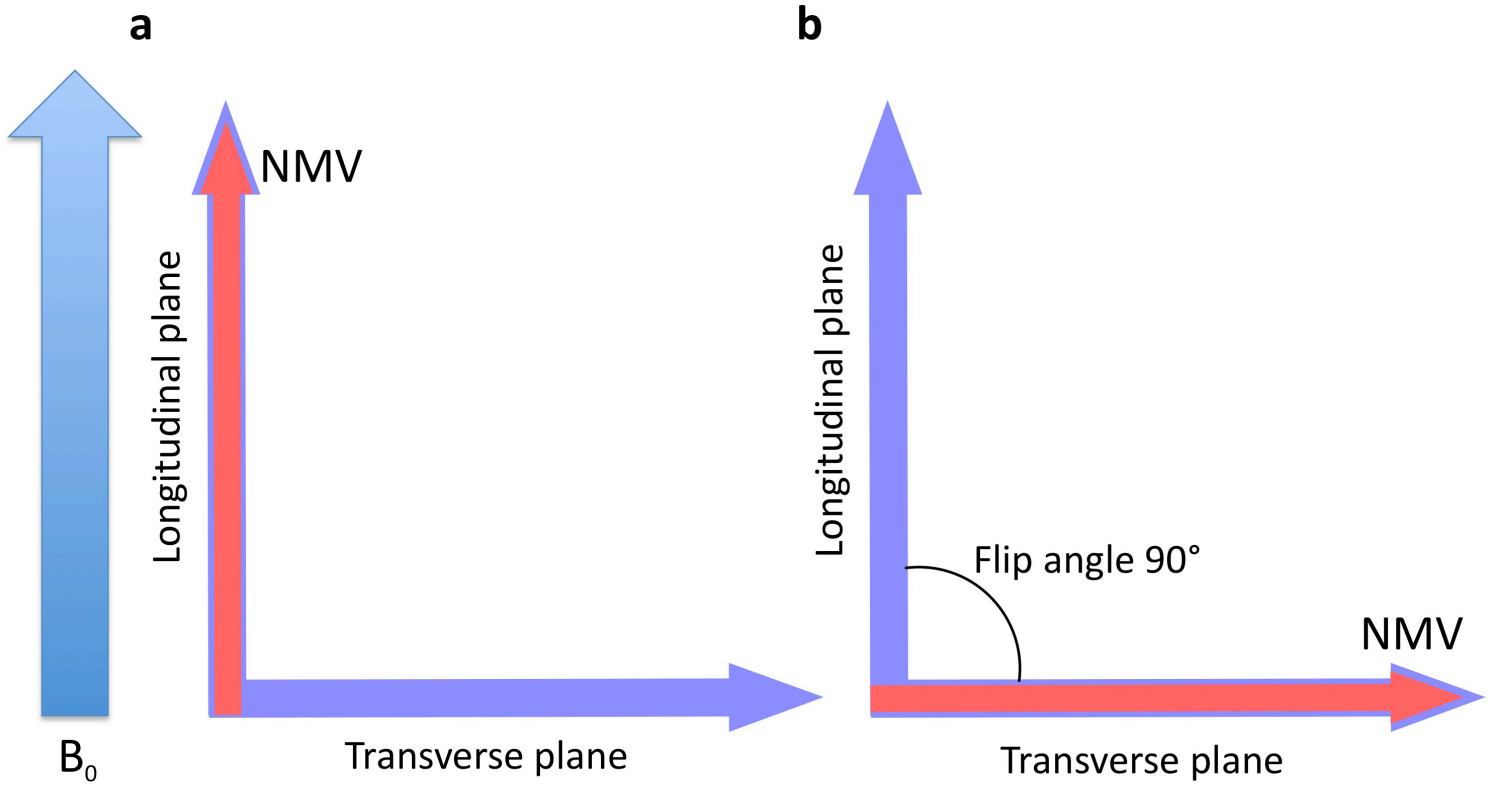

Figure A2.4 Longitudinal and transverse magnetisation
When considering the "fixed frame", precession is ignored and only the x and y components of the NMV are considered. At baseline (**a**) the NMV is aligned with B_0. When a radiofrequency pulse is applied (**b**), the NMV is deflected into the transverse plane inducing a signal in the receiver coil.
NMV - Net magnetisation vector; B_0 - External magnetic field.

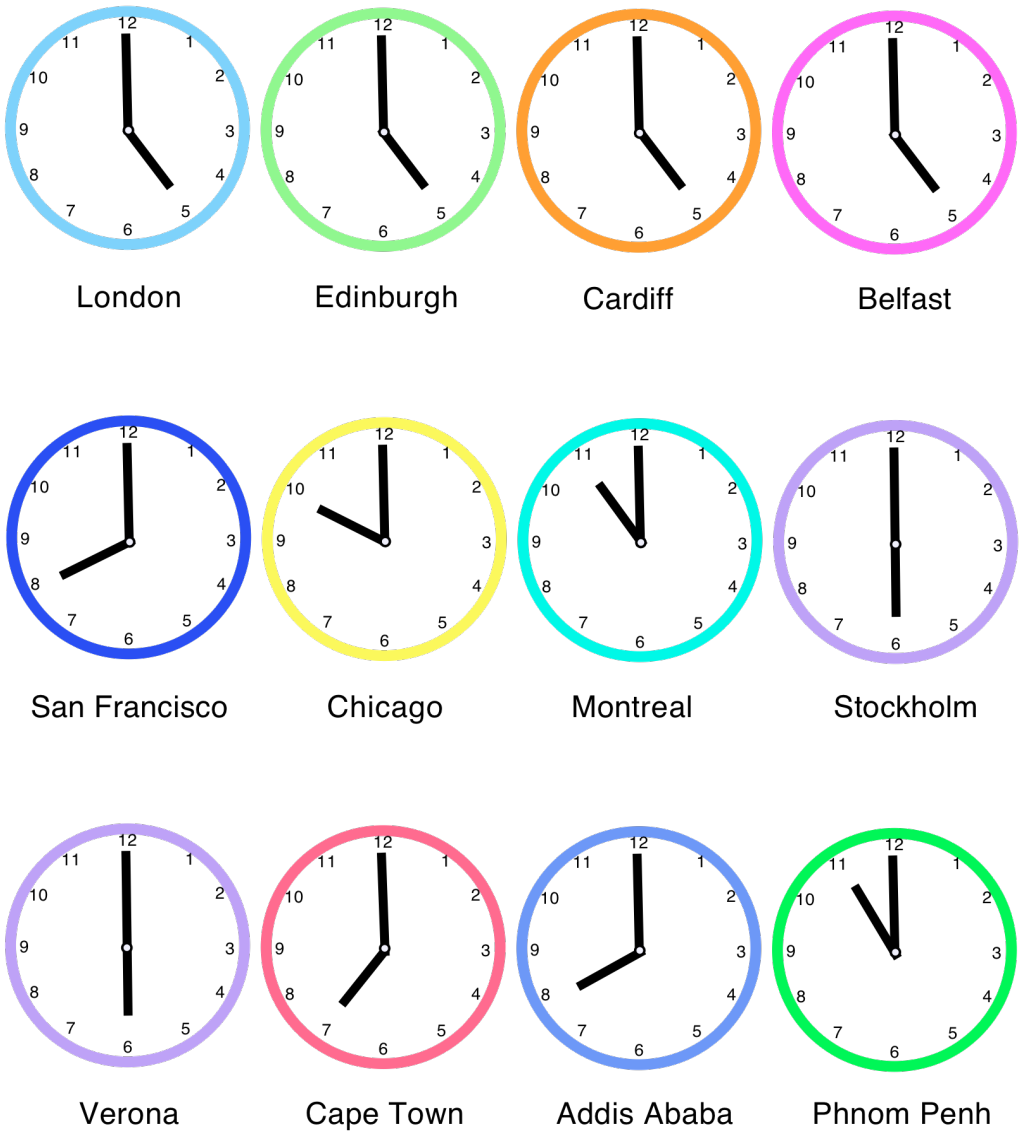

Figure A2.5 Phase coherence
The hour hands of clocks all over the world have the same frequency. The hour hands of all clocks in the United Kingdom are at the same position (ie they are in phase) but in other countries point to different times (ie they are out of phase).

precesses about B_0, a coil placed in the transverse plane is exposed to an oscillating magnetic field. The resulting voltage induced in the coil constitutes the signal. The frequency is equal to the Larmor frequency and the magnitude is determined by the magntitude of the transverse component of the NMV.

1.6 RELAXATION

At the end of the radiofrequency pulse the NMV tends to realign with B_0. This process of relaxation involves a proportion of protons in the spin down, high-energy state returning to the spin up, low-energy state by emitting some of the energy that they had gained from the RF pulse. The second component of relaxation is loss of phase-coherence of spinning protons.

During relaxation longitudinal magnetisation is regained and this is called T1 recovery. There is also a loss of transverse magnetisation called T2 decay that occurs simultaneously with but independently of T1 recovery (Figure A2.6a).

As a result of the decay of transverse magnetisation, the signal in the receiver coil decreases with time after the end of the RF pulse and this is called free induction decay (FID). FID is influenced by a number of factors including interactions between spinning nuclei and their environment, and inhomogeneities in the magnetic field which cause nuclei to precess at slightly different frequencies.

T1 recovery occurs when spinning nuclei emit energy to the surrounding environment or lattice (spin-lattice relaxation). Recovery of longitudinal magnetisation is an exponential process described by a tissue-specific constant called

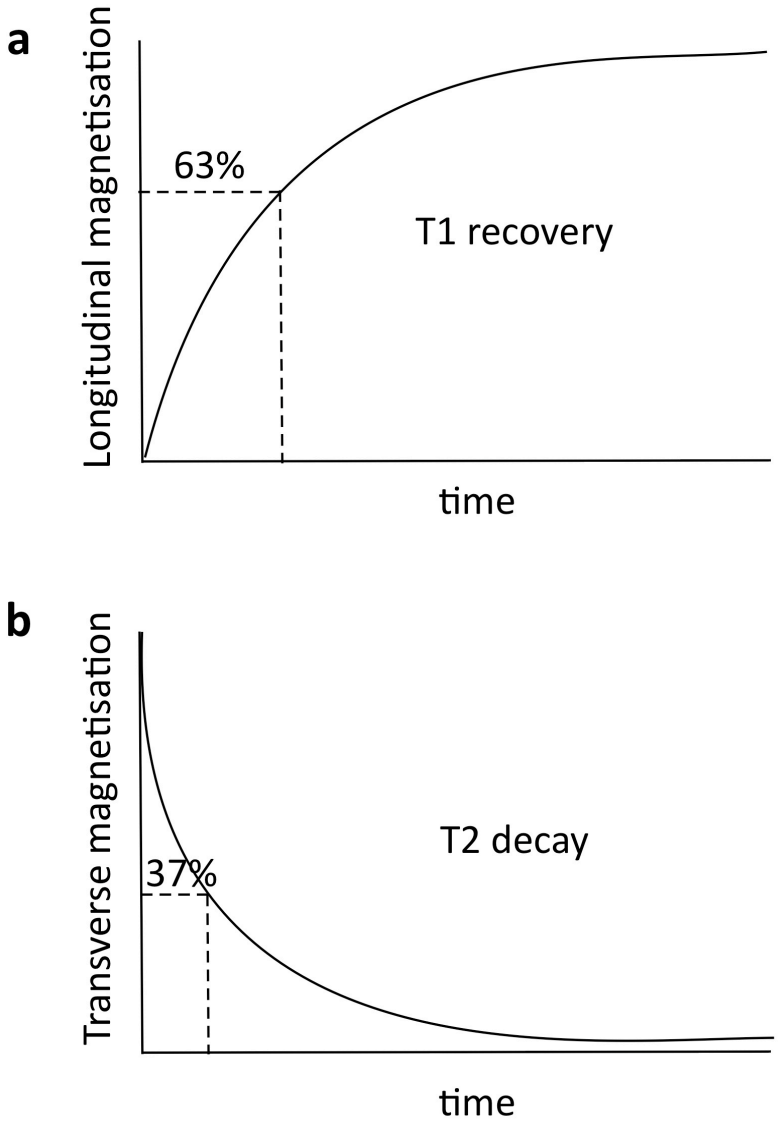

Figure A2.6 (a) T1 recovery and (b) T2 decay
T1 recovery occurs as a result of spin-lattice interactions and longitudinal magnetisation is regained (**a**). The T1 value is the time taken for 63% of longitudinal magnetisation to be recovered. T2 decay is loss of transverse magnetisation and occurs as a result of spin-spin interactions between magnetic nuclei (**b**). The T2 value is the time taken for transverse magnetisation to decay to 37% of its original value.
T1 recovery and T2 decay occur simultaneously but are independent of each other.

the T1 relaxation time which represents the time taken to recover 63% of the longitudinal magnetisation.

Transfer of energy to neighbouring nuclei (spin-spin relaxation) results in exponential T2 decay of coherent transverse magnetisation (Figure A2.6b). Spinning nuclei exhibit random motion and as they come into close proximity with each other there is a small change in the local magnetic field which in turn causes a small change in the precessional frequency. As they move apart again they return to the Larmor frequency but are now slightly out of phase with each other. As a result of serial interactions with other nuclei there is complete loss of phase-coherence. Note that there is no net loss of energy from the population of spinning nuclei but rather a transfer of energy amongst nuclei. The T2 relaxation time is the time taken for the transverse magnetisation to decay to 37% of its original value.

Since loss of phase-coherence occurs much more rapidly than realignment with B_0, the T2 relaxation time is much shorter than the T1 relaxation time for a particular tissue.

T2* decay is the combination of T2 decay (spin-spin interaction) and loss of phase-coherence due to small magnetic field inhomogeneities. If the local magnetic field strength around a spinning proton is slightly higher or lower than B_0, the proton will spin slightly faster or slower than its neighbours because the precessional frequency given by the Larmor equation is proportional to field strength. This results in very

rapid loss of phase-coherence occurring immediately after application of the RF pulse. The T2* value is always shorter than the T2 value.

The T1 and T2 relaxation rates of a tissue depend on three key factors: inherent energy of the tissue, how tightly packed the molecules are and how closely the molecular tumbling rate matches the Larmor frequency. Energy transfer between nuclei (i.e. spin-spin energy transfer) is more efficient if the molecules are closely related to each other and T2 relaxation time is short. If the molecular tumbling rate and the Larmor frequency are similar, efficient transfer of energy occurs between spinning nuclei and the surrounding lattice resulting in rapid T1 relaxation. In addition, tissues such as fat with low inherent energy can readily absorb energy dissipated into the lattice.

In fat the molecules are large, densely packed and have a low tumbling rate which is similar to the Larmor frequency. They also have low inherent energy. There is therefore efficient transfer of energy between nuclei and the surrounding lattice (spin-lattice relaxation) resulting in rapid T1 recovery (short T1 time) (Figures A2.7 and 8). There is also efficient transfer of energy amongst the hydrogen nuclei (spin-spin relaxation) and the T2 decay is rapid (short T2 time).

Water, by comparison, consists of small, high-energy molecules with a high tumbling rate. Spin-spin and spin-lattice energy transfer is therefore inefficient

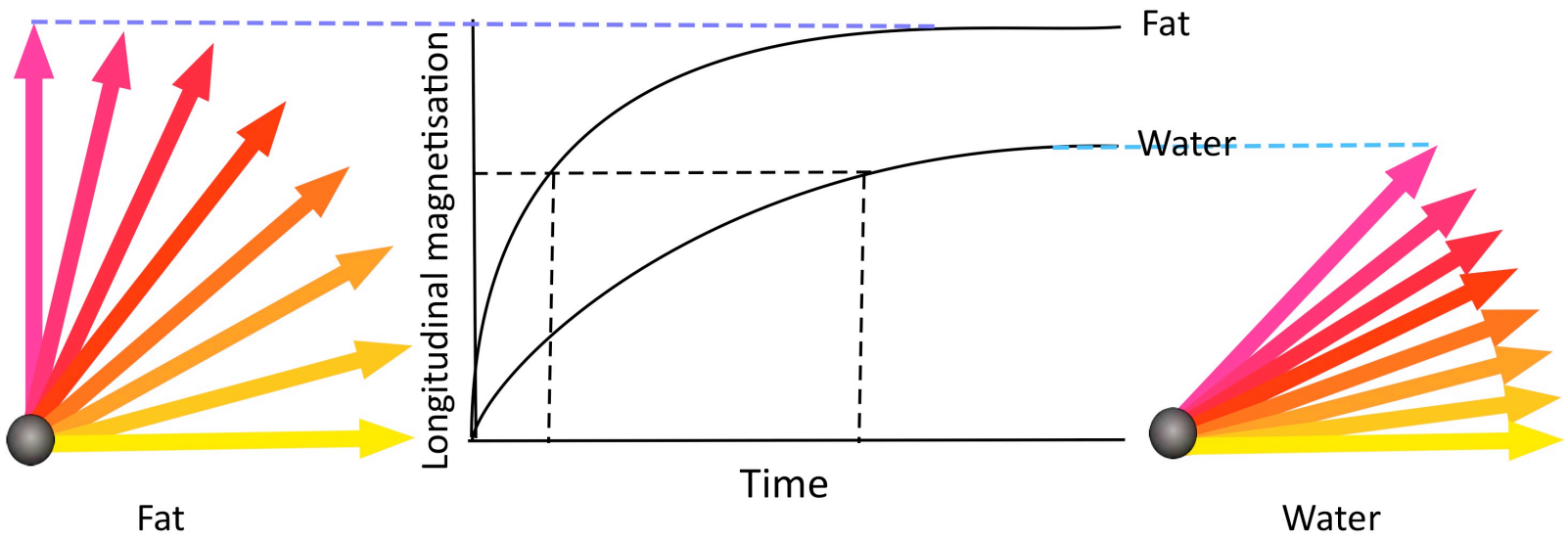

Figure A2.7 T1 recovery in fat and water
T1 recovery is faster in fat than in water because there is efficient transfer of energy between the spinning nuclei and the surrounding lattice.

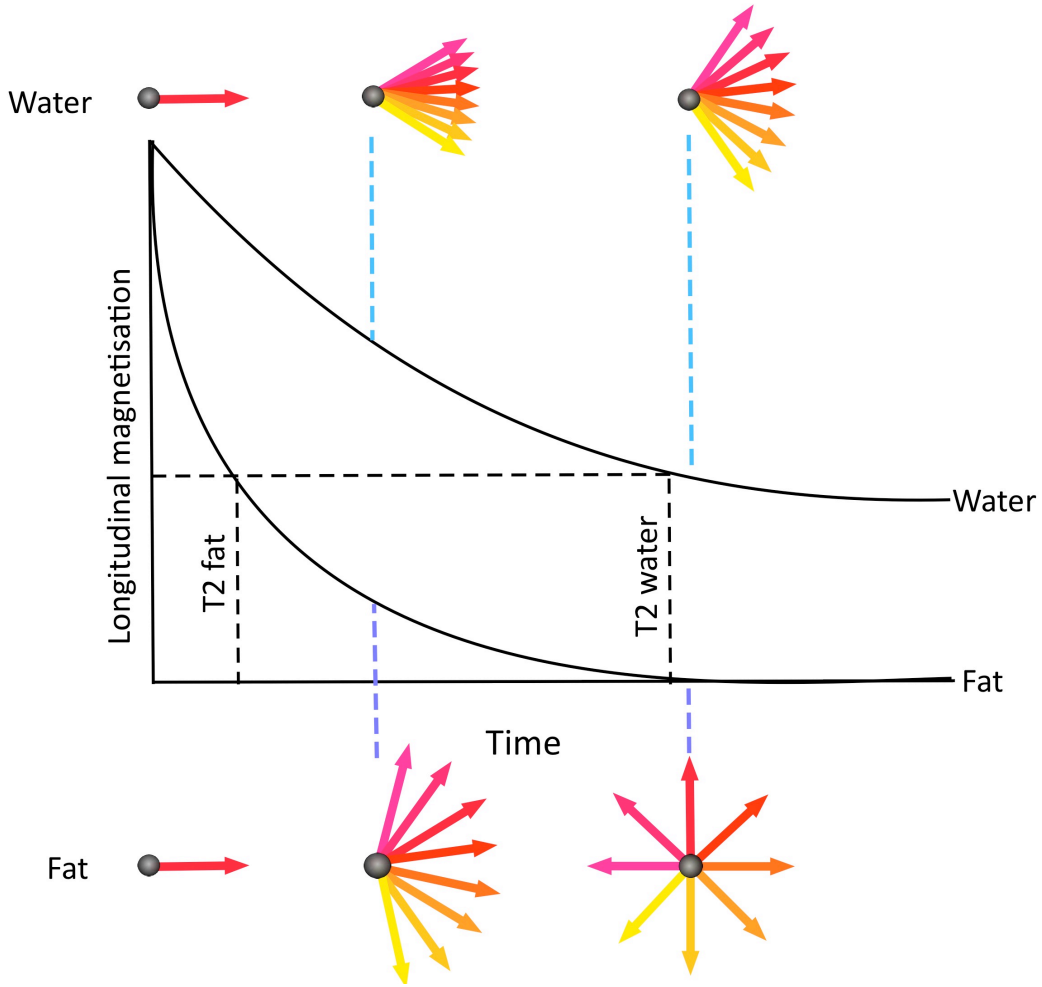

Figure A2.8 T2 decay in fat and water
T2 decay in fat is rapid and in water occurs more slowly because the molecules are closely packed together, the molecular tumbling rate is similar to the Larmor frequency and the molecules have low inherent energy. These factors favour transfer of energy between spinning nuclei resulting in a short T2 time. Water, by comparison, consists of small, high energy molecules with a high tumbling rate resulting in poor transfer of energy between nuclei as well as between nuclei and the surrounding lattice.

resulting in slow T1 recovery (long T1 time) and slow T2 decay (long T2 time) (Figures A2.7 and 8).

1.7 BASIC SIGNAL PARAMETERS

A simple sequence consists of a series of RF pulses followed by a period of relaxation during which the signal is sampled.

The repetition time (TR) is the time between the radiofrequency pulses and determines the degree of T1 recovery that is allowed to occur. The TR therefore gives the T1 weighting of the sequences.

The echo time (TE) is the time that elapses between application of the RF pulse and sampling of the signal which determines the amount of T2 decay that is allowed to occur. Using a long echo time therefore increases the T2 weighting of the sequence.

1.8 CONTRAST AND WEIGHTING

T1, T2 and T2* decay occur to a certain extent in all MR images. However by manipulating the echo time and TR it is possible to weight the image so that one of these weightings predominates. This increases the contrast between different tissues and enables image interpretation.

In a T1 weighted (T1W) image the difference in T1 times between fat and water is maximised. This is achieved by using a short TR so that there is a large difference in longitudinal relaxation between fat and water (Figure A2.9a). If a long TR was used

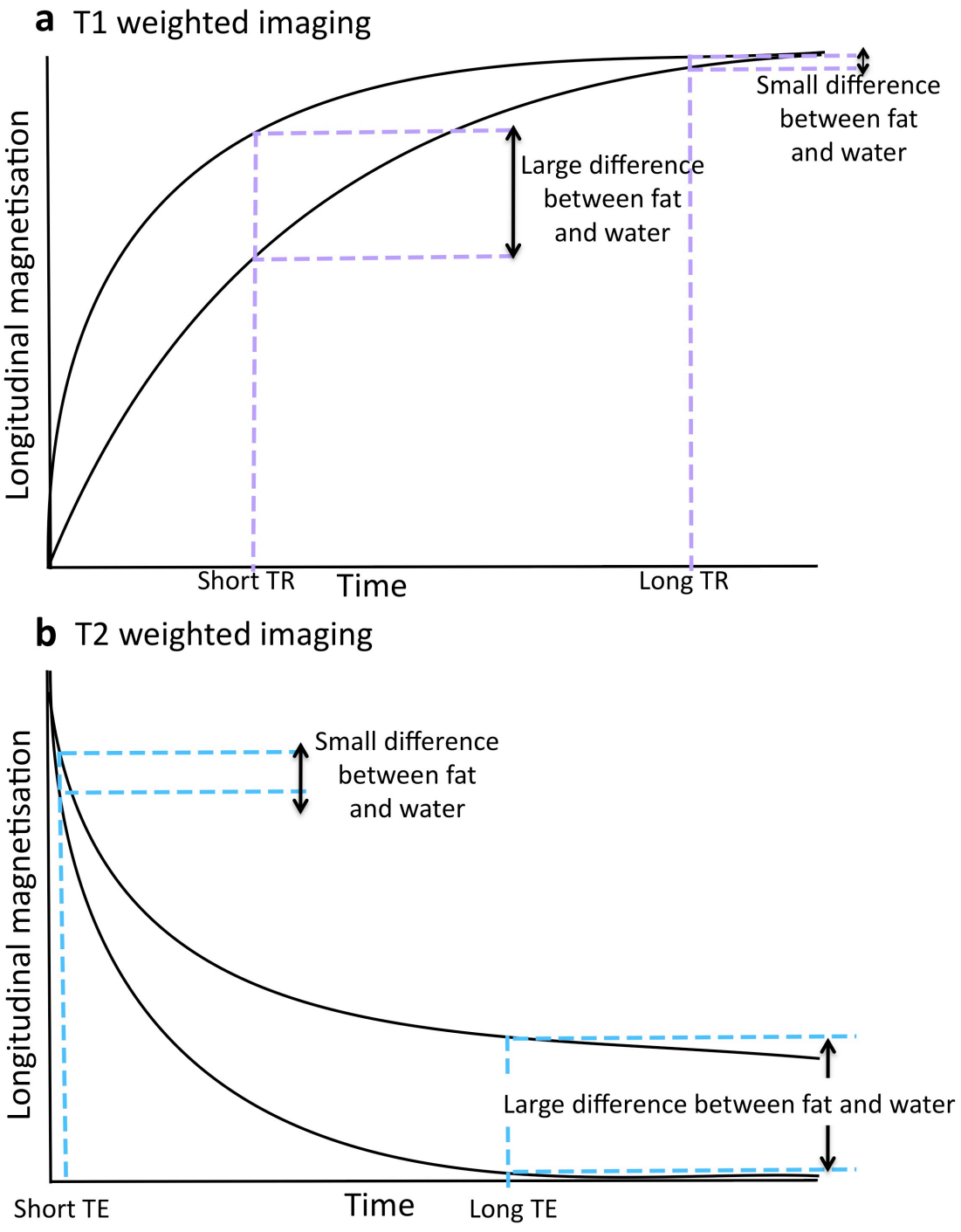

Figure A2.9 T1 weighted and T2 weighted imaging
In a T1 weighted image (**a**), the TR is short to maximise the contrast between water and fat. The T2 effects are minimised by using a short TE.
In T2 weighted imaging (**b**), the TE is long to maximise the contrast between water and fat by allowing the signals in both water and fat to decay. In addition, the T1 effects are minimised by using a long TR.
TR - Repetition time; TE - Echo time.

vectors from both fat and water would have realigned fully with B_0 and no difference would be detected. In conjunction with a short TR, a short echo time is used to minimise the T2 weighting.

In a T2 W image the difference in T2 times between fat and water is maximised (Figure A2.9b). This is achieved by using a long echo time so that both fat and water signals have an opportunity to decay and a difference between them can be detected. To minimise the T1 weighting of the image the TR is long so that full T1 relaxation has occurred in both fat and water.

To obtain a proton density image both the T1 and T2 effects are minimised so that the image reflects the proton density of tissues. To achieve this a long TR and a short echo time are used.

1.9 SPIN ECHO SEQUENCES

T2* decay is very rapid and without compensation the signal would reach zero before T1 and T2 weighting had been achieved. Following application of a RF pulse, spinning protons begin to precess at different rates due to local magnetic field inhomogeneities and phase-coherence is lost.

This situation is commonly likened to racing cars driving at different speeds on a circular track (Figure A2.10). At a specified time, t (where t=TE/2), the faster cars will be further round the track. If at that point in time the cars turned round and drove

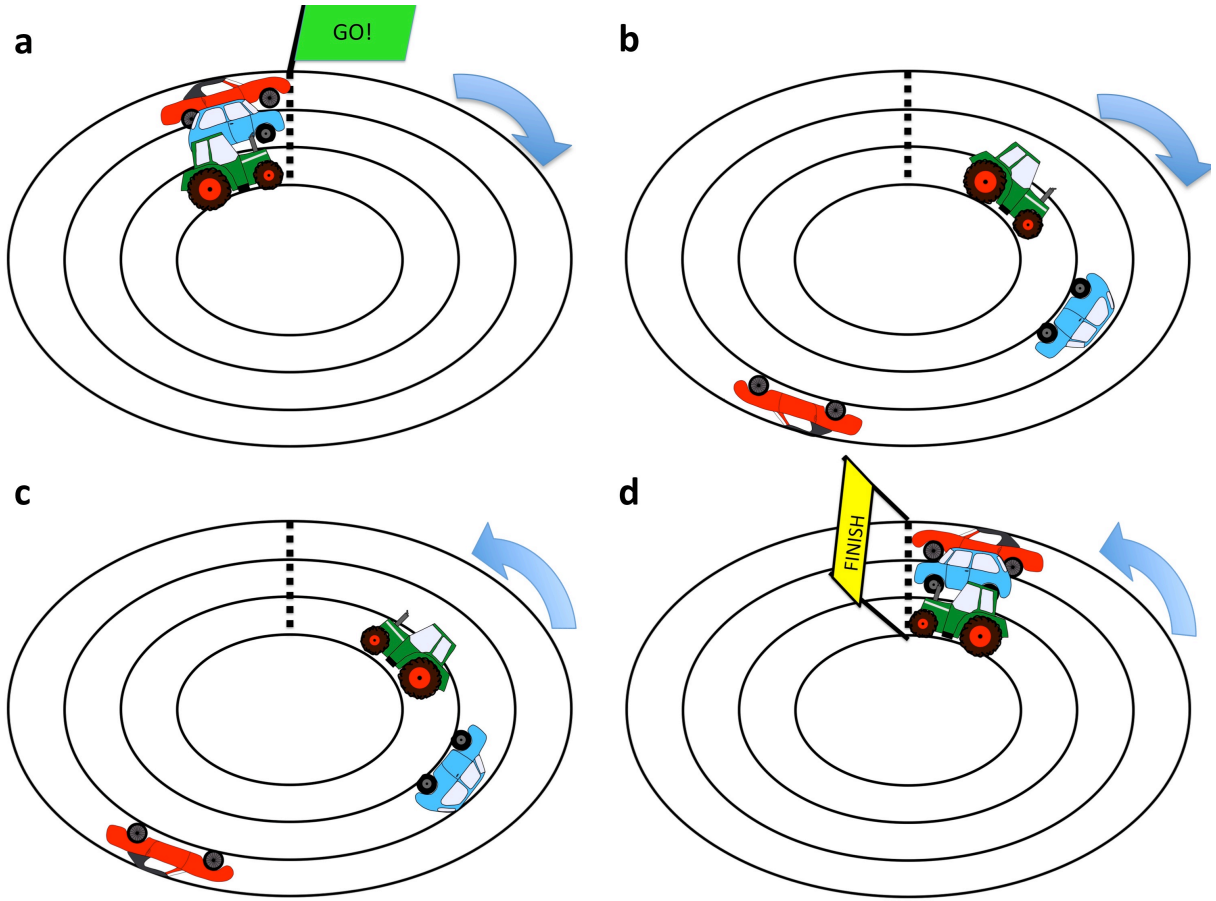

Figure A2.10 Spin echo sequences
Spin echo sequences can be understood using the analogy of a car race. All cars start at the same point on the track (**a**) but travel at different speeds and at the half way stage in the race (t=TE/2) are at different points on the track (**b**). If they then stop and start driving the other way round the track (**c**) they will reach the finishing line together at a time 2t (where 2t=TE) (**d**).
TE - Echo time.

at the same speed the opkposite way round the track they would all cross the line simultaneously at a time 2*t* (where 2*t*=TE).

A spin echo sequence uses a similar principle (Figure A2.11). A 90^{o} RF pulse is applied flipping the NMV into the transverse plane. The precessing protons begin to dephase immediately due to T2* effects and phase-coherence is lost. At a time *t* (where *t*=TE/2), a further 180^{o} RF pulse is applied which reverses the direction of the NMV. The protons which are precessing more rapidly 'catch up' with the slowly precessing protons and at a time, 2*t* (where 2*t*=TE), the protons are back in phase and the signal is sampled.

1.10 GRADIENT ECHO SEQUENCES

A magnetic field gradient is induced by a current passing through a magnetic coil in the bore of the magnet. It interacts with the main magnetic field such that the composite field strength varies along the axis of B_0. At the magnetic isocentre the field strength is equal to that of B_0, but away from the isocentre in one direction it increases and in the other direction it decreases (Figure A2.12). Since the precessional frequency is proportional to the magnetic field strength, protons in different parts of the magnetic field will precess at different frequencies resulting in gradual dephasing of coherent transverse magnetisation (Figure A2.13). A second equal but opposite gradient can be applied to rephase the individual magnetic moments restoring phase-coherence**.** The signal induced in the receiver coil at this point is called the gradient echo.

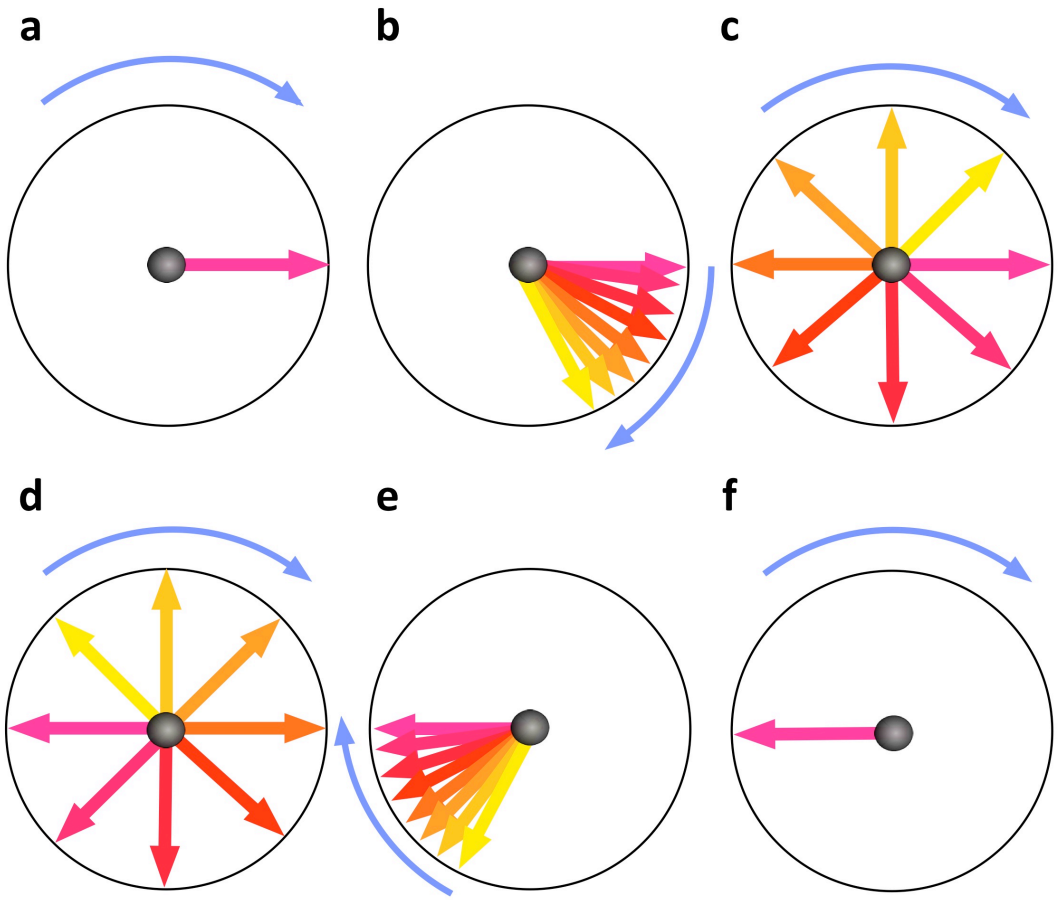

Figure A2.11 Spin echo sequences
An excitatory 90° radiofrequency pulse is applied and flips the NMV into the transverse plane (**a**). There is spontaneous rapid loss of phase coherence as a result of T2* decay (**b** and **c**). A 180° radiofrequency pulse is applied which inverts the NMV (**d**). Rephasing occurs (**e**) with restoration of phase coherence and the spin echo is sampled at TE (**f**).
NMV - Net magnetisation vector; TE - Echo time.

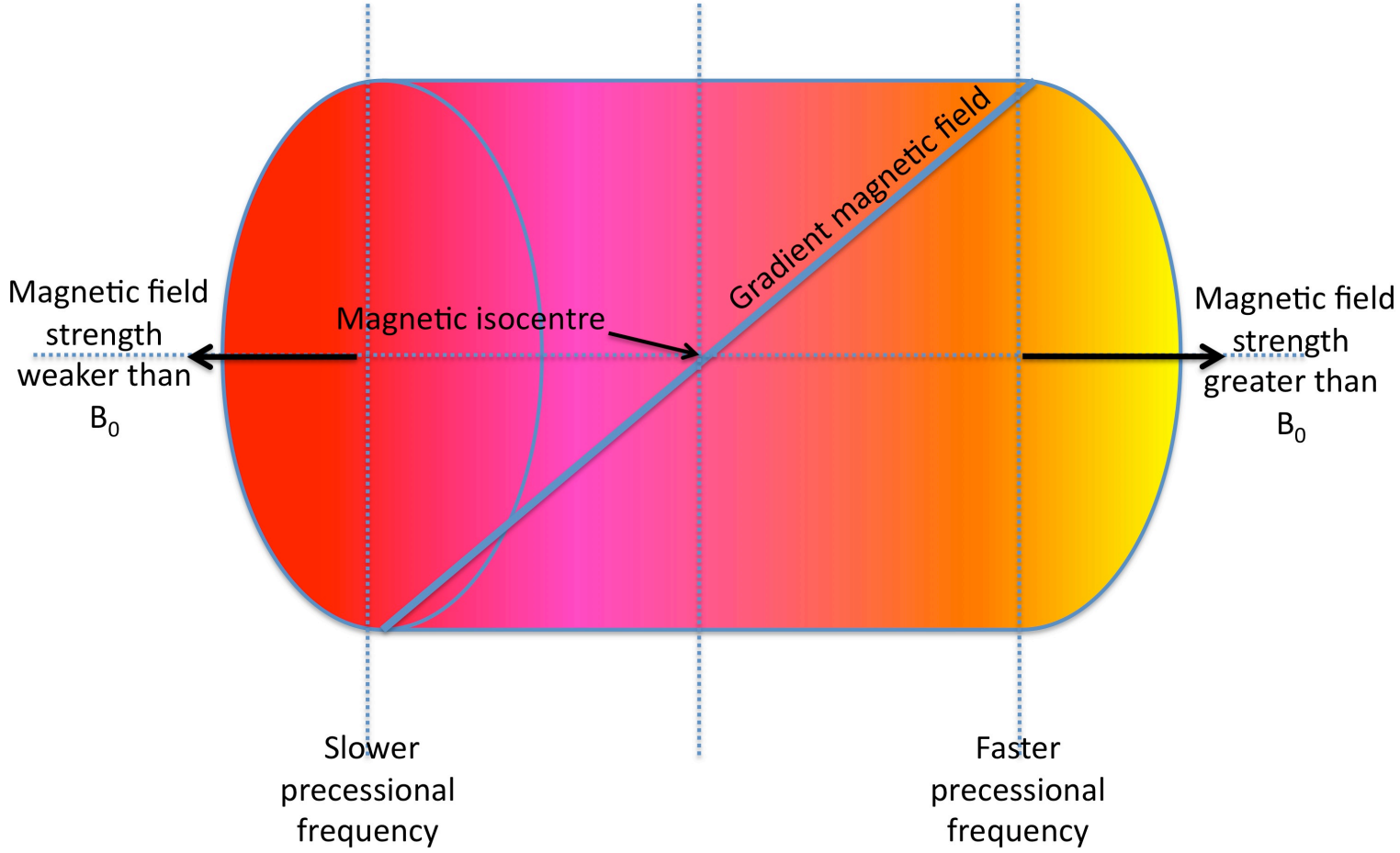

Figure A2.12 Gradient echo
In a gradient echo sequence a gradient magnetic field is applied at an angle to B_0. Magnetic nuclei in different parts of the imaging volume experience different field strengths of magnitude slightly greater or less than B_0. Because precessional frequency is proportional to field strength, some nuclei slow down and some speed up so that they are all slightly out of phase.
B_0 - External magnetic field.

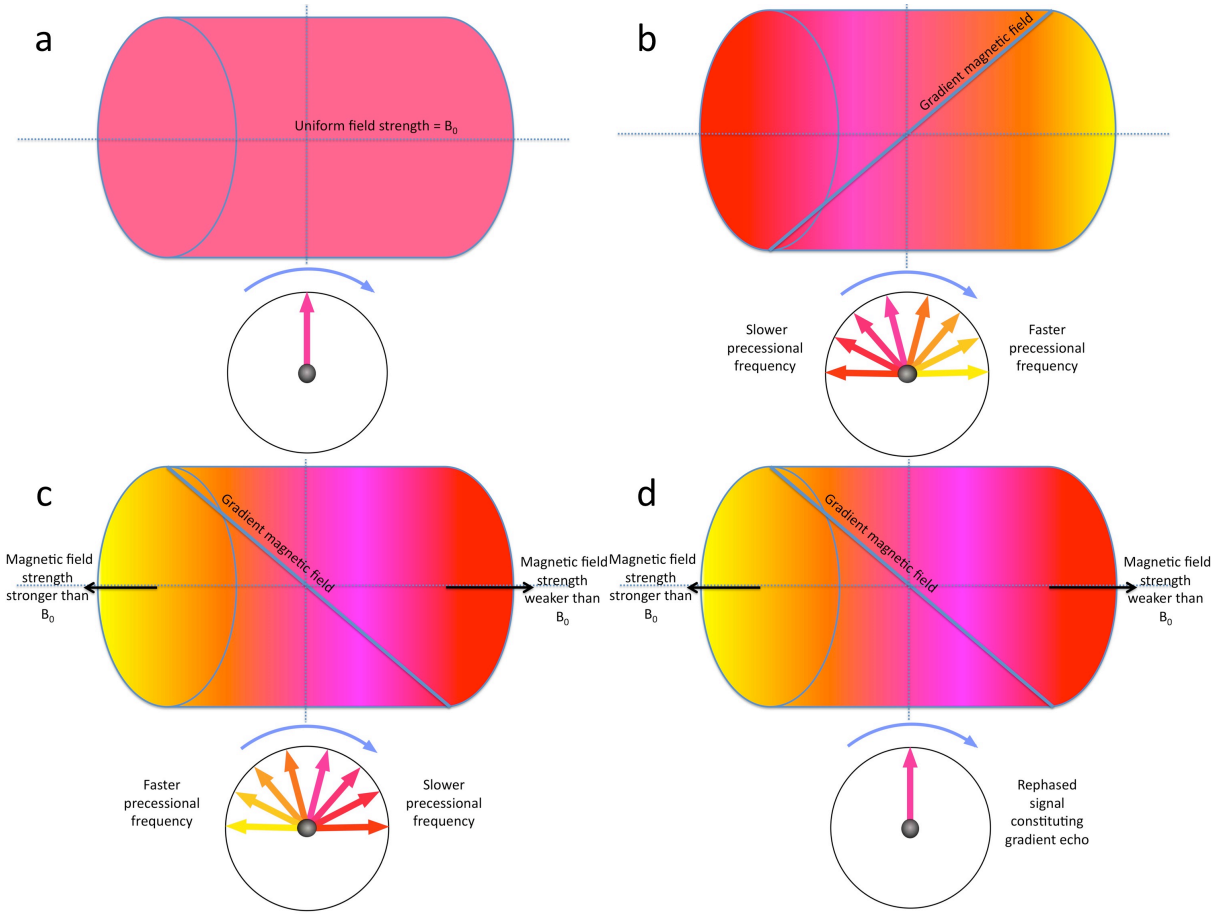

Figure A2.13 Gradient echo
Spinning nuclei align with B_0 and are in phase (**a**). When a gradient magnetic field is applied, protons begin to spin at different frequencies depending upon the composite field strength that they are exposed to and dephasing occurs (**b**). A second equal but opposite gradient is applied which rephases the spins (**c**) and phase coherence is restored (**d**). The signal sampled at this point is called the gradient echo.
B_0 - External magnetic field.

Whilst spin echo sequences always use excitatory RF pulses that flip the NMV through 90°, gradient echo sequences can use smaller flip angles. By using a smaller flip angle, full recovery of longitudinal magnetisation occurs more rapidly and the TR can be shorter. In addition, rephasing is faster using a gradient compared to a 180º RF pulse allowing shorter echo time to be used. These factors mean that the scanning time is shorter compared to spin echo sequences.

Compared to images acquired using spin echo sequences, gradient echo images are acquired much more quickly but have a poorer signal-to-noise ratio due to the short TR and small flip angle. Furthermore, gradient echo sequences make no compensation for T2* decay making them highly sensitive to magnetic field inhomogeneities. T2* weighting is maximised by the use of long echo time and long TR (although in practice TR is still much shorter than that used in spin echo sequences).

1.11 MULTI ECHO SEQUENCES AND T2* VALUE

In a multi echo gradient echo sequence the signal is sampled at multiple echo times following a single RF pulse. Compared to acquiring the echoes individually following separate RF pulses, the use of a multi echo sequence reduces the acquisition time and, because the echoes are collected only milliseconds apart, avoids the need to register sequential images to each other.

The signal decays exponentially with increasing echo time. The rate of decay of signal intensity is determined by the decay constant the T2* value calculated by the

equation S(t)=S(0)exp-(t/T2*), where S(t) is the signal intensity at time t, and S(0) is the signal intensity at time 0.

Endogenous iron and iron nanoparticle-based MRI contrast agents induce local magnetic field inhomogeneities resulting in rapid dephasing of coherent transverse magnetisation. The rate of decay of signal intensity with echo time is increased with a corresponding reduction in T2* value. Changes in T2* value have been exploited for the detection of endogenous iron accumulation such as occurs in haemochromatosis and transfusion-related iron overload in patients with thalassaemia major. Using multi echo sequences, a reduction in T2* value is observed in the myocardium and the liver in patients with systemic iron overload. [Anderson *et al* 2001; Wood *et al* 2005; Storey *et al* 2007].

1.12 CONTRAST AGENTS

Contrast agents may be used to enhance the differences between different tissue components and increase the specificity of MRI to distinguish normal from pathological tissue. The choice of agent is contingent upon the diagnostic question.

Paramagnetic substances such as gadolinium shorten the T1 relaxation time in tissues in which they accumulate. Consequently these tissues appear bright on T1W images.

Superparamagnetic contrast agents such as superparamagnetic particles of iron oxide (SPIO) induced local magnetic field inhomogeneities leading to a rapid loss of phase-coherence amongst magnetic nuclei. The effect of this is a shortening of the

T2 and T2* relaxation times and a profound reduction in the signal intensity on T2W and particularly T2*W images. As a result, tissues in which SPIO accumulate appear dark on T2W and T2*W scans. SPIO also have a T1 shortening effect which is most obvious at low concentrations whilst at higher concentrations T2* susceptibility effects predominate [Canet *et al* 1993; Torabi *et al* 2004].

Papers arising from this Thesis

Abdominal aortic aneurysm growth predicted by uptake of ultrasmall superparamagnetic particles of iron oxide: a pilot study

Jennifer M.J. Richards, Scott I. Semple, Thomas J. MacGillivray, Calum Gray, Jeremy P. Langrish, Michelle Williams, Marc Dweck, William Wallace, Graham McKillop, Roderick T.A. Chalmers, O. James Garden and David E. Newby

Circ Cardiovasc Imaging 2011; 4:274-281

In Vivo Mononuclear Cell Tracking Using Superparamagnetic Particles of Iron Oxide: Feasibility and Safety in Humans

Jennifer M.J. Richards, Catherine A. Shaw, Ninian N. Lang, Michelle C. Williams, Scott I.K. Semple, Thomas J. MacGillivray, Calum Gray, Julie H. Crawford, Shirjel R. Alam, Anne P.M. Atkinson, Elaine K. Forrest, Carol Bienek , Nicholas L. Mills, Anne Burdess, Kev Dhaliwal, A. John Simpson, William A. Wallace, Adam T. Hill, P. Huw Roddie, Graham McKillop, Thomas A. Connolly, Giora Z. Feuerstein, G. Robin Barclay, Marc L. Turner, David E. Newby

Circ Cardiovasc Imaging 2012; 5:509-517

Magnetic resonance assessment of accumulation of superparamagnetic particles of iron oxide in cardiovascular tissue: application in patients with abdominal aortic aneurysms

Jennifer M.J. Richards, Thomas J. MacGillivray, Calum Gray, Catherine A. Shaw, Graham McKillop, William A. Wallace, Roderick T.A. Chalmers, O. James Garden[2], David E. Newby, Scott I.K. Semple

Submitted

Circulation
Cardiovascular Imaging
JOURNAL OF THE AMERICAN HEART ASSOCIATION

American Heart Association
Learn and Live

Abdominal Aortic Aneurysm Growth Predicted by Uptake of Ultrasmall Superparamagnetic Particles of Iron Oxide : A Pilot Study

Jennifer M.J. Richards, Scott I. Semple, Thomas J. MacGillivray, Calum Gray, Jeremy P. Langrish, Michelle Williams, Marc Dweck, William Wallace, Graham McKillop, Roderick T.A. Chalmers, O. James Garden and David E. Newby

Circ Cardiovasc Imaging 2011;4;274-281; originally published online February 8, 2011;
DOI: 10.1161/CIRCIMAGING.110.959866
Circulation: Cardiovascular Imaging is published by the American Heart Association. 7272 Greenville Avenue, Dallas, TX 72514
 Print ISSN: 1941-9651. Online ISSN: 1942-0080

Abdominal Aortic Aneurysm Growth Predicted by Uptake of Ultrasmall Superparamagnetic Particles of Iron Oxide

A Pilot Study

Jennifer M.J. Richards, MD; Scott I. Semple, PhD; Thomas J. MacGillivray, PhD; Calum Gray, PhD; Jeremy P. Langrish, MD; Michelle Williams, MD; Marc Dweck, MD; William Wallace, MD; Graham McKillop, MD; Roderick T.A. Chalmers, MD; O. James Garden, MD; David E. Newby, MD

Background—Abdominal aortic aneurysms are a major cause of death. Prediction of aneurysm expansion and rupture is challenging and currently relies on the simple measure of aneurysm diameter. Using MRI, we aimed to assess whether areas of cellular inflammation correlated with the rate of abdominal aortic aneurysm expansion.

Methods and Results—Stable patients (n=29; 27 male; age, 70±5 years) with asymptomatic abdominal aortic aneurysms (4.0 to 6.6 cm) were recruited from a surveillance program and imaged using a 3-T MRI scanner before and 24 to 36 hours after administration of ultrasmall superparamagnetic particles of iron oxide (USPIO). The change in T2* value on T2*-weighted imaging was used to detect accumulation of USPIO within the abdominal aortic aneurysm. Histological examination of aneurysm tissue confirmed colocalization and uptake of USPIO in areas with macrophage infiltration. Patients with distinct mural uptake of USPIO had a 3-fold higher growth rate (n=11, 0.66 cm/y; $P=0.020$) than those with no (n=6, 0.22 cm/y) or nonspecific USPIO uptake (n=8, 0.24 cm/y) despite having similar aneurysm diameters (5.4±0.6, 5.1±0.5, and 5.0±0.5 cm, respectively; $P>0.05$). In 1 patient with an inflammatory aneurysm, there was a strong and widespread uptake of USPIO extending beyond the aortic wall.

Conclusions—Uptake of USPIO in abdominal aortic aneurysms identifies cellular inflammation and appears to distinguish those patients with more rapidly progressive abdominal aortic aneurysm expansion. This technique holds major promise as a new method of risk-stratifying patients with abdominal aortic aneurysms that extends beyond the simple anatomic measure of aneurysm diameter.

Clinical Trial Registration—URL: http://www.clinicaltrials.gov. Unique identifier: NCT00794092.

(*Circ Cardiovasc Imaging*. 2011;4:274-281.)

Key Words: abdominal aortic aneurysm ■ inflammation ■ MRI

Abdominal aortic aneurysms (AAA) have a prevalence of 5% in men over the age of 65 years, and acute rupture is associated with a mortality rate of 65% to 85%. AAAs are responsible for 2% to 3% of deaths in men age ≥65 years and account for >15 000 deaths in the United States.[1–3] Open surgical or endovascular intervention to prevent rupture is considered when the perceived risk of rupture outweighs the risk of procedural complications with a diameter threshold of 5.5 cm being considered the appropriate time to intervene.[4–6] However, up to one-fifth of ruptured AAA are <5.5 cm in diameter,[7] and many patients present with AAA diameters considerably >5.5 cm without prior symptoms or rupture.[8] Apart from the simple measurement of aneurysm diameter, there are currently no methods of predicting which patients with AAA are at risk of further aneurysm growth and rupture. We therefore need better methods to guide preventative intervention in these patients.

Clinical Perspective on p 281

Aortic aneurysms arise when the aortic wall develops excessive medial neovascularization, infiltration of macrophages and lymphocytes, and irreversible proteolytic degradation and remodeling of the extracellular matrix. These pathological processes do not affect the aorta uniformly but are focal in nature with mural neovascularization, inflammation, and matrix metalloproteinase (MMP) activity occurring at sites of low tensile strength[9] and AAA rupture.[10–12] These areas of increased biological activity within the aortic aneu-

Received June 15, 2010; accepted January 31, 2011.

From the Centre for Cardiovascular Science (J.M.J.R., J.P.L., M.W., M.D., D.E.N.), University of Edinburgh, Edinburgh, United Kingdom; the Centre of Clinical and Surgical Sciences (Surgery) (J.M.J.R., R.T.A.C., O.J.G.), Edinburgh, United Kingdom; the University of Edinburgh Clinical Research Imaging Centre (J.M.J.R., S.I.S., T.J.M., C.G., D.E.N.), University of Edinburgh, Edinburgh, United Kingdom; and the Department of Pathology (W.W.) and the Department of Radiology (G.M.), Royal Infirmary of Edinburgh, Edinburgh, United Kingdom.

Correspondence to Jennifer M.J. Richards, MD, Centre of Cardiovascular Science, Chancellor's Building, Little France Crescent, Edinburgh, EH16 4SB. E-mail jenny.richards@ed.ac.uk

Circ Cardiovasc Imaging **is available at http://circimaging.ahajournals.org** **DOI: 10.1161/CIRCIMAGING.110.959866**

rysm wall are therefore putative targets for novel imaging techniques.

MRI is emerging as a useful investigative tool for cardiovascular disease that can distinguish the different atherosclerotic plaque components, such as the lipid-rich core and areas of calcification.[13] Standard gadolinium-based MRI identifies areas of thrombus formation and fibrosis in abdominal aortic aneurysms.[14] Recently, a novel class of MRI contrast agents containing superparamagnetic particles of iron oxide (SPIO) has been developed that provides additional biological and functional information through the detection of cellular inflammation within tissues. Ultrasmall SPIO (USPIO), with particle sizes in the range 10 to 30 nm, escape immediate recognition by the reticulo-endothelial system and persist for longer in the bloodstream allowing them to be used to assess the accumulation of macrophages within vascular and lymphatic tissues.[15–19] Current preparations are biodegradable and safe for clinical administration.[20–22]

USPIO accumulate in the aortas of hypercholesterolemic rabbits[23] and in murine models of AAAs.[24] In humans, USPIO accumulate in ruptured or rupture-prone carotid plaques rather than stable plaques,[17,18] and treatment with atorvastatin reduces both inflammation and USPIO uptake in carotid plaques.[19] However, the use of USPIO has not been explored in patients with AAAs. The aims of this study were to determine whether USPIO uptake can be used to detect areas of cellular inflammation within the wall of the AAA and to determine whether this correlates with aneurysm growth rates.

Methods

Subjects

Patients were recruited from the outpatient aneurysm surveillance program at the Royal Infirmary of Edinburgh between August 2009 and December 2009. Patients had an AAA with a diameter >4.0 cm on ultrasound examination of the aorta. Patients who were under the age of 40 years or pregnant and those who had active systemic inflammatory or malignant disease, renal dysfunction (estimated glomerular filtration rate <25 mL/min), hepatic cirrhosis (Child Pugh score B or C), or a contraindication to MRI scanning were excluded from the study. The research ethics committee and the Medicines and Healthcare Products Regulatory Agency approved the study, which was conducted in accordance with the Declaration of Helsinki. All participants gave written informed consent.

Demographic and clinical data, including medical history and medications, were obtained through patient interview and source hospital records. Patients were being monitored in the aneurysm surveillance program involving serial ultrasound-based measurements of the maximum anteroposterior diameter of the AAA, usually at 6-month intervals. Scans were undertaken by accredited clinical vascular scientists with interobserver coefficient of variation of aortic diameter measurements of 3.5% in our laboratory.[25] Because of the stacatto growth pattern of AAA and need for a contemporary measurement,[26] the annual growth rate was determined from 2 ultrasound scans performed 6 months apart, with one conducted before and the other after the MRI examination.

Contrast Agent Administration

The preparation containing USPIO (Sinerem, Guerbet, France) consists of iron oxide nanoparticles stabilized with dextran and sodium citrate. Supplied as a dry powder, it was first reconstituted in 10 mL of 0.9% saline and then the weight-adjusted dose of 2.6 mg/kg was diluted further in 100 mL of 0.9% saline. The USPIO was then administered through a filter as a slow infusion over 30 minutes through a peripheral 20G intravenous cannula.

Magnetic Resonance Imaging

Participants underwent MRI in a whole-body, 3-T Siemens Magnetom Verio scanner (Siemens, Erlangen, Germany) before and 24 to 36 hours[27] after administration of the contrast agent. Routine clinical coronal and sagittal breath-held T2-weighted multislice HASTE localizer sequences were used to identify the position and extent of the aneurysm, after which a respiratory-gated, ECG-triggered T2-weighted (T2W) turbo spin-echo sequence was used to acquire detailed anatomic data (TR/TE 2R-R intervals/72 ms; flip angle, 180°; matrix, 192×256; field of view, 400×400 mm; slice width, 5 mm). A multi-echo, gradient-echo T2*W sequence (TE, 4.9, 7.7, 10.5, 13.3 ms; TR, 133 ms; flip angle, 15°; matrix 192×256; field of view 400×400 mm; slice width 5 mm) was used to acquire axial images of the entire aneurysm with slice positions corresponding to those of the T2W images. The echo times for the T2*W sequences were selected such that fat and water were in-phase for each echo to minimize phase shift artifact and errors in T2* measurements. The field of view used for both sequences was typically 400×400 mm but was adjusted for larger subjects to minimize phase-wrap artifacts. T2W images give excellent discrimination of the boundaries between the flow lumen, thrombus, wall, and surrounding tissues. T2*W sequences have less distinct soft tissue contrast but are exquisitely sensitive to the effects of USPIO accumulation. At the postcontrast scan, slice positions were selected to match those of the precontrast scan as closely as possible by reference to the vertebral bodies.

In a subset of 19 patients, T1W images were acquired before and 5 minutes after the bolus administration of 0.2 mg/kg of gadolinium (Dataram, Guerbet Pharmaceuticals, France), using a turbo spin-echo acquisition (TR/TE 1 R-R interval/28 ms; flip angle, 180°; matrix, 192×256; field of view, 400×400 mm; slice width, 5 mm). Gadolinium-enhanced sequences were performed after the baseline T2W and T2*W sequences were acquired, 2 hours before USPIO administration and approximately 24 hours before the post-USPIO MRI scan. Because gadolinium has a plasma half-life in the region of 2 hours and, unlike USPIO, is not readily taken up into the intracellular compartment, USPIO enhancement is unlikely to have been affected by preadministration of gadolinium.

Image Analysis

So that the soft tissue discrimination of the T2W images could be used to complement the iron sensitivity of the T2*W images, and to allow direct comparison of the precontrast and postcontrast data, all the images were registered to the precontrast T2W image using a semiautomatic rigid 3D voxel registration protocol (Analyze, Mayo Clinic). Bowel and abdominal wall motion were found to compromise registration of the aorta itself and this was minimized by excluding these structures from the volume for registration as far as possible. A region of interest (ROI) encompassing the aortic wall and thrombus but excluding the flow lumen was drawn on each slice of the precontrast T2W image. The 4 echoes in the multi-echo T2*W sequence were combined to generate a T2* map, in which the data represented the T2* value $[S(t)=S(0)\exp-(t/Ts^*)]$ for each voxel. The T2* value is the decay constant for the exponential decay of signal intensity with time. In the presence of USPIO, the signal decays more rapidly due to local field inhomogeneities and the T2* value is reduced. A 3×3 voxel gaussian filter was applied to the individual echoes to reduce noise, and experimentally determined thresholds for the coefficient of determination ($r^2>0.4$) and sum of squared deviations due to error (SSE <0.2) were used to exclude data that did not have an acceptable straight-line fit when ln signal intensity (SI) was plotted against echo time.

The previously delineated ROI was applied to the T2* maps that had been registered to the precontrast T2W scan. The percent change in T2* value (%ΔT2*) after the administration of USPIO was calculated on a voxel-by-voxel basis and displayed on a color scale (%ΔT2*=(T2* value scan 1−T2* value scan 2)/(T2* value scan 1)×100). From the 95th percentile of the %ΔT2* value observed in a group of patients not receiving USPIO, we established a threshold

of significance for %ΔT2* of 59%, above which an observed change in T2* value can be attributed to USPIO uptake. All voxels with values for %ΔT2* below this threshold appear blue on the color map, whereas voxels above this threshold appear on a yellow-red color scale. This facilitates data interpretation and minimizes observer bias.

To assess the gadolinium enhancement on T1W images, the precontrast and postcontrast images were registered to the precontrast T2W image. The previously delineated ROI was applied to the T1 images. The percent change in SI was calculated (%Δ SI) on a voxel-by-voxel basis and displayed on a color scale (%Δ SI=(SI scan 2−SI scan 1)/(SI scan 1)×100). By convention, an increase in SI of >50% of the baseline value was taken to be significant.

Classification of Aneurysms

Cellular inflammation is an important pathological process in the development of AAA, with the associated proteolytic degradation of the aortic wall representing the key step leading to AAA expansion and rupture. We were interested to see whether aneurysm expansion rate is increased in aneurysms with USPIO uptake in (1) the aortic wall or (2) the associated thrombus. Therefore, 2 independent observers, blinded to the patient demographics, and aneurysm diameter, and growth rate, reviewed the color map images and classified them into 3 clear predefined groups according to their appearance:

Group 1 had no mural or thrombus USPIO uptake, except for isolated periluminal T2* enhancement occurring immediately adjacent to, and in continuity with, the lumen.

Group 2 had diffuse USPIO uptake that was distinct from the periluminal thrombus and the aortic wall.

Group 3 had focal areas (with at least 10 contiguous voxels) of USPIO uptake within the aortic wall of the aneurysm distinct from periluminal area and thrombus.

Differences in classification were resolved by consensus.

Histology

For patients undergoing open surgical repair within 48 hours of USPIO administration, samples of aortic wall were obtained from the arteriotomy site on the anterior aspect of the aneurysm sac. Samples were fixed in formalin, embedded in paraffin, sectioned, and stained to look at the architecture (hematoxylin and eosin and elastin–van Gieson) and USPIO accumulation (Prussian blue). The distribution of macrophages was assessed by immunohistochemical staining for macrophages (mouse, anti-human CD68 monoclonal antibody; DAKO).

Statistical Analysis

The data were normally distributed. Continuous data were compared with 1-way ANOVA with Tukey post test comparison (Minitab), and categorical data were analyzed using the χ^2 test with cross-tabulation (SPSS). Statistical significance was taken as 2-sided $P<0.05$.

Results

Patients

Twenty-nine patients (27 male) were recruited into the trial, with a mean age of 70±5 years and mean AAA diameter of 5.2 cm (range, 4.0 to 6.6 cm). All aneurysms were fusiform and confined to the abdominal aorta. One patient had an inflammatory aneurysm with ureteric obstruction and a raised erythrocyte sedimentation rate of 100 mm/h (reference range, 1 to 10 mm/h). The remaining patients were asymptomatic. As anticipated, patients had a range of cardiovascular risk factors and comorbidities (Table). During the study period, 4 patients underwent open surgical repair of their AAA (2 in group 1 and 2 in group 3), 2 patients were treated by endovascular aneurysm repair (1 in group 2 and 1 in group 3), and 1 patient in group 3 died of a ruptured aneurysm, having been assessed and considered unfit for operative intervention. It was not possible to calculate a growth rate for 4 patients (1 in group 1, 1 in group 2, and 2 in group 3) who had only a single diameter measurement, either because they proceeded straight to surgery or had only recently presented to the surveillance program.

Table. Clinical and Aneurysm Characteristics of Patients With Abdominal Aortic Aneurysm

	Group 1 (n = 7)	Group 2 (n = 9)	Group 3 (n = 13)	All (n = 29)
Age, y	70±4	72±6	69±6	70±5
Male:female, % men	7:0 (100)	9:0 (100)	11:2 (85)	27:2 (93)
Cigarette smokers				
Current	2 (29)	2 (22)	6 (46)	10 (34)
Previous	5 (71)	7 (78)	7 (54)	19 (66)
Diabetes mellitus	2 (29)	1 (11)	1 (8)	4 (14)
Hypertension	7 (100)	3 (33)	7 (54)	17 (59)
Hypercholesterolemia	6 (86)	7 (78)	8 (62)	21 (72)
Ischemic heart disease	4 (57)	2 (22)	6 (46)	12 (41)
Peripheral arterial disease	2 (29)	1 (11)	1 (8)	4 (14)
Cerebrovascular disease	1 (14)	1 (11)	1 (8)	3 (10)
Active systemic inflammatory disease	0 (0)	0 (0)	0 (0)	0 (0)
Active malignancy	0 (0)	0 (0)	0 (0)	0 (0)
Drugs				
Aspirin±clopidogrel	4 (57)	6 (67)	9 (69)	19 (66)
Warfarin	2 (29)	2 (22)	0 (0)	4 (14)
Statin	6 (86)	9 (100)	11 (85)	26 (90)
β-blocker	3 (43)	2 (22)	6 (46)	11 (38)
ACE inhibitor/ARB	3 (43)	2 (22)	4 (31)	9 (31)

Values are mean ± SD or n (%).

ACE indicate angiotensin-converting enzyme inhibitor; ARB, angiotensin II receptor blocker.

USPIO Administration

The administration of USPIO was well tolerated, with no significant adverse events. There was a relatively even distribution of patients within the three categories of USPIO uptake (Table). Patients in the 3 groups were similar in terms of age, sex, use of medications, initial aneurysm diameter, and all comorbidities except hypertension ($P=0.024$). In patients undergoing open surgical AAA repair, histology confirmed the accumulation of USPIO that colocated with immunohistochemical staining for CD68-positive macrophages (Figure 1).

MRI With USPIO

Patients had between 10 and 20 slices to cover the entire aneurysm with a total of 351 slices for analysis. Registration within the main body of the aneurysm was excellent for all scans although 9.7±1.39% of the data were discarded due to poor straight-line fit when ln SI was plotted against echo time. Classification of AAA according to USPIO uptake (Figure 2) was consistent and reproducible with excellent interobserver agreement and a κ statistic of 0.89. There appeared to be no differences in USPIO uptake whether or not patients had received preadministration of gadolinium.

The effect of USPIO accumulation is to accelerate dephasing of transverse magnetization, resulting in rapid loss of signal with

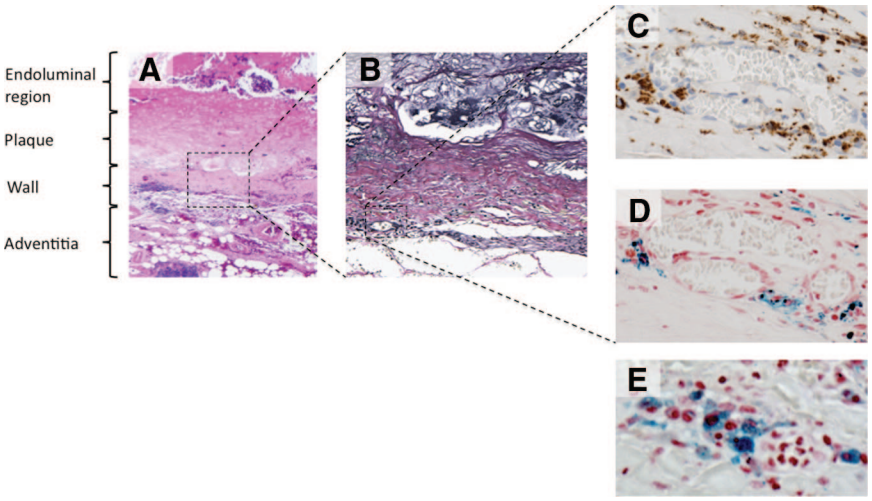

Figure 1. Representative histological sections of the aortic wall. **A**, Hematoxylin and eosin (×20) of the full thickness of the aortic wall including atherosclerotic plaque, adherent thrombus and periadventitial fatty tissue. **B**, Elastin–van Gieson stain (×100) of the aortic wall showing complete destruction of the normal wall structure including fibrosis (collagen, pink) of the media and adventitia and virtual absence of intact medial elastic fibers (black). **C**, Prussian blue staining for iron demonstrating colocalization of CD68-postive macrophages (×400; brown) with **D**, Ultrasmall superparamagnetic particles of iron oxide particles (×400;blue). **E**, High-power (×1000) Prussian blue staining shows intracytoplasmic accumulation of USPIO within macrophages.

increasing echo time and hence a reduction in the decay constant, the T2* value. The magnitude of the change in T2* value was encoded for each voxel, with a large reduction in T2* value reflecting a greater accumulation of USPIO. We have previously defined a threshold (59%) above which the change in T2* value can be attributed to USPIO accumulation rather than variability of the measurement. In all patients, there was nonspecific USPIO uptake in the periluminal region consistent with transition of the particles from the blood pool (Figure 2). Interestingly the same region of the thrombus enhanced rapidly on T1W MRI with gadolinium (Figure 3). In group 3, in addition to the presence of focal areas of USPIO uptake (at least 10 contiguous voxels), there was a higher proportion of USPIO-positive voxels in the aortic wall compared with the other 2 groups ($P<0.0001$), supporting the correct classification of patients into the 3 groups (Figure 4A).

Patients with distinct focal areas of increased USPIO uptake in the wall of the aneurysm (group 3) had aneurysm growth rates that were 3-fold higher than patients without (group 1) or with nonspecific (group 2) uptake of USPIO

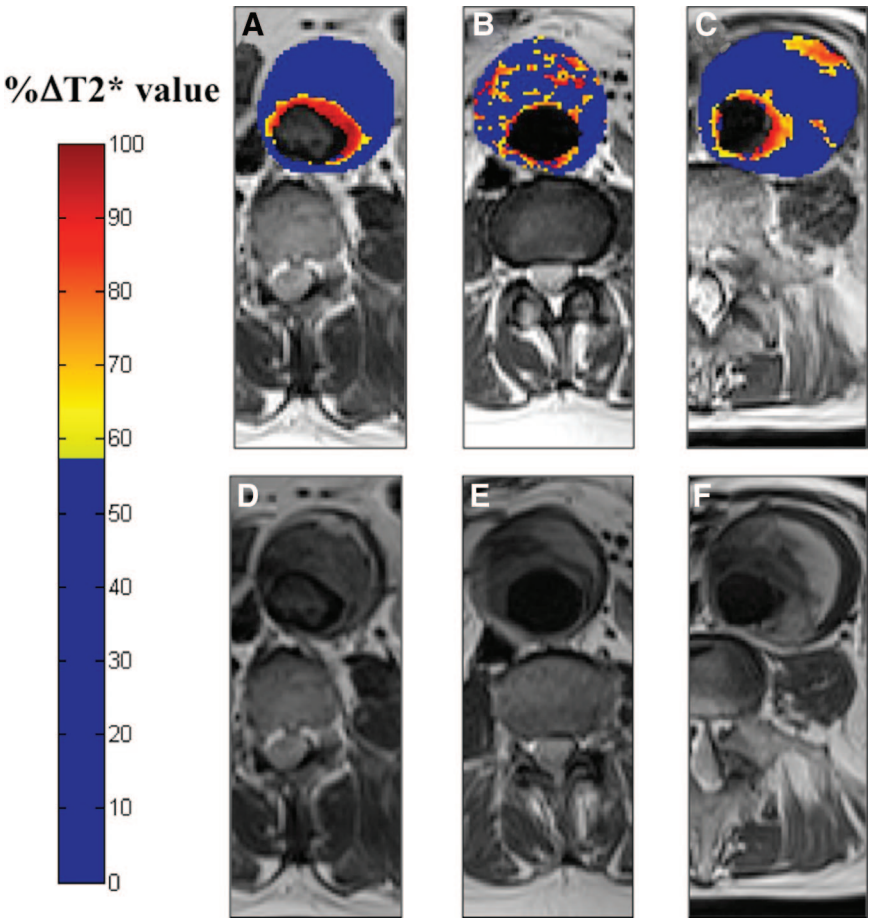

Figure 2. Color maps (**A** through **C**) showing representative abdominal aortic aneurysm (AAA) slices from patients in each of the 3 groups alongside the corresponding T2W anatomic images (**D** through **F**). The color scale represents the magnitude of the change in T2* value, with blue indicating minimal change and red indicating a large change in T2* value. We have previously defined the threshold above which changes in T2* value can be attributed to ultrasmall superparamagnetic particles of iron oxide particles (USPIO) accumulation. Only changes in T2* value above the threshold are presented on the graduated (yellow-red) color scale; data below the threshold appear blue. A distinctive pattern is seen for each patient group: **A**, Group 1 shows a large change in T2* value only in the periluminal area; **B**, group 2, diffuse patchy changes in T2* throughout the intraluminal thrombus but no distinct focal area of USPIO uptake affecting the aortic wall; and **C**, group 3, discrete focal area of USPIO uptake involving the wall of the AAA that is distinct from the periluminal region. This patient subsequently died suddenly from presumed ruptured AAA.

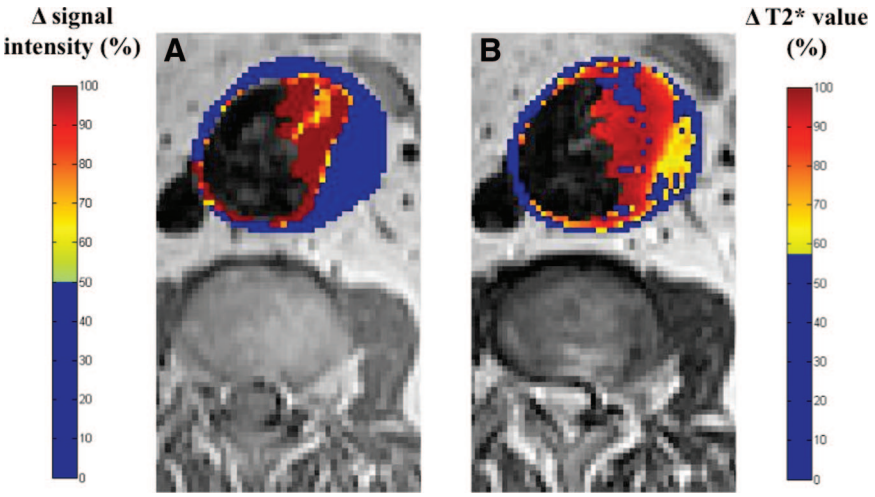

Figure 3. The blood pool contrast agent gadolinium (**A**) enhances only the periluminal halo region of the thrombus and the fibrous cap. Ultrasmall superparamagnetic particles of iron oxide particles (**B**) enhancement is seen not only in the periluminal halo but also in the deep layer of the thrombus and in the aortic wall.

(P=0.020; Figure 4B). Interestingly, there was no difference in baseline aneurysm diameter across the three groups (Figure 4B). The percentage of USPIO positive voxels in the aortic wall correlated with the AAA growth rate (r=0.46; P=0.028).

One patient in group 3 had an inflammatory aneurysm; a specific subtype of AAA characterized by systemic inflammation, a thickened, fibrosed aortic wall, and fibrosis and inflammation extending beyond the aorta into surrounding tissues. This produced a unique change in T2* pattern with intense USPIO uptake extending beyond the wall of the AAA (Figure 5).

Discussion

We have shown for the first time that uptake of USPIO in AAAs identifies cellular inflammation and appears to distinguish those patients with more rapidly progressive abdominal aortic aneurysm expansion. This technique holds major promise as a new method of risk-stratifying patients with AAAs that extends beyond the simple anatomic measure of aneurysm diameter.

We used a smart contrast agent that consists of 20-nm dextran-coated iron oxide nanoparticles. After intravenous administration, these USPIO circulate within the blood pool with a long half-life and are engulfed by macrophages. They accumulate at sites of cellular inflammation at sufficient concentrations to cause signal changes on MRI. As a result of their superparamagnetic properties, they induce local field inhomogeneities leading to rapid dephasing of the transverse magnetization of spinning protons and thus loss of coherent signal. Although these agents exhibit T1 relaxivity, the predominant extravascular effect of USPIO at 3T is to cause a dropout of signal on T2W and especially T2*W images.[28] Because of the mixed T1 and T2/T2* effects of USPIO, we chose to measure their effect on the rate of exponential signal decay by calculating the decay constant, T2* value, from the signal intensities at 4 echo times rather than relying on the signal intensity at a single echo time. This proved to be a highly sensitive technique, and variations in the change of T2* value identified areas of cellular inflammation that were confirmed on subsequent histological examination of aneurysm tissue obtained at the time of open surgery.

Within the study population, we observed distinct patterns of spatial variation in the change of T2* value and were able to divide patients into 3 groups on this basis. Patients in group 1 had a high change in T2* value only in the periluminal

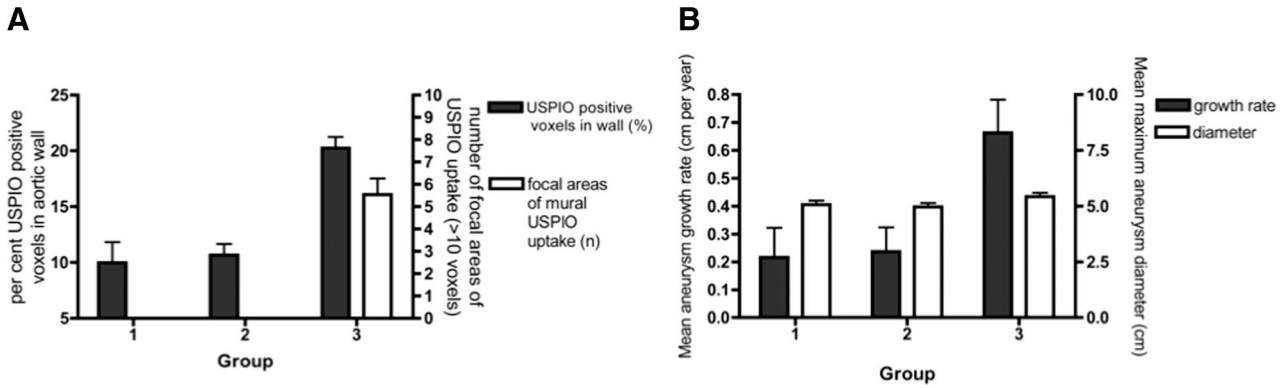

Figure 4. A, Percent ultrasmall superparamagnetic particles of iron oxide particles (USPIO)-positive voxels in the aortic wall (solid bars) and focal areas of increase USPIO uptake (open bars). USPIO-positive voxels were higher in group 3 compared with the other 2 groups (P<0.001). **B**, Relationship of diameter and growth rate with patient group. Initial aneurysm diameters (open bars) are similar for the 3 groups, but the aneurysm growth rates (solid bars) are higher for patients in group 3 (0.66 cm/y) compared with those in groups 1 (0.22 cm/y) and 2 (0.24 cm/y; P=0.020).

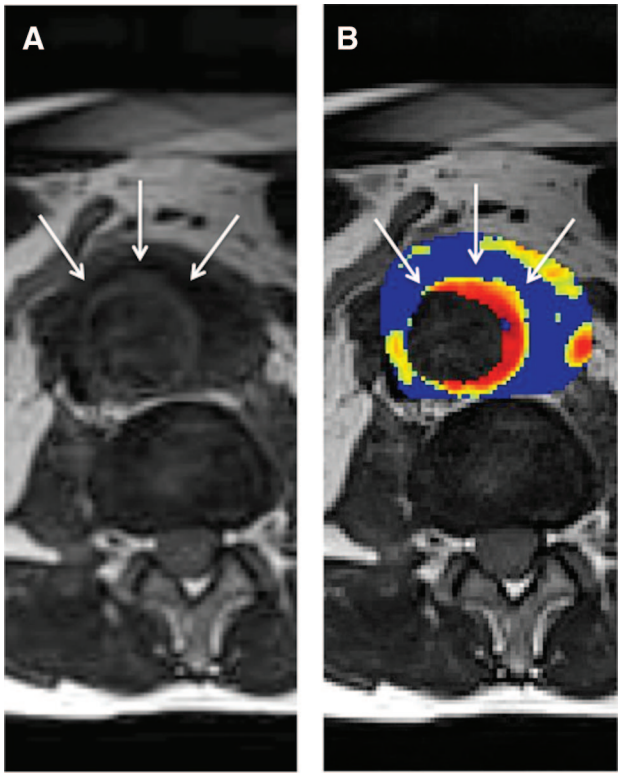

Figure 5. A, Distinctive appearance of an inflammatory abdominal aortic aneurysm (AAA) on T2W imaging. The aortic wall is indicated by arrows. **B**, Regions with a large percent change in T2* value are present outwith the aortic wall showing inflammation extending into surrounding tissues as is typical of an inflammatory AAA (see color scale Figure 2). This patient had ureteric obstruction and an erythrocyte sedimentation rate of >100 mm/h (reference range, 1 to 10 mm/h).

aspect of the aneurysm, this "halo effect" being a constant finding in all study patients. Intraluminal thrombus is a consistent feature of AAA and usually has a laminar appearance with the mural component having been deposited first and subsequent growth of the thrombus occurring by further deposition of fibrin, platelets, and red blood cells on the inner luminal aspect.[29] The universal finding of a large change in T2* value in the periluminal region of the aneurysm is therefore likely to reflect trapping of USPIO in fresh potentially gelatinous thrombus that is typically friable and highly cellular because of its close proximity to flowing blood.[30] It was interesting to observe that this region also enhanced rapidly with gadolinium, consistent with a less selective and more generalized uptake of contrast agents in this region. A previous study using the larger SPIO particles (80 to 150 nm) demonstrated their accumulation in the luminal layer of aortic thrombus, resulting in an MRI signal that correlated with histological evidence of leukocyte infiltration (CD68 and CD66b) and levels of matrix metalloproteinases.[31] As acknowledged by the authors, these large SPIO particles are not well suited to vascular tissue imaging because of their short plasma half-life that limits their sensitivity for detecting vessel wall inflammation.

The second group of patients had a heterogeneous pattern of change in T2* signal within the thrombus but no uptake in the aortic wall. The role of the thrombus in aneurysm expansion and rupture is uncertain.[30,32,33] Some macrophages are present deep within the thrombus, but, alternatively, this signal pattern may reflect USPIO within the canaliculi that traverse the thrombus, conducting fluid, small molecules and, to a certain extent, cells from the lumen toward the aortic wall.[30] This pattern of USPIO uptake and inflammation within the thrombus is of uncertain significance but interestingly did not appear to be associated with accelerated aneurysm growth.

In the third group of patients, we found 1 or more distinct focal areas of inflammation involving the wall itself and spatially distinct from the periluminal halo. This finding was associated with an increased growth rate compared to patients without mural USPIO uptake. This high growth rate (0.66 cm/y) is clinically significant because the average aneurysm growth in screened populations is 0.26 cm/y, and growth rates >0.2 cm/y are associated with increased AAA-related events.[34–36] We are unable to exclude the possibility that differences in the incidence of hypertension among patients in the 3 groups influenced AAA growth rate; however, this seems unlikely because the groups with the highest (group 2) and lowest (group 1) incidence of hypertension had similarly low growth rates. In patients with ruptured AAA, histology of the aneurysm wall has shown areas of increased biological activity and these correlate with a reduction in wall tensile strength.[9–12] It would be interesting to determine whether, in patients with AAA and abdominal pain of uncertain etiology, USPIO imaging could distinguish between those with impending rupture and those with non–AAA-related abdominal pain. Finally, whether this pattern of USPIO uptake in AAA may prove to be a marker for future AAA-related events is unclear and requires a large, prospective study.

Existing techniques for surveillance of AAA and estimation of risk of rupture rely solely on diameter measurements, but clinical data from aneurysm screening and surveillance programs suggest that there is considerable scope to improve on this. Of those aneurysms detected by screening that are <5.5 cm in diameter, 1 in 14 will rupture over the following 3 years[34] and together account for up to one-fifth of all ruptured AAA.[7] However, simply reducing the diameter threshold for intervention would not improve mortality.[4,6] Furthermore, small aneurysms exhibit a bimodal distribution for growth with half remaining small and only half continuing to grow.[34] Having been shown to reduce AAA-related mortality by 53%, aneurysm screening is being introduced in many countries across the world.[1,37] However, screening considerably increases the number of patients under long-term surveillance, and only around 30% of these patients will require future intervention.[1,34] Taken together, these observations support a need for a more sophisticated and individualized method of predicting clinical events in patients with AAA so that screening, surveillance, and intervention can be targeted at high-risk patients, reducing the overall economic cost and decreasing morbidity and mortality. We believe USPIO imaging represents a logical and important new approach that has the potential to address these major unmet clinical needs.

In conclusion, we have demonstrated that assessment of USPIO uptake with MRI can be used to detect focal hotspots

of inflammation in asymptomatic AAA and that mural USPIO uptake is associated with more rapid expansion of AAA. A large prospective clinical trial with a longer duration of follow-up would be required to confirm the findings of the present study and assess the role of MRI and USPIO in the prediction of AAA-related clinical events. This would also enable a more sophisticated MRI-based assessment of growth and its relationship to areas of USPIO uptake. If successful, this technique has a number of potential highly relevant clinical applications that include informing selection of patients for intervention to prevent rupture, rationalization of AAA screening resources to target high-risk patients, and application as a biomarker to investigate the utility of novel therapeutic interventions for AAA.

Acknowledgments

We are grateful to the staff of the Vascular Surgical Service, the Wellcome Trust Clinical Research Facility, and the Clinical Research Imaging Centre for their help with this study.

Sources of Funding

This work was supported by the British Heart Foundation including a BHF Clinical PhD Training Fellowship (FS/07/060; Dr Richards).

Disclosures

Guerbet Pharmaceuticals provided the contrast agent (Sinerem) but did not provide further funding or contribute to the study design, data analysis, or interpretation of results.

References

1. Ashton HA, Buxton MJ, Day NE, Kim LG, Marteau TM, Scott RA, Thompson SG, Walker NM. The Multicentre Aneurysm Screening Study (MASS) into the effect of abdominal aortic aneurysm screening on mortality in men: a randomised controlled trial. *Lancet*. 2002;360:1531–1539.
2. Office for National Statistics in England and Wales, Mortality Statistics, 2008.
3. General Register Office for Scotland Mortality Statistics, 2008.
4. Mortality results for randomised controlled trial of early elective surgery or ultrasonographic surveillance for small abdominal aortic aneurysms: the UK Small Aneurysm Trial Participants. *Lancet*. 1998;352:1649–1655.
5. Hirsch AT, Haskal ZJ, Hertzer NR, Bakal CW, Creager MA, Halperin JL, Hiratzka LF, Murphy WR, Olin JW, Puschett JB, Rosenfield KA, Sacks D, Stanley JC, Taylor LM Jr, White CJ, White J, White RA, Antman EM, Smith SC Jr, Adams CD, Anderson JL, Faxon DP, Fuster V, Gibbons RJ, Hunt SA, Jacobs AK, Nishimura R, Ornato JP, Page RL, Riegel B. ACC/AHA Guidelines for the Management of Patients with Peripheral Arterial Disease (lower extremity, renal, mesenteric, and abdominal aortic): a collaborative report from the American Associations for Vascular Surgery/Society for Vascular Surgery, Society for Cardiovascular Angiography and Interventions, Society for Vascular Medicine and Biology, Society of Interventional Radiology, and the ACC/AHA Task Force on Practice Guidelines (writing committee to develop guidelines for the management of patients with peripheral arterial disease): summary of recommendations. *J Vasc Interv Radiol*. 2006;17:1383–1398.
6. Lederle FA, Wilson SE, Johnson GR, Reinke DB, Littooy FN, Acher CW, Ballard DJ, Messina LM, Gordon IL, Chute EP, Krupski WC, Busuttil SJ, Barone GW, Sparks S, Graham LM, Rapp JH, Makaroun MS, Moneta GL, Cambria RA, Makhoul RG, Eton D, Ansel HJ, Freischlag JA, Bandyk D. Immediate repair compared with surveillance of small abdominal aortic aneurysms. *N Engl J Med*. 2002;346:1437–1444.
7. Darling RC, Messina CR, Brewster DC, Ottinger LW. Autopsy study of unoperated abdominal aortic aneurysms: the case for early resection. *Circulation*. 1977;56:II161–II164.
8. Powell JT, Brown LC, Greenhalgh RM, Thompson SG. The rupture rate of large abdominal aortic aneurysms: is this modified by anatomical suitability for endovascular repair? *Ann Surg*. 2008;247:173–179.
9. Vallabhaneni SR, Gilling-Smith GL, How TV, Carter SD, Brennan JA, Harris PL. Heterogeneity of tensile strength and matrix metalloproteinase activity in the wall of abdominal aortic aneurysms. *J Endovasc Ther*. 2004;11:494–502.
10. Choke E, Thompson MM, Dawson J, Wilson WR, Sayed S, Loftus IM, Cockerill GW. Abdominal aortic aneurysm rupture is associated with increased medial neovascularization and overexpression of proangiogenic cytokines. *Arterioscler Thromb Vasc Biol*. 2006;26:2077–2082.
11. Wilson WR, Anderton M, Schwalbe EC, Jones JL, Furness PN, Bell PR, Thompson MM. Matrix metalloproteinase-8 and -9 are increased at the site of abdominal aortic aneurysm rupture. *Circulation*. 2006;113:438–445.
12. Thompson MM, Jones L, Nasim A, Sayers RD, Bell PR. Angiogenesis in abdominal aortic aneurysms. *Eur J Vasc Endovasc Surg*. 1996;11:464–469.
13. Cai J, Hatsukami TS, Ferguson MS, Kerwin WS, Saam T, Chu B, Takaya N, Polissar NL, Yuan C. In vivo quantitative measurement of intact fibrous cap and lipid-rich necrotic core size in atherosclerotic carotid plaque: comparison of high-resolution, contrast-enhanced magnetic resonance imaging and histology. *Circulation*. 2005;112:3437–3444.
14. Kramer CM, Cerilli LA, Hagspiel K, DiMaria JM, Epstein FH, Kern JA. Magnetic resonance imaging identifies the fibrous cap in atherosclerotic abdominal aortic aneurysm. *Circulation*. 2004;109:1016–1021.
15. Harisinghani MG, Barentsz J, Hahn PF, Deserno WM, Tabatabaei S, van de Kaa CH, de la Rosette J, Weissleder R. Noninvasive detection of clinically occult lymph-node metastases in prostate cancer. *N Engl J Med*. 2003;348:2491–2499.
16. Heesakkers RA, Hovels AM, Jager GJ, van den Bosch HC, Witjes JA, Raat HP, Severens JL, Adang EM, van der Kaa CH, Futterer JJ, Barentsz J. MRI with a lymph-node-specific contrast agent as an alternative to CT scan and lymph-node dissection in patients with prostate cancer: a prospective multicohort study. *Lancet Oncol*. 2008;9:850–856.
17. Kooi ME, Cappendijk VC, Cleutjens KB, Kessels AG, Kitslaar PJ, Borgers M, Frederik PM, Daemen MJ, van Engelshoven JM. Accumulation of ultrasmall superparamagnetic particles of iron oxide in human atherosclerotic plaques can be detected by in vivo magnetic resonance imaging. *Circulation*. 2003;107:2453–2458.
18. Trivedi RA, Mallawarachi C, JM UK-I, Graves MJ, Horsley J, Goddard MJ, Brown A, Wang L, Kirkpatrick PJ, Brown J, Gillard JH. Identifying inflamed carotid plaques using in vivo USPIO-enhanced MR imaging to label plaque macrophages. *Arterioscler Thromb Vasc Biol*. 2006;26:1601–1606.
19. Tang TY, Howarth SP, Miller SR, Graves MJ, Patterson AJ, JM UK-I, Li ZY, Walsh SR, Brown AP, Kirkpatrick PJ, Warburton EA, Hayes PD, Varty K, Boyle JR, Gaunt ME, Zalewski A, Gillard JH. The ATHEROMA (Atorvastatin Therapy: Effects on Reduction of Macrophage Activity) Study: evaluation using ultrasmall superparamagnetic iron oxide-enhanced magnetic resonance imaging in carotid disease. *J Am Coll Cardiol*. 2009;53:2039–2050.
20. Bernd H, De Kerviler E, Gaillard S, Bonnemain B. Safety and tolerability of ultrasmall superparamagnetic iron oxide contrast agent: comprehensive analysis of a clinical development program. *Invest Radiol*. 2009;44:336–342.
21. Bourrinet P, Bengele HH, Bonnemain B, Dencausse A, Idee JM, Jacobs PM, Lewis JM. Preclinical safety and pharmacokinetic profile of ferumoxtran-10, an ultrasmall superparamagnetic iron oxide magnetic resonance contrast agent. *Invest Radiol*. 2006;41:313–324.
22. Muller K, Skepper JN, Posfai M, Trivedi R, Howarth S, Corot C, Lancelot E, Thompson PW, Brown AP, Gillard JH. Effect of ultrasmall superparamagnetic iron oxide nanoparticles (Ferumoxtran-10) on human monocyte-macrophages in vitro. *Biomaterials*. 2007;28:1629–1642.
23. Ruehm SG, Corot C, Vogt P, Kolb S, Debatin JF. Magnetic resonance imaging of atherosclerotic plaque with ultrasmall superparamagnetic particles of iron oxide in hyperlipidemic rabbits. *Circulation*. 2001;103:415–422.
24. Turner GH, Olzinski AR, Bernard RE, Aravindhan K, Boyle RJ, Newman MJ, Gardner SD, Willette RN, Gough PJ, Jucker BM. Assessment of macrophage infiltration in a murine model of abdominal aortic aneurysm. *J Magn Reson Imaging*. 2009;30:455–460.
25. Wilson KA, Hoskins PR, Lee AJ, Fowkes FG, Ruckley CV, Bradbury AW. Ultrasonic measurement of abdominal aortic aneurysm wall compliance: a reproducibility study. *J Vasc Surg*. 2000;31:507–513.
26. Kurvers H, Veith FJ, Lipsitz EC, Ohki T, Gargiulo NJ, Cayne NS, Suggs WD, Timaran CH, Kwon GY, Rhee SJ, Santiago C. Discontinuous,

staccato growth of abdominal aortic aneurysms. *J Am Coll Surg*. 2004; 199:709–715.
27. Trivedi RA, U-King-Im JM, Graves MJ, Cross JJ, Horsley J, Goddard MJ, Skepper JN, Quartey G, Warburton E, Joubert I, Wang L, Kirkpatrick PJ, Brown J, Gillard JH. In vivo detection of macrophages in human carotid atheroma: temporal dependence of ultrasmall superparamagnetic particles of iron oxide-enhanced MRI. *Stroke*. 2004;35:1631–1635.
28. Corot AC, Port M. Guilbert I, Robert P, Raynal I, Robic C, Raynaud J-S, Prigent P, Dencausse A, Idee J-M. Superparamagnetic Contrast Agents. In: Modo MMJ, Bulte JWM, eds. *Molecular and Cellular MR Imaging*. Boca Raton, FL: CRC Press; 2007:60–78.
29. Touat Z, Ollivier V, Dai J, Huisse MG, Bezeaud A, Sebbag U, Palombi T, Rossignol P, Meilhac O, Guillin MC, Michel JB. Renewal of mural thrombus releases plasma markers and is involved in aortic abdominal aneurysm evolution. *Am J Pathol*. 2006;168:1022–1030.
30. Adolph R, Vorp DA, Steed DL, Webster MW, Kameneva MV, Watkins SC. Cellular content and permeability of intraluminal thrombus in abdominal aortic aneurysm. *J Vasc Surg*. 1997;25:916–926.
31. Nchimi A, Defawe O, Brisbois D, Broussaud TK, Defraigne JO, Magotteaux P, Massart B, Serfaty JM, Houard X, Michel JB, Sakalihasan N. MR imaging of iron phagocytosis in intraluminal thrombi of abdominal aortic aneurysms in humans. *Radiology*. 2010;254:973–981.
32. Kazi M, Zhu C, Roy J, Paulsson-Berne G, Hamsten A, Swedenborg J, Hedin U, Eriksson P. Difference in matrix-degrading protease expression and activity between thrombus-free and thrombus-covered wall of abdominal aortic aneurysm. *Arterioscler Thromb Vasc Biol*. 2005;25: 1341–1346.
33. Vorp DA, Lee PC, Wang DH, Makaroun MS, Nemoto EM, Ogawa S, Webster MW. Association of intraluminal thrombus in abdominal aortic aneurysm with local hypoxia and wall weakening. *J Vasc Surg*. 2001;34: 291–299.
34. Thompson AR, Cooper JA, Ashton HA, Hafez H. Growth rates of small abdominal aortic aneurysms correlate with clinical events. *Br J Surg*. 2010;97:37–44.
35. Lederle FA, Johnson GR, Wilson SE, Ballard DJ, Jordan WD Jr, Blebea J, Littooy FN, Freischlag JA, Bandyk D, Rapp JH, Salam AA. Rupture rate of large abdominal aortic aneurysms in patients refusing or unfit for elective repair. *JAMA*. 2002;287:2968–2972.
36. Brady AR, Thompson SG, Fowkes FG, Greenhalgh RM, Powell JT. Abdominal aortic aneurysm expansion: risk factors and time intervals for surveillance. *Circulation*. 2004;110:16–21.
37. Screening for abdominal aortic aneurysm: recommendation statement. *Ann Intern Med.* 2005;142:198–202.

CLINICAL PERSPECTIVE

Abdominal aortic aneurysm (AAA) rupture is a catastrophic event associated with a very high mortality rate. Patients with known AAA are therefore enrolled in a surveillance program involving serial ultrasound scanning to monitor changes in aneurysm diameter, taken as a surrogate for risk of rupture. Patients with an aneurysm >5.5 cm in diameter are perceived to be at high risk and are offered surgical or endovascular aneurysm repair. Although AAA diameter is the best predictor of rupture currently available, up to 20% of ruptured AAA are <5.5 cm. Large studies have shown no mortality benefit for early surgery over continued surveillance in this group of patients. Conversely, many patients have AAA considerably larger than 5.5 cm without rupture. We therefore need an improved method of predicting rupture for individual patients. Rupture is thought to occur in regions of the aortic wall featuring intense inflammation and proteolytic activity. We used MRI with a novel contrast agent consisting of ultrasmall superparamagnetic particles of iron oxide (USPIO) to identify focal inflammation within the aortic wall. The key finding is that USPIO uptake within the aortic wall was associated with a rate of aneurysm expansion (0.66 cm/y) 3-fold higher than AAA with no mural USPIO uptake. If confirmed in larger longitudinal studies, these results suggest that USPIO-enhanced MRI may be a more accurate way to predict disease progression than diameter alone in patients with AAA, facilitating selection of patients for preventative surgery.

Circulation
Cardiovascular Imaging
JOURNAL OF THE AMERICAN HEART ASSOCIATION

American Heart Association
Learn and Live

In Vivo Mononuclear Cell Tracking Using Superparamagnetic Particles of Iron Oxide : Feasibility and Safety in Humans

Jennifer M.J. Richards, Catherine A. Shaw, Ninian N. Lang, Michelle C. Williams, Scott I.K. Semple, Thomas J. MacGillivray, Calum Gray, Julie H. Crawford, Shirjel R. Alam, Anne P.M. Atkinson, Elaine K. Forrest, Carol Bienek, Nicholas L. Mills, Anne Burdess, Kev Dhaliwal, A. John Simpson, William A. Wallace, Adam T. Hill, P. Huw Roddie, Graham McKillop, Thomas A. Connolly, Giora Z. Feuerstein, G. Robin Barclay, Marc L. Turner and David E. Newby

Circ Cardiovasc Imaging 2012;5;509-517; originally published online July 10, 2012;
DOI: 10.1161/CIRCIMAGING.112.972596
Circulation: Cardiovascular Imaging is published by the American Heart Association. 7272 Greenville Avenue, Dallas, TX 72514
 Print ISSN: 1941-9651. Online ISSN: 1942-0080

In Vivo Mononuclear Cell Tracking Using Superparamagnetic Particles of Iron Oxide

Feasibility and Safety in Humans

Jennifer M.J. Richards, MD*; Catherine A. Shaw, PhD*; Ninian N. Lang, MD, PhD; Michelle C. Williams, MD; Scott I.K. Semple, PhD; Thomas J. MacGillivray, PhD; Calum Gray, PhD; Julie H. Crawford, MD; Shirjel R. Alam, MD; Anne P.M. Atkinson; Elaine K. Forrest; Carol Bienek, PhD; Nicholas L. Mills, MD, PhD; Anne Burdess, MD; Kev Dhaliwal, MD; A. John Simpson, MD, PhD; William A. Wallace, MD; Adam T. Hill, MD; P. Huw Roddie, MD; Graham McKillop, MD; Thomas A. Connolly, PhD; Giora Z. Feuerstein, PhD; G. Robin Barclay, PhD; Marc L. Turner, MD, PhD; David E. Newby, MD, PhD

Background—Cell therapy is an emerging and exciting novel treatment option for cardiovascular disease that relies on the delivery of functional cells to their target site. Monitoring and tracking cells to ensure tissue delivery and engraftment is a critical step in establishing clinical and therapeutic efficacy. The study aims were (1) to develop a Good Manufacturing Practice–compliant method of labeling competent peripheral blood mononuclear cells with superparamagnetic particles of iron oxide (SPIO), and (2) to evaluate its potential for magnetic resonance cell tracking in humans.

Methods and Results—Peripheral blood mononuclear cells $1–5\times10^9$ were labeled with SPIO. SPIO-labeled cells had similar in vitro viability, migratory capacity, and pattern of cytokine release to unlabeled cells. After intramuscular administration, up to 10^8 SPIO-labeled cells were readily identifiable in vivo for at least 7 days using magnetic resonance imaging scanning. Using a phased-dosing study, we demonstrated that systemic delivery of up to 10^9 SPIO-labeled cells in humans is safe, and cells accumulating in the reticuloendothelial system were detectable on clinical magnetic resonance imaging. In a healthy volunteer model, a focus of cutaneous inflammation was induced in the thigh by intradermal injection of tuberculin. Intravenously delivered SPIO-labeled cells tracked to the inflamed skin and were detectable on magnetic resonance imaging. Prussian blue staining of skin biopsies confirmed iron-laden cells in the inflamed skin.

Conclusions—Human peripheral blood mononuclear cells can be labeled with SPIO without affecting their viability or function. SPIO labeling for magnetic resonance cell tracking is a safe and feasible technique that has major potential for a range of cardiovascular applications including monitoring of cell therapies and tracking of inflammatory cells. (***Circ Cardiovasc Imaging*. 2012;5:509-517.**)

Clinical Trial Registration—URL: http://www.clinicaltrials.gov; Unique identifier: NCT00972946, NCT01169935.

Key Words: inflammation ■ macrophages ■ magnetic resonance imaging

Stem cell and other cell-based therapies have emerged as potential, novel treatment options for a wide range of diseases including acute myocardial infarction and severe heart failure.[1–5] Ensuring the delivery of a sufficient number of cells to the target site is critical to the development and assessment of these therapies. Several methods have been proposed for tracking cells in vivo, but their translation into the clinical setting has been hampered for many reasons including limitations of the imaging modality in humans and the failure of reagents to comply with Good Manufacturing Practice (GMP) standards: a prerequisite for clinical use.

Clinical Perspective on p 517

Received January 6, 2012; accepted May 31, 2012.

From the Centre of Cardiovascular Science (J.M.J.R., C.A.S., N.N.L., M.C.W., S.R.A., N.L.M., A.B., D.E.N.), Clinical Research Imaging Centre (J.M.J.R., M.C.W., S.I.K.S., T.J.M., C.G., G.M., D.E.N.), Centre for Regenerative Medicine (J.H.C., G.R.B., M.L.T.), Centre for Inflammation Research, University of Edinburgh (K.D., A.J.S.), and Department of Pathology (W.A.W.), University of Edinburgh, Edinburgh; Scottish National Blood Transfusion Service Cell Therapy Research Group, Edinburgh (J.H.C., G.R.B., M.L.T.); Scottish National Blood Transfusion Service, Edinburgh (A.P.M.A., E.K.F., C.B.); Institute of Cellular Medicine, Newcastle University, Newcastle upon Tyne (A.J.S.); Department of Respiratory Medicine (A.T.H.), Department of Haematology (P.H.R.), and the Department of Radiology (G.M.), National Health Service (NHS) Lothian, Edinburgh; and Translational Medicine Research Collaboration, Glasgow (T.A.C., G.Z.F.), United Kingdom.

*Drs Richards and Shaw contributed equally to this work.

The online-only Data Supplement is available with this article at http://circimaging.ahajournals.org/lookup/suppl/doi:10.1161/CIRCIMAGING.112.972596/-/DC1.

Correspondence to Jennifer M.J. Richards, MD, Centre of Cardiovascular Science, The University of Edinburgh, The Chancellor's Building, Little France Crescent, Edinburgh EH16 5SA, United Kingdom. E-mail jenny.richards@ed.ac.uk

Radio-imaging techniques, such as scintigraphy and positron emission tomography, can be sensitive but offer poor spatial resolution and expose patients to ionizing radiation. In addition, although some radiotracers have a long half-life (eg, 89-Zircuronium 78.4 h, 124-Iodine 100.3 h) those that are most widely available have a short half-life (eg, 18-Fluorine), limiting the duration of follow-up. By virtue of its high spatial resolution, excellent soft tissue contrast, and avoidance of ionizing radiation, magnetic resonance imaging (MRI) is ideally suited to human cell-tracking studies. MRI contrast agents consisting of dextran-coated superparamagnetic particles of iron oxide (SPIO) are available for use in humans and have been used for clinical liver imaging. SPIO possess intense superparamagnetism and, by inducing local magnetic field inhomogeneities, cause rapid dephasing of spinning protons. The T2* relaxation time is shortened, causing a profound reduction in signal intensity on T2- and particularly T2*-weighted (T2*W) imaging. Compared with paramagnetic agents such as gadolinium, SPIO are detectable at much lower concentrations and are readily taken up by resident macrophages in the reticuloendothelial system. SPIO are not toxic to cells and are biodegradable in vivo.[6–11] It is important to note, however, that the safety of intravenous administration of SPIO-labeled cells in humans has yet to be demonstrated, and would be critical for the development and Food and Drug Administration approval of novel clinical cell-tracking agents.

An effective method has been described for incorporating SPIO into phagocytic cells using protamine sulphate as a polycationic transfection agent to enhance its uptake through electrostatic interactions.[12] We have modified and translated this method into a GMP-compliant protocol and successfully (1) labeled human peripheral blood mononuclear cells (PBMC), (2) confirmed normal cell viability and function, and (3) delivered and tracked SPIO-labeled cells in vivo in humans.

Methods

Ethical and Regulatory Considerations

Clinical studies (NCT00972946; NCT01169935) were approved by the local research ethics committee and conducted in accordance with the Declaration of Helsinki with the written informed consent of all participants.

Cell Labeling With SPIO

Cell Collection

Blood was collected by venesection into citrate or by leukapheresis (COBE Spectra; Gambro BCT, Lakewood, CO) to yield 1–5×10^8 or 1–5×10^9 PBMC, respectively.

Edinburgh Protocol for Labeling Mononuclear Cells With SPIO

A GMP-compliant protocol for labeling PBMC with SPIO was optimized (online-only Data Supplement Methods and online-only Data Supplement Figure I). PBMC were isolated by density-gradient separation and suspended in 0.9% saline (4×10^6 cells/mL). Endorem (100 μg/mL; Guerbet, Villepinte, France) and protamine sulphate (4 μg/mL; Prosulf) were added to the cell suspension, which was incubated at room temperature for 2 hours with continuous agitation.

For clinical studies, cell preparation and labeling was undertaken in a GMP facility. At the end of the incubation period, labeled cells were supplied in a low-adherence bag (Cryocyte; Baxter, Deerfield, IL) for reinfusion.

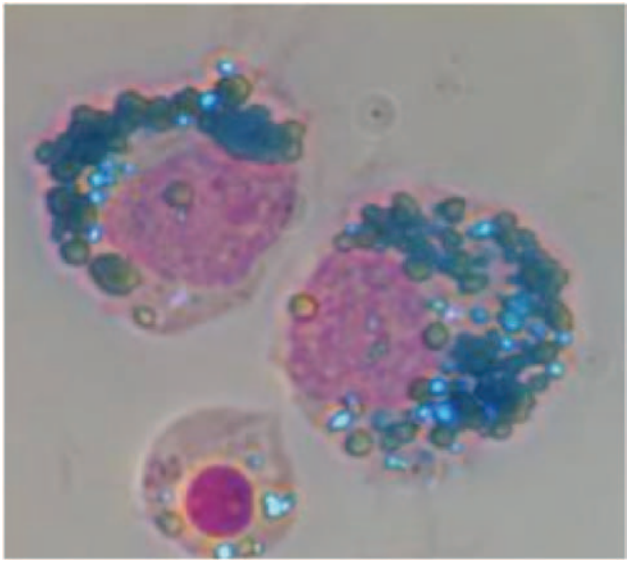

Figure 1. Cellular uptake of superparamagnetic particles of iron oxide (SPIO). Cytospin preparation of peripheral blood mononuclear cells (PBMC) labeled with SPIO and stained with Prussian blue and Nuclear Fast red. Iron nanoparticles are seen within the cytoplasm.

Evaluation of the Effects of SPIO Labeling on Cell Viability and Function

Isolation of Monocytes From PBMC

Monocytes were isolated from PBMC suspensions using indirect immunomagnetic selection (Monocyte Isolation Kit II; Miltenyi Biotec, Auburn, CA).

Cellular Iron Uptake

Cellular SPIO uptake was confirmed by Prussian blue staining of methanol-fixed cytospin preparations. Cellular iron content was determined using the Ferrozine assay (Sigma-Aldrich, Gillingham, Dorset, United Kingdom).

Cell Viability

Monocytes were allowed to adhere for 1 hour in 24-well tissue culture plates (10^6 cells per well; 37°C; 5% CO_2) after which the supernatant was harvested and exchanged to prevent continued uptake of SPIO and to avoid interference of excess SPIO with assays.

SPIO-labeled and unlabeled cells were harvested at 1, 24, and 72 hours, exposed to fluorescein isothiocyanate-annexin V and propidium iodide, and analyzed by flow cytometry. The percentages of cells positive for annexin V binding, propidium iodide staining, or both were combined to give the percentage cytotoxicity. Viability was also assessed at 24, 48, and 72 hours using a colorimetric lactate dehydrogenase assay (Roche Diagnostics Ltd, West Sussex, United Kingdom).

Cytokine Release

Cells were plated out as described in the preceding section. The concentration of the proinflammatory cytokines released from cells 24, 48, and 72 hours postlabeling was measured using a cytometric bead array kit (Becton Dickinson, Franklin Lakes, NJ).

Migratory Capacity

In vitro migratory capacity was assessed using a modified Boyden chamber. Labeled and unlabeled purified monocytes (2.5×10^5 cells per well) were allowed to migrate for 2 hours through a microporous (5 μmol/L) membrane (Corning Costar, Corning, NY) toward monocyte chemoattractant protein-1 (R&D Systems, Abingdon, United Kingdom). Transmigration was quantified by counting the cells adherent to the undersurface of the membrane.

Clinical Studies

Participants underwent formal clinical assessment and were excluded if they had renal dysfunction (estimated glomerular filtration rate <25 mL/min), hepatic dysfunction (Childs-Pugh score B or C), positive virology screen, pregnancy, breastfeeding, blood dyscrasia, anemia (hemoglobin concentration <12g/dL), iron storage disorder, active malignancy, chronic inflammatory condition, risk factors for protamine allergy, intercurrent illness, or contraindication to MRI scanning.

Intramuscular Administration

Six healthy volunteers received three 2-mL intramuscular thigh injections of unlabeled autologous PBMC (10^7), SPIO-labeled autologous PBMC (10^7), and SPIO alone. Participants underwent MRI scanning in a 1.5 T scanner immediately and at 7 days.

Phased-Dose Intravenous Administration of Labeled Cells

To establish the safety of intravenous administration of SPIO-labeled cells, we undertook a phased-dosing study in which 2 volunteers each received 6 increasing doses of SPIO-labeled autologous PBMC (10^4–10^9 cells) over 4 study visits. Cell infusions were performed in a clinical research facility with noninvasive physiological monitoring (pulse oximetry, noninvasive blood pressure, and temperature) and clinical observation during cell reinfusion and the subsequent observation period. Cells were administered through a blood giving set with a 200-μmol/L macroaggregate filter. Each cell infusion lasted 30 to 60 minutes (depending on volume) and was followed by a 60-minute observation period.

Blood was sampled at each visit before reinfusion and 1 hour postinfusion of labeled cells. Blood was drawn for full blood count, routine biochemistry, and coagulation parameters including prothrombin time, activated partial thromboplastin time, fibrinogen, and D-dimer.

Intravenous Administration of Labeled Cells

Twelve healthy volunteers were recruited and received a low dose of SPIO-labeled autologous PBMC obtained from a 250-mL venesection (≈$1–5\times10^8$ cells; n=6) or a high dose of cells obtained from a standard leukapheresis collection (≈$1–5\times10^9$ cells; n=6). Intravenous cell infusions were performed, and blood samples were obtained as described earlier in the article. These participants underwent MRI scanning in a 3T scanner before and 2 hours, 24 hours, 48 hours, and 7 days after administration of cells.

Mantoux Test

A local cutaneous inflammatory response was induced in the thigh of healthy volunteers using the Mantoux test: intradermal injection of 2 units of tuberculin purified protein derivative. In previously exposed individuals, tuberculin purified protein derivative stimulates a type IV delayed, cell-mediated hypersensitivity reaction involving an influx of neutrophils initially (≈6 hours), and subsequently of monocytes (12–48 hours) and lymphocytes (12–96 hours) into the dermal skin layer.[13,14] Twenty-four hours after the Mantoux test, participants underwent a standard leukapheresis collection and later the same day received an infusion of ≈10^9 SPIO-labeled autologous PBMC. T2-weighted and T2*W imaging was performed before and 2, 24, and 48 hours after the administration of cells. A skin biopsy was obtained from the site of the Mantoux test 96 hours after administration of cells (120 hours after the Mantoux test), fixed in 4% paraformaldehyde and stained with Prussian blue.

Magnetic Resonance Imaging

Volunteers receiving cells intramuscularly underwent MRI scanning of the thigh in a 1.5 T Phillips scanner using a T2-weighted sequence with a long echo time (TE; 137 ms).

Volunteers undergoing intravenous infusions were scanned using a 3T Magnetom Verio scanner (Siemens, Erlangen, Germany). Routine localizer sequences were applied after which T2-weighted (TE 87 ms; repetition time 1800 ms; matrix 256×192; field of view 380×285 mm) and T2*W (multiecho TE, 4.1–22.1 ms; repetition time, 100 ms; flip angle, 15°; matrix, 282×512; field of view, 282×410 mm; slice width, 5 mm) breath-hold sequences were used to acquire axial images of the upper abdomen.

T1-weighted (3-dimensional volumetric interpolated breath-hold examination; TE/repetition time, 2.0/5.5ms; matrix, 416×416; field of view, 210×210 mm; slice width, 5mm) and T2*W (2-dimensional multislice gradient echo; TE, 9.8, 12.3, 14.8ms; repetition time, 120.0ms; matrix size, 312×384; field of view, 203×250 mm; slice width, 5mm) axial images of the thigh were acquired after Mantoux testing.

Image Analysis

After local administration of SPIO or cells, T2-weighted axial images of the thigh were inspected for evidence of a change in signal intensity.

After systemic administration of SPIO-labeled cells, transaxial abdominal images were analyzed on the basis of R2*. T2* is the decay constant for the decay of signal intensity with increasing TE, and its inverse R2* (T2*=1/R2*) has been used to evaluate tissue iron concentration.[15]

From the multiecho T2*W data, a 6-echo R2* map was generated. Regions of interest were selected on the initial echo (4.1 ms) taking care to avoid major blood vessels and motion artifact. Five regions of consistent size (0.5 cm^2) were selected in the spleen, liver, skeletal muscle (control), and background noise, and copied to the R2* map. Relationship to distinctive anatomical features was used to ensure that regions chosen were consistent across the 5 study visits.

For cell tracking to the site of the Mantoux test, higher spatial resolution was required to allow visualization of the skin and subcutaneous tissue. The individual echoes were acquired separately and had to be registered together for R2* map generation using in-house software. Regions of interest were selected in the inflamed skin, normal unaffected skin (control), skeletal muscle (control), liver, and spleen.

Statistical Analysis

In vitro data were analyzed by Mann-Whitney *U* test. Blood results and physiological monitoring data were compared by Wilcoxon signed rank test (SPSS Inc, Chicago, IL). R2* MRI data were analyzed by the Friedman test with Dunn correction. Exact testing was used throughout, and 2-sided $P<0.05$ was regarded as statistically significant.

Results

In Vitro Evaluation of the Effect of SPIO Labeling on Cell Viability and Function

It is important that the behavior of SPIO-labeled mononuclear cells remains unchanged in terms of cell viability and function so that the results of in vivo cell-tracking studies accurately reflect the biological processes being observed. See online-only Data Supplement Methods section for more detail.

Confirmation of SPIO Uptake

Prussian blue staining of labeled cells demonstrated intracellular accumulation of iron nanoparticles (Figure 1). The entire PBMC population, including both lymphocytes and monocytes, was exposed to SPIO but SPIO uptake was predominantly confined to phagocytic monocytes (online-only Data Supplement Figure II). The median (interquartile range) iron content of labeled monocytes was 17 (14–22) pg per cell compared with 1.3 (0.7–1.4) pg per cell for unlabeled monocytes (P=0.03).

Assessment of Cytotoxicity

SPIO labeling had no effect on cellular release of inflammatory cytokines (Figure 2). Viability of labeled and unlabeled cells was equivalent up to 72 hours postlabeling (Figure 3A and 3B).

Effect of SPIO Labeling on Chemotaxis

Cell-tracking studies are critically dependent on the ability of labeled cells to migrate to the target site. Cells labeled according to the optimized Edinburgh protocol migrated in equivalent

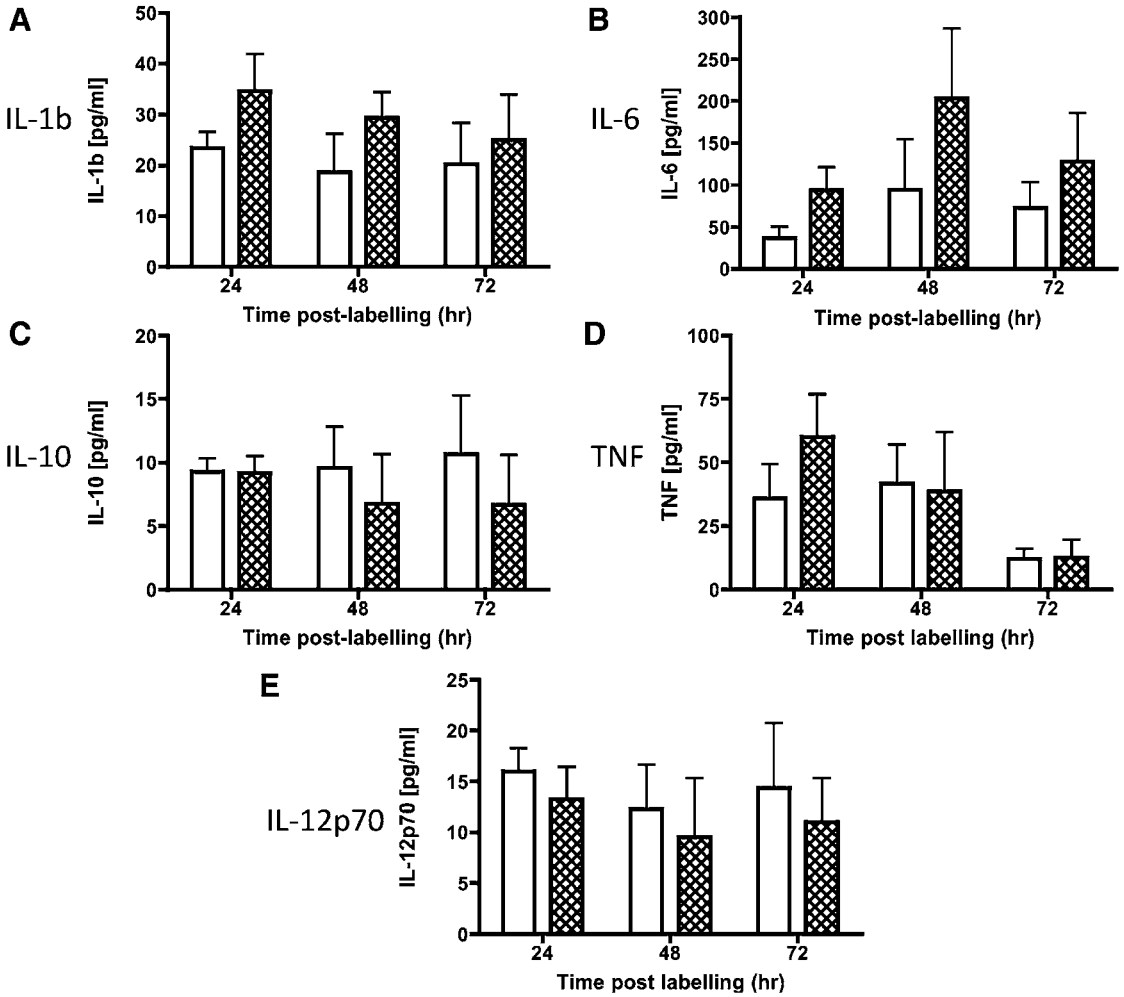

Figure 2. Effect of superparamagnetic particles of iron oxide (SPIO) labeling on cytokine release. SPIO labeling did not affect the cytokine (interleukin-1 [IL-1], IL-6, IL-10, tumor necrosis factor [TNF], IL-12p70) release profile up to 72 hours postlabeling ($P>0.05$ for all cytokines, at all time points; n=4).

numbers to unlabeled cells (154 [150–184] SPIO-labeled cells versus 112 [105–188] unlabeled cells at 50-ng/mL monocyte chemoattractant protein-1; median [interquartile range]; $P=0.29$). Prussian blue staining confirmed the presence of SPIO in the cytoplasm of migrating labeled cells. (Figure 3C–3I)

Clinical Studies

Intramuscular Administration

Injections were performed successfully in all participants without complication. A signal deficit was observed at the site of administration of SPIO alone and SPIO-labeled cells (Figure 4). Although an edematous change was noted at the site of injection of unlabeled cells, no dropout of signal was seen. These findings were consistent for all 6 participants and persisted for at least 7 days.

Safety of Intravenous Administration of SPIO-Labeled Cells

In the phased-dosing study, all cell infusions in both participants were well tolerated with no early or late clinical side effects. A further 12 volunteers then received a low dose ($2.03\pm0.18\times10^8$ cells; n=6) or a high dose of SPIO-labeled autologous PBMC obtained from a standard leukapheresis collection ($2.23\pm0.51\times10^9$ cells; n=6).

Cell infusions had no effect on heart rate, blood pressure, or temperature (Table 1), and there were no clinically significant microembolic events after cell administration. Peripheral perfusion, monitored continuously by digital pulse oximetry during and for an hour after cell infusion, was unaffected. Demonstrating further that labeled cells did not have a procoagulant effect in vivo, infusion of SPIO-labeled cells did not affect any coagulation variable, and there were no clinically significant effects on routine clinical hematological and biochemical variables (Table 2).

MRI Scanning

After administration of labeled cells, the signal intensity was reduced in the liver and spleen on T2- (Figure 5) and T2*W imaging.

The use of 6 TEs for R2* value calculation was validated by plotting signal intensity against TE. Even at longer TE, the signal was clearly distinct from the background noise level, and exponential decay of signal intensity with time was confirmed.

There was a marked increase in R2* in the liver and spleen ($P<0.001$) after administration of cells (Figure 5) reflecting dose-dependent accumulation of SPIO-labeled cells at these sites. There was no change in R2* in skeletal muscle (negative control).

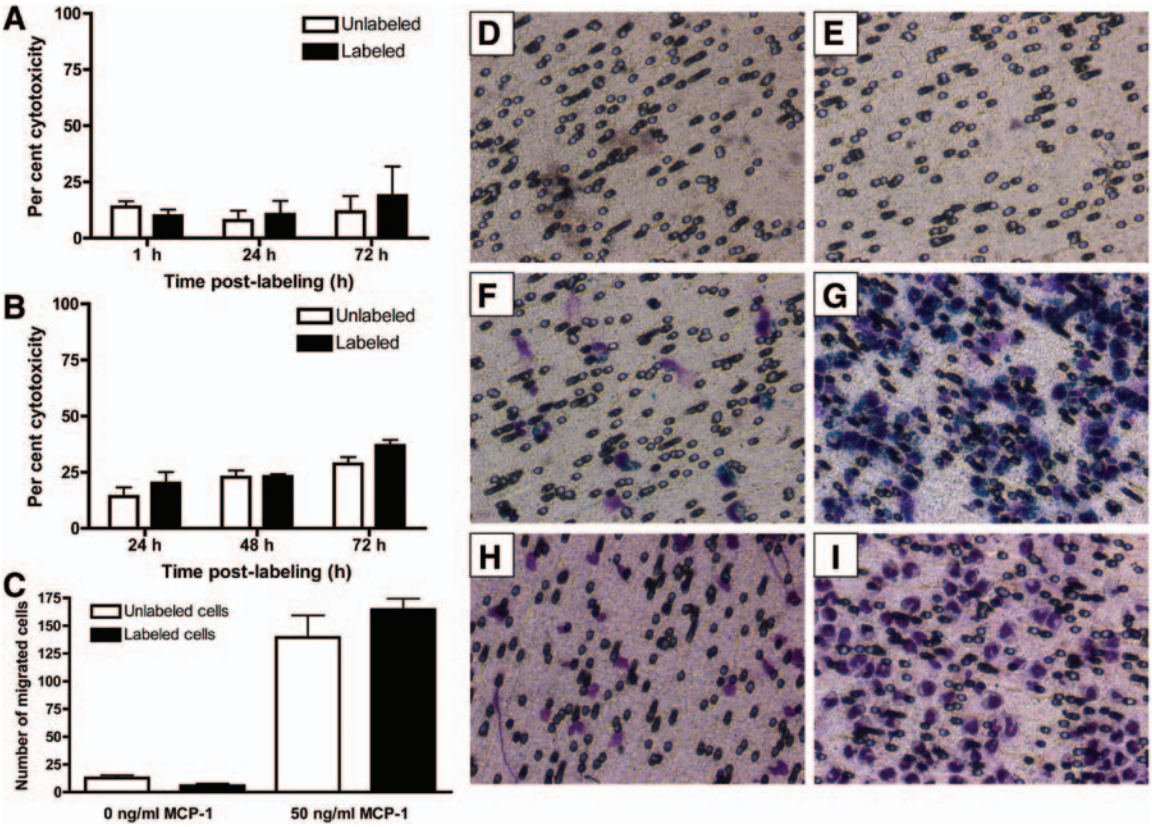

Figure 3. Effect of superparamagnetic particles of iron oxide (SPIO) labeling on cell viability and chemotaxis. Labeling mononuclear cells with SPIO had no effect on cell viability measured either by flow cytometric analysis of annexin V binding in combination with propidium iodide (PI) staining (**A**) or a colorimetric assay for lactate dehydrogenase release (**B**). There was no difference in viability between unlabeled and labeled cells at any time point investigated ($P>0.05$ for both methods at all time points; n=3). In an in vitro migration assay, cells were allowed to migrate through a 5-μmol/L microporous membrane toward 0 or 50 ng/mL of the chemokine human recombinant monocyte chemoattractant protein-1 (MCP-1). **C**, Quantification of chemotaxis demonstrated that SPIO labeling did not affect migratory capacity compared with unlabeled cells ($P>0.05$ for both 0 and 50 ng/mL MCP-1; n=6). Migrated cells adhered to the undersurface of the membrane and were stained with DiffQuik physiological stain (staining nuclei purple) and counterstained with Prussian blue causing SPIO particles carried in the cytoplasm to appear blue. Comparison was made of cells labeled according to the original protocol, which clumped and were unable to migrate (**D** and **E**), with cells labeled according to the Edinburgh protocol (**F** and **G**) that remained in single cell suspension and migrated in equivalent numbers to unlabeled cells (**H** and **I**).

Cell Tracking to an Inflammatory Focus

At 24 and 48 hours after administration of SPIO-labeled cells, an increase in R2* was observed in inflamed skin ($P<0.001$) but not adjacent normal skin or skeletal muscle ($P>0.05$; Figure 6). Prussian blue staining of skin biopsies obtained from the site of the Mantoux test 96 hours after administration of cells, revealed occasional iron-laden cells in the inflamed skin consistent with the diminishing monocyte/macrophage cell numbers by this stage in a type IV hypersensitivity response. In controls (negative Mantoux response),

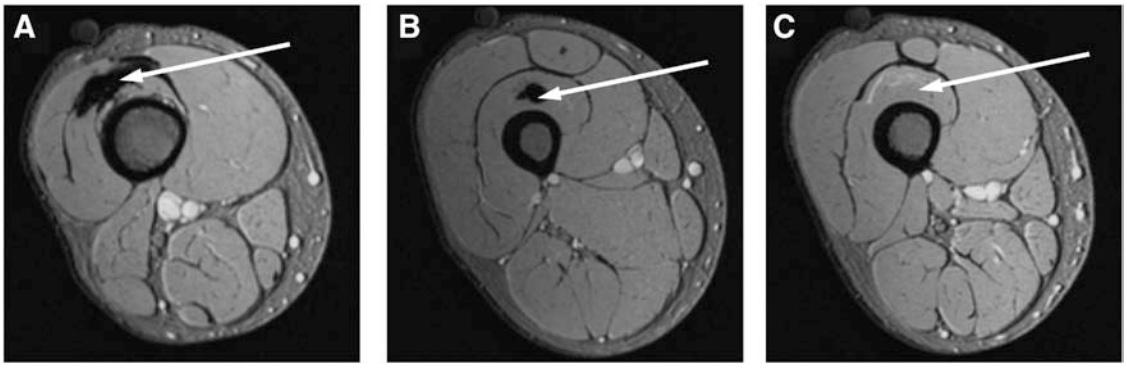

Figure 4. Magnetic resonance imaging scanning after intramuscular administration of cells. T2-weighted imaging of the thigh after intramuscular administration of labeled cells. A signal deficit is seen in relation to injection of superparamagnetic particles of iron oxide (SPIO) alone (**A**) and SPIO-labeled cells (**B**) but not unlabeled cells (**C**). These findings were consistent for all 6 participants.

Table 1. Noninvasive Physiological Monitoring Parameters (Median and IQR) Before and at the End of Infusion of 1–5×109 SPIO-Labeled PBMC (n=12)

	Preinfusion Median (IQR)	Postinfusion Median (IQR)	*P*
Systolic blood pressure, mm Hg	126 (120–133)	121 (114–130)	0.13
Diastolic blood pressure, mm Hg	74 (68–85)	74 (67–79)	0.69
Heart rate, beats per minute	67 (58–78)	68 (58–76)	0.20
Temperature, °C	36.9 (36.4–37.0)	36.9 (36.7–37.2)	0.42
Oxygen saturations on air, %	99 (98–100)	99 (98–100)	1.00

IQR indicates interquartile range; PBMC, peripheral blood mononuclear cells; and SPIO, superparamagnetic particles of iron oxide.

Table 2. Hematological, Biochemical, and Coagulation Variables Before and After Infusion of 1–5×109 SPIO-Labeled PBMC (n=12)

	Normal Range	Preinfusion Median (IQR)	Postinfusion Median (IQR)	*P*
Hemoglobin, g/L	115–165	133 (120–148)	130 (120–140)	0.06
White blood count,×10^9/L	4.0–11.0	5.9 (5.2–7.6)	7.4 (5.4–9.7)	0.28
Platelets,×10^9/L	150–350	259 (195–274)	235 (194–280)	0.33
Prothrombin time, s	10.5–13.5	11 (11–12)	11 (11–12)	0.18
Activated partial thromboplastin time, s	26–36	29 (29–32)	30 (27–32)	0.67
Fibrinogen, g/L	1.5–4	2.9 (2.3–3.4)	2.7 (2.3–3.2)	0.10
D-Dimer, ng/mL	0–230	—	67 (52–200)	—
Urea, mmol/L	2.5–6.6	4.4 (3.6–5.2)	4.4 (4.0–5.1)	0.68
Creatinine, μmol/L	60–120	64 (58–78)	67 (52–78)	0.67
Sodium, mmol/L	135–145	140 (139–141)	140 (138–141)	0.40
Potassium, mmol/L	3.6–5.0	4.1 (3.8–4.4)	4.0 (3.9–4.2)	0.26
TCO_2, mmol/L	20–30	27 (25–28)	27 (25–30)	0.16
Bilirubin, μmol/L	3–16	11 (9–15)	10 (8–15)	0.31
Alanine amino transferase, U/L	10–55	20 (16–22)	19 (14–30)	0.57
Alkaline phosphatase, U/L	40–125	72 (53–82)	68 (48–89)	0.67

PBMC indicates peripheral blood mononuclear cells; SPIO, superparamagnetic particles of iron oxide; IQR indicates interquartile range; and TCO_2, total CO2.

there was no change in R2* in the skin at the site of the Mantoux test, in adjacent normal skin, or in skeletal muscle (*P*>0.05; Figure 7).

Discussion

In the present study, we have demonstrated, for the first time, that human mononuclear cells can be labeled with SPIO under GMP-compliant conditions without affecting cell viability or migratory capacity. Furthermore, labeled cells can be visualized in vivo at clinically relevant field strengths after local or systemic administration, and it is important to note that SPIO-labeled cells can be tracked to a site of focal inflammation in humans. This technique therefore has the potential to track the distribution, time course, and fate of cells administered systemically as part of cell therapy: a critical component of the

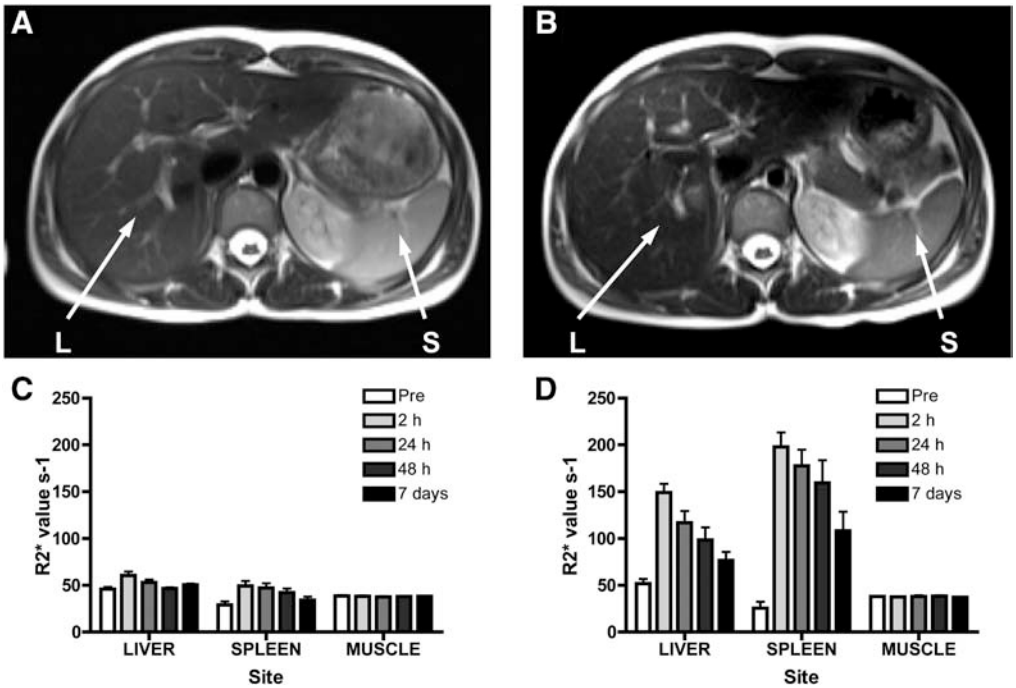

Figure 5. Magnetic resonance imaging of the upper abdomen after systemic administration of cells. T2-weighted transaxial slice through the upper abdomen before (**A**) and after (**B**) intravenous administration of superparamagnetic particles of iron oxide (SPIO)-labeled cells. Signal intensity is reduced in the liver (L) and spleen (S) after administration of cells. Change in R2* from baseline 2 hours, 24 hours, 48 hours, and 7 days after intravenous administration of a low dose (**C**; 1–5×10^8 peripheral blood mononuclear cells [PBMC]; n=6) or a high dose (**D**; 1–5×10^9 PBMC; n=6) of SPIO-labeled cells. An increase in R2* is seen in the spleen (*P*<0.001) and liver (*P*<0.001) but not skeletal muscle (control; *P*>0.05).

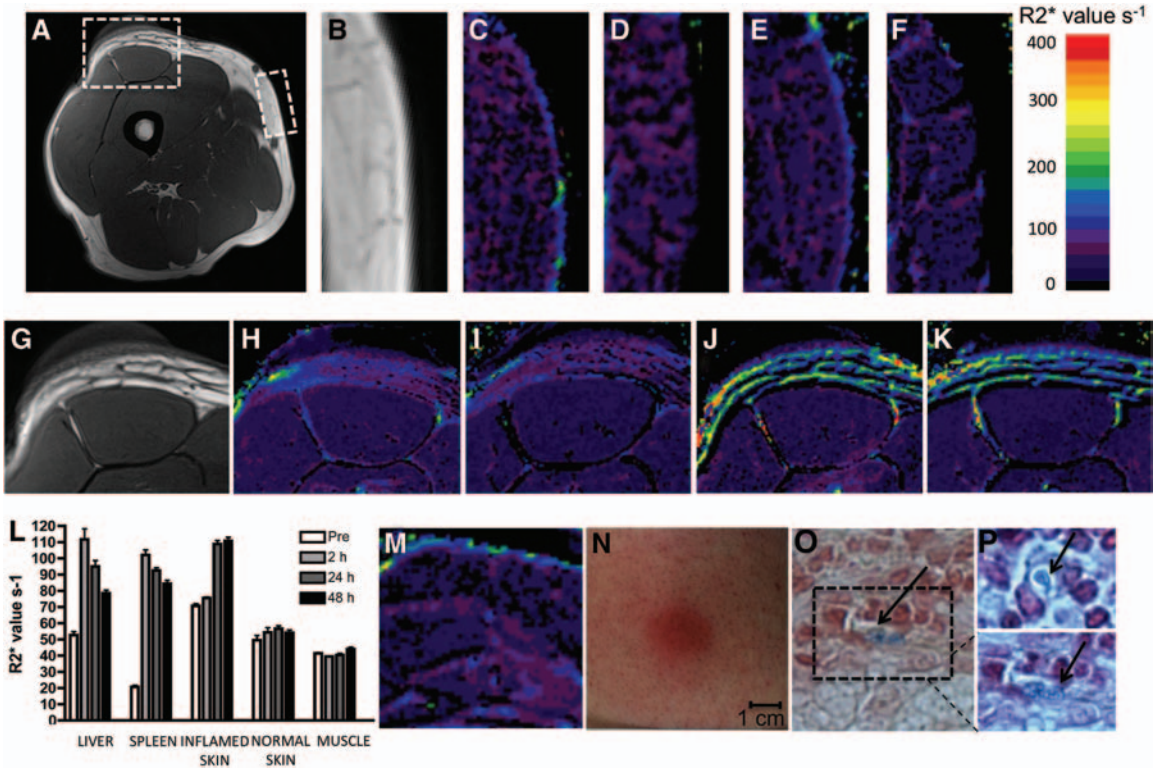

Figure 6. Cell tracking to a region of cutaneous inflammation. **A**, T1-weighted axial image of the thigh 24 hours after the Mantoux test and (**B**) a magnified area of normal unaffected skin/subcutaneous tissue. A thick layer of aqueous jelly was applied to the skin to minimize artifact occurring at the interface between the outer layer of skin and the surrounding air. R2* maps before (**C**) and 2 hours (**D**), 24 hours (**E**), and 48 hours (**F**) after infusion of superparamagnetic particles of iron oxide (SPIO)–labeled cells show no change in R2* in normal skin/subcutaneous tissue on the medial aspect of the thigh after cell administration. The skin and subcutaneous tissue thickens in the region of the Mantoux test on the anterior thigh (**G**). Corresponding R2* maps of this inflamed skin (**H**) show a marked increase in R2* 2 hours (**I**), 24 hours (**J**), and 48 hours (**K**) after administration of SPIO-labeled cells. Consistent with accumulation of SPIO-labeled cells, a significant increase in R2* is observed 24 and 48 hours after cell administration in inflamed skin in the region of the Mantoux test (**L**; $P<0.001$) as well as in the liver and the spleen ($P<0.001$), but not in unaffected normal skin or skeletal muscle (control; $P>0.05$). No change in R2* was seen if labeled cells were administered in the absence of a positive Mantoux response (**M**). The strongly positive cutaneous response to the Mantoux test is clearly visible in the anterior thigh (**N**). SPIO-loaded cells are seen on Prussian blue staining of a skin biopsy from this area 96 hours after cell infusion (**O** and **P**).

development of cellular therapeutic strategies, and ultimately of monitoring the success of treatment.

It is essential that techniques for labeling cells for cell-tracking studies do not impair cell function. We were able to demonstrate in vitro that cells labeled according to the Edinburgh protocol were viable and exhibit normal in vitro migration toward the chemokine monocyte chemoattractant protein-1.

There are several mechanisms through which SPIO might logically be expected to affect cell viability and function. However, it would appear that monocytes and macrophages, as professional scavengers, have an excellent capacity to deal with ingested iron and resist potentially toxic effects.[16] We have demonstrated in vitro that viability, cytokine production, and migratory capacity are unaffected by SPIO labeling. This is consistent with the majority of studies that have shown preservation of both viability and function after SPIO labeling of a variety of cell types including mesenchymal, hematopoietic, neural, and adipose-derived stem cells,[6–11] with only a few reporting adverse effects and 1 showing increased proliferation of SPIO-labeled mesenchymal stem cells.[17–19] It is worth recognizing the diversity in cell-labeling protocols used across these studies that may explain such findings.

It is important to note that we have shown for the first time that intravenous administration of SPIO-labeled cells in humans is safe. Although several SPIO agents have been approved for intravenous administration, the Food and Drug Administration has not approved the intravenous administration of cells labeled with SPIO ex vivo. These safety data are therefore critical for the further development and subsequent Food and Drug Administration approval of novel SPIO-based cell-tracking agents, facilitating translation into the clinical setting. Although ferumoxide (Endorem, Feridex) is no longer clinically available, several alternative agents are currently being developed for clinical use. We have here shown the feasibility of SPIO cell tracking and established the potential use of SPIO as reporters for novel cell-tracking agents.[20]

Several recent publications have reported tracking of labeled cells to a site of inflammation after both local and systemic administration in the preclinical setting.[21–26] Migration of cells to a target site has also been demonstrated in humans after local administration. de Vries et al[27] labeled human dendritic cells with ultrasmall SPIO (20nm diameter), injected them directly into peripheral lymph nodes in patients with melanoma, and demonstrated their migration to regional lymph nodes on MRI scanning and histology of surgical resection specimens.

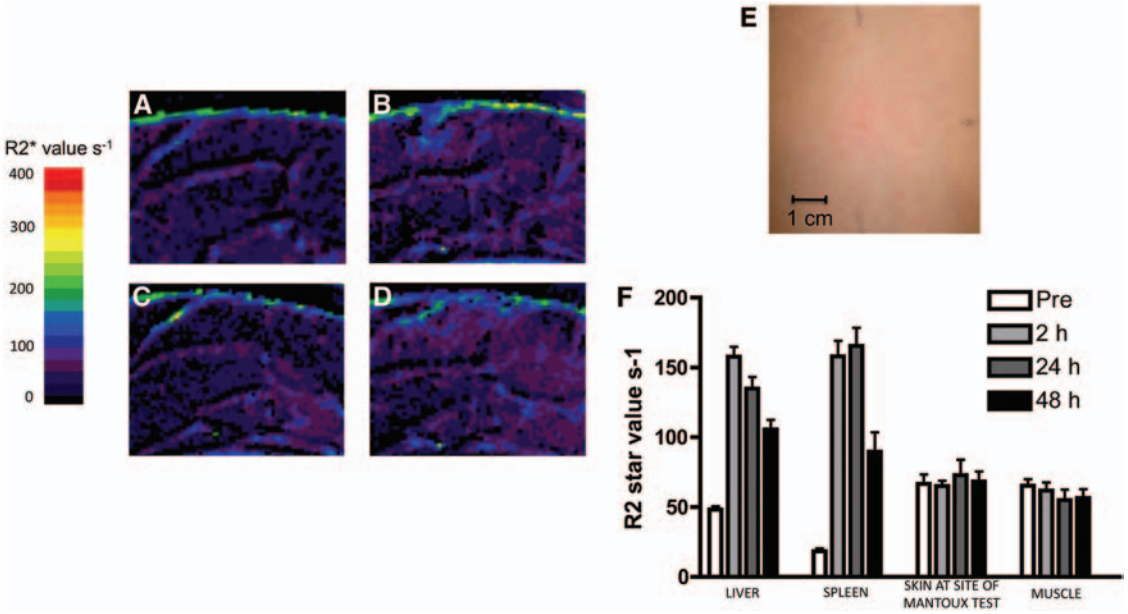

Figure 7. Negative Mantoux response (control). R2* maps before (**A**) and 2 hours (**B**), 24 hours (**C**), and 48 hours (**D**) after infusion of superparamagnetic particles of iron oxide (SPIO)–labeled cells show no change in R2* in skin and subcutaneous tissue at the site of the Mantoux test after cell administration, although there is some artifact at the skin interface in all 4 images. There is no evidence of an inflammatory response in the skin at the site of the Mantoux test (**E**). **F**, R2* increased significantly in the liver and spleen ($P<0.001$) but not in the skin at the site of the Mantoux test or skeletal muscle ($P>0.05$) after administration of SPIO-labeled cells.

SPIO-labeled pancreatic islet cells have been detected in the liver after portal venous administration, and SPIO-labeled mesenchymal stem cells have been tracked to the site of injury after intracerebral injection in a patient with a traumatic brain injury.[28,29] However, this is the first report of successful tracking of SPIO-labeled cells to a target site after systemic intravenous administration. This finding substantially broadens the potential applications for SPIO-labeled cell tracking.

We have shown that at clinically relevant field strengths, it is readily possible to image ≈10^8 mononuclear cells (containing ≈1–5×10^7 monocytes) after local or intravenous administration, and others have imaged as few as 1.5×10^5 cells in a target site after local delivery of 7.5×10^6 cells.[27] If there was any concern regarding the effect of SPIO labeling on the likely success of cell-based treatments, it would therefore be possible to label a small but representative proportion of the total number of cells given, allowing visualization of the fate and distribution of cells, but leaving the majority of cells for engraftment or other desired function. For nontherapeutic applications such as inflammatory cell tracking, a much higher dose of labeled cells could be administered to increase the sensitivity for detecting labeled cells in the target site. We have demonstrated that 1–5×10^9 SPIO-labeled autologous PBMC can be given safely: 100-fold greater than that needed for detection on MRI scanning.

An alternative control for the Mantoux component of the present study would have been to administer saline or unlabeled cells to participants with a positive Mantoux response, and this could be undertaken as part of a future study. It is acknowledged that although MRI can detect accumulation of SPIO-labeled cells at a target site, further quantification of cell number is currently challenging because clustering of iron nanoparticles magnifies their magnetic effects, confounding attempts at quantification. However, novel positive imaging sequences may address this issue in the future. Further work is required to establish the duration of specificity of SPIO accumulation in tissues to indicate the continued presence of delivered cells at the target site. It would also be important to define the time course of SPIO clearance from tissues if serial administration of cells was considered.

In conclusion, this is the first report of successful magnetic resonance cell tracking in humans after systemic administration of cells. Using a GMP-compliant protocol, human mononuclear cells can be labeled with SPIO on a clinical scale without affecting their viability or migratory capacity, and intravenous administration of SPIO-labeled cells in humans is safe. Cells can be imaged at clinical MRI field strengths after local or systemic administration. This technology for in vivo cell tracking has many potential cardiovascular applications that include monitoring of cell-based therapies for cardiovascular disease and dynamic leukocyte trafficking.

Acknowledgments

We thank the staff of the Wellcome Trust Clinical Research Facility, the Scottish National Blood Transfusion Service, the Cell Separator Unit, and the Clinical Research Imaging Centre for their contribution to the study, along with the Orthotics Department, the nursing staff of the Tuberculosis Clinic and nurses of the Royal Infirmary of Edinburgh.

Sources of Funding

This work was supported by an award from the Translational Medicine Research Collaboration. Drs Newby (CH/09/002), Richards (FS/07/060), and Semple (Centre of Research Excellence Award) were supported by the British Heart Foundation. The Wellcome Trust Clinical Research Facility and the Clinical Research Imaging Centre were supported by NHS Research Scotland through NHS Lothian.

Disclosures

None.

References

1. Gyöngyösi M, Lang I, Dettke M, Beran G, Graf S, Sochor H, Nyolczas N, Charwat S, Hemetsberger R, Christ G, Edes I, Balogh L, Krause KT, Jaquet K, Kuck KH, Benedek I, Hintea T, Kiss R, Préda I, Kotevski V, Pejkov H, Zamini S, Khorsand A, Sodeck G, Kaider A, Maurer G, Glogar D. Combined delivery approach of bone marrow mononuclear stem cells early and late after myocardial infarction: the MYSTAR prospective, randomized study. *Nat Clin Pract Cardiovasc Med*. 2009;6:70–81.
2. Wollert KC, Meyer GP, Lotz J, Ringes-Lichtenberg S, Lippolt P, Breidenbach C, Fichtner S, Korte T, Hornig B, Messinger D, Arseniev L, Hertenstein B, Ganser A, Drexler H. Intracoronary autologous bone-marrow cell transfer after myocardial infarction: the BOOST randomised controlled clinical trial. *Lancet*. 2004;364:141–148.
3. Yousef M, Schannwell CM, Köstering M, Zeus T, Brehm M, Strauer BE. The BALANCE Study: clinical benefit and long-term outcome after intracoronary autologous bone marrow cell transplantation in patients with acute myocardial infarction. *J Am Coll Cardiol*. 2009;53:2262–2269.
4. Fuchs S, Kornowski R, Weisz G, Satler LF, Smits PC, Okubagzi P, Baffour R, Aggarwal A, Weissman NJ, Cerqueira M, Waksman R, Serrruys P, Battler A, Moses JW, Leon MB, Epstein SE. Safety and feasibility of transendocardial autologous bone marrow cell transplantation in patients with advanced heart disease. *Am J Cardiol*. 2006;97:823–829.
5. Perin EC, Dohmann HF, Borojevic R, Silva SA, Sousa AL, Silva GV, Mesquita CT, Belém L, Vaughn WK, Rangel FO, Assad JA, Carvalho AC, Branco RV, Rossi MI, Dohmann HJ, Willerson JT. Improved exercise capacity and ischemia 6 and 12 months after transendocardial injection of autologous bone marrow mononuclear cells for ischemic cardiomyopathy. *Circulation*. 2004;110(11 Suppl 1):II213–II218.
6. Arbab AS, Yocum GT, Rad AM, Khakoo AY, Fellowes V, Read EJ, Frank JA. Labeling of cells with ferumoxides-protamine sulfate complexes does not inhibit function or differentiation capacity of hematopoietic or mesenchymal stem cells. *NMR Biomed*. 2005;18:553–559.
7. Farrell E, Wielopolski P, Pavljasevic P, Kops N, Weinans H, Bernsen MR, van Osch GJ. Cell labelling with superparamagnetic iron oxide has no effect on chondrocyte behaviour. *Osteoarthr Cartil*. 2009;17:961–967.
8. Hu SL, Zhang JQ, Hu X, Hu R, Luo HS, Li F, Xia YZ, Li JT, Lin JK, Zhu G, Feng H. *In vitro* labeling of human umbilical cord mesenchymal stem cells with superparamagnetic iron oxide nanoparticles. *J Cell Biochem*. 2009;108:529–535.
9. Ju S, Teng G, Zhang Y, Ma M, Chen F, Ni Y. *In vitro* labeling and MRI of mesenchymal stem cells from human umbilical cord blood. *Magn Reson Imaging*. 2006;24:611–617.
10. Neri M, Maderna C, Cavazzin C, Deidda-Vigoriti V, Politi LS, Scotti G, Marzola P, Sbarbati A, Vescovi AL, Gritti A. Efficient *in vitro* labeling of human neural precursor cells with superparamagnetic iron oxide particles: relevance for *in vivo* cell tracking. *Stem Cells*. 2008;26:505–516.
11. Wang L, Deng J, Wang J, Xiang B, Yang T, Gruwel M, Kashour T, Tomanek B, Summer R, Freed D, Jassal DS, Dai G, Glogowski M, Deslauriers R, Arora RC, Tian G. Superparamagnetic iron oxide does not affect the viability and function of adipose-derived stem cells, and superparamagnetic iron oxide-enhanced magnetic resonance imaging identifies viable cells. *Magn Reson Imaging*. 2009;27:108–119.
12. Arbab AS, Yocum GT, Kalish H, Jordan EK, Anderson SA, Khakoo AY, Read EJ, Frank JA. Efficient magnetic cell labeling with protamine sulfate complexed to ferumoxides for cellular MRI. *Blood*. 2004;104:1217–1223.
13. Vukmanovic-Stejic M, Reed JR, Lacy KE, Rustin MH, Akbar AN. Mantoux Test as a model for a secondary immune response in humans. *Immunol Lett*. 2006;107:93–101.
14. Kumar V, Abbas AK, Fausto N, Mitchell RN. *Robbins Basic Pathology*. 8th Edition. Amsterdam, The Netherlands: Saunders/Elsevier; 2007.
15. Wood JC, Enriquez C, Ghugre N, Tyzka JM, Carson S, Nelson MD, Coates TD. MRI R2 and R2* mapping accurately estimates hepatic iron concentration in transfusion-dependent thalassemia and sickle cell disease patients. *Blood*. 2005;106:1460–1465.
16. Pawelczyk E, Arbab AS, Pandit S, Hu E, Frank JA. Expression of transferrin receptor and ferritin following ferumoxides-protamine sulfate labeling of cells: implications for cellular magnetic resonance imaging. *NMR Biomed*. 2006;19:581–592.
17. Huang DM, Hsiao JK, Chen YC, Chien LY, Yao M, Chen YK, Ko BS, Hsu SC, Tai LA, Cheng HY, Wang SW, Yang CS, Chen YC. The promotion of human mesenchymal stem cell proliferation by superparamagnetic iron oxide nanoparticles. *Biomaterials*. 2009;30:3645–3651.
18. Bulte JW, Kraitchman DL, Mackay AM, Pittenger MF. Chondrogenic differentiation of mesenchymal stem cells is inhibited after magnetic labeling with ferumoxides. *Blood*. 2004;104:3410–2; author reply 3412.
19. Kostura L, Kraitchman DL, Mackay AM, Pittenger MF, Bulte JW. Feridex labeling of mesenchymal stem cells inhibits chondrogenesis but not adipogenesis or osteogenesis. *NMR Biomed*. 2004;17:513–517.
20. Cromer Berman SM, Walczak P, Bulte JW. Tracking stem cells using magnetic nanoparticles. *Wiley Interdiscip Rev Nanomed Nanobiotechnol*. 2011;3:343–355.
21. Anderson SA, Glod J, Arbab AS, Noel M, Ashari P, Fine HA, Frank JA. Noninvasive MR imaging of magnetically labeled stem cells to directly identify neovasculature in a glioma model. *Blood*. 2005;105:420–425.
22. Cao AH, Shi HJ, Zhang Y, Teng GJ. *In vivo* tracking of dual-labeled mesenchymal stem cells homing into the injured common carotid artery. *Anat Rec (Hoboken)*. 2009;292:1677–1683.
23. Kim U, Shin DG, Park JS, Kim YJ, Park SI, Moon YM, Jeong KS. Homing of adipose-derived stem cells to radiofrequency catheter ablated canine atrium and differentiation into cardiomyocyte-like cells. *Int J Cardiol*. 2011;146:371–378.
24. Song M, Kim Y, Kim Y, Ryu S, Song I, Kim SU, Yoon BW. MRI tracking of intravenously transplanted human neural stem cells in rat focal ischemia model. *Neurosci Res*. 2009;64:235–239.
25. Kraitchman DL, Heldman AW, Atalar E, Amado LC, Martin BJ, Pittenger MF, Hare JM, Bulte JW. *In vivo* magnetic resonance imaging of mesenchymal stem cells in myocardial infarction. *Circulation*. 2003;107:2290–2293.
26. Loebinger MR, Kyrtatos PG, Turmaine M, Price AN, Pankhurst Q, Lythgoe MF, Janes SM. Magnetic resonance imaging of mesenchymal stem cells homing to pulmonary metastases using biocompatible magnetic nanoparticles. *Cancer Res*. 2009;69:8862–8867.
27. de Vries IJ, Lesterhuis WJ, Barentsz JO, Verdijk P, van Krieken JH, Boerman OC, Oyen WJ, Bonenkamp JJ, Boezeman JB, Adema GJ, Bulte JW, Scheenen TW, Punt CJ, Heerschap A, Figdor CG. Magnetic resonance tracking of dendritic cells in melanoma patients for monitoring of cellular therapy. *Nat Biotechnol*. 2005;23:1407–1413.
28. Toso C, Vallee JP, Morel P, Ris F, Demuylder-Mischler S, Lepetit-Coiffe M, Marangon N, Saudek F, James Shapiro AM, Bosco D, Berney T. Clinical magnetic resonance imaging of pancreatic islet grafts after iron nanoparticle labeling. *Am J Transplant*. 2008;8:701–706.
29. Zhu J, Zhou L, XingWu F. Tracking neural stem cells in patients with brain trauma. *N Engl J Med*. 2006;355:2376–2378.

CLINICAL PERSPECTIVE

In the coming years, regenerative medicine and cell-based therapies may become important options to limit and even regress a wide range of diseases. In clinical trials, however, it is challenging to evaluate the efficacy of cell-based treatments because there is no currently available method of determining the proportion of administered cells reaching and remaining in the target therapeutic site. As a result, there is considerable interest in the development of strategies that would enable noninvasive clinical cell tracking to determine the distribution and time course of infused cells. Magnetic resonance imaging is ideal for this purpose because it combines high-spatial resolution with excellent soft tissue contrast while avoiding ionizing radiation. We have labeled autologous peripheral blood mononuclear cells with a magnetic resonance imaging contrast agent containing superparamagnetic particles of iron oxide (SPIO). We have shown the safety and feasibility of SPIO cell labeling and tracking in humans. Furthermore, this is the first study to demonstrate that SPIO-labeled cells can be tracked to a target site of inflammation following intravenous administration. SPIO cell tracking could therefore be a useful tool for the assessment and further development of cell-based treatment options. In addition, SPIO cell tracking could be applied to dynamic leukocyte trafficking to investigate the contribution of inflammatory processes to disease pathology and to evaluate the effects of novel pharmacological interventions

SUPPLEMENTAL MATERIAL

Methods

Optimization of a GMP-compliant protocol for SPIO labeling of human mononuclear cells

One of the aims of the study was to develop a GMP compliant method of labeling cells with SPIO for cell tracking studies in humans. A range of transfection agents, including poly-L-lysine and the HIV-TAT peptide, has been used to accelerate and maximize SPIO uptake by cells *in vitro*.[1] Most of these transfection agents are unsuitable for use in clinical studies due to their cytotoxicity and potentially harmful systemic effects. An effective method has been described for incorporating SPIO into phagocytic cells using protamine sulphate as a polycationic transfection agent to enhance its uptake through electrostatic interactions.[2] Since both SPIO and protamine sulphate are approved for human use, this method is suitable for labeling cells for clinical studies. We have modified and translated this method into a GMP-compliant protocol.

Using the method described by Arbab et al [2] as a starting point, we sought to establish a protocol for clinical-scale labeling of human mononuclear cells with SPIO under GMP-compliant conditions. In order to guide the method-development process, the *in vitro* labeling efficiency, viability and function of labeled cells were determined following each iteration of the protocol, and the results for the final optimized protocol are reported in the main body of the manuscript.

Initially, processing of the high cell numbers required for clinical cell tracking studies according to the Arbab method had caused problems with cell clumping and

loss of a substantial proportion of cells was encountered. In addition there was a requirement to adapt the Arbab method for use in the GMP setting and to condense the protocol such that cells could be procured and processed for re-infusion on the same day. Particular considerations for the translation of a laboratory method into a GMP protocol include suitability of reagents and vessels for human use, access to an appropriate facility that meets GMP-requirements, and suitability of the protocol to be performed in a reproducible way by a number of operators in different facilities.

In vitro evaluation of cellular effects of SPIO labelling

Immunomagnetic separation of monocytes from peripheral blood mononuclear cells

Using indirect magnetic labelling, monocytes were isolated from PBMC for assessment of cellular iron content and migratory capacity. This technique involves indirect immunomagnetic labelling of non-monocytes (including T cells, B cells, NK cells and basophils) using a cocktail of biotin-conjugated antibodies (CD3, CD7, CD16, CD19, CD56, CD123, Glycophorin A) and magnetic anti-biotin Microbeads (Monocyte Isolation Kit II, Miltenyi Biotec).

PBMC were centrifuged (300 g for 10 min), the supernatant was aspirated entirely and the cell pellet was resuspended in 30 μL per 10^7 cells of buffer (PBS, 0.5% bovine serum albumin, 2 mM EDTA). 10 μL of FcR blocking reagent and 10μL of biotin-antibody cocktail per 10^7 cells were added and the mixture was incubated for 10 min at 4 °C. 30 μL of buffer and 20 μL of anti-biotin microbeads per 10^7 cells were added and the mixture was incubated for 15 min at 4 °C. Cells were washed in 2 mL of buffer and centrifuged at 300 g for 10 min before being re-suspended in 500

μL of buffer. A MACS column was placed in a magnetic field (1.5 T) and primed with 3 mL of buffer. Cells were passed through a pre-separation filter (pore size 100 μm) into the column and the effluent containing the monocytes was collected. Non-monocytes were retained within the column. Flow cytometry confirmed the monocyte purity to be approximately 90%.

Quantification of cellular iron content

Cellular iron content was assessed using the Ferrozine assay. 10^5 monocytes were lysed for 10 min in 100 μL of 1% triton. 100 μL of iron-releasing reagent (a freshly mixed solution of equal volumes of 1.4 M HCl and 4.5% $KMnO_4$ in distilled water) was added and the tubes were incubated at 60 °C for 2 h to release protein-bound iron (eg haemoglobin, ferritin). The mixture was then cooled to room temperature and 30 μL of the iron detection reagent was added (6.5 nM Ferrozine, 6.5 mM Neocuprine, 2.5 M ammonium acetate and 1 M ascorbic acid in distilled water). After 30 min, 280 μL of the resulting solution was transferred to a 96 well plate.

In order to determine the actual iron content of the test solutions a standard curve was generated using solutions of known concentration of $FeCl_3$ in 10 mM HCl (range 0-300 μM). 100 μL of 50 nM NaOH and 100 μL of the iron detection reagent were added to 100 μl of the iron standard solution. After 30 min, 280 μL of the solution was transferred to the 96-well plate. A plate reader was used to measure the light absorbance at 490 nm. The iron content was expressed in picograms (pg) of iron per cell.

Cell viability

Cells were allowed to adhere for 1 hour in 24-well tissue culture plates (10^6 cells/well; 37°C; 5% CO_2) following which the medium was harvested and exchanged for fresh Iscove's modified Dulbecco's medium (IMDM) supplemented with penicillin (100 U/mL), streptomycin (100 U/mL) and 10% autologous serum. This prevented continued uptake of SPIO and avoided interference of excess SPIO with the assays.

Flow Cytometry: annexin V binding and propidium iodide (PI) staining

Cells were harvested for analysis at 1, 24 and 72 h using 0.25% trypsin and EDTA. Cell suspensions were incubated for 10 min on ice in annexin V-binding buffer (Hank's balanced salt solution (HBSS) containing 5 mM $CaCl_2$) with FITC-annexin V. PI (final concentration 2 μg/mL) was added to the cell suspension/annexin V binding buffer mixture for 1 min prior to analysis using a FACSCalibur flow cytometer (Becton Dickinson, USA) equipped with CellQuest data analysis software.

Annexin V binds to phosphatidylserine expressed at the surface of cells in the early phase of apoptosis, and propidium iodide staining indicates permeability of the cell membrane in necrotic cells and cells in the late phase of apoptosis. Cells that were negative for both annexin V binding and PI staining were classed as viable. The percentage of cells that were positive for annexin V binding, PI staining, or both were combined to give an overall percentage of cytotoxicity.

Lactate Dehydrogenase Assay

The potential cytotoxicity of SPIO-labeling was also assessed using a lactate dehydrogenase assay (LDH; Roche, Diagnostics Ltd, UK) according to the

manufacturer's instructions. LDH is ubiquitous in all cells, is released following cell membrane damage and can be used to measure cytotoxicity.

After 24, 48 or 72 h supernatants were collected for LDH measurement. Remaining cells were lysed and LDH was measured in the cell lysates in order to calculate the total LDH activity. The LDH activity in the supernatant as a percentage of the total (supernatant plus lysed cells) was calculated to give the percentage cytotoxicity.

Quantification of Cytokine release

The concentration of the inflammatory cytokines interleukin (IL)-1b, IL-6, IL-8, IL-10, IL-12p70, and tumour necrosis factor (TNF) released from cells post labelling was measured using a cytometric bead array kit (Human Inflammatory Cytokine Kit; Becton Dickinson, USA) according to the manufacturer's instructions.

Labeled and unlabeled cells were plated as described above for 24, 48 and 72 h. Cell supernatants were harvested and stored (-70°C) for batch analysis. Each sample (25 µL) was incubated (3 h; room temperature; protected from light) with the mixed Human Inflammation Capture Bead suspension (25 µL) in a round-bottomed 96 well tissue culture plate. Analysis was performed by FACSArray cytometer (Becton Dickinson, USA) equipped with FACSArray data analysis software. The concentration of each cytokine was calculated from a standard curve generated from the Human Inflammation Standards provided.

Migratory capacity

Labeled and unlabeled MACS-purified monocytes were loaded into the upper chamber ($2.5x10^5$ cells/well) of a modified Boyden chamber (Transwell polycarbonate inserts; 5 μM pore size, 24-well plates; Corning Costar, USA). Cells were allowed to migrate for 2 h (37°C with 5% CO_2) through the microporous membrane into the lower chamber containing 600 μL RPMI (Sigma Aldrich) with and without the chemokine human monocyte chemoattractant protein 1 (MCP-1; Recombinant Human CCL2/MCP-1, R&D Systems; 50ng/mL). Cells that had actively migrated through the membrane and adhered to its underside were fixed (100% methanol; 10 min) and stained with DiffQuik™ physiological stain as well as with the Prussian Blue stain for iron. Transmigration was quantified by counting the number of cells present in five randomly selected high power light microscopy fields (x40).

Results

Development of a GMP-compliant protocol for labeling human mononuclear cells with SPIO

Using the method described by Arbab *et al*[2] as a starting point, the Edinburgh protocol was established for clinical-scale labeling of human mononuclear cells with SPIO under GMP-compliant conditions. Initial processing of high cell numbers caused problems with cell clumping (Supplemental Figure 1) and a high proportion of cells was lost during the labelling process.

In pursuit of a protocol that would minimize cell clumping, maximize yield and maintain SPIO uptake, we added SPIO (Endorem) and protamine sulphate directly into the cell suspension avoiding the formation of large complexes. Continuous agitation using a roller-mixer avoided gravitational sedimentation during incubation, exposing all cells to SPIO uniformly and reducing clumping. When cells were labeled in suspension, SPIO became cell-associated almost immediately, initially adhering to the outer surface of the cell and subsequently being incorporated into the cell during the remainder of the incubation period. In contrast to the situation when cells are labeled whilst adherent or when allowed to settle out of suspension, almost no free SPIO remained at the end of the incubation period if continuous agitation was employed.

In vitro evaluation of cellular effects of SPIO labelling

These results are described in the main body of the manuscript

Supplementary Figure 1. SPIO labeled cells

Labeling a high number of cells by the original method resulted in significant clumping (a). However when cells were labeled according to the Edinburgh protocol, which has been optimized for processing cells on a clinical scale, cells remained in a single-cell suspension (b).

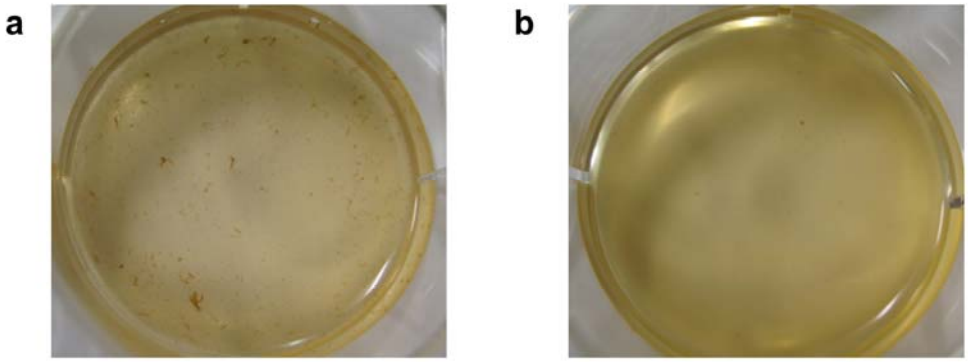

Supplementary Figure 2. Uptake of SPIO by CD14+ monocytes

Granularity (side scatter) of CD14+ cells was examined by flow cytometry as a surrogate marker of nanoparticle internalization. Labeled and unlabeled cells were stained with phycoerythrin (PE)-conjugated anti-human CD14 antibodies (1:1000 dilution; BD Biosciences, UK) prior to analysis by a FACScalibur Flow Cytomter (Beckman Coulter, USA) equipped with CellQuest data analysis software. (a) CD14 positive cells (monocytes) increased their side scatter following SPIO labeling (b) indicating increased granularity and SPIO internalization.

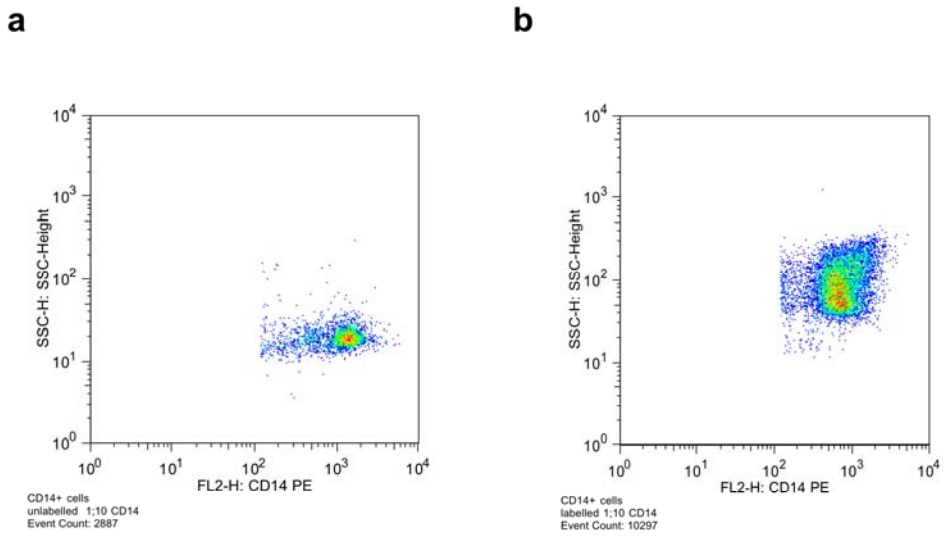

References

1. Arbab AS, Yocum GT, Wilson LB, Parwana A, Jordan EK, Kalish H, Frank JA. Comparison of transfection agents in forming complexes with ferumoxides, cell labeling efficiency, and cellular viability. *Molecular imaging : official journal of the Society for Molecular Imaging.* 2004;3:24-32.
2. Arbab AS, Yocum GT, Kalish H, Jordan EK, Anderson SA, Khakoo AY, Read EJ, Frank JA. Efficient magnetic cell labeling with protamine sulfate complexed to ferumoxides for cellular MRI. *Blood.* 2004;104:1217-1223.